Search for the Higgs Boson in the WH Production Mode with $H \to WW^*$ Decay using the ATLAS Detector

Petar Kevin Rados

Submitted in total fulfilment of the requirements
of the degree of Doctor of Philosophy

May 2018

School of Physics
The University of Melbourne

Produced on archival quality paper

Abstract

In order for fundamental particles to attain mass, the electroweak symmetry of the Standard Model (SM) of particle physics must be broken. The simplest way of breaking this symmetry is via the SM Higgs Mechanism, and it predicts the existence of a new particle called the SM Higgs boson. This particle should be experimentally accessible at the high-energy frontier, and so its discovery is considered as one of the most important goals in modern particle physics. This goal was partially achieved in July 2012, when the ATLAS and CMS experiments at the Large Hadron Collider (LHC) announced the discovery of a Higgs-like particle with a mass of around 125 GeV. The next step for both experiments is to scrutinize the properties of this new particle in order to determine whether it is, in fact, the SM Higgs boson.

One high-priority objective of the ATLAS experiment is to confirm the SM predictions for Higgs boson production at the LHC. The main result presented in this thesis contributes to this objective by searching for the WH production mode with subsequent $H \rightarrow WW^*$ decay. The $H \rightarrow WW^*$ decay channel provides a sensitive probe of WH production due to its large branching ratio and clean detector signature. Moreover, this signal process provides important information on the Higgs boson couplings, since it only involves couplings to W bosons at both the production and decay vertices at tree-level.

The search for this signal process was conducted using LHC proton-proton collision data collected by the ATLAS detector. This data was recorded at centre-of-mass energies of 7, 8 and 13 TeV corresponding to integrated luminosities of 4.5, 20.3 and 5.8 fb^{-1}, respectively. The analysis strategy was first developed using the 7 and 8 TeV data samples and it was used to measure the relative signal strength with respect to the SM expectation. For a Higgs boson of mass 125 GeV, the observed value of the signal strength was determined to be $0.72\ ^{+1.2}_{-1.1}$ (stat.) $^{+0.4}_{-0.3}$ (sys.). The analysis method was then extended to perform the first measurement of the signal strength at 13 TeV, with this quantity measured to be $3.2\ ^{+3.7}_{-3.2}$ (stat) $^{+2.3}_{-2.7}$ (sys). An overall excess was observed at 0.66σ (0.77σ) significance with respect to the background-only hypothesis in the 7+8 TeV (13 TeV) data. All measurements are in agreement with the SM expectations.

Declaration

This is to certify that:

1. this thesis comprises only my original work towards the PhD except where indicated in the Preface,

2. due acknowledgement has been made in the text to all other material used,

3. the thesis is less than 100,000 words in length, exclusive of tables, bibliographies and appendices.

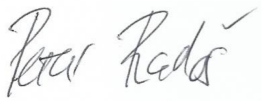

Petar Kevin Rados

Preface

The ATLAS Collaboration consists of over 3000 scientific authors from 38 countries and represents one of the largest collaborative efforts in science. Considering this, it is very rare that any substantial body-of-work within ATLAS will be done by a student in isolation. When conducting research projects, a student will typically work within groups that each have a specific purpose within the larger collaboration.

The work of this author is presented in chapters 4 and 5 of this thesis, and was done in concert with several different ATLAS working groups detailed below. The three earlier chapters provide an introduction, the motivation and a description of the experimental setup relevant to this author's work. The final chapter of this thesis summarizes the main results of this work.

Section 4.1 provides context to the work of this author presented later in chapter 4. Section 4.2 summarizes a relevant paper released by the ATLAS Collaboration [1] on work conducted by the ATLAS Tau Trigger and Offline Tau Identification working groups. This is done to give context to this author's work conducted within the ATLAS Tau Trigger working group, which is presented in section 4.3. This work was done under the supervision of E. Barberio and P. Urquijo, and was included in the previously mentioned paper. This work included: the development of the software framework, preparation of the data and MC samples, development of the tag-and-probe method, measurements of the tau trigger efficiencies in data, measurements of the tau trigger efficiency correction factors for simulation, and the measurements of the energy resolutions at each trigger-level.

Section 4.4 summarizes a relevant technical design report released by the ATLAS Collaboration [2] on work conducted by the ATLAS FTK working group. This is done to give context to this author's work performed within that group, which is presented in section 4.5. This work was done under the supervision of E. Barberio and P. Urquijo and in collaboration with V. Cavaliere, and was included in the previously mentioned technical design report. This work included: the measurement of FTK tracking efficiencies and track multiplicities for tau leptons, the development of a tau trigger algorithm that uses FTK tracks, and the performance measurements of this algorithm. The results shown specifically in subsection 4.5.5 were not the work of this author and were performed later by the ATLAS FTK working group. This subsection is

included in order to demonstrate how the trigger algorithm developed by this author improves the sensitivity of analyses performed by ATLAS in the $H \to \tau\tau$ decay channel.

Chapter 5 presents the work of this author conducted within the VH production mode subgroup of the ATLAS $H \to WW$ working group. This work was done under the supervision of E. Barberio and T. Kubota, with the $\sqrt{s} = 7$ and 8 TeV analysis released by the ATLAS Collaboration in a paper [3] and the $\sqrt{s} = 13$ TeV analysis in a conference note [4]. The $\sqrt{s} = 7$ and 8 TeV analysis presented in chapter 5 was done in collaboration with the following members, in alphabetical order, of the VH subgroup: T. Baroncelli, M. Biglietti, V. Bortolotto, B. Di Micco, A. Farilla, A. Huitfeldt, T. Kubota, D. Orestano, D. Puddu, L. Shan, J. Smith, C. Taccini and M. Trovatelli. The $\sqrt{s} = 13$ TeV analysis was done in collaboration with the following members of the same subgroup: C. Bertella, M. Biglietti, A. Farilla, A. Huitfeldt, T. Kubota, R. Munoz, D. Puddu, C. Shmitt, O. Whitton and N. Wieseotte. The work of this author covered most aspects of the analyses, including: the collaborative development of the analysis framework, preparation of the data and MC samples, electron and muon trigger studies, definition and optimization of the analysis selection, development of the background estimation methods, evaluation of the experimental uncertainties, calculation and inclusion of the theoretical uncertainties, and running the statistical fit.

Appendix A includes a description of the BDT method used in two of the signal regions from the $\sqrt{s} = 7$ and 8 TeV analysis of the VH subgroup. Appendix C includes results from the combination of all analyses performed by the ATLAS $H \to WW$ working group at $\sqrt{s} = 7$ and 8 TeV. Both the BDT methd and the statistical combination of all the analyses were not the work of this author. Appendices C and D include additional plots from the analyses presented in chapter 5.

Acknowledgements

I would first like to thank both Prof. Elisabetta Barberio and Dr. Takashi Kubota. Elisabetta has been my senior supervisor during both my MSc and PhD degrees at The University of Melbourne, and I have worked in close collaboration with Takashi throughout my graduate studies. Their mentorship, encouragement and support have been invaluable to my research activities, and I can only hope to emulate their example in my future career.

I would also like to thank both past and present members of the Experimental Particle Physics group at Melbourne and the ARC Centre of Excellence for Particle Physics at the Terascale (CoEPP). There are too many people worthy of thanks to list here but, in alphabetical order, I would like to give a special thanks to: L. Boland, S. Crosby, N. Dawe, A. Huitfeldt, D. Jennens, B. Le, P. McNamara, M. Milesi, R. Munoz, F. Nuti, L. Ong, N. Rodd, T. Shao, J. Smith, L. Spiller, KG. Tan, G. Taylor, T. Taylor, P. Urquijo, O. Whitton, and D. Zanzi. Graduate studies can often be a lonely pursuit, but I have been fortunate to be embedded in a friendly, supportive and knowledgeable particle physics community both in Melbourne and Australia at large.

Throughout my graduate studies I have had the pleasure of collaborating with numerous ATLAS colleagues from all around the world. This includes, but is not limited to, the people mentioned in the Preface of this thesis. Publishing the tau performance paper, the FTK technical design report, the $\sqrt{s} = 7$+8 TeV Higgs analysis paper and the $\sqrt{s} = 13$ TeV Higgs analysis conference note required huge group efforts, and everyone played an important role.

Finally to my father Milan, my mother Monica, my brother Krizan, my sister Elanore, my brother-in-law Tomi, my niece Tihana and my nephew Markus. No words can describe how much I appreciate your help and support not only during my graduate studies, but throughout my entire life. Thank you from the bottom of my heart.

To my family, for all their love and support.
Thank you Milan, Monica, Krizan, Elanore, Tomi, Tihana and Markus.

Contents

1

Introduction

Particle physics is a particular field in science that aims to understand the most fundamental building blocks of matter and their interactions. The benchmark theoretical framework in this field is known as the Standard Model (SM), and over the last four decades its ability to explain high-energy phenomena has been rigorously scrutinized. Although the theory has, so far, passed all experimental tests with a great degree of success, it is known to be incomplete.

One of the main open questions in particle physics is which mechanism breaks the electroweak symmetry of the SM and thus generates particle masses. The simplest mechanism is the SM Higgs Mechanism, and it predicts the existence of a particle known as the SM Higgs boson. This particle should be experimentally accessible at the high-energy frontier, and so its discovery is regarded as one of the most important goals in particle physics.

The Large Hadron Collider (LHC) is a particle accelerator that can collide protons at unprecedented center-of-mass energies ($\sqrt{s}$) of up to 14 TeV. It was built at CERN, near Geneva, and since March 2010 has been operating at $\sqrt{s} = 7, 8$ and more recently 13 TeV. One of the primary physics goals of the LHC is to either prove or refute the existence of the SM Higgs boson. This goal was partially achieved on the 4^{th} of July,

2012, when the ATLAS and CMS experiments at the LHC announced the discovery of a Higgs-like particle with a mass of approximately 125 GeV [5, 6].

The next step for the Higgs program at ATLAS is to measure the properties of this new particle to confirm whether it is, in fact, the one predicted by the SM Higgs Mechanism. To this end, directly observing each of its production modes is essential. Since the discovery of the Higgs-like particle, the ATLAS experiment has confirmed the existence of the dominant gluon fusion production mode and found significant evidence for the subdominant vector-boson fusion mode, at rates consistent with the SM predictions [7]. However, finding direct evidence for the more rare production modes must also be achieved in order to complete the picture of SM Higgs boson production. The associated production of the Higgs boson with a W boson, referred to throughout this thesis as WH production, has the next largest cross section after vector-boson fusion and is therefore a promising next candidate for direct observation.

The main result presented in this thesis is a search for the SM Higgs boson in the WH production mode followed by $H \to WW^*$ decay. This search was performed using proton-proton collision data collected by the ATLAS detector at $\sqrt{s} = 7$, 8 and 13 TeV. The $H \to WW^*$ decay channel is a good candidate for the direct observation of WH production since it has the second largest branching fraction at the measured Higgs boson mass, and it provides a clean detector signature. In addition, the combined production and decay process is interesting due to its sensitivity to any deviations to the SM prediction of the coupling between the Higgs and W bosons.

This thesis also includes studies conducted by this author relating to the ATLAS tau trigger. The tau trigger plays a key role in collecting data used in many ATLAS physics analyses, including the search for the SM Higgs boson in the $H \to \tau\tau$ decay channel. Two studies are presented. The first is the measurement of the tau trigger performance at $\sqrt{s} = 8$ TeV using a tag-and-probe method targeting $Z \to \tau\tau$ decays. The second study explores the potential of using the ATLAS Fast Tracker upgrade to improve tau trigger performance in future ATLAS runs at $\sqrt{s} = 14$ TeV.

This thesis is organized as follows. The next chapter provides the motivations for the SM Higgs boson studies presented in this thesis. A description of the LHC, the ATLAS detector and how collision events are reconstructed is presented in chapter 3. Chapter 4 is dedicated to the ATLAS tau trigger studies. Chapter 5 presents the search for the WH production of the SM Higgs boson with $H \to WW^*$ decay. The final chapter summarizes the key results presented in this thesis.

2

The Standard Model Higgs Boson

This chapter provides both the theoretical and experimental motivations for the SM Higgs boson studies presented in this thesis. This will first include, in section 2.1, an overview of the SM of particle physics and the Higgs Mechanism. The ways in which the SM Higgs boson can be produced at the LHC and subsequently decay will be described in sections 2.2 and 2.3, respectively. Finally, section 2.4 will summarize the discovery of the Higgs-like particle, its subsequent measurements from the ATLAS experiment at $\sqrt{s}$ = 7 and 8 TeV, and the next steps for the ATLAS Higgs program at $\sqrt{s}$ = 13 and 14 TeV.

2.1 The Standard Model and the Higgs Mechanism

Scientists in the field of particle physics have made incredible progress over the years towards their common goal of understanding the properties of the basic building blocks of matter and how they interact. We now know that everything in the universe is made up from a handful of fundamental particles whose interactions are governed by four fundamental forces. Our current most complete understanding of how these

particles and three of the forces[1] are related to each other is provided by a theoretical framework known as the SM [8–11]. Since it was formulated in the early 1970s, the SM has precisely predicted a wide variety of phenomena and through many experiments has become one of the most well-tested theories in physics [12,13]. The particle content of the SM is shown in figure 2.1, and will be detailed in sections 2.1.1 and 2.1.2.

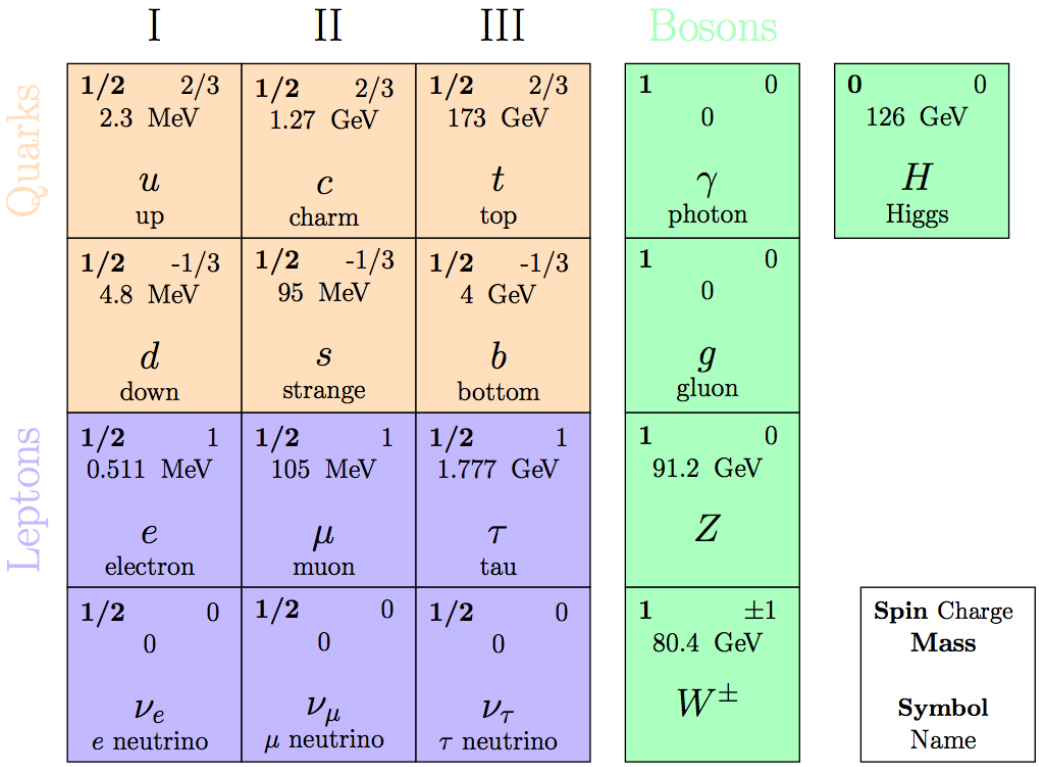

Figure 2.1 Summary of the fundamental particles in the SM. The quarks (orange), leptons (violet) and their three generation structure (I, II and III) are shown. The gauge and Higgs bosons (green) are also shown. The mass, spin and electric charge quantum numbers are specified for each particle. Details are provided in sections 2.1.1 and 2.1.2.

[1]The gravitational force is not accounted for in the SM.

2.1.1 Fermions

The twelve particles which make up matter are called fermions, and each of them has spin $\frac{1}{2}$. Every fermion has a corresponding anti-fermion with the same mass but opposite electric charge. The fermions consist of six quarks and six leptons, organized into three generations where each contains one pair of quarks and one pair of leptons. The higher generations are copies of the lower generations, with larger masses but the same quantum numbers.

The quarks in each family contain one up-type quark and one down-type quark. Up-type quarks have an electric charge of $+\frac{2}{3}$, while for down-type quarks it is $-\frac{1}{3}$. In the order of the generations these include: the up and down, the charm and strange, and the top and bottom quarks. Quarks have never been observed in isolation, and rather exist in bound states known as hadrons.

The leptons in each generation contain one charged lepton, with electric charge 1, and one electrically neutral neutrino. Neutrinos are assumed to be massless in the SM, and it is not yet known whether they are different from their anti-particles. In the order of the generations these include: the electron and electron neutrino, the muon and muon neutrino, and the tau and tau neutrino.

2.1.2 Gauge Bosons

The SM accounts for the electromagnetic, weak and strong forces through the exchange of another class of particles called gauge bosons that have spin 1. The electromagnetic interaction is mediated by the massless photon, while for the weak interaction it is the massive $W^{\pm}$ and Z bosons. Together, the electromagnetic and weak interactions are unified under the electroweak (EW) interaction. The photon couples to particles with electric charge, while the massive gauge bosons couple to particles that carry weak isospin. The massless gluons, for which there are eight, mediate the strong interaction between particles carrying colour charge.

2.1.3 Gauge Symmetries

The SM is based on the mathematical framework of quantum field theory in which particles are described by quantized fields, and the field dynamics are encapsulated

in a Lagrangian density. As dictated by Noether's theorem [14], conservation laws, such as the one associated to electric charge, are the byproduct of imposing certain symmetries on the SM Lagrangian.

Particles that are free and non-interacting are described by a Lagrangian that is symmetric under global gauge transformations. However, new terms enter the Lagrangian after requiring, in addition, invariance under local gauge transformations. The interactions of the SM mediated by gauge bosons, as described earlier in section 2.1.2, are encoded in these additional terms.

The particular unitary group of local gauge transformations that describe the symmetries of the SM Lagrangian is:

$$SU(3)_C \times SU(2)_L \times U(1)_Y \tag{2.1}$$

The non-Abelian $SU(3)_C$ gauge symmetry governs the strong interaction between the quarks and gluons which carry colour charge (C). The unified EW interaction is determined by the $SU(2)_L \times U(1)_Y$ gauge symmetry which, if you recall, was mediated by the photon, $W^{\pm}$ and Z bosons. Here, the Y is the weak hypercharge and the L signifies that the weak interaction only occurs between left-handed particles (or right-handed anti-particles).

2.1.4 The Higgs Mechanism

The $SU(2)_L \times U(1)_Y$ local gauge symmetry of the EW interaction requires that the $W^{\pm}$ and Z bosons are massless. Moreover, the global $SU(2)$ symmetry and parity violation prohibit fermion masses. We know that the quarks, charged leptons, $W^{\pm}$ and Z bosons do in fact have mass; so clearly something fundamental is missing from the picture described in section 2.1.3.

A solution to this problem was proposed in 1964-1965 by Brout and Englert [15], Higgs [16, 17] and Kibble, Guralnik and Hagan [18] in what is now known as the Brout-Englert-Higgs Mechanism. This mechanism will be referred to, hereafter, as simply the SM Higgs Mechanism.

In the SM Higgs Mechanism, particles acquire mass after the EW symmetry has been spontaneously broken. This is achieved by introducing into the SM a new complex scalar field ϕ, called the Higgs field, with quanta that are weak isospin doublets with

four degrees of freedom. The Higgs field has an associated energy potential $V(\phi)$ in which it could occupy an infinite number of non-unique and degenerate vacuum states. The EW symmetry is broken when the Higgs field arbitrarily and so, we say, spontaneously settles into a particular vacuum state.

The simplest form for $V(\phi)$ that breaks the EW symmetry in the desired way is:

$$V(\phi) = -\mu^2\phi^\dagger\phi + \frac{\lambda}{2}(\phi^\dagger\phi)^2 \tag{2.2}$$

which is bounded from below for $\mu^2 > 0$ and $\lambda > 0$. It has a local maximum at $\phi = 0$ and a ring of degenerate absolute minima at:

$$v = \sqrt{\frac{\mu^2}{\lambda}}e^{i\theta} \tag{2.3}$$

The shape of $V(\phi)$ is shown in figure 2.2. In this figure, the ball rolling down the hill symbolizes ϕ spontaneously settling into a particular vacuum states ϕ_0 and, in doing so, acquiring the non-zero vacuum energy in equation 2.3.

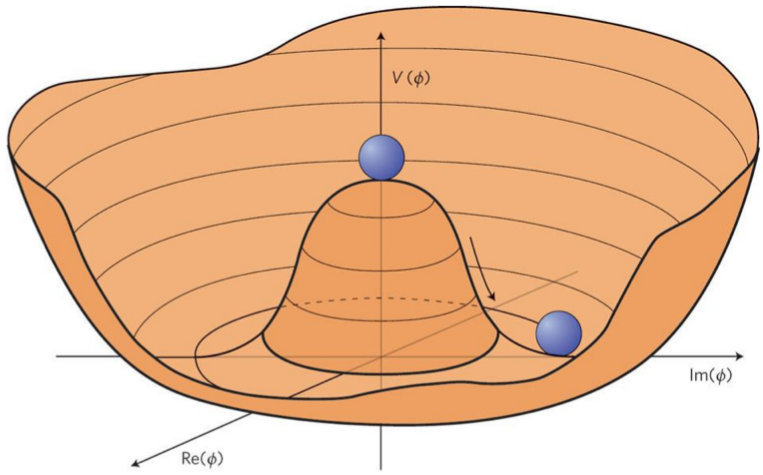

Figure 2.2 The shape of $V(\phi)$ in the phase space of the complex field ϕ.

The vacuum energy can be selected where $\theta = 0$, without loss of generality, and then ϕ_0 becomes:

$$\phi_0 = \frac{1}{\sqrt{2}}\begin{pmatrix} 0 \\ v \end{pmatrix} \tag{2.4}$$

where $v = 246$ GeV. We can then consider excitations in the Higgs field by expanding around ϕ_0:

$$\phi = \frac{1}{\sqrt{2}} \begin{pmatrix} \sigma_1 + i\sigma_2 \\ v + \sigma_3 + i\sigma_4 \end{pmatrix} \tag{2.5}$$

where σ_1, σ_2, σ_3 and σ_4 are the fields four degrees of freedom.

After passing the Higgs field excitations though the EW Lagrangian with $V(\phi)$, new mass terms are produced. The photon remains massless, while three of the degrees of freedom (σ_1, σ_2 and σ_4) become the longitudinal polarizations of the now massive $W^{\pm}$ and Z bosons. The remaining physical degree of freedom, σ_3, is a new massive boson. Its predicted to be electrically neutral, have spin 0 and positive parity[2]. This is the SM Higgs boson, symbol H, and its mass (m_H) is not predicted by the SM. This particle will be referred to, hereafter, as simply the Higgs boson. By manually including Yukawa-type interactions, the fermion masses can also be generated.

The mass of a particle is determined by the strength of its coupling to the Higgs boson. One key feature of the couplings is that they are proportional to the mass of the fermions and the mass squared of the weak bosons. All of the possible couplings are illustrated in figure 2.3.

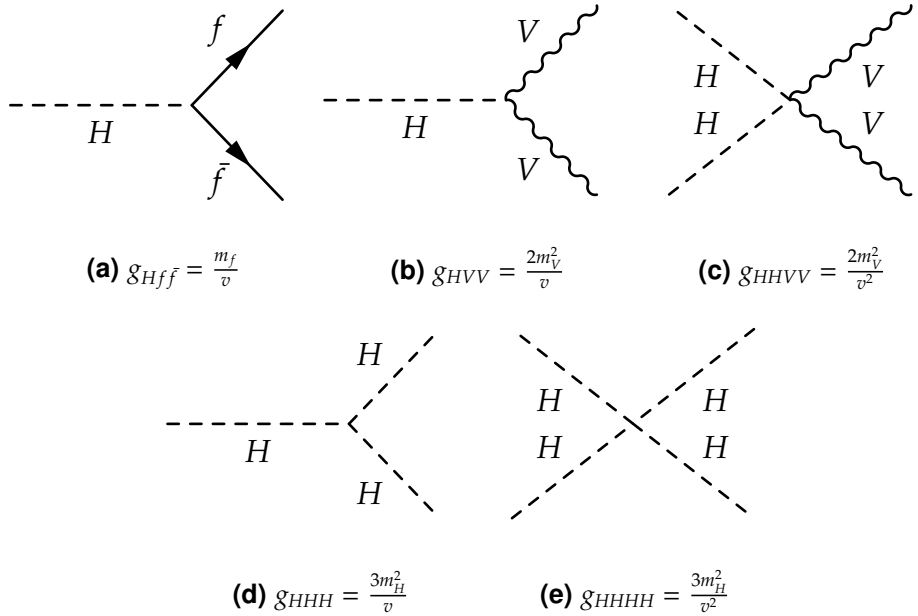

(a) $g_{Hf\bar{f}} = \frac{m_f}{v}$ **(b)** $g_{HVV} = \frac{2m_V^2}{v}$ **(c)** $g_{HHVV} = \frac{2m_V^2}{v^2}$

(d) $g_{HHH} = \frac{3m_H^2}{v}$ **(e)** $g_{HHHH} = \frac{3m_H^2}{v^2}$

Figure 2.3 Couplings of the SM Higgs boson (a) to fermions, (b)-(c) to gauge bosons ($V = W^{\pm}$ or Z) and (d)-(e) to itself [19].

[2]Parity is a measure of how a particles mirror image behaves.

2.2 Higgs Boson Production at the LHC

When protons collide at the LHC many quarks and gluons are produced which can subsequently interact. We call these particles partons, and their relative proportions are determined by what are called parton distribution functions (PDFs). The PDFs describe the probability of finding a parton with a certain longitudinal momentum fraction of the proton, and they depend on the energy of the proton-proton interaction. At LHC energies the PDFs are dominated by gluons and light (first and second generation) quarks, and so most physics processes at the LHC are initiated by pairs of these particles.

Although they are prevalent in LHC collisions, the gluons are massless and, as their name suggests, the light quarks have small masses. Therefore, their couplings to the Higgs boson are either zero or very small and so direct production of the Higgs boson from these particles is heavily suppressed. Instead, pairs of gluons or light quarks will first produce intermediate particles with larger masses, and thus larger Higgs boson couplings, such as weak bosons and top-quarks. The main Higgs boson production modes at the LHC are shown in figure 2.4. Their predicted cross sections as a function of m_H for proton-proton collisions at $\sqrt{s}$ = 8 TeV are shown in figure 2.5. The cross sections for m_H = 125 GeV, which is compatible with the observed value, are shown in table 2.1 for both $\sqrt{s}$ = 7 and 8 TeV collisions.

	ggF	**VBF**	***WH***	***ZH***	$t\bar{t}H$
$\sigma^{7\text{TeV}}$ [pb]	$15.13\ ^{+15\%}_{-15\%}$	$1.222\ ^{+2.8\%}_{-2.4\%}$	$0.5785\ ^{+3.5\%}_{-3.5\%}$	$0.3351\ ^{+5.6\%}_{-5.6\%}$	$0.08632\ ^{+12\%}_{-18\%}$
$\sigma^{8\text{TeV}}$ [pb]	$19.27\ ^{+15\%}_{-15\%}$	$1.578\ ^{+2.8\%}_{-3.0\%}$	$0.7046\ ^{+3.4\%}_{-3.4\%}$	$0.4153\ ^{+5.6\%}_{-5.6\%}$	$0.1293\ ^{+12\%}_{-17\%}$
$\sigma^{8\text{TeV}}$ / $\sigma^{7\text{TeV}}$	1.274	1.291	1.218	1.239	1.498

Table 2.1 The predicted Higgs boson production cross sections in proton-proton collisions at $\sqrt{s}$ = 7 and 8 TeV, for m_H = 125 GeV [20]. The errors correspond to the total theoretical uncertainties. The last row shows that central value of the ratio between the $\sqrt{s}$ = 8 and 7 TeV cross sections.

The gluon fusion (ggF) production mode is the dominant one at the LHC, with the largest contribution coming from the process involving a top-quark loop as seen in figure 2.4a. Although the cross section is large, to first order there is only a Higgs boson produced and so it can be difficult to distinguish this process from backgrounds such as Z/γ^* production. The theoretical uncertainties on the ggF production cross sections

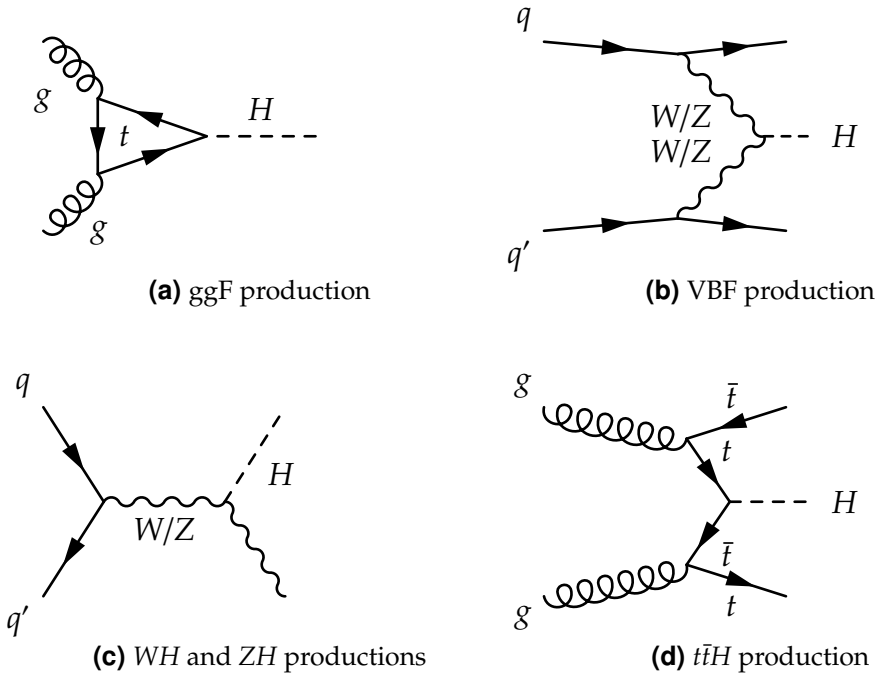

(a) ggF production

(b) VBF production

(c) WH and ZH productions

(d) $t\bar{t}H$ production

Figure 2.4 Feynman diagrams for the main Higgs boson production modes at the LHC.

include those associated to the renormalization and factorization scale dependence of the higher order QCD calculations (QCD scales), the choice of PDF and the strong coupling constant (α_s) [20]. The ggF production cross sections, in particular, tends to have relatively large QCD scale uncertainties.

The vector boson fusion (VBF) production mode has the second largest cross section, although it still a factor of around 12 smaller then ggF for $m_H = 125$ GeV. Nevertheless, it provides a more distinct signature due to presence of two final state quarks, as seen in figure 2.4b, that hadronize into two back-to-back jets[3] in the forward regions of the ATLAS detector. The VBF production mode is an EW process at tree-level and so its cross section has a smaller overall theoretical uncertainties compared to ggF.

The WH and ZH production modes have the next largest cross sections which are factors of about 2 and 4 times smaller then VBF, respectively, for $m_H = 125$ GeV. In these processes a W or Z boson is produced in association with the Higgs boson as seen in figure 2.4c. Although the cross sections are relatively small, these modes have excellent background rejection when either the associated W or Z bosons decay leptonically ($W \to \ell\nu$ or $Z \to \ell\ell$, where ℓ is a charged lepton). Like the VBF mode, the

[3]Jets are collimated sprays of hadrons. Additional information will be provided in chapter 3.

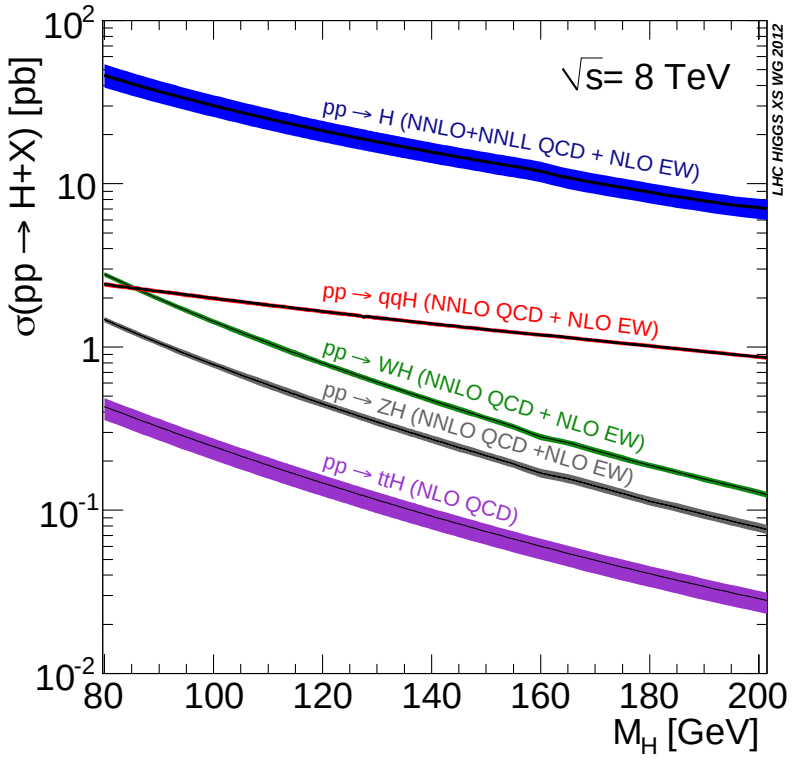

Figure 2.5 The predicted Higgs boson production cross sections in proton-proton collisions at $\sqrt{s} = 8$ TeV, as a function of m_H in the low-mass range [20]. The ggF (blue), VBF (red), WH (green), ZH (grey) and $t\bar{t}H$ (purple) production modes are shown. The theoretical uncertainties are indicated by the bands.

WH and ZH modes are EW at tree-level and so they also benefit from relatively small theoretical uncertainties on the cross sections. The WH production mode is the target of the Higgs boson search presented in this thesis.

Finally, the $t\bar{t}H$ production mode has the smallest cross section that is about 9-11 times smaller then the combined WH and ZH production modes for $m_H = 125$ GeV. Nevertheless, this mode is interesting since it provides a direct probe of the top-quark Yukawa coupling.

2.3 Higgs Boson Decay

The Higgs boson has a short lifetime of around 10^{-22} s [21] and so after being produced at the LHC it will decay before reaching the active regions of the ATLAS detector. There

are many channels through which the Higgs boson can decay. The branching ratio (BR) of a particular decay channel is partially determined by the coupling strength of the decay particles to the Higgs boson. The BR can become suppressed if the Higgs boson mass is smaller then the combined mass of the decay particles, which limits the available phase space. The BRs are shown in figure 2.6 as a function of m_H and in figure 2.7 for m_H = 125 GeV.

The decays into WW and ZZ have the largest BRs out of the bosonic decay channels over the full m_H range. WW is larger since there are more combinatorics with W compared to Z decays, and more available phase space since the W mass (m_W) is smaller then the Z mass (m_Z). For m_H below around 160 GeV, both the WW and ZZ channels start to become suppressed ($2m_W$, $2m_Z > m_H$) and only one of the weak bosons is produced on-shell. Such decays are written WW^* and ZZ^*, where "$*$" indicates a virtual particle that is off-shell.

For m_H = 125 GeV the WW^* decay channel has a large BR at 21%, which is the largest of the bosonic decays and the second largest of all possible decay channels. The BR of ZZ^* is 3% and for $\gamma\gamma$ it is less then 1%. The $\gamma\gamma$ BR is so small since the decay process can only occur at second order of perturbation theory through W boson and top-quark loops. Nevertheless, both the $\gamma\gamma$ and ZZ^* channels compensate for their small BRs by providing very clean detector signatures and the ability to reconstruct m_H with a high degree of precision. The $Z\gamma$ decay has a tiny BR but a clean signature, and although decays into two gluons have a sizable BR they provides little sensitivity due to huge backgrounds.

The decays of the Higgs boson into fermions also have significant BRs in the low-mass region. Although top-quarks have the largest Yukawa coupling due to their large mass, decays into $t\bar{t}$ pairs are negligible since they are heavily suppressed ($2m_t >> m_H$). Rather, it is the decay into $b\bar{b}$ pairs that provides not only the largest fermionic BR, but the largest BR of all possible decay channels at 58% for m_H = 125 GeV. However, this channel suffers from large backgrounds and so it is searched for in the WH and ZH production modes, providing much needed background rejection at the expense of the reduced production cross sections.

The second largest BR into fermions is for the decay into a pair of tau leptons. The $\tau\tau$ channel does not suffer from as large backgrounds as for decays into $b\bar{b}$, and so it actually provides the most sensitive probe of the Higgs boson Yukawa couplings. Decays into $\mu\mu$ have a very small BR but a good m_H resolution, and the BR of $c\bar{c}$ is modest but the backgrounds are huge.

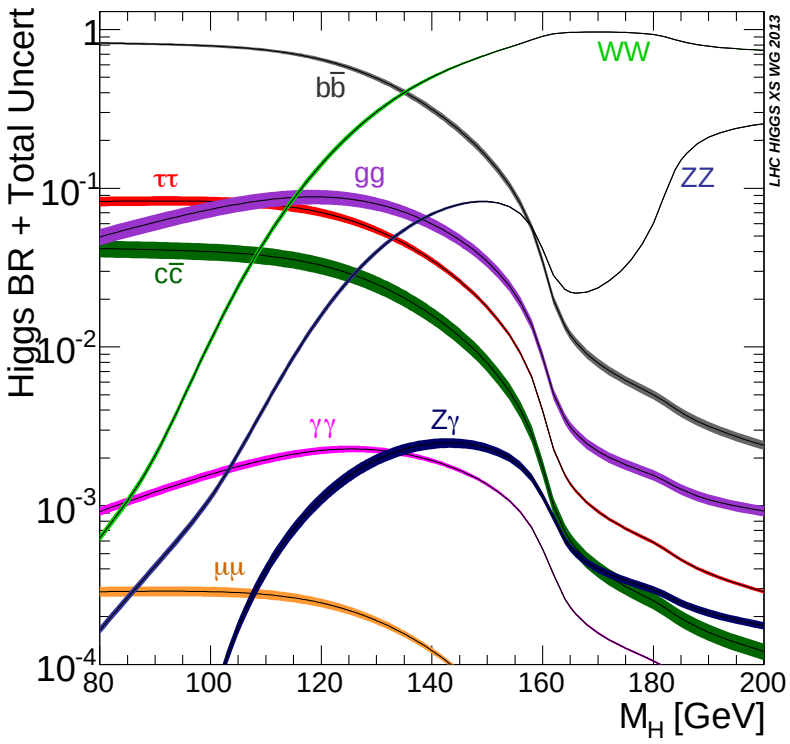

Figure 2.6 Higgs boson decay branching ratios as a function of m_H in the low mass range [20]. The theoretical uncertainties are shown by the bands.

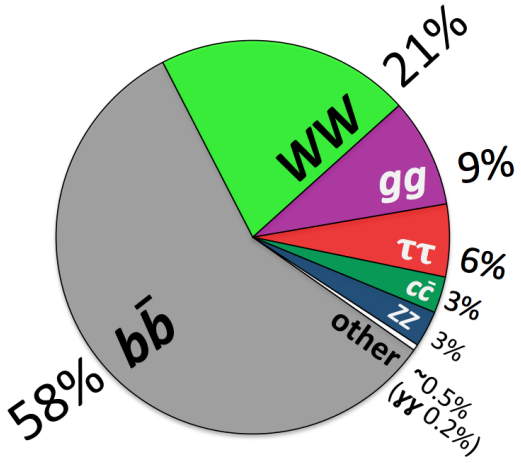

Figure 2.7 The percentage of the total Higgs boson branching ratio for each decay channel at $m_H = 125$ GeV [20]. The colours in the pie chart correspond to those in figure 2.6.

2.3.1 $H \rightarrow WW^* \rightarrow \ell\nu\ell\nu$ decay topology

The Higgs boson search presented in this thesis targets $H \rightarrow WW^*$ decays with subsequent $WW^* \rightarrow \ell\nu\ell\nu$ decay, where ℓ is an electron or muon. This decay process provides a clean detector signature due the presence of two high momentum leptons and large missing energy from the two undetected neutrinos.

There is another feature of this decay process where the two leptons tend to have a small angular separation. This is due to correlations in the directions of the leptons originating from the spin of the Higgs boson and the properties of the weak interaction. This unique topology can be illustrated in a simplified one-dimensional example, which will be provided below.

The projection of a particle's spin along its direction of motion is called its helicity (λ). Since W bosons have mass, they can have three possible helicity values: -1, 0 or 1. This is also the case if a W boson is off-shell, since it will still have a non-zero mass value. The Higgs boson has a spin and thus helicity value of zero, and so in the Higgs boson rest frame the WW pair must also have a total helicity value of zero. As illustrated in figure 2.8, these conditions require the WW pair to have one of three possible helicity configurations: (1,1), (-1,-1) or (0,0).

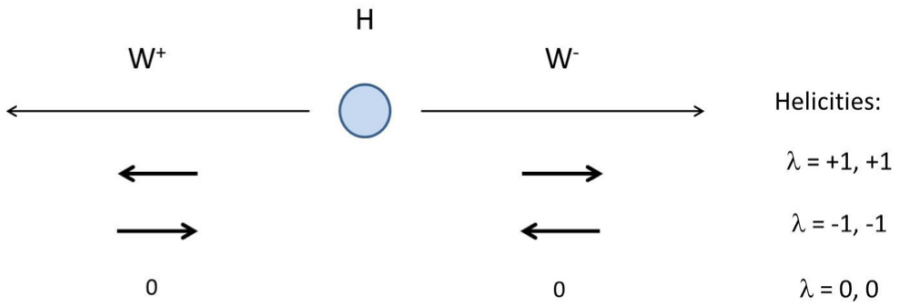

Figure 2.8 The three allowed WW helicity configurations, in the rest frame of the Higgs boson. The direction of motion and spin of the W bosons are represented by the large arrows and small bold arrows, respectively. The helicities (λ) of the W bosons are indicated on the right.

Recall from section 2.1.3 that the EW gauge symmetry of the SM requires that the weak interaction only occur between left-handed particles or right-handed anti-particles. This requires the neutrinos and anti-neutrinos from the WW decays to have negative or positive helicity values, respectively.

We can now move to the rest frame of the W bosons, in which only three possible $\ell\nu\ell\nu$ helicity configurations are allowed due to the property of the weak interaction mentioned previously. These are shown in figure 2.9, and in all three configurations the two leptons from the WW decay are required to have the same direction of motion.

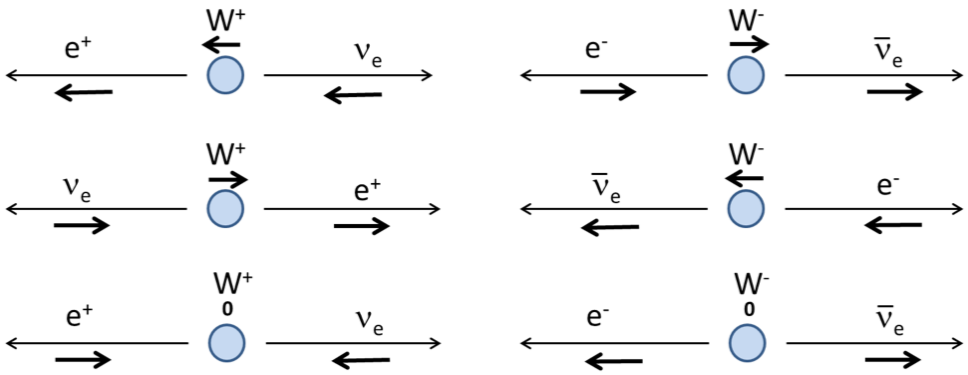

Figure 2.9 The three allowed $\ell\nu\ell\nu$ helicity configurations, in the rest frame of the W bosons. The arrow notation is the same as in figure 2.8

If the two leptons have the same direction of motion in the rest fame of the W bosons, then in the laboratory frame of the ATLAS detector they should have correlated directions and a relatively small angular separation. This unique topology of $H \to WW^* \to \ell\nu\ell\nu$ decays is exploited in the Higgs boson analyses presented in this thesis.

2.4 Discovery and Results from ATLAS

2.4.1 Prior to the LHC

Prior to the LHC, the Higgs boson mass had already been heavily constrained. Theoretical constraints from the requirement of unitarity on the amplitude of longitudinal W scattering $W_L W_L \to W_L W_L$ [22–25] require $m_H \lesssim 800$ GeV. Other theoretical arguments concerning the finiteness of the Higgs self-coupling [26] and vacuum stability [27] prefer $m_H \lesssim 160$ GeV and $m_H > 129.4 \pm 1.8$ GeV, respectively. Indirect limits were set on the Higgs boson mass using precision electroweak results [28] for $m_H < 158$ GeV at 95% confidence level (CL). Direct searches at LEP [29] and the Tevatron [30–32] excluded at 95% CL the $m_H < 114.4$ GeV region and the regions $147 > m_H < 180$ GeV and $100 > m_H < 103$ GeV, respectively.

2.4.2 Discovery of a Higgs-like Particle

On the 4$^{\text{th}}$ of July, 2012 the ATLAS and CMS experiments announced the discovery of a new Higgs-like particle with mass of around 125 GeV [5, 6]. For the ATLAS experiment, this discovery was the result of a combination of searches in three di-boson decay channels: $H\to ZZ^*$ (4 leptons), $H\to\gamma\gamma$ and $H\to WW^*$ ($e\nu\mu\nu$). LHC proton-proton collision data at $\sqrt{s}$ = 7 and 8 TeV was used corresponding to integrated luminosities of 4.8 fb^{-1} and 5.8 fb^{-1}, respectively. The observation had a significance of 5.9 standard deviations (σ), exceeding the 5σ threshold required to claim discovery.

2.4.3 ATLAS measurements at $\sqrt{s}$ = 7 and 8 TeV

The di-boson discovery channel analyses from ATLAS have been subsequently updated including the full 20.3-20.7 fb^{-1} dataset collected at $\sqrt{s}$ = 8 TeV. In addition, many other analyses have been performed such as those targeting the fermionic $H\to\tau\tau$ and $H\to b\bar{b}$ decay channels. Some of the main results from ATLAS using the complete $\sqrt{s}$ = 7 and 8 TeV datasets will be summarized in this section. These results are compatible with the corresponding results from CMS [13, 33].

Figure 2.10a shows the four lepton invariant mass distribution that was used to confirm the existence of the Higgs boson at 8.1σ significance in the $H\to ZZ^*$ decay channel. The di-photon invariant mass distribution from the $H\to\gamma\gamma$ analysis is shown in figure 2.10b, from which the signal was confirmed at 5.2σ. Due to their excellent mass resolutions, these channels are used to perform the measurement of the Higgs boson mass. The mass is derived from a combined fit to the invariant mass spectra in both channels [34], and measured to be:

$$m_H = 125.36 \pm 0.37\ (\text{stat})\ \pm 0.18\ (\text{sys})\ \text{GeV}$$

where the labels "stat" and "sys" refer to statistical and systematic uncertainties, respectively.

As was mentioned in section 2.3, the $H\to WW^*$ decay channel has the second largest BR at the measured Higgs boson mass and the sequential decay $H\to WW^*\to\ell\nu\ell\nu$ provides a clean experimental signature. This makes the $H\to WW^*$ channel analysis a good candidate for observing the Higgs boson although, due to the presence of neutrinos in the final state, it has a relatively poor mass resolution. The analysis is divided into categories based on the number of jets. The ggF production mode is

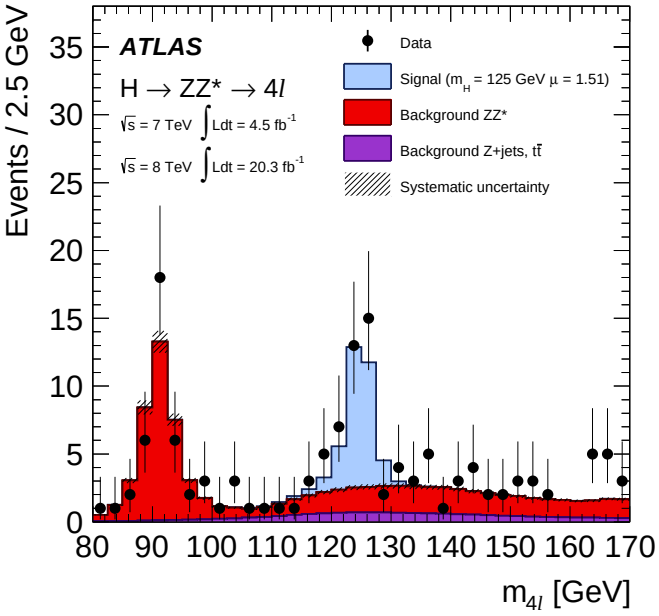

(a)

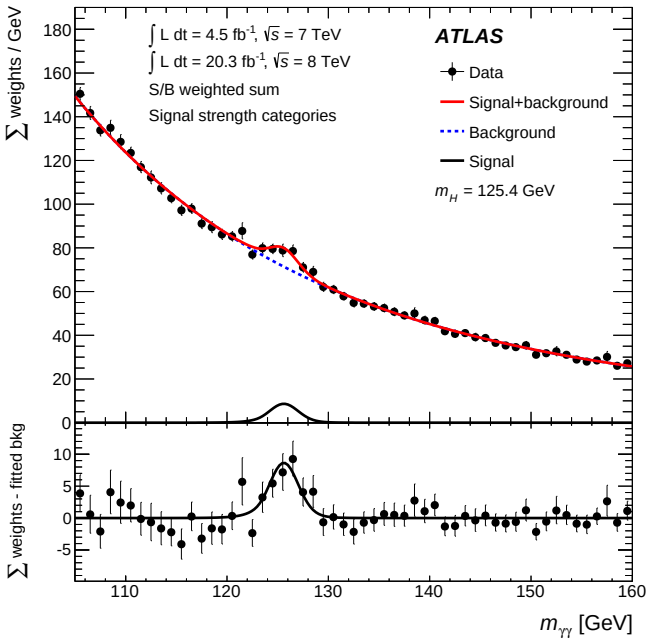

(b)

Figure 2.10 Distributions of (a) the four lepton invariant mass for events passing the $H \to ZZ^*$ analysis selection criteria and (b) the di-photon invariant mass for events passing the $H \to \gamma\gamma$ analysis selection criteria [34]. Data (black points) are compared to the signal and background expectation (stacked filled histograms in (a) and solid red line in (b)). The lower panel in (b) shows the background subtracted data (black points) compared to the signal expectation (solid black line).

targeted in events with less then two jets, while events with two or more jets provide sensitivity to the VBF mode. The transverse mass distribution[4] is used to provide the final separation between the signal and backgrounds, and is shown in figures 2.11a and 2.11b for the ggF and VBF categories, respectively. A clear excess in data is observed providing confirmation at 6.1σ significance of the $H\rightarrow WW^*$ decay channel [35].

Analyses targeting the WH and ZH production modes with $H\rightarrow WW^*$ decay were also performed [3]. This author contributed to the search for the WH production mode in the three lepton channel, and the results of this analysis will be presented in chapter 5. When including the WH and ZH mode analyses in the $H\rightarrow WW^*$ combination, the $H\rightarrow WW^*$ decay channel is confirmed at 6.5σ. Additional results from the full $H\rightarrow WW^*$ combination can be found in appendix B.

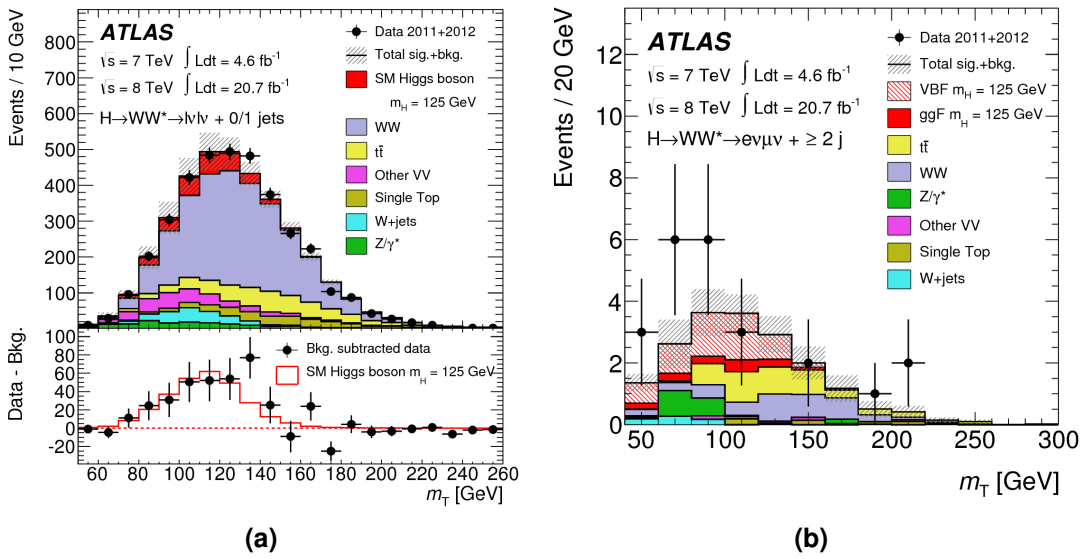

Figure 2.11 Distributions of the transverse mass after passing the $H\rightarrow WW^*$ selection criteria in (a) the ggF category and (b) the VBF category [35]. Data (black points) are compared to the signal and background expectation (stacked filled histograms). The lower panel in (a) shows the background subtracted data (black points) compared to the signal expectation (red line).

To confirm the Higgs Mechanism also generates fermion masses by the inclusion of Yukawa-type interactions, it is necessary to demonstrate the direct coupling of the Higgs boson to fermions. The most sensitive probe of the Yukawa couplings is provided by the $H\rightarrow\tau\tau$ decay channel, in which the analysis targets the ggF and VBF

[4] $m_T = \sqrt{(E_{\mathrm{T}}^{ll} + E_{\mathrm{T}}^{\mathrm{miss}})^2 - |\mathbf{p}_{\mathrm{T}}^{ll} + \mathbf{E}_{\mathrm{T}}^{\mathrm{miss}}|^2}$ with $E_{\mathrm{T}}^{ll} = \sqrt{|\mathbf{p}_{\mathrm{T}}^{ll}|^2 + m_{ll}^2}$

production modes in all combinations of leptonic ($\tau \to \ell \nu_\ell \nu_\tau$, $\ell = e, \mu$) and hadronic ($\tau \to \nu_\tau$ + hadrons) tau decays. Figure 2.12a shows the estimated $\tau\tau$ invariant mass after all selections for the combined channels. Evidence of the $H \to \tau\tau$ decay is obtained with a significance of 4.5σ [36].

At the measured Higgs boson mass, the decay channel with the largest BR of all possible decays is $H \to b\bar{b}$. However, this channel suffers from huge backgrounds and so it is restricted to the WH and ZH production modes. These production modes provide a more distinct detector signatures at the expense of lower cross sections. Nevertheless, this channel still plays an important role in confirming the Yukawa couplings and the WH and ZH production modes. Figure 2.12b shows the $b\bar{b}$ invariant mass after all selections in the $\sqrt{s} = 8$ TeV dataset. A small excess is observed above the background expectation, corresponding to a significance of 1.4σ [37].

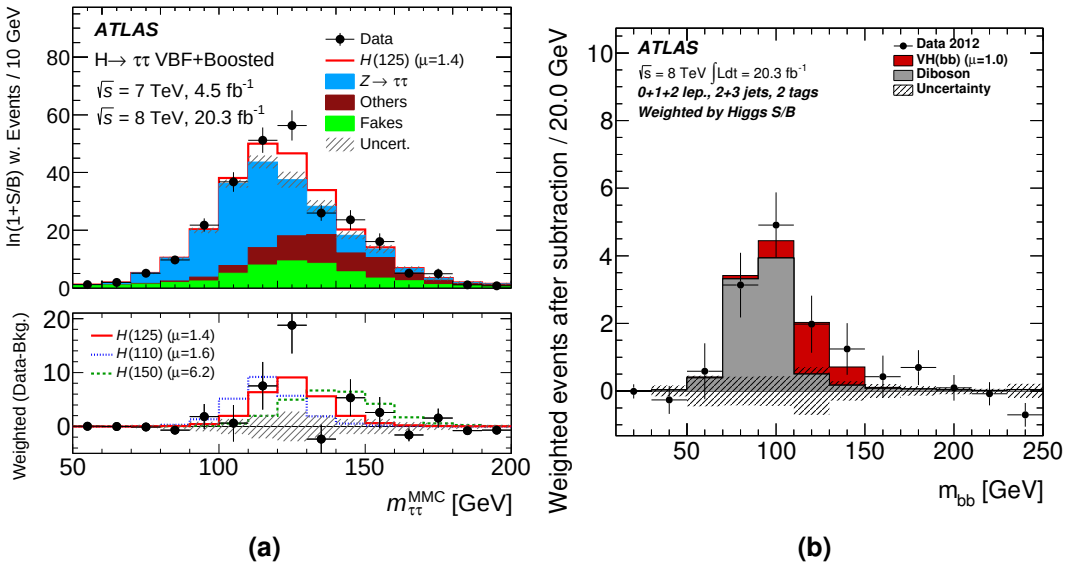

Figure 2.12 Distributions of (a) the estimated $\tau\tau$ invariant mass in the combined $\sqrt{s} = 7$ and 8 TeV datasets for all events passing the $H \to \tau\tau$ selections [36], and (b) the $b\bar{b}$ invariant mass in the $\sqrt{s} = 8$ TeV dataset for all events passing the $H \to b\bar{b}$ selections [37]. In (a) the data (black points) are compared to the signal and total background expectations (stacked histograms), where the lower panel shows the background subtracted data. In (b) the background subtracted data is shown, where all backgrounds are subtracted except the diboson processes. Events in both distributions are weighted by the signal significance.

All of the bosonic and fermionic decay channel analyses conducted by the ATLAS Collaboration at $\sqrt{s} = 7$ and 8 TeV were combined to perform many Higgs boson

property measurements [7]. The combination provides confirmation of the ggF production mode at over 5σ, and evidence for the VBF mode at 4.3σ. No strong evidence was found for the WH, ZH and $t\bar{t}H$ production modes. The observed significance for these more rare production modes are 2.1σ, 0.9σ and 2.5σ, respectively.

The observed signal strength (μ_{obs}), the measured signal yield relative to the SM prediction, for the combined decay channels at the measured Higgs boson mass is determined to be:

$$\mu_{\text{obs}} = \frac{\sigma_{\text{obs}}}{\sigma_{SM}} = 1.18 \pm 0.10\ (\text{stat}) \pm 0.07\ (\text{sys})^{+0.08}_{-0.07}\ (\text{theo})$$

where the label "theo" refers to the signal theoretical uncertainties. The signal strength measurements in the individual decay channels are shown in figure 2.13. Both the combined and individual decay channel measurements are consistent with the SM expectation of unity within the uncertainties.

The signal strength can also be measured for the different production modes. Figure 2.14 shows the signal strength likelihood contours for weak boson mediated (VBF + WH + ZH) versus fermion mediated (ggF + $t\bar{t}H$) production modes. These are shown separately for the individual decay channels. By taking the ratio of the two previously mentioned quantities, the individual decay channels can be combined in a way that removes the dependence on the BRs. Fitting this ratio across all decay channels gives:

$$\frac{\mu_{\text{obs}}^{\text{VBF+WH+ZH}}}{\mu_{\text{obs}}^{\text{ggF}+t\bar{t}H}} = 0.96\ ^{+0.33}_{-0.26}\ (\text{stat})\ ^{+0.20}_{-0.13}\ (\text{sys})\ ^{+0.18}_{-0.10}\ (\text{theo})$$

which is in good agreement with the SM expectation of unity within the uncertainties.

The Higgs boson coupling strengths can also be extracted in a leading-order coupling framework [7] that has the following assumptions:

1. The signal in each decay channel comes from the decay of a single resonance around the measured mass.

2. The width of the Higgs boson near the measured mass is negligible such that:

$$\sigma \times BR(i \to \text{H} \to f) = \frac{\sigma_i \Gamma_f}{\Gamma_{\text{H}}}$$

   where σ_i is the production cross-section for initial state i, Γ_f is the partial width to final state f and Γ_{H} is the total Higgs boson width.

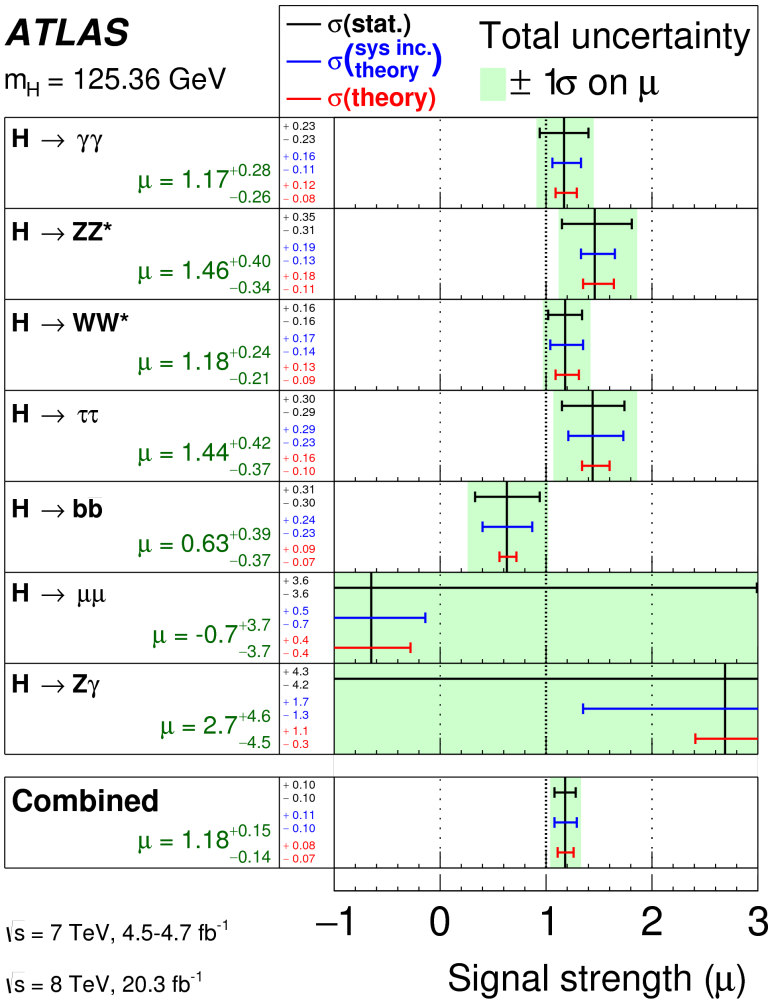

Figure 2.13 The measured signal strength in each of the decay channels and in the combination [7]. Statistical uncertainties are shown in black, systematic uncertainties (including theory uncertainties) in blue and the theory component of the systematic uncertainty alone in red. The total uncertainties are represented by the green bands.

3. Only differences in the absolute values of coupling strength need be accounted for.

Coupling scale factors (κ_j) are defined such that σ_j and Γ_j associated with particle j are scaled from their leading order SM expected values by a factor of κ_j^2. In this way:

$$\sigma \times BR(i \to \mathrm{H} \to f) = \sigma_{\mathrm{SM}} \times BR(i \to \mathrm{H} \to f)_{\mathrm{SM}} \times \frac{\kappa_i^2 \, \kappa_f^2}{\kappa_{\mathrm{H}}^2}$$

The benchmark model assumes no undetected or invisible Higgs boson decays exist, and that there is a universal coupling strength scale factor to bosons (κ_{V}) and fermions

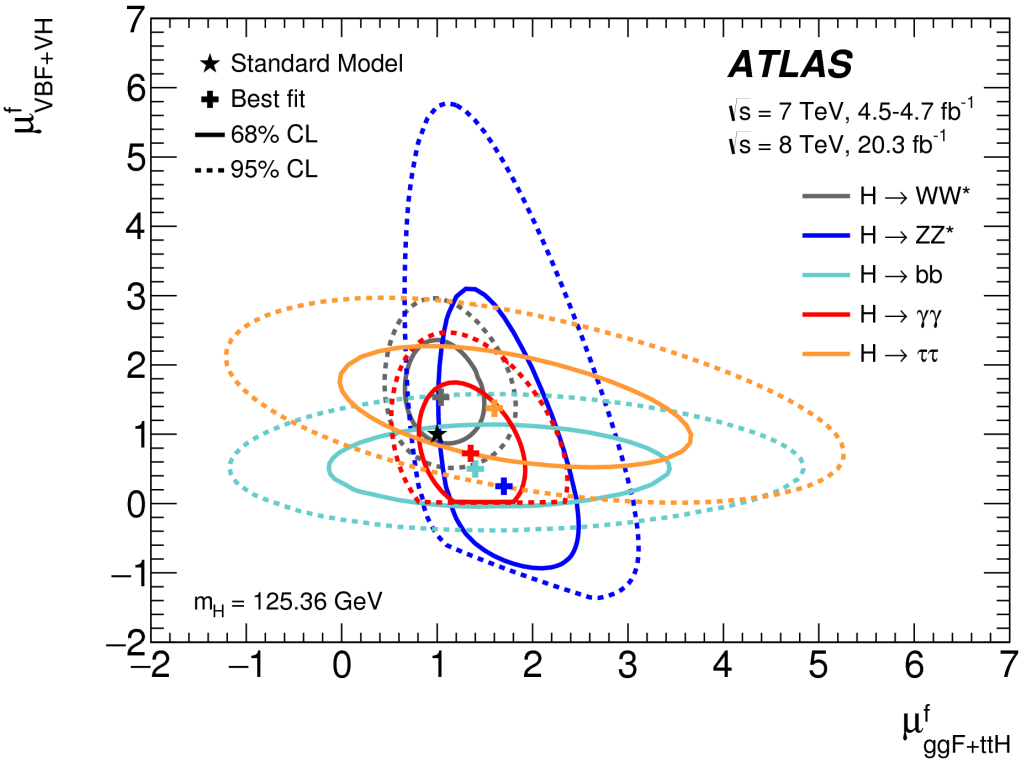

Figure 2.14 Likelihood contours in the signal strength for the bosonic version fermionic production modes in the individual decay channels [7]. The 68% CL is shown with solid lines, and the 95% CL with dashed lines. The measured value for the combined decay channels is shown with + , and the SM expectation with a star.

(κ_F). Figure 2.15 shows the results of the fit for this benchmark model, and how each decay channel contribute to the combined measurement. The best fit values of κ_V and κ_F for the combined measurement are:

$$\begin{aligned} |\kappa_V| &= 1.09\ ^{+0.05}_{-0.05}\ (\text{stat})\ ^{+0.03}_{-0.03}\ (\text{sys})\ ^{+0.04}_{-0.03}\ (\text{theo}) \\ |\kappa_F| &= 1.11\ ^{+0.12}_{-0.11}\ (\text{stat})\ ^{+0.10}_{-0.09}\ (\text{sys})\ ^{+0.06}_{-0.05}\ (\text{theo}) \end{aligned} \tag{2.6}$$

which are compatible with the SM expectations of unity within the uncertainties.

Measurements of the spin and parity of the Higgs boson have also been performed [38]. In these measurements, kinematic distributions from the di-boson decay channels are used to compare the shape expectations for the SM prediction ($J^P = 0^+$) to alternative spin and parity hypotheses ($0^-, 1^+, 1^-, 2^+$ and mixed states). All alternative hypotheses were excluded at above 99% CL, in favor of SM 0^+ hypothesis.

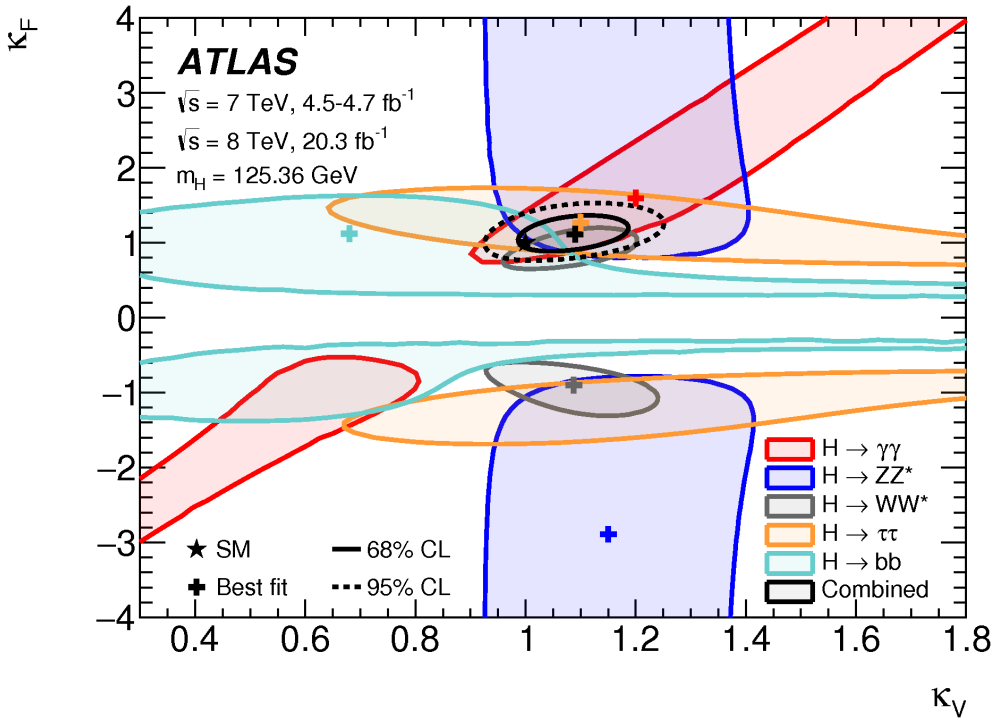

Figure 2.15 68% CL likelihood contours for the universal scale factors κ_F and κ_V for each of the decay channels and their combination [7]. The values of best fit are shown with +.

To summarize, a Higgs-like particle was discovered with a mass of around 125 GeV using the full $\sqrt{s}$ = 7 TeV and partial 8 TeV datasets. Subsequently, many Higgs boson measurements have been performed by ATLAS including the full $\sqrt{s}$ = 8 TeV dataset. The ZZ^*, $\gamma\gamma$ and WW^* decay channels and the ggF production mode were confirmed at over 5σ significance. Evidence at over 4σ significance was observed for the $\tau\tau$ decay channel and the VBF production mode. There was no statistically significant evidence for the $b\bar{b}$ decay channel or the rare WH, ZH and $t\bar{t}H$ production modes. Combined measurements of the signal strengths, couplings, spin and parity were performed. They were all measured to be consistent with the SM expectations and the corresponding measurements from CMS within the current level of precision.

2.4.4 Next Steps

The LHC began its second run in late 2015 at the higher proton-proton collision energy of $\sqrt{s}$ = 13 TeV, and in the coming years this will rise to 14 TeV. The increased collision

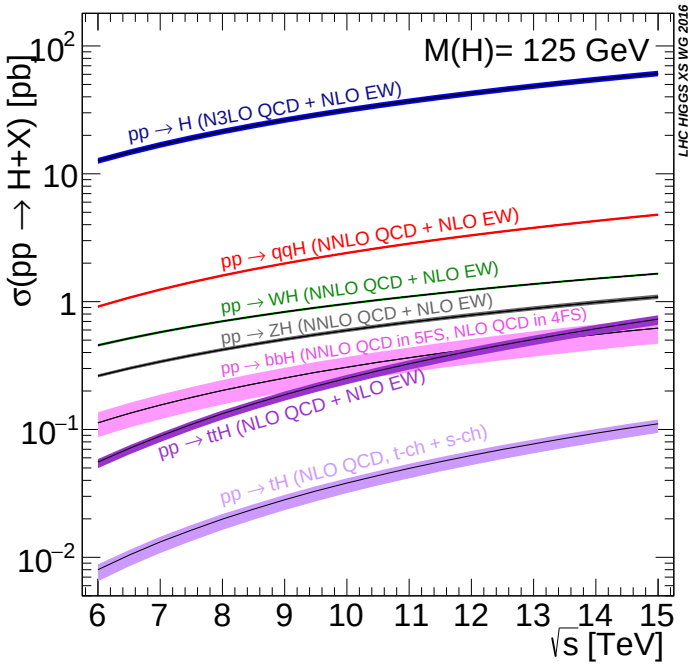

Figure 2.16 The predicted Higgs boson production cross sections as a function of the $\sqrt{s}$ of the proton-proton collisions, for m_H = 125 GeV [39]. The error bands show the theoretical uncertainties.

energy provides a substantial boost to the Higgs boson production cross sections. The predicted cross sections are shown in figure 2.16 and table 2.2. The increase from $\sqrt{s}$ = 8 to 13 TeV causes the ggF, VBF, WH and ZH production cross sections to increase by a factor of about 2-2.5, while the $t\bar{t}H$ mode increases by a factor of almost 4. An additional boost to the cross sections of around 10-20% comes from the increase from $\sqrt{s}$ = 13 to 14 TeV.

	ggF	**VBF**	***WH***	***ZH***	***$t\bar{t}H$***
$\sigma^{13\text{TeV}}$ [pb]	$48.58\ ^{+12\%}_{-14\%}$	$4.013\ ^{+2.4\%}_{-2.1\%}$	$1.373\ ^{+2.4\%}_{-2.6\%}$	$0.8837\ ^{+5.4}_{-4.7\%}$	$0.5072\ ^{+11\%}_{-15\%}$
$\sigma^{13\text{TeV}}$ / $\sigma^{8\text{TeV}}$	2.521	2.543	1.949	2.128	3.923
$\sigma^{14\text{TeV}}$ [pb]	$54.67\ ^{+12\%}_{-14\%}$	$4.547\ ^{+2.4\%}_{-2.1\$}$	$1.514\ ^{+2.2\%}_{-2.5\%}$	$0.9858\ ^{+5.4\%}_{-4.9\%}$	$0.6137\ ^{+11\%}_{-14\%}$
$\sigma^{14\text{TeV}}$ / $\sigma^{13\text{TeV}}$	1.125	1.133	1.103	1.116	1.210

Table 2.2 The predicted Higgs boson production cross sections for proton-proton collisions at $\sqrt{s}$ = 13 and 14 TeV, for m_H = 125 GeV [39]. The errors correspond to the total theoretical uncertainties. The second row shows the central values of the ratio between the $\sqrt{s}$ = 13 and 8 TeV cross sections. The final row shows the same thing but for the $\sqrt{s}$ = 14 and 13 TeV cross sections.

The LHC is expected to operate at the higher collision energies for total of around 20 years. The second run is expected to end in late 2018 followed by a third run from 2021-2023, where during both runs the LHC is expected to deliver around 300 fb^{-1} of data [40]. After the High Luminosity LHC (HL-LHC) upgrade [41], data collection should commence again in 2025 and continue for around 10 years to deliver approximately 2 ab^{-1} of data.

The combination of the increased production cross sections and substantially larger datasets will allow many new and improved Higgs boson measurements from the ATLAS experiment. The mass, signal strength, couplings, spin and parity measurements will become more precise and, if they exist, reveal any deviations from the SM predictions. Two more specific objectives of the ATLAS Higgs program most relevant to the studies presented in this thesis are detailed below.

One important goal will be to claim discovery in the $H\rightarrow\tau\tau$ channel alone, more tightly constrain the tau lepton Yukawa coupling and perform the first measurements in this channel of the spin and parity. In order to collect the proton-proton collision data for these measurements, a tau trigger system that can efficiently identify interesting events containing tau leptons will be essential. Studies relating to the ATLAS tau trigger will be presented in chapter 4.

Another high priority objective will be to first find direct evidence for and eventually claim independent discoveries of the rare WH, ZH and $t\bar{t}H$ production modes. The analyses presented in chapter 5 contribute to this objective by performing a direct search for the WH production mode with $H\rightarrow WW^*$ decay. This process also provides important information on the Higgs to W boson coupling strength, since the combined production and decay process involves only this coupling at tree-level.

3

Experimental Setup

The world's leading particle physics laboratory is operated by the European Organization for Nuclear Research (CERN) and consists of an extensive network of accelerators, particle experiments and computing facilities. It is located along the French-Swiss border near the city of Geneva, and is home to the LHC [42] which is the world's largest and most powerful particle accelerator. The LHC can accelerate protons or lead ions up to unprecedented energies and collide them inside four particle detectors situated along its circumference. The proton-proton collision data used in the studies presented in this thesis was collected by one of these detectors called ATLAS (A Toroidal LHC Apparatus) [43].

This chapter will provide an overview of the experimental setup used for the studies presented in this thesis. This will include a description of the LHC in section 3.1 and the ATLAS detector in section 3.2. Finally, details regarding the reconstruction of collision events will be provided in section 3.3.

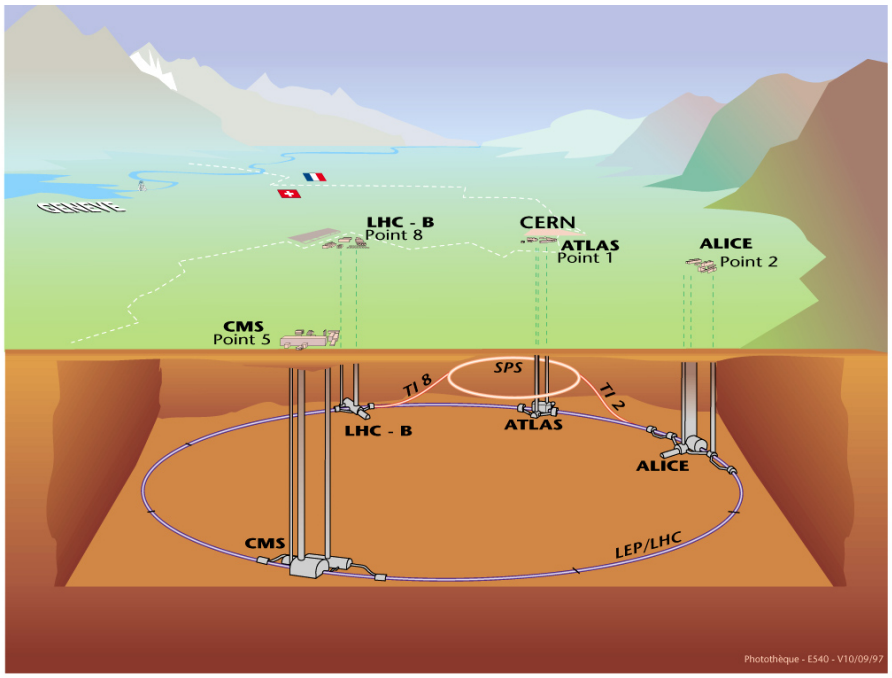

Figure 3.1 The LHC site and the position of its four particle detectors [44].

3.1 The Large Hadron Collider

The LHC is situated in a tunnel on the CERN site that was previously occupied by the Large Electron Positron (LEP) collider from 1989 to 2000. This tunnel straddles the French-Swiss border, has a circumference of 27 km and lies between 45-170 m underground. Construction of the LHC began in 1998 while LEP was still in operation, and the first proton beam was successfully steered around the full LHC ring in September of 2008. The LHC can accelerate bunches of protons or lead ions and brings them to collision at the centres of four particle detectors: ALICE, ATLAS, CMS and LHCb. The positions of these detectors around the LHC ring are shown in figure 3.1.

ATLAS and CMS are general purpose detectors designed to probe a broad range of physics phenomena, including those related to the SM Higgs boson. These two experiments provide each other with healthy competition and a means of validating results, since any discovery made by one detector should be corroborated by the other. The other two experiments are designed with more specific goals in mind. The LHCb detector specifically targets b-hadron decays in order to probe phenomena such as the origin of the matter-antimatter asymmetry in the universe. ALICE uses lead ion collisions to study the quark-gluon plasma which is postulated to have existed during the early universe.

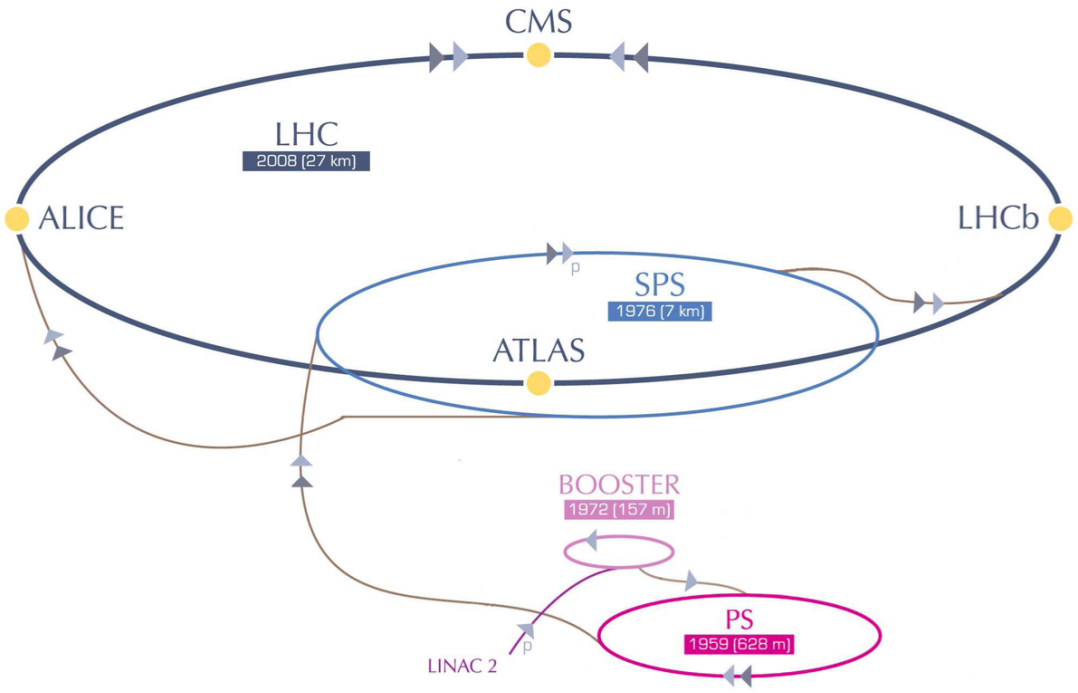

Figure 3.2 The LHC accelerator complex [45].

3.1.1 Collision Energy

The proton beam energy is increased gradually before collisions occur by using a series of accelerators on the CERN site. These accelerators are collectively referred to as the LHC accelerator complex and are illustrated in figure 3.2. Initially, 50 MeV protons are generated by the linear accelerator LINAC 2, which are then directed to the Proton Synchrotron Booster where they are accelerated to 1.4 GeV. At this stage, they are injected into the Proton Synchrotron (PS) which further accelerates them to 26 GeV. The final stage before injection to the main ring of the LHC is the Super Proton Synchrotron (SPS) which increases the beam energy to 450 GeV. The LHC itself provides the final boost, accelerating the protons up to a maximum beam energy of 7 TeV corresponding to a maximum centre-of-mass energy of $\sqrt{s} = 14$ TeV.

Since its first major proton-proton collision run starting in March 2010, the LHC has operated at a range of centre-of-mass energies. Up until the end of 2011 it was operating at $\sqrt{s} = 7$ TeV. This was increased to 8 TeV during 2012, and 13 TeV from late 2015 until the present date. In the coming years the LHC is expected to eventually operate at the maximum 14 TeV.

3.1.2 Luminosity

Besides increasing the collision energy, the only other means of increasing the number of collision events per second (N) is by operating the LHC at a higher luminosity ($\mathcal{L}$). The event rate is related to the luminosity in the following way:

$$N = \mathcal{L}\sigma \,, \tag{3.1}$$

where σ is the cross section of the particular physics process. Since the cross sections of the Higgs boson production modes are relatively small, it is important to maximize the luminosity of the LHC.

The LHC and the ATLAS detector were designed to operate at a maximum luminosity of 10^{34} cm^{-2}s^{-1} [42, 43]. The luminosity depends on the LHC beam parameters [42]:

$$\mathcal{L} = \frac{N_b^2 n_b^2 f_{rev} \gamma}{4\pi\epsilon_n \beta^*} F \,, \tag{3.2}$$

where:

- N_b is the number of protons per bunch, n_b is the number of bunches per beam, f_{rev} is the revolution frequency and γ is the relativistic factor.
- ϵ_n is the normalized transverse beam emittance and β^* is a measure of the beam focus at the collision point.
- F is the geometric reduction factor due to the crossing angle of the beams at the interaction point.

The proton-proton collision data used in the studies presented in this thesis was collected by the ATLAS detector from March 2011 up until early June 2016. During this time, the LHC collided bunches of order 10^{11} protons every 25-50 ns and achieved a peak luminosity of 7.8×10^{33} cm^{-2}s^{-1} [46–49]. The peak luminosity reached during each of the 2011, 2012, 2015 and 2016 data taking periods is shown in table 3.2.

The cumulative luminosity over time both delivered by the LHC and recorded by the ATLAS detector is shown in figure 3.3. The ATLAS detector efficiently recorded data during the time periods considered, with an average efficiency of around 92%. The size of the data samples used in the studies presented in thesis are summarized in table 3.1. The column titled "good for physics" indicates the size of the data samples after applying quality criteria to suppress non-collision backgrounds such as cosmic-ray

muons, beam-related backgrounds, or noise in the calorimeters. After applying the data quality criteria, the total integrated luminosity of the datasets are 4.5, 20.3 and 5.8 fb^{-1} at $\sqrt{s} = 7$, 8 and 13 TeV, respectively.

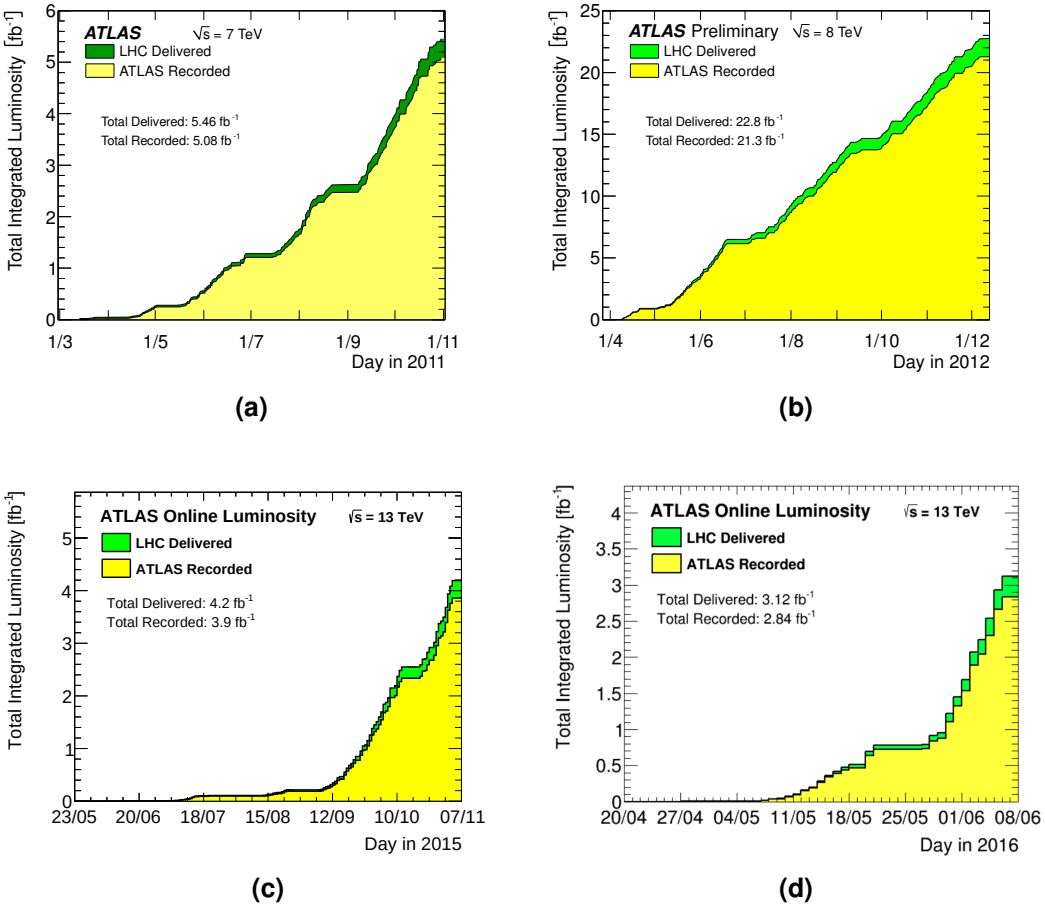

Figure 3.3 The total integrated luminosity versus time delivered by the LHC (green) and recorded by the ATLAS detector (yellow) during: (a) 2011, (b) 2012, (c) 2015 and (d) up until early June 2016 [46–49].

Year ($\sqrt{s}$)	LHC delivered	ATLAS recorded	Good for physics
2011 (7 TeV)	5.46 fb^{-1}	5.08 fb^{-1}	4.5 fb^{-1}
2012 (8 TeV)	22.8 fb^{-1}	21.3 fb^{-1}	20.3 fb^{-1}
2015-2016 (13 TeV)	7.32 fb^{-1}	6.74 fb^{-1}	5.8 fb^{-1}

Table 3.1 The total integrated luminosity delivered by the LHC, recorded by the ATLAS detector and passing data quality criteria (good for physics). [46–49].

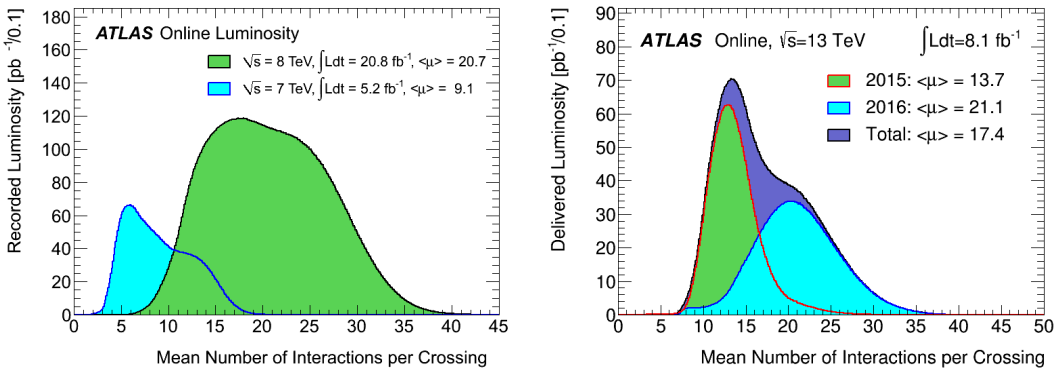

Figure 3.4 The luminosity-weighted distributions of the $\mu_{\text{pile-up}}$ parameter for the proton-proton collision data collected during (a) 2011 (blue) and 2012 (green), and (b) 2015 (green) and 2016 (blue) [46–49].

3.1.3 Collision Environment

Although operating the LHC at high luminosities increased the number of events originating from rare physics processes, it also resulted in a challenging collision environment. Raising the luminosity also increases the amount of overlapping proton-proton interactions in each collision event, resulting in a significant amount of mostly low-momentum signals in the ATLAS detector. This phenomenon is known as "pile-up", and it can have contributions from both in-time and out-of-time effects [50]. Any simultaneous proton-proton interactions that occur within the same bunch crossing will contribute to in-time pile-up. Out-of-time pile-up can occur if the interactions from neighbouring bunch-crossings can leave signals in the detector within the processing time for a single event.

The contribution from both in-time and out-of-time pile-up can be parameterized in terms of the mean number of interactions per bunch crossing ($\mu_{\text{pile-up}}$). The ATLAS detector was designed to operate with an average $\mu_{\text{pile-up}}$ parameter of 22 [42,43]. The luminosity-weighted distribution of this parameter during the $\sqrt{s}$ = 7, 8 and 13 TeV data taking periods is shown in figure 3.4. For the data samples used in the studies presented in this thesis, the average $\mu_{\text{pile-up}}$ parameter is 9.1, 20.7, 13.7 and 21.1 during 2011, 2012, 2015 and 2016, respectively. The effects of pile-up are included in simulated collision events following a procedure that will be described in section 3.3.3.

	2011	2012	2015	2016
$\sqrt{s}$ [TeV]	7	8	13	13
Peak $\mathcal{L}$ [$\text{cm}^{-2}\text{s}^{-1}$]	3.7×10^{33}	7.7×10^{33}	5.0×10^{33}	7.8×10^{33}
Total integrated $\mathcal{L}$ [fb^{-1}]	4.5	20.3	3.2	2.6
Average pile-up	9.1	20.7	13.7	21.1

Table 3.2 Summary of the proton-proton collision energy, maximum luminosity, total integrated luminosity (good for physics) and pile-up conditions for the data samples used in the studies presented in this thesis [46–49].

3.2 The ATLAS Detector

ATLAS [43] is a multi-purpose detector designed to perform precision tests of the SM, discover and measure the properties of the SM Higgs boson, and search for evidence of physics beyond the SM. The detector is installed in a cavern along the LHC at CERN's main site in Meyrin, Switzerland. With dimensions of 44 m in length and 25 m in height it is the largest experiment at the LHC, and weighs approximately 7000 tonnes. A diagram of the ATLAS detector is shown in figure 3.5.

The ATLAS detector is composed of several layers of sub-detectors arranged in a cylindrical geometry around the nominal proton-proton collision point. Each sub-detector is designed to measure different particle properties, and together they build a detailed picture of each collision event. Starting from the beam line and moving radially outward they include: the Inner Detector which enables the tracking of charged particles, the calorimeters which measure the energy of neutral and charged particles and the Muon Spectrometer that provides additional tracking for muons. The central barrel region of the detector is enclosed by two end-caps. A solenoid magnet surrounds the Inner Detector, a large toroid magnet spans the outer barrel region of ATLAS and two smaller toroids span the outer end-caps. Their magnetic fields bend the trajectory of charged particles, allowing the measurement of their momentum and charge.

The high luminosity and pile-up conditions of the LHC presented certain challenges when initially designing the ATLAS detector [43]. In general, the physics goals of the ATLAS experiment require fast, radiation-hard electronics and sensors with fine granularity and a large acceptance in solid angle around the collision point. The performance goals of the ATLAS detector are listed in table 3.3 and detailed below.

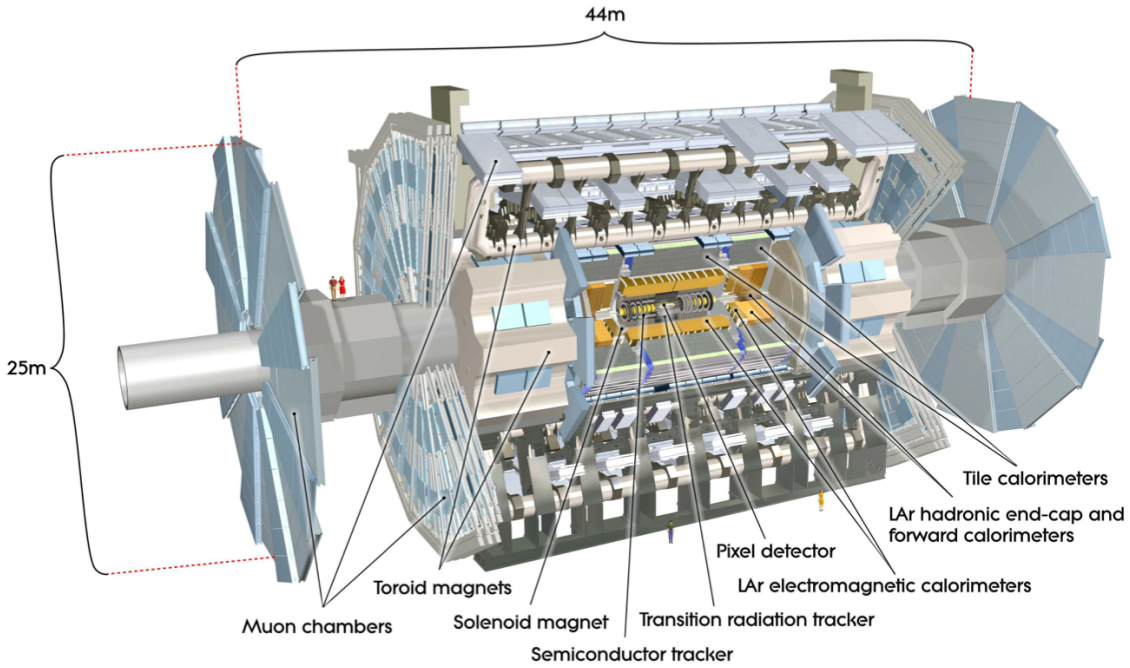

Figure 3.5 A cut-away view of the ATLAS detector showing the position of the main detector components [43]. To provide some perspective regarding the size of the detector, two people are shown standing within the muon chambers on the left of the diagram.

Detector component	**Target resolution**	**$\lvert\eta\rvert$ coverage**	
		Measurement	Trigger
Tracking	$\frac{\sigma_{p_T}}{p_T} = 0.05\%\ p_T \oplus 1\%$	< 2.5	-
Electromagnetic calorimetry	$\frac{\sigma_E}{E} = \frac{10\%}{\sqrt{E}} \oplus 0.7\%$	< 3.2	< 2.5
Hadronic calorimetry			
Barrel and endcap	$\frac{\sigma_E}{E} = \frac{50\%}{\sqrt{E}} \oplus 3\%$	< 3.2	< 3.2
Forward	$\frac{\sigma_E}{E} = \frac{100\%}{\sqrt{E}} \oplus 10\%$	$3.1 < \lvert\eta\rvert < 4.9$	$3.1 < \lvert\eta\rvert < 4.9$
Muon spectrometer	$\frac{\sigma_{p_T}}{p_T} = 10\%$ at $p_T = 1$ TeV	< 2.7	< 2.4

Table 3.3 Performance goals of the ATLAS detector [43]. E and p_T are in units of GeV, unless otherwise specified.

The tracking systems were designed to provide high precision measurements over a wide momentum range, with the Muon Spectrometer able to unambiguously determine the charge of high momentum muons. Some tracking components of the Inner Detector were placed very close to the beam. This enables the reconstruction of secondary vertices that are crucial to the identification of tau leptons and b-quark initiated jets. The calorimeter system was designed to have fine granularity and good energy resolution, both of which are essential for the reconstruction and identification of leptons, photons and jets. It was also designed to provide an almost complete coverage of the nominal collision point, which is particularly important for reconstructing the missing energy in events. The trigger system was designed to be efficient for low momentum particles, and provide a sufficient level of background rejection for the recording and storage of data.

The ATLAS coordinate system and a brief overview of each of its sub-detectors will be provided in the remainder of this section. A more comprehensive description is available in ref. [43].

3.2.1 Coordinate System

The ATLAS detector is described by a right-handed Cartesian coordinate system with its origin at the nominal collision point. The z-axis lies tangent to the beam with the positive z-axis pointing in an anti-clockwise direction around the LHC ring. The x-y plane is transverse to the beam, with the positive x-axis pointing radially inward to the centre of the LHC and the positive y-axis pointing upwards towards the surface.

As the detector exhibits cylindrical symmetry about the beam line, it is often more convenient to use cylindrical coordinates. In this case the z direction remains the same and r is the distance from the centre of the beam pipe. The angle from the positive z-axis towards the x-y plane is denoted θ, with values ranging from 0 at the positive z-axis to π at the negative z-axis. The angle from the positive x-axis towards the positive y-axis is denoted ϕ, with values ranging from -π at the negative y-axis to π at the positive y-axis. The radial distance r, the polar angle θ and the azimuthal angle ϕ are determined from the Cartesian coordinates in the following way:

$$\begin{aligned} r &= \sqrt{x^2 + y^2}\,, \\ \phi = \tan^{-1}\left(\frac{x}{y}\right)\,, &\quad \theta = \tan^{-1}\left(\frac{r}{z}\right)\,, \end{aligned} \tag{3.3}$$

It is also convenient to express the polar angle in a different form known as the pseudorapidity:

$$\eta = -\ln\left[\tan\left(\frac{\theta}{2}\right)\right] \tag{3.4}$$

Pseudorapidity is invariant under Lorentz transformations and the cross-sections of physics processes are roughly constant as a function of it. The angular separation between particles in the η-ϕ plane is calculated as:

$$\Delta R = \sqrt{\Delta\eta^2 + \Delta\phi^2} \tag{3.5}$$

It is common practice to project the momentum and energy vectors of particles into the x-y plane. These quantities are called the transverse momentum and transverse energy, and their magnitudes are denoted p_T and E_T respectively. These quantities can be calculated using the polar angle in the following way:

$$p_T = \sqrt{p_x^2 + p_y^2} = |\mathbf{p}|\sin(\theta)\,, \qquad E_T = E\sin(\theta)\,, \tag{3.6}$$

3.2.2 Inner Detector

The ATLAS Inner Detector (ID) records hits from charged particles passing through it within a pseudorapidity range $|\eta| < 2.5$ and with full coverage in ϕ. The ID sits within a superconducting solenoid, and its uniform 2 T magnetic field bends the charged particle trajectories. The hits from the ID are used to reconstruct the corresponding tracks, and precise measurements of p_T and charge can be inferred from the track curvature. The ID also allows for the accurate measurement of the vertex locations from which the charged particles originate.

The ID consists of three sub-systems that use different detection technologies. In order of their closeness to the beam they include: the Pixel Detector, the SemiConductor Tracker (SCT) and the Transition Radiation Tracker (TRT). The granularity of the sub-systems increase inward towards the beam. The barrel modules of the Pixel Detector and SCT are arranged in cylindrical layers around the beam axis and their end-cap modules form disks that are perpendicular to the beam. An illustration of the ID is shown in figure 3.6a, with the radial scale of each barrel layer shown in figure 3.6b. The Pixel Detector, SCT and TRT will be described, in turn, below.

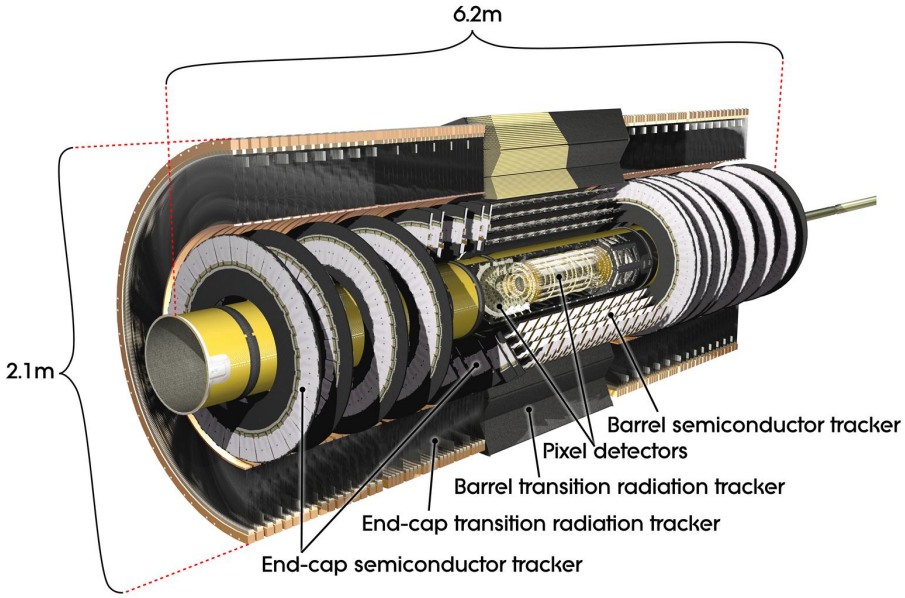

(a)

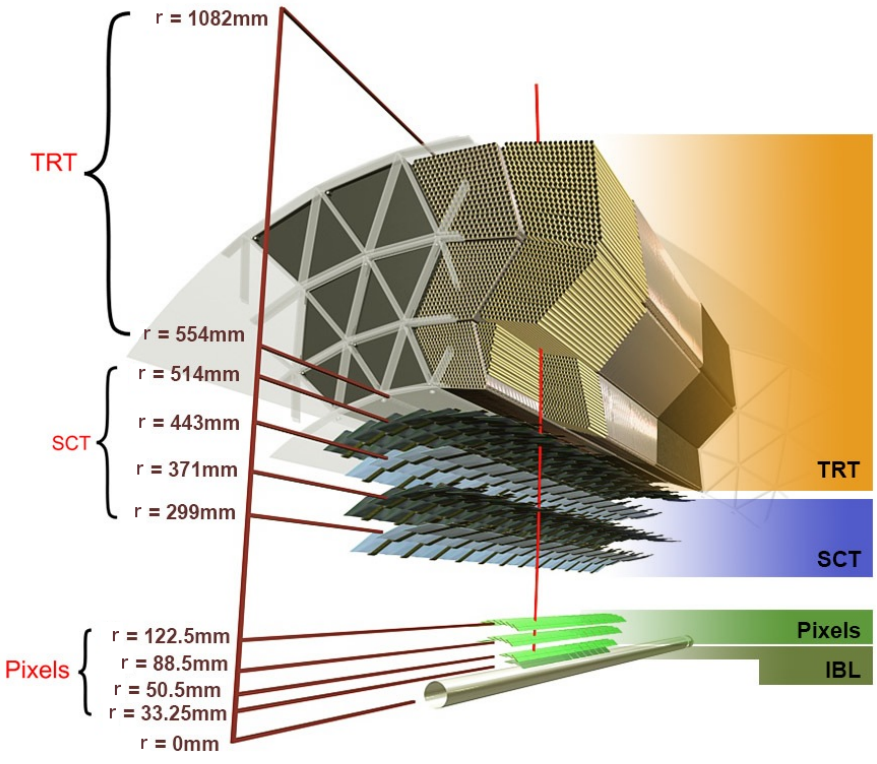

(b)

Figure 3.6 (a) A cut-away view of the ID showing each of the barrel and end-cap components [43], and (b) a transverse slice of the ID showing the radial scale of each barrel layer [43].

Pixel Detector

The silicon-based Pixel Detector is located closest to the beam, has the finest granularity and provides coverage that is complete in ϕ and partial in η ($|\eta| < 2.5$). It was originally built was three concentric cylindrical layers in the barrel region and three disks in each end-cap. An additional innermost barrel layer, the Insertable *B*-Layer (IBL), was installed after the $\sqrt{s} = 7$ and 8 TeV data taking periods in order to improve the overall performance and pile-up robustness of the Pixel Detector [51]. Including the IBL, the Pixel Detector consists of 1968 sensor modules that in total contain over 86 million individual pixels, each with its own readout channel. The pixels in the IBL (other layers) are of size 50×250 (50×400) μm^2 in the *r*-*z* plane and provide hit coordinate measurements with an intrinsic resolution of 8 (10) μm in *r*-ϕ and 40 (115) μm along z.

SemiConductor Tracker

The SCT surrounds the Pixel Detector, provides the same coverage in ϕ and η, and utilizes a silicon microstrip sensor technology. It consists of 4088 modules that tile four concentric cylindrical layers in the barrel region and nine disk layers in each end-cap, with a total of over 6 million readout channels. Each module has a silicon strip on both sides that can individually perform a one dimensional hit position measurement. The upper and lower strips have a small stereo angle between them of 40 mrad, allowing the coordinate along the module axis to also be measured. The SCT modules have an intrinsic hit coordinate resolution of 17 μm in *r*-ϕ and 580 μm along z.

Transition Radiation Tracker

The TRT surrounds the SCT and has the same coverage in ϕ but a reduced coverage in η ($|\eta| < 2.0$). It is built from polyamide straw tubes of 4 mm diameter that are packed into chambers filled with mainly xenon gas. To reduce operational costs during $\sqrt{s} =$ 13 TeV data taking, a larger proportion of the chambers were filled with an argon gas mixture. The tubes are arranged perpendicular to the beam in the barrel and radially in the end-caps, and have in total over 350, 000 readout channels. A gold-plated tungsten wire is suspended within each tube, and an electrical potential of 1530 V is maintained between the tube walls and the wires. Charged particles traversing the TRT will ionize the gas and generate an avalanche of fee electron that will drift towards the closest anode wire. The times at which the electrical signals pass certain thresholds

are recorded, from which drift-circles can later be reconstructed. The size of the signals can also be used to discriminate between electrons and pions, since the prior tends emit more transition radiation in the TRT. The tubes only allow measurements in r-ϕ and with a relatively coarse intrinsic resolution of 130 μm. This is compensated for by the fact that charged particles tend to register more hits in the TRT, typically 22-36 per particle, that are spread over larger distances.

3.2.3 Calorimeters

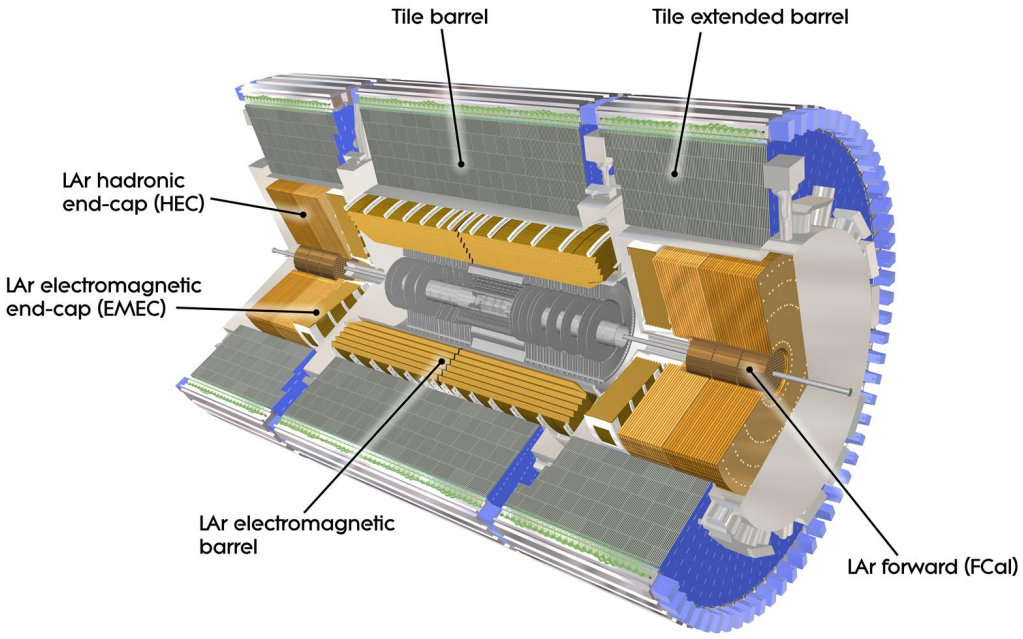

Figure 3.7 A cut-away view of the ATLAS calorimeter system showing the different components of the electromagnetic and hadronic calorimeters [43].

The energies of both neutral and charged particles are measured in ATLAS using a system of sampling calorimeters that surround the ID as shown in figure 3.7. They are built from layers of dense material designed to absorb incident particles and initiate showers of additional particles, and layers of active material that produce an output signal proportional to the shower energy. An electromagnetic calorimeter (ECAL) is designed to absorb and measure the energies of electrons and photons, while a hadronic calorimeter (HCAL) targets hadrons. The combined systems provide energy measurements with good resolution and an almost complete coverage of the nominal collision point, both of which enable the accurate reconstruction of missing energy.

Electromagnetic Calorimeter

The ECAL consists of absorber plates made of lead and active regions filled with liquid argon (LAr). It is built from many lead-LAr layers shaped in an accordion-like geometry, as shown in figure 3.8, that has a smaller charge collection time compared to more simple geometries [52]. The ECAL is designed to have full ϕ coverage and a large acceptance in η. It consists of a barrel component that covers $|\eta| < 1.475$ and a co-axial wheel in each end-cap covering $1.375 < |\eta| < 3.2$. The total thickness of the ECAL ranges from 22-24 radiation lengths[1].

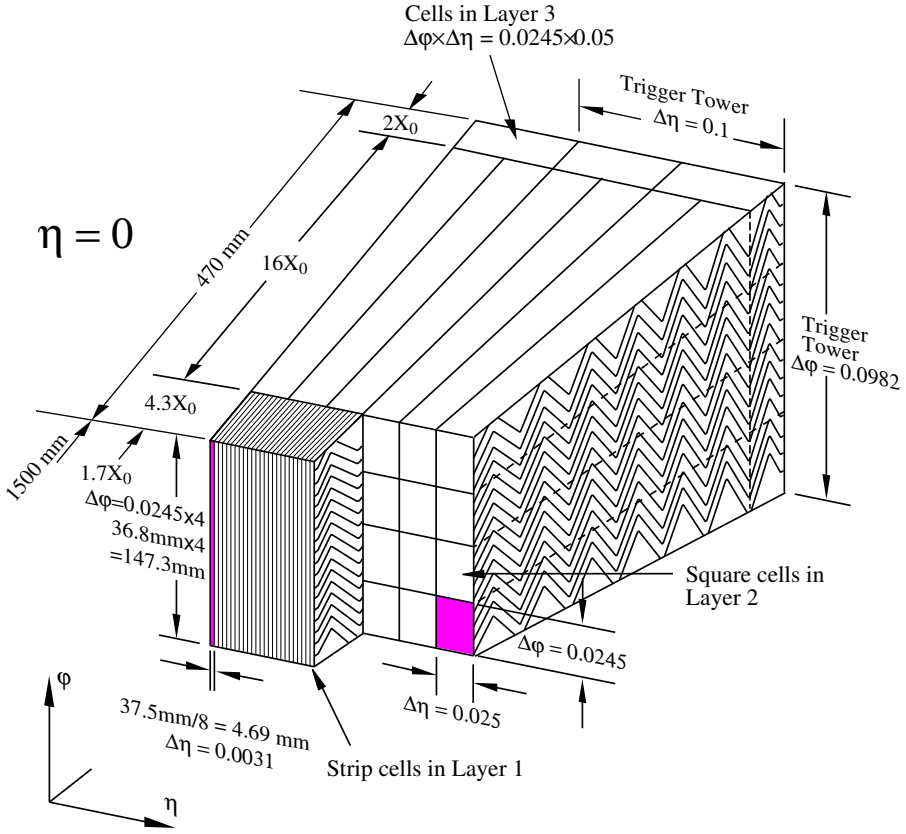

Figure 3.8 Diagram of an ECAL barrel module [43]. The characteristic accordion geometry of the lead-LAr layers is shown, as well as the granularity in η and ϕ for each of the three barrel layers.

Incident photons will interact with the lead plates and first generate electron-positron pairs via conversion. If electrons or positrons themselves enter the ECAL, they will initially emit photons via bremsstrahlung that subsequently undergo conversion. For both kinds of incident particles, the chain of photon conversion and bremsstrahlung

[1] A radiation length is the mean distance travelled through a material by a high-energy electromagnetic particle before losing 1/e of its original energy.

will continue until the generated particles fall below a critical energy threshold of approximately 10 MeV. This produces electromagnetic showers consisting of photons, electrons and positrons throughout the lead-LAr layers. The charged particles in the showers will ionize the LAr and generate free charges that are collected by electrodes. The resulting electrical signals are measured, and their size is proportional to the energy deposited in each layer.

The ECAL has three layers in the barrel, as seen in figure 3.8, and two in the end-caps. A tight localization of the energy deposits is enabled by the fine granularity in η of the first barrel layer (0.0031×0.1 in $\Delta\eta \times \Delta\phi$). The bulk of the calorimeter material is contained in the second barrel layer and is composed of square cells with a granularity of 0.025×0.025. The final barrel layer has a reduced cell granularity of 0.050×0.025, and for the cells in the end-cap layers it is 0.1×0.1. In order to correct for energy lost in dead material before entering the ECAL, presampler detectors are placed in front of the first barrel layer and most of the first end-cap layer ($1.5 < |\eta| < 1.8$) .

Hadronic Calorimeter

The HCAL surrounds the ECAL, has a complete coverage in ϕ and an almost complete coverage in η ($|\eta| < 4.9$). It uses layers of steel, copper or tungsten to absorb incident hadrons and initiate showers of additional hadrons via electromagnetic or inelastic nuclear interactions. The energies of the hadronic showers are measured using either LAr or plastic scintillator tiles as the active material. For the latter, the hadrons inside the showers will excite the scintillator material which then emits light that is transformed into electrical signals by photo-multiplier tubes. The combined HCAL and ECAL have a total thickness of approximately 10 nuclear interaction lengths[2], with the HCAL providing over 8, that is sufficient to contain the hadronic showers.

The HCAL consists of three sub-systems: the Tile Calorimeter, the Hadronic End-cap Calorimeter (HEC) and the Forward Calorimeter (FCal). The Tile Calorimeter covers the barrel and extended-barrel regions ($|\eta| < 1.7$), and is made of alternate layers of steel absorbers and active plastic scintillator tiles. The HEC consists of two independent wheels per end-cap that cover $1.5 < |\eta| < 3.2$ and are built from copper absorbers with active regions filled with LAr. Finally, the FCal consists of three modules in each end-cap that cover the forward region ($3.1 < |\eta| < 4.9$). The first module of the FCal uses copper absorbers and the other two use tungsten, with all modules

[2] A nuclear interaction length is the mean distance travelled through a material by a hadronic particle before undergoing an inelastic nuclear interaction.

using LAr as the active material. The three sub-systems of the HCAL have coarser granularity compared to the ECAL [43], but provide a sufficient level of precision for the reconstruction of jets and missing energy in ATLAS.

3.2.4 Muon Spectrometer

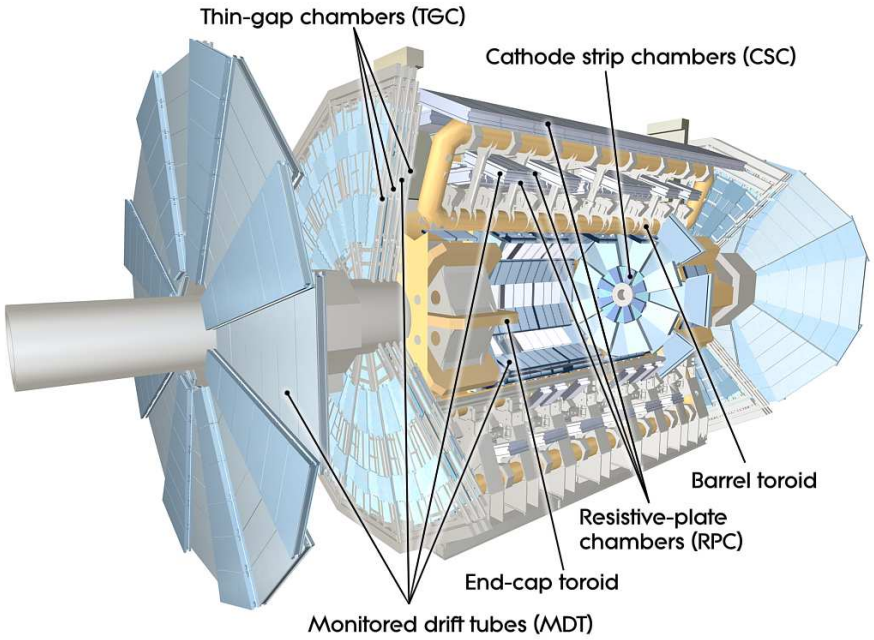

Figure 3.9 A cut-away view of the ATLAS MS and toroid magnets [43].

Most muons produced in LHC collisions are minimally ionizing particles, and so escape the previously mentioned sub-detectors leaving hits in the ID and depositing only small amounts of energy in the calorimeters. Since muons experience limited bending in the magnetic field of the solenoid, the ID struggles to provide precise muon track p_T measurements and reliable charge assignment at high p_T. The Muon Spectrometer (MS) surrounds the HCAL and is designed to provide additional tracking for muons within $|\eta| < 2.7$ and with full ϕ coverage. Its large toroid magnet in the barrel region and two smaller toroids in the end-caps result in muon tracks with larger arcs, allowing for precise muon p_T and charge measurements over the full p_T range. The MS consists of four sub-systems as shown in figure 3.9. Muon tracking is performed by two kinds of precision detectors: the Monitored Drift Tubes (MDTs) and Cathode Strip Chambers (CSCs). The other two sub-systems use fast-response detectors that provide information for triggering, and include the Resistive Plate Chambers (RPCs) and Thin Gap Chambers (TGCs).

MDT modules exist in both the barrel and end-cap regions of the MS, and contain between 3-8 layers of anode wires within 3 cm diameter tubes. The tubes are filled with an Ar/CO_2 gas mixture, and the charged particle detection mechanism is similar to that of the TRT. The MDTs provide precise muon hit coordinate measurements within $|\eta| < 2.7$, with their innermost layer restricted to $|\eta| < 2$. The remaining forward region ($2 < |\eta| < 2.7$) contains the highest muon flux and is covered by the CSCs. The CSCs are multi-wire proportional chambers that can also provide precision hit coordinates but with a rate capacity that is higher then the MDTs. The RPCs and TGCs can rapidly provide information to the trigger with sufficient spatial and time resolution. The RPCs are gaseous parallel electrode-plate detectors while the TGCs, like the CSCs, are multi-wire proportional chambers. They cover the barrel ($|\eta| < 1.05$) and end-cap ($1.05 < |\eta| < 2.7$) regions, respectively.

3.2.5 Trigger

At its design luminosity the LHC delivers proton-proton collisions at a rate of 40 MHz, which exceeds the capacities of the data collection network and data storage system of the ATLAS experiment. The ATLAS trigger system [53–55] performs the critical task of identifying the subset of events that contain the most interesting physics for further analysis. In doing so, it reduces the event rate to a level that is low enough to be recorded. The trigger system contains multiple levels where each subsequent level further brings down the event rate by using increasingly more sophisticated reconstruction and identification techniques. A general description of the trigger system is provided below. Additional information on the specific triggers used in the studies presented in this thesis will be provided in section 3.3.2.

The trigger system operational during $\sqrt{s} = 7$ and 8 TeV data taking is illustrated in figure 3.10, and consists of three levels. The hardware-based Level 1 (L1) rapidly identifies regions-of-interest (ROIs) in the detector using reduced granularity information from the calorimeters and the fast-response components of the MS. The delay between a collision event and the L1 trigger decision (latency) is at most 2.5 μs. L1 reduces the event rate to about 75 kHz and passes along its data through a readout system to the High-Level Trigger (HLT).

The HLT is software-based and consists of two levels: the Level 2 (L2) and the Event Filter (EF). L2 brings down the event rate to around 3 kHz by using the full detector granularity within the ROIs and including, for the first time, information from the precision tracking systems. The average latency at L2 is 40 ms but can take up to 100

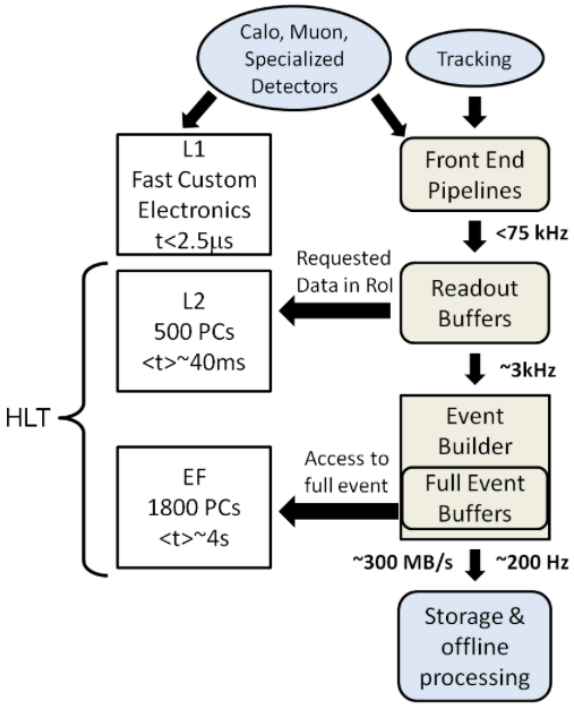

Figure 3.10 A schematic of the ATLAS trigger system operational during $\sqrt{s}$ = 7 and 8 TeV data taking [55]. Note that the two levels of the HLT (L2 and EF) were unified into a single level during $\sqrt{s}$ = 13 TeV data taking.

ms in high pile-up conditions. Finally, the EF has access to the full detector information and executes reconstruction and identification techniques that are very similar to those used offline. The event rate is brought down to roughly 200 Hz at EF, with an average latency of approximately 4 s.

In order to cope with the higher event rates expected during $\sqrt{s}$ = 13 TeV data taking, the ATLAS trigger system received several upgrades [54]. The L1 upgrades include changes to the calorimeter and muon trigger systems, and the addition of a new topological trigger module. Regarding the HLT, the previously mentioned L2 and EF were merged into a single level. This merger allows for better resource sharing and an overall simplification of both the hardware and software. The data collection network and data storage system were also upgraded, increasing the output event rate to 100 kHz after L1 and 1 kHz after the HLT. Although it was not yet available in the $\sqrt{s}$ = 13 TeV data used in this thesis, a Fast TracKer (FTK) system [2] will be added to the future ATLAS trigger. The FTK upgrade will enable global track reconstruction at the full L1 output rate, with more details provided in the context of the FTK studies presented in chapter 4.

3.3 Event Reconstruction

The proton-proton collision events provided by the LHC are reconstructed using specialized algorithms developed for the ATLAS detector. During data taking (online), events are partially reconstructed by the algorithms implemented in the ATLAS trigger system. More sophisticated algorithms are subsequently run to provide the full event reconstruction used in offline studies.

The offline studies presented in this thesis use data recorded by the muon, electron and tau trigger systems; and utilize the offline reconstruction of tracks, vertices, energy clusters, leptons, jets and missing transverse energy. Both the offline and trigger-level reconstruction algorithms will be described in sections 3.3.1 and 3.3.2, respectively. Finally, an overview of the ATLAS data processing chain is provided in section 3.3.3.

3.3.1 Offline Reconstruction

Tracks and vertices

When charged particles pass through the ATLAS ID they can interact with and leave signals in each of the pixel, SCT and TRT sub-detectors. These signals provide a three-dimensional picture of each charged particles path through the ID, where the paths are helical in form due to the magnetic field of the solenoid. The most likely helical paths can be reconstructed in an algorithmic construction known as tracks. The properties of the charged particles, such as their charge and momentum, can then be inferred from the curvature of the track trajectories.

Track reconstruction is a challenging task given the pile-up conditions of the ATLAS detector. It is possible for individual collision events to contain thousands of track candidates [56], with the ID producing a large volume of raw data. The data must first be converted into a form that is appropriate for the tracking algorithms. This involves building three-dimensional space points from the raw pixel and SCT hit coordinates, as well as calibrated drift circles from the raw TRT timing information [57]. Tracks are then reconstructed from this information in two stages [56, 58, 59].

The first stage targets tracks that are associated to charged particles directly produced from the proton-proton collisions, or those originating from the decays of particles with a lifetime shorter then 3×10^{-11}s. This is achieved using an inside-out algorithm that

starts from the space points of the first pixel layer and then extends them radially outward. This algorithm begins by constructing track seeds with at least three matching space-points from the pixel layers and first SCT layer. From these seeds the algorithm iteratively adds matching hits throughout the SCT using a Kalman filter [60], and a fit is then performed to estimate the helical trajectory of each track candidate. Any outlying hit clusters are then removed, ambiguities in the association of the hits to the tracks are resolved and selections on track quality criteria are applied to reduce fake tracks. The remaining track candidates are then extrapolated into the TRT and, finally, refitted using the combined information of the pixel, SCT and TRT sub-detectors.

The second stage recovers any tracks that did not have enough pixel hits from which to build a seed in the first stage. This can occur for tracks associated to charged particles that originate from photon conversions or the decays of long-lived particles. The track seeds for the second stage are built from any unused segments in the TRT, and are extrapolated inward using an outside-in algorithm. This algorithm searches for any matching space points from the SCT and pixel layers that were not already associated to a track in the first stage.

Multiple tracks can have a common origin or vertex. Primary vertices are defined as those compatible with originating from the nominal interaction region of the ATLAS detector, and are reconstructed using an iterative vertex finding algorithm [61]. Although each event can contain many primary vertices, the offline studies presented in this thesis define one of them as *the* primary vertex (PV). The PV is identified as the vertex with the largest value of the sum of the squared p_T of its associated tracks, with at least three of the tracks having p_T above 400 MeV. Some processes, such as those involving the decays of b quarks or tau leptons, can produce secondary vertices that are displaced from the nominal interaction region.

The helical trajectory of a reconstructed track is parameterized at its point of closest approach to the z-axis using a perigee representation (d_0, z_0, ϕ_0, θ, $\frac{q}{p}$). The coordinate system can be centered at either the nominal interaction point of the ATLAS detector or at a particular vertex. The track helix parameters are defined as:

- d_0 and z_0: the transverse and longitudinal impact parameters. They measure the distance of closest approach in the transverse plane and z-direction, respectively.

- ϕ_0 and θ: the azimuth and polar angles.

- $\frac{q}{p}$: the ratio of the track electric charge ($q = \pm 1$) to the magnitude of its momentum.

Energy clusters

When particles pass through the ATLAS calorimeter system they can produce particle showers, where each shower will deposit its energy in a cluster of calorimeter cells. The identification and energy reconstruction of the initial particles requires the association of each cell to the correct cluster. There are two main clustering algorithms used in ATLAS. One of them is for purely electromagnetic showers that deposit energy only in the ECAL, and the other also targets hadronic showers that can deposit energy in both the ECAL and HCAL.

A sliding window algorithm [62–64] is utilized for the purely electromagnetic showers. This algorithm uses a window of 3×5 units, each with size 0.025×0.025 in (η, ϕ) space, and scans across the entire ECAL. The total transverse energy of a cluster is taken as the sum of the energies of each cell in the window. The clusters are then passed to dedicated particle reconstruction algorithms, such as those for electrons and photons, if their transverse energy is above 2.5 GeV. This relatively simple clustering algorithm is appropriate given that electromagnetic showers tend to be well contained and have little variation in shower shape.

In contrast, the hadronic showers exhibit large variations depending on the type of particle that initiates the shower. Considering this, a more sophisticated topological clustering (topoclustering) algorithm [65–69] is used that does not assume any particular shower shape. The three dimensional topoclusters are seeded by calorimeter cells that have a signal-to-noise ratio of at least four. In order to suppress noise, the algorithm then iteratively includes only the surrounding cells that have a signal-to-noise ratio of at least two. After this step, a single layer is added consisting of all neighboring cells and then any topoclusters that contain multiple local maxima are split. This last point avoids the aggregation of nearby showers into a single topocluster. The total transverse energy of the topoclusters is taken as the sum of the energy of its cells, and its position is taken as the energy weighted average of the position of its cells.

To account for variations in the calorimeter response to showers initiated by different kinds of particles, the reconstructed energy of the clusters are corrected using custom calibration schemes. The electromagnetic energy (EM) scale is used to calibrate the energy of the purely electromagnetic showers, under the assumption that electrons or photons initiate them. Topocluster energies are corrected according to a shower shape dependent local hadron calibration (LC) scheme [70]. This corrects for the effects of invisible or escaped energy, the presence of dead material and signal losses due to out-of-cluster deposits that fail the noise thresholds.

Muons

Since muons are minimally ionizing particles at LHC energies, they will pass through the entirety of the ATLAS detector. Along their path they can leave hits in the ID and MS, and deposit small amounts of energy in the calorimeters. Therefore, the reconstruction of muons comes largely from tracking and is performed in two stages [71,72]. The first stage builds tracks from straight-line segments using the MS stations, and then extrapolates them back to the interaction point while accounting for any energy losses in the calorimeters. The second stage searches for matching tracks in the ID, where the matching scheme is based on the agreement between the MS and ID track parameters. Finally, combined tracks are formed by taking the covariance weighted average of the two sets of track parameters [73].

There are two types of muon candidates relevant to the studies presented in this thesis: Stand-Alone (SA) and Combined (CB). SA muons have tracks in the MS but not in the ID, and so they will only pass the first stage of reconstruction. In contrast, CB muons have a track in both the MS and ID and so their reconstruction involves both stages. Overall, the CB muons make up over 95% of the offline candidates and have the best performance in terms of reconstruction efficiency and the rejection of fake, non-prompt and cosmic muons.

The studies presented in this thesis consider muons in the region $|\eta| < 2.5$ and with p_T above at least 15 GeV. Only CB muons are considered in the $\sqrt{s} = 7$ and 8 TeV data samples. In the $\sqrt{s} = 13$ TeV data sample, both CB and SA muons are included if they pass a Medium identification criteria [72]. This criteria was designed to minimize the systematic uncertainties associated with the muon reconstruction and calibration. In all data samples and over most of the p_T and η range considered, the offline reconstruction efficiency is close to 99% [71,72].

The muon candidates in each collision event are required to originate from the PV. To this end, selections are applied to the z_0 and d_0 impact parameters of the tracks calculated with respect to that vertex. Upper thresholds are imposed on both the absolute value of z_0 multiplied by $\sin(\theta)$ ($|z_0 \sin(\theta)|$) and the d_0 significance, defined as its absolute value divided by the uncertainty ($|d_0|/\sigma_{d_0}$). The values of the upper bounds applied to both of these quantities are summarized in table 3.4.

To further reduce contributions from misidentified muons, both track and calorimeter-based isolation selections are applied. These selections utilize cones around the muon candidates, and restrict the amount of detector activity contained within them. The

track-based isolation uses the scalar sum of the p_T of the tracks from the PV that are inside a cone, excluding the track of the muon itself, relative to its offline p_T ($\sum_{\text{rel.}}^{\Delta R} p_T^{\text{track}}$, where ΔR is the size of the cone). The calorimeter-based isolation considers the scalar sum of the transverse energies of the calorimeter cells within a cone, excluding the energy associated with the muon itself, relative to its offline p_T ($\sum_{\text{rel.}}^{\Delta R} E_T^{\text{calo}}$). The size of the isolation cones and the upper bound on the isolation variables are summarized in table 3.4, and both quantities were chosen to maximize the sensitivity to the relevant signal processes[3]. In some cases tighter isolation criteria are applied for muons with lower p_T, since they provide better background rejection.

A more sophisticated isolation scheme is used in the $\sqrt{s} = 13$ TeV data sample. A Gradient criteria [72] is applied to all muon candidates, where the track and calorimeter-based selections are both p_T and η dependent, and are tuned to provide an efficiency of 90-99% depending on p_T. Several of such criteria from ref. [72] were considered, with the Gradient criteria chosen since it provided the best sensitivity to the relevant signal process.

	$\sqrt{s}$ = 7 TeV	$\sqrt{s}$ = 8 TeV	$\sqrt{s}$ = 13 TeV
Identification	CB	CB	CB and SA (Medium)
$\lvert\eta\rvert$	< 2.5	< 2.5	< 2.5
p_T [GeV]	> 15	> 15, 26	> 15
$\lvert z_0 \sin(\theta)\rvert$ [mm]	< 1.0	< 1.0	< 0.5
$\lvert d_0\rvert/\sigma_{d_0}$	< 3.0	< 3.0	< 3.0
Isolation for high-p_T	$\sum_{\text{rel.}}^{0.2} E_T^{\text{calo}} < 10\%$ $\sum_{\text{rel.}}^{0.2} p_T^{\text{track}} < 4\%$	$\sum_{\text{rel.}}^{0.2} E_T^{\text{calo}} < 10\%$, 2% $\sum_{\text{rel.}}^{0.2,0.4} p_T^{\text{track}} < 4\%$, 6%	Gradient
Isolation for low-p_T	$\sum_{\text{rel.}}^{0.2} E_T^{\text{calo}} < 7\%$ $\sum_{\text{rel.}}^{0.2} p_T^{\text{track}} < 4\%$	$\sum_{\text{rel.}}^{0.2} E_T^{\text{calo}} < 7\%$, 2% $\sum_{\text{rel.}}^{0.2,0.4} p_T^{\text{track}} < 4\%$, 6%	Gradient

Table 3.4 Summary of the offline selection criteria for muons that is used in the studies presented in this thesis. The separation between the high- and low-p_T regions is at 20 GeV for the $\sqrt{s}$ = 7 and 8 TeV data samples, and 25 GeV for the $\sqrt{s}$ = 13 TeV data sample. Wherever two comma-separated values are given for the $\sqrt{s}$ = 8 TeV selections, the first value refers to the Higgs boson analysis of chapter 5 and the second to the tag-and-probe method of chapter 4 .

[3] The signal process for the analyses presented in chapter 5 is the WH production of the Higgs boson with $H \to WW^*$ decay (m_H = 125 GeV). For the tag-and-probe method presented in chapter 4 it is the $Z \to \tau\tau$ process. Note that the tag-and-probe method uses only the $\sqrt{s}$ = 8 TeV data sample, whereas the Higgs boson analyses use the $\sqrt{s}$ = 7, 8 and 13 TeV data samples.

Electrons

When electrons pass through the ATLAS detector they leaves hits in the ID and deposit their energy in the ECAL. Therefore, the offline reconstruction of electrons involves both tracking and clustering algorithms, and occurs in three steps [63, 64]. First, the energy clusters in the ECAL are reconstructed using the sliding window algorithm defined earlier. Next, tracks from the ID with p_T above 500 MeV are extrapolated to the middle layer of the ECAL and matched to a cluster if they lie within $\Delta\eta < 0.05$ and $\Delta\phi < 0.1$. If multiple tracks are matched to a particular cluster, then the closest track in ΔR is chosen with priority given to those with hits in both the pixel and SCT sub-detectors. Finally, for all matched clusters, the sliding window algorithm is run again but with the window size reoptimized separately for the barrel and end-cap regions of the ECAL. The new windows have a size of 3×7 and 5×5 units in the barrel and end-cap regions, respectively.

Many of the electron candidates that pass the reconstruction stage originate from photon conversions and hadrons misidentified as electrons. To reduce these contributions, the candidates are also required to pass identification criteria [63, 64] using variables built from calorimeter and tracking information. The variables that provide the best discrimination are based on the calorimeter shower shape, the quality of the match between the track and cluster, and the amount of transition radiation emitted in the ID. Many different kinds of identification criteria are defined, each of which targets a different level of efficiency and purity. Some of these criteria are cut-based, where sequential selections are applied on the discriminating variables. Others are likelihood-based, where the variables are used to train a multivariate likelihood and working points are defined by applying different thresholds on its output.

The studies presented in this thesis consider offline electrons reconstructed within the region $|\eta| < 2.47$, except in the transition region between barrel and endcap of the ECAL ($1.37 < |\eta| < 1.52$), and with p_T above at least 15 GeV. In these studies, several different electron identification criteria are used. For the $\sqrt{s} = 7$ TeV data sample, a Medium [74] cut-based criteria is used that provides an electron identification efficiency of up to 92%. The likelihood-based LooseLH, MediumLH and VeryTightLH operating points [63] are utilized in the $\sqrt{s} = 8$ TeV data sample, corresponding to identification efficiencies of up to 96%, 94% and 88%, respectively. In the $\sqrt{s} = 13$ TeV data sample, the likelihood-based MediumLH and TightLH [64] operating points are used that provide up to 94% and 88% efficiency, respectively.

Requirements on the $|z_0 \sin(\theta)|$ and d_0 significance are applied to the electron tracks to ensure that they originate from the PV. To further bring down contributions from hadrons misidentified as electrons, both track- and calorimeter-based isolation criteria are applied. The definitions of the electron isolation variables and the thresholds applied to them are very similar to what was described previously for the offline muons. The Gradient operation point [64] is again used in the $\sqrt{s}$ = 13 TeV data sample for the isolation of the electron candidates.

The precise offline electron selections used in the studies presented in this thesis are shown in table 3.5. Both the electron identification and isolation criteria were chosen to maximize the sensitivity to the relevant signal processes (see footnote 3). In some cases tighter electron identification and isolation criteria are used for electrons with lower p_T, since they provide better rejection against backgrounds.

	$\sqrt{s}$ = 7 TeV	$\sqrt{s}$ = 8 TeV	$\sqrt{s}$ = 13 TeV
Identification for high-p_T	Medium	LooseLH, MediumLH	MediumLH
Identification for low-p_T	Medium	VeryTightLH, MediumLH	TightLH
$\lvert\eta\rvert$	< 2.47	< 2.47	< 2.47
p_T [GeV]	> 15	> 15, 20	> 15
$\lvert z_0 \sin(\theta)\rvert$ [mm]	< 1.0	< 0.4	< 0.5
$\lvert d_0\rvert/\sigma_{d_0}$	< 10	< 3.0	< 5.0
Isolation for high-p_T	$\sum^{0.2}_{\text{rel.}} E_T^{\text{calo}} < 10\%$ $\sum^{0.2}_{\text{rel.}} p_T^{\text{track}} < 4\%$	$\sum^{0.2}_{\text{rel.}} E_T^{\text{calo}} < 10\%$, 2% $\sum^{0.2,0.4}_{\text{rel.}} p_T^{\text{track}} < 4\%$, 6%	Gradient
Isolation for low-p_T	$\sum^{0.2}_{\text{rel.}} E_T^{\text{calo}} < 7\%$ $\sum^{0.2}_{\text{rel.}} p_T^{\text{track}} < 4\%$	$\sum^{0.2}_{\text{rel.}} E_T^{\text{calo}} < 7\%$, 2% $\sum^{0.2,0.4}_{\text{rel.}} p_T^{\text{track}} < 4\%$, 6%	Gradient

Table 3.5 Summary of the offline selection criteria for electrons that is used in the studies presented in this thesis. The separation between the high- and low-p_T regions is at 20 GeV for the $\sqrt{s}$ = 7 and 8 TeV data samples, and 25 GeV for the $\sqrt{s}$ = 13 TeV data sample. Wherever two comma-separated values are given for the $\sqrt{s}$ = 8 TeV selections, the first value refers to the Higgs boson analysis of chapter 5 and the second to the tag-and-probe method of chapter 4 .

Jets

Quarks and gluons can never be observed in isolation. If they are produced in the initial hard scatter interaction of a proton-proton collision, they will fragment into showers of partons that will eventually form hadrons. This process is called hadronization, and the resulting collimated collections of hadrons that can be observed by the ATLAS detector are called jets. The hadrons in jets will deposit energy in the ECAL and HCAL, and any charged hadrons will also leave tracks in the ID.

Offline jet reconstruction in ATLAS is performed using a successive recombination algorithm [75, 76] that associates calorimeter energy deposits to jet candidates. The inputs to this algorithm are the LC calibrated topoclusters in each event, and their grouping is based on a particular spatial separation metric:

$$d_{ij} = \min(k_{ti}^{2m}, k_{tj}^{2m}) \frac{\Delta_{ij}^2}{R^2} \tag{3.7}$$

where i and j refer to a particular topocluster pair, $\Delta_{ij}^2 = (\eta_i - \eta_j)^2 + (\phi_i - \phi_j)^2$, R is a parameter used to set the characteristic jet radius and k_t is the topocluster transverse momentum. The parameter m sets the power of the momentum (k_t) weighting to distance (Δ_{ij}) scales, and is chosen to be -1. This choice results in the size of jets being largely determined by the higher p_{T} topoclusters. The resulting algorithm is called anti-k_t, with additional information provided in refs. [75, 76].

For the offline studies presented in this thesis, the R parameter is set to 0.4 and the resulting jets are reconstructed over the region $|\eta| < 4.5$. Offline jets are required to have p_T larger than 25 GeV except for $|\eta| > 2.4$, where the threshold is raised to 30 GeV. The increased threshold in the forward region reduces the contribution from jets originating from pile-up. A final refinement of the jet energy calibration, on top of the LC scheme, is performed using what is called the jet energy scale (JES). The JES correction is estimated from data using *in-situ* techniques that exploit the p_T balance between jets and other objects in Z/γ^*+jets, γ+jets and QCD di-jet events [67, 69].

Additional requirements are applied in order to further reduce pile-up jets. In the $\sqrt{s}$ = 7 and 8 TeV data samples the jet vertex fraction (JVF) [77] is used, which is the ratio of the sum of the p_T of all tracks associated to a jet to that of the subset of tracks from the PV. Each jet in the $\sqrt{s}$ = 8 TeV data sample with p_T below 50 GeV and $|\eta| < 2.4$ is required to have a JVF value larger then 0.5. Due to less severe pile-up conditions, the threshold is increased to 0.75 in the $\sqrt{s}$ = 7 TeV data sample. In the $\sqrt{s}$ = 13 TeV data

sample a multivariable algorithm called the jet vertex tagger (JVT) [78] is used instead. The JVT output is required to be larger than 0.64, which provides a 92% efficiency for non pile-up jets.

b-jet tagging

The ability to efficiently discriminate between jets that were initiated by b-quarks as opposed to gluons or other lighter quarks is critical to the studies presented in this thesis. If a b-quark is produced in the hard scatter interaction of a proton-proton collision, either directly or from the subsequent decay of a top-quark, it will hadronize into a jet containing a b-hadron. Due to the relatively large mass of b-hadrons their decay products have a relatively large momentum transverse to the b-hadron flight path, and so b-quark initiated jets tend to be wider. Moreover, due to the relatively long lifetime of b-hadrons, the tracks associated to such jets tend to have larger impact parameters and can originate from secondary vertices.

Jets that were initiated by b-quarks are referred to in this thesis as b-jets, and their identification is referred to as b-jet tagging. The discriminating variables used in b-jet tagging algorithms are based on the unique features of b-jets mentioned above. There are three main algorithms used in ATLAS [79]:

- IP3D algorithm: uses the impact parameters of tracks associated to jets in order to separate b-jets from gluon and light-quark initiated jets.

- SV1 algorithm: uses the properties of secondary vertices to distinguish between the different kinds of jets.

- Jet fitter algorithm: identifies b-jet candidates by looking for a common path along which the PV, the secondary vertex and any subsequent vertices lie.

To maximize the performance of b-jet tagging in ATLAS, the three algorithms are combined using artificial neural networks that assign a score to each jet representing how likely it is to be initiated by a b-quark. The combined algorithm that was developed for the $\sqrt{s}$ = 7 and 8 TeV data samples is called MV1 [80]. For the $\sqrt{s}$ = 13 TeV data sample, the new IBL pixel layer and several algorithmic enhancements were included into what is called MV2 [81].

The tagging of b-jets is limited to the coverage of the ID ($|\eta| < 2.5$), and for jet p_T above 25 GeV in the $\sqrt{s} = 7$ TeV data sample and 20 GeV otherwise. For the studies presented in this thesis, an operating point that is 85% efficient in identifying b-jets is adopted for both the MV1 and MV2 algorithms. This corresponds to a rejection of a factor of 10 and 33 against jets originating from light-quarks or gluons for MV1 and MV2, respectively [80, 81]. The b-jet tagging operating point was chosen to maximize the sensitivity to the relevant signal processes (see footnote 3).

Tau leptons

Due to their short lifetime, tau leptons will decay before reaching the active regions of the ATLAS detector and so are reconstructed and identified via their decay products. About one third of decays occur in the leptonic mode, producing two neutrinos and an electron or muon. The remaining decays occur in the hadronic mode, producing a neutrino and a number of neutral and charged hadrons consisting mostly of pions and kaons. These hadrons form a jet, referred to as a τ-jet, that tends to be have a narrower collimation and lower track multiplicity compared to quark or gluon initiated (QCD) jets. A more detailed introduction to tau leptons and their decays will be provided in the context of the ATLAS tau trigger in chapter 4. While leptonic tau decays are covered by the offline reconstruction and identification of electrons and muons, ATLAS uses dedicated algorithms [1, 82] for the τ-jets from hadronic tau decays.

The reconstruction of τ-jets is seeded by anti-k_t ($R = 0.4$) jets that lie within the coverage of the ID and have p_T above 10 GeV. Since τ-jets are typically more collimated then QCD jets, a core region ($\Delta R < 0.2$) is defined around each jet barycentre. The topoclusters contained within the core region are used to re-calculate the direction and estimate the total transverse energy of the τ-jet candidates. An isolation region is then formed around the core region ($0.2 < \Delta R < 0.4$), and tracks are assigned to the τ-jets in both regions. To ensure the track assignment is robust against pile-up, a dedicated algorithm called the Tau Jet Vertex Association (TJVA) [83] is used to calculate the most likely vertex of origin for each τ-jet candidate. The tracks associated to τ-jets are required to pass track quality requirements on the number of pixel and SCT hits, and selections on the d_0 and z_0 impact parameters calculated with respect to the TJVA vertex. The sum of the track charges in the core region is used to determine the tau lepton charge, and the number of tracks in this region is used to classify them as 1-prong or multi-prong (exactly one track or at least two tracks, respectively). The transverse energy of the τ-jet candidates is corrected using a custom calibration, separate from the JES, called

the tau energy scale (TES) [1, 82]. The TES correction is applied on top of the LC calibration of the anti-k_t jet seeds, and is measured using $Z \to \tau\tau$ and $W \to \tau\nu_\tau$ events.

Many of the τ-jet candidates that pass the reconstruction stage originate from misidentified QCD jets, and so they are required to pass additional identification criteria. The identification algorithms relevant to the studies presented in this thesis use multivariate techniques based on a Boosted Decision Trees (BDT) [84] method. The BDT is trained using a set of track and calorimeter-based variables [1, 82] that provide good discrimination against QCD jets. These variables are based on the narrowness of the calorimeter shower and the spread of tracks, the impact parameters of the tracks, the invariant mass of the tracks and the track multiplicity in the isolation region. The BDT is trained separately for 1-prong and multi-prong τ-jet candidates, and three operating points are defined based on the target τ-jet identification efficiency. These working points are called Loose, Medium and Tight and their respective target efficiencies are 70% (65%), 60% (55%) and 40% (35%) for 1-prong (multi-prong) candidates.

Although QCD jets are by far the most significant background for τ-jet identification, it is also possible for electrons or muons to mimic the signature of 1-prong τ-jets. Dedicated algorithms for vetoing electrons and muons are defined [1] to help reduce these backgrounds. The electron veto algorithm uses a BDT method and is trained using variables based on the calorimeter shower shape and the emission of transition radiation. It is less likely for a muon to be misidentified as a 1-prong τ-jet, but it can occur in the rare situation where the muon track is wrongly associated to a calorimeter cluster with sufficient energy. To reduce this minor background, a cut-based muon veto algorithm is used that exploits the fraction of energy deposited in the EM calorimeter and the fraction of energy carried by the highest momentum track.

Overlap removal

It is possible that multiple of the previously defined offline objects are close together in $\eta - \phi$ space. In these situations, one of the overlapping objects is retained and the others are removed. The studies presented in this thesis adopt different schemes for resolving overlaps, the details of which will be provided below.

In the Higgs boson analysis presented in chapter 5 using the $\sqrt{s} = 7$ and 8 TeV data samples, the higher-p_T lepton is retained if two electrons or two muons candidates overlap within $\Delta R < 0.1$. This can occur, for example, if a prompt electron undergoes bremsstrahlung in the ID material producing more than one electron candidate in its

vicinity. If a muon and an electron are separated by $\Delta R < 0.1$, then only the muon candidate is retained. This usually indicates that a muon has undergone bremsstrahlung in the ID or calorimeter materials. A high-p_T electron will usually also be reconstructed as a jet, so a jet is removed if it overlaps with an electron within $\Delta R < 0.3$. In contrast, if a muon and a jet are separated by $\Delta R < 0.3$, the muon candidate is removed since it is more likely to be a non-prompt muon from a b-hadron decay.

In the tag-and-probe method presented in chapter 4 using the $\sqrt{s} = 8$ TeV data sample, τ-jets are included in addition to the above mentioned offline objects. For these particular studies, offline objects are considered to be overlapping if they are separated by $\Delta R < 0.2$. The overlaps are resolved by retaining the objects in the following order of priority: muons, electrons, τ-jets and jets.

Finally, a different approach is adopted in the Higgs boson analysis using the $\sqrt{s} =$ 13 TeV data sample presented in chapter 5. The electron-electron, muon-muon and electron-muon overlaps are resolved using a set of harmonized criteria [85] that were developed by a dedicated task force within the ATLAS Collaboration. These criteria are more sophisticated than the purely ΔR-based criteria mentioned above, and are shared by many ATLAS analyses using $\sqrt{s} = 13$ TeV data. Jets are discarded if they overlap within $\Delta R < 0.2$ of an electron, or if they are separated by $\Delta R < 0.2$ with a muon and have fewer than three associated tracks. For the remaining jet-electron and jet-muon overlaps within $\Delta R < 0.4$, the leptons are rejected if the jet passes the previously mentioned JVT requirement.

Missing transverse energy

Although the energy of the protons accelerated by the LHC is precisely known, the momentum carried by the constituent partons after a proton-proton collision is not. However, the component of the partons momentum transverse to the beam pipe will be negligible. Therefore, by conservation of momentum, the transverse momenta of all particles in an event will be balanced with the magnitude of their vectorial sum close to zero.

The only particles in the SM that will not interact with any of the ATLAS detector materials are neutrinos. Although neutrinos cannot be detected directly, their presence in an event can be inferred by a large imbalance in the reconstructed transverse momentum of all the detected particles. In this way, the missing transverse momentum that would otherwise balance the vectorial sum is carried away by the escaping neutri-

nos. More modest contributions to the transverse momentum imbalance can originate from resolution effects in the offline reconstruction, pile-up effects, cracks and dead or transition regions in the detector, cosmic-ray or beam halo muons, detector noise and other temporal detector defects.

The offline reconstruction of the missing transverse momentum [86–88] involves the calculation of the negative vectorial sum of the transverse momenta of all objects selected by the ATLAS offline reconstruction and identification algorithms, and any remaining "soft" objects that typically have low values of p_T. The calculation can thus be summarized as:

$$-\left(\sum_{\text{selected}} \mathbf{p_T} + \sum_{\text{soft}} \mathbf{p_T} \right) \tag{3.8}$$

where the choice of soft and selected objects differ between different methods of reconstructing the missing transverse momentum. Two methods of reconstruction are considered in the studies presented in this thesis: one is calorimeter-based and the other is track-based.

The calorimeter-based missing transverse momentum is referred to in this thesis as $\boldsymbol{E_T^{\text{miss}}}$ and its magnitude as E_T^{miss}. This quantity benefits from the large coverage of the ATLAS calorimeter system and its sensitivity to electrically neutral particles. The offline objects that enter the selected term in eq. 3.8 include muons, electrons, photons and jets (including b-jets and τ-jets). Any remaining jets and clusters of calorimeter cells are included in the soft object term. To suppress pile-up effects that worsen the E_T^{miss} resolution, the soft term in the $\sqrt{s}$= 8 and 13 TeV data samples is scaled by quantity called the soft term vertex fraction (STVF) [89]. The STVF is computed as the scalar p_T sum of all soft term tracks associated with the PV to that of all vertices.

The track-based missing transverse momentum [90] is referred to in this thesis as $\boldsymbol{p_T^{\text{miss}}}$ and its magnitude as p_T^{miss}. It is calculated as the vectorial sum of the transverse momenta of all tracks in an event that originate from the PV and have a p_T above 500 MeV. In order to account for electrically neutral particles that do not have associated tracks, the sum of track momenta in jets is replaced by their energy measured in the calorimeters. The resolution of this quantity is more robust against pile-up compared to the calorimeter-based variant, however it is limited to the coverage of the ID and it is less sensitive to any neutral particles contained in events.

3.3.2 Online Reconstruction

Muon trigger

The ATLAS L1 muon trigger [54, 91] uses custom built hardware to process signals from the fast-response components of the MS, in order to rapidly identify ROIs in the detector that potentially contain muon candidates. The muon ROIs are identified by the presence of a spatial and temporal coincidence of hits in the RPCs or TGCs pointing to the nominal interaction region. The ROIs can have several p_T thresholds, where the low and high thresholds require a coincidence in two and three layers, respectively. The requirement of an additional coincidence between the inner and middle TGC layers was added for the $\sqrt{s}$ = 13 TeV data sample, significantly reducing the rate of misidentified muons at L1 [54].

The muon HLT refines the L1 ROIs by including the hit information from the high resolution MDT and CSC components of the MS [54, 91]. Muon candidates are reconstructed by the HLT in two stages, with both stages following the principal of offline CB muon reconstruction. The first stage brings down the event rate using a more rapid algorithm that only includes the MDT hits, while the algorithm of the second stage is very similar to offline and uses the full precision of both the MDT and CSC chambers. HLT muons candidates can also be required to pass track-based isolations selections that are similar to offline, but consider only ID tracks in the isolation cones.

The studies presented in this thesis use data recorded by single muon triggers that are not prescaled and provide the lowest available p_T thresholds at the HLT[4]. Table 3.6 shows a summary of the L1 and HLT requirements for these triggers. The p_T thresholds increase during data taking from 11-20 GeV and 18-24 GeV at L1 and the HLT, respectively. The HLT muon candidates are also required to be isolated in the $\sqrt{s}$ = 8 and 13 TeV data samples. The p_T thresholds at L1 and the HLT were raised and HLT isolation was applied in order to reduce the event rate to a manageable level given the increasing luminosity.

The isolated HLT triggers mentioned above were used in conjunction with a higher-p_T threshold HLT trigger that does not have an isolation requirement. The p_T thresholds for these non-isolated triggers increased during data taking from 36-50 GeV. The absence of isolation helps regain trigger efficiency for high-p_T muons.

[4] A single muon trigger requires at least one trigger-level muon candidate to be reconstructed in an event. For a trigger that is not prescaled, every event that fires the trigger is recorded for offline analysis.

	$\sqrt{s}$ = 7 TeV	$\sqrt{s}$ = 8 TeV	$\sqrt{s}$ = 13 TeV
L1 muon trigger	11	15	2015: 15 2016: 20
HLT muon trigger	18	24i or 36	2015: 20i or 50 2016: 24i or 50

Table 3.6 Summary of the single muon triggers used in the studies presented in this thesis. The numbers indicate the minimum lepton p_T requirements (in GeV), and the letter "i" indicates an isolation requirement. The "or" is logical. The L1 trigger that is specified is the one that seeds the lower-p_T HLT trigger.

Tau trigger

A description of the L1 and HLT tau trigger is provided in chapter 4 in the context of the tau trigger studies presented in that chapter.

Electron trigger

The ATLAS L1 calorimeter (L1Calo) trigger [54, 92] rapidly identifies ROIs using information from the ECAL and HCAL systems. Rather then using the full precision of the calorimeters in the ROIs, it uses trigger towers with a reduced granularity of 0.1×0.1 in $\Delta\eta \times \Delta\phi$. The algorithms of the L1Calo trigger can be used to identify a wide range of particle candidates including electrons, photons, jets and τ-jets. In order to cope with the increased luminosity during $\sqrt{s}$ = 13 TeV data taking, several components of the L1Calo electronics received upgrades [54]. For example, new multi-chip modules were installed for the pre-processor system [93] that allows a dynamic pedestal correction to mitigate pile-up effects [54] . At L1, an electron trigger is defined by a lower threshold on the total transverse energy of the ROIs and, in some cases, a requirement on the isolation energy. The algorithms used to calculate these quantities follow the procedure of the L1 tau trigger described in chapter 4.

Electrons are reconstructed and identified in the HLT [54] first using a simplified but fast algorithm to reduce the event rate, followed by more precise algorithms. The fast algorithm builds energy clusters in the L1 ROIs using the full granularity information of the ECAL. Since electrons deposit most of their energy in the second layer of the

ECAL, the algorithm finds the cell in this layer with the largest energy in the ROI. A sliding window algorithm is run around this seed, and a cluster is required to match a track within $\Delta\eta < 0.2$. Identification algorithms that are very similar to offline are then run on the matched clusters in the remaining ROIs. The electron triggers used in the studies presented in this thesis apply Medium cut-based identification criteria in the $\sqrt{s}$ = 7 TeV data sample, and the likelihood-based Loose, Medium or Tight working points otherwise. Additional track- and calorimeter-based isolation selections can be applied to the HLT electron candidates, following the same principle as offline.

The data used in the studies presented in this thesis was collected with non-prescaled single electron triggers that have the lowest available p_T thresholds at the HLT. The requirements of these triggers at L1 and the HLT are summarized in table 3.7. The L1 and HLT p_T thresholds increase from 14-20 GeV and 20-24 GeV, respectively, in response to the increasing luminosity during data taking. Isolation requirements are required at both L1 and the HLT in the $\sqrt{s}$ = 8 TeV data sample, and in the 2016 component of the $\sqrt{s}$ = 13 TeV data sample. In order to mitigate efficiency loss at high-p_T, the isolated HLT electron triggers are used in conjunction with up to two non-isolated triggers that have higher-p_T thresholds.

	$\sqrt{s}$ = 7 TeV	$\sqrt{s}$ = 8 TeV	$\sqrt{s}$ = 13 TeV
L1 electron trigger	14-16	18i	2015: 20 2016: 20i
HLT electron trigger	20-22M	24Mi or 60M	2015: 24M or 60M or 120L 2016: 24Ti or 60M or 120L

Table 3.7 Summary of the single electron triggers used in the studies presented in this thesis. The numbers indicate the minimum lepton p_T requirements (in GeV), and the letter "i" indicates an isolation requirement. The letters "L", "M" and "T" next to the threshold value stand for the Loose, Medium and Tight HLT identification criteria, respectively. The "or" is logical. The L1 trigger that is specified is the one that seeds the lower-p_T HLT trigger.

3.3.3 The ATLAS Processing Chain

There are two kinds of event samples considered in the studies presented in this thesis. The data samples are one kind, and consist of the real proton-proton collision events collected by the ATLAS detector. The other kind includes the simulated Monte Carlo

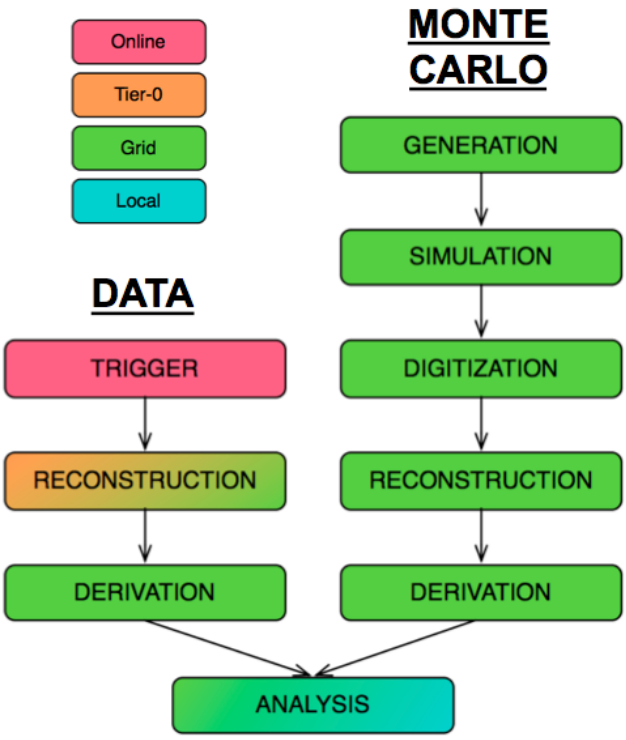

Figure 3.11 Summary of the ATLAS processing chain. The colour coding is indicated on the top left, and represents the resources used at each step in the chain. The online (red), Tier 0 of the GRID (orange), lower-tiers of the GRID (green) and local computing resources (blue) are indicated.

(MC) events generated for different physics processes, that are collectively referred to as the MC samples. Both the data and MC samples are prepared for analysis using the ATLAS processing chain illustrated in figure 3.11. Each step in this chain will be briefly summarized below, with a more complete description available in refs. [94–97].

The ATLAS trigger system records the data samples online, and the raw data is passed to the Tier 0 of the LHC computing GRID [98]. Using the Tier 0 computing resources, the raw data undergoes prompt offline reconstruction and is prepared in a ROOT-readable xAOD format [97]. The lower-tiers of the GRID are available for any reprocessings of the data samples, as well as the production and subsequent processing of the MC samples. An ATLAS software framework known as Athena [96] is used for all stages of the processing chain up until the final analyses. The analyses typically use local computing resources to run dedicated analysis frameworks. The frameworks used to conduct the studies presented in this thesis are based on ROOT [99].

The MC samples are prepared via a simulation chain [94] that includes four stages. The event generation is the first stage and involves the simulation of the hard scattering process followed by the modeling of the parton showering, hadronization, and the underlying event. Many generators exist for LHC physics simulation, and the particular ones used in the studies presented in this thesis were chosen according to their suitability for the relevant physics processes. For some processes the same generator is used for all steps in the event generation, while for others the generator used for the hard scatter is interfaced with a different one for the remaining steps. The second stage in the simulation chain is the detector simulation that uses a framework called GEANT 4 [100]. This framework simulates how the particles from the event generation will interact with the detector material, how they will shower, and how much energy they will deposit in each of the detector elements. The third stage in the chain is called digitization and it turns the simulated energy deposits into a detector response that look like the raw data from the ATLAS detector. In the final stage of the simulation chain, the MC samples undergo offline reconstruction in a way that is coherent with the data samples.

At this point in the processing chain both the data and MC samples are in the same xAOD format, and contain similar information. One difference is that the MC samples not only have available the reconstructed objects but also the "truth" information of the original generated events. Also, a particular method is used to correctly account for pile-up in the MC samples. This method first involves generating soft interactions with PYTHIA [101, 102] and overlaying them on top of the generated hard scattering event. The events in the MC samples are produced with a range of values for the $\mu_{\text{pile-up}}$ parameter, with the associated distribution chosen so that it roughly matches the expected pile-up conditions online. The simulated events are then reweighted so that the $\mu_{\text{pile-up}}$ distribution matches the one observed in the data samples [103].

The xAOD samples are too big to analyze directly. In order to reduce their size they are further processed in a derivation stage, the output of which is in another ROOT-readable format called DxAOD [97]. Different derivations and associated DxAOD samples exist according to the needs of the various physics groups of the ATLAS Collaboration. The final analysis frameworks are capable of reading the information in the DxAOD samples, and apply corrections to them according to the recommendations of the ATLAS performance groups.

4

Tau Trigger Studies

Physics processes involving tau leptons play a crucial role in understanding particle physics at the high-energy frontier. The most sensitive probe of the Yukawa couplings of the Higgs boson to fermions is provided by the $H \to \tau\tau$ decay channel [36]. In addition, processes involving tau leptons provide a window into physics beyond the SM such as models with extended Higgs sectors [104–106], supersymmetry [107–109], heavy gauge bosons [110] and leptoquarks [111]. The ability to efficiently trigger on events containing tau leptons is, therefore, of particular importance to the ATLAS experiment.

In this chapter two studies are presented relating to the ATLAS tau trigger. The first is the measurement of the tau trigger performance using a tag-and-probe method targeting $Z \to \tau\tau$ decays. These measurements were performed using LHC proton-proton collision data at $\sqrt{s} = 8$ TeV corresponding to an integrated luminosity of 20.3 fb^{-1}. This study was published by the ATLAS Collaboration in a paper [1], and was the task assigned to this author to attain qualification within the collaboration.

In future runs of the LHC the luminosity will increase substantially and necessitate new detector upgrades to help cope with increased event rates and pile-up. One of these upgrades is a system of electronics being developed for the ATLAS detector, called

the Fast TracKer (FTK), that will be capable of performing global track reconstruction after each L1 trigger accept. The second study presented in this chapter explored the potential for the FTK to improve tau trigger performance in future proton-proton collisions at $\sqrt{s}$ = 14 TeV. These studies were included in the ATLAS FTK Technical Design Report [2].

This chapter is organized as follows. Section 4.1 provides an introduction to tau leptons and their decays. A general overview of the ATLAS tau trigger system that was operational during $\sqrt{s}$ = 8 TeV data taking is provided in section 4.2. The study relating to the measurements of the tau trigger performance at $\sqrt{s}$ = 8 TeV is presented in section 4.3. A general overview of the FTK is provided in section 4.4, with the studies exploring the potential of using FTK tracks in the tau trigger presented in section 4.5. Finally, a conclusion is provided in section 4.6.

4.1 Introduction to Tau Leptons

Tau leptons have a relatively long lifetime and a proper decay length of 87 μm [21], and so typically decay before reaching the active regions of the ATLAS detector. Because of this, they are identified through their decay products. About one third of decays occur in the leptonic mode ($\tau \rightarrow \nu_\tau \ell \nu_\ell$, where ℓ is an electron or muon). With a mass of 1.777 GeV [21] the tau lepton is the only lepton heavy enough to decay hadronically ($\tau \rightarrow \nu_\tau$+ hadrons), and does so in about two thirds of all cases. The leptonic and hadronic tau decay modes are illustrated in figures 4.1a and 4.1b, respectively.

A number of neutral and charged hadrons will be produced in hadronic tau decays. One or three charged pions ($\pi^\pm$) are produced in 70% and 21% of the decays, respectively. These will be referred to as 1-prong and 3-prong decays, hereafter. Charged kaons ($K^\pm$) are present in the majority of the remaining 9% of hadronic decays. In 60% of all decays, up to two associated neutral pions (π^0) are also produced.

The leptonic and hadronic tau decays will be referred to in this chapter as τ_{lep} and τ_{had} decays. The neutral and charged hadrons stemming from the τ_{had} decays make up the visible decay products of the tau lepton, and will be referred to as τ-jets. The τ_{lep} decays are covered by the electron and muon triggers of the ATLAS detector. The purpose of the ATLAS tau trigger, rather, is to identify the τ-jet from τ_{had} decays.

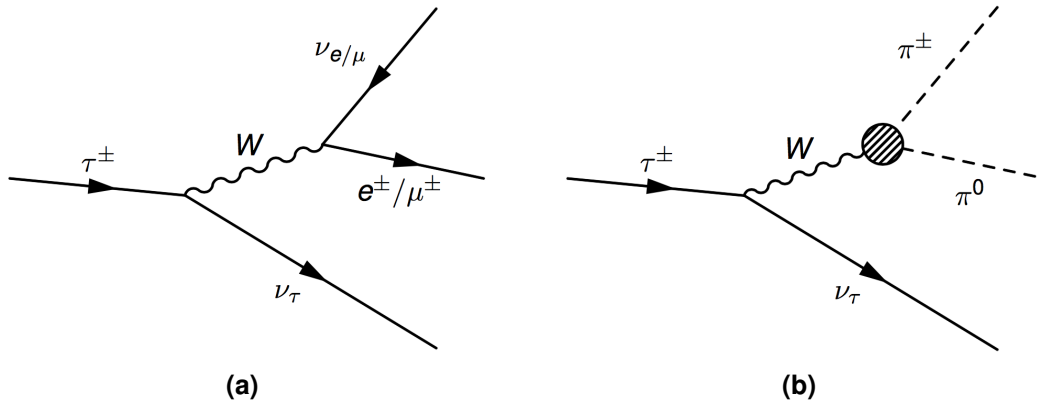

Figure 4.1 (a) A leptonic tau decay and (b) an example of a hadronic tau decay. The blob in (b) represents a possible intermediate resonance of bound quark pairs.

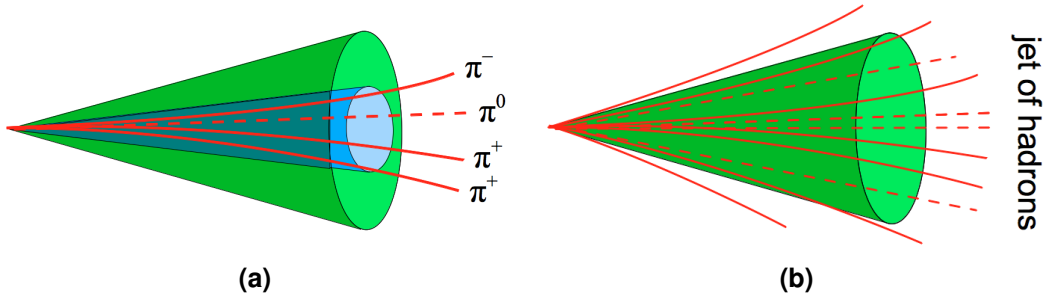

Figure 4.2 (a) A τ-jet with three associated tracks (3-prong decay), where the visible decay products are contained within a narrower cone (blue). (b) A QCD jet where its associated neutral and charged hadrons are distributed throughout a larger cone.

The main background when reconstructing and identifying τ-jets comes from quark or gluon-initiated jets (QCD jets). QCD jets can mimic τ-jets, and are far more common in proton-proton collisions at the LHC. However, we can discriminate between them by exploiting the unique signature of τ-jets as illustrated in figure 4.2. Compared to QCD jets, τ-jets tend to have lower track multiplicity (mainly one track from 1-prong or three tracks from 3-prong decays) and form a narrower shower shape in the calorimeters. These features are exploited by the ATLAS tau trigger system.

4.2 The ATLAS Tau Trigger

During its operations at $\sqrt{s} = 8$ TeV, the LHC reached instantaneous luminosities of nearly 10^{34} cm^{-2}s^{-1} with bunch crossings occurring every 50 ns. This resulted in a large

event rate and detector activity from pile-up. With this in mind, it was necessary to design an ATLAS tau trigger system that could reduce the event rate to a manageable level for disk storage, while efficiently extracting the most interesting physics events containing τ-jets in a pile-up robust manner.

In this section, the ATLAS tau trigger system that was implemented during $\sqrt{s} = 8$ TeV data taking is described. Each subsequent level of the tau trigger (L1, L2 and EF) used algorithms with increasing levels of data analysis complexity and sophistication. A general overview of the τ-jet reconstruction and identification algorithms implemented at each level of the trigger is presented below. A more complete description can be found in refs. [1, 112].

4.2.1 Level 1

At L1, τ-jet candidates were rapidly identified as ROIs in the detector using calorimeter energy deposits. Each ROI was built with two distinct regions: a core region and an isolation region. These regions were defined using trigger towers in both the ECAL and HCAL with a reduced granularity of $\Delta\eta \times \Delta\phi = 0.1 \times 0.1$. The core region was defined as a square of 2×2 trigger towers, with the isolation region defined as a box of towers in the ECAL around the core region. An illustration of a L1 τ-jet candidate is shown in figure 4.3.

The energy of a τ-jet ROI was calculated as the total transverse energy (E_T) in the two most energetic neighboring central towers in the ECAL core region, and in the 2×2 towers in the HCAL, all calibrated with the EM scale. The isolation energy at L1 was calculated as the E_T deposited in the isolation region.

4.2.2 Level 2

The L2 tau trigger used the full granularity of all calorimeter layers within the ROIs. The centre of a τ-jet energy deposit was calculated as the energy-weighted sum of the calorimeter cells within $\Delta R < 0.4$ of a L1 ROI seed. After noise suppression was applied to the cells, the E_T at L2 was calculated using only the cells within a signal cone of $\Delta R < 0.2$ around the centre.

The ATLAS tracking systems were available for the first time at L2, and a fast tracking algorithm (TauB) was run using only the hits from the pixel and SCT components of the ID. TauB tracking took an average of 37 ms to run at the highest pile-up conditions

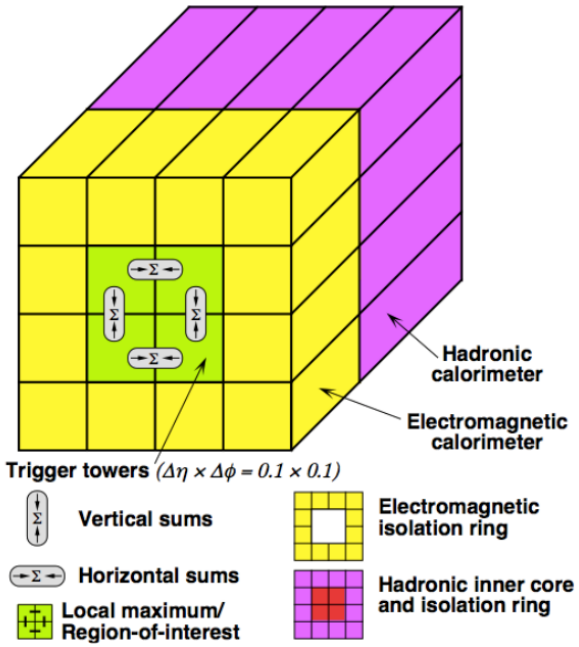

Figure 4.3 Illustration of a τ-jet ROI [54], showing the core and isolation regions built from trigger towers in the calorimeters.

during 2012 data taking ($\mu_{\text{pile-up}} \approx 40$). Although this was fast compared to offline and EF-level tracking, it was still not fast enough to meet the tight latency constraints at L2. Considering this, it was necessary to first apply some selections on calorimeter variables in order to reduce the ROI rate before TauB tracking began. Selections were typically applied to the E_T, and the fraction of E_T deposited in a region of $\Delta R < 0.1$ compared to the full signal cone (f_{core}).

Calorimeter-based shower shape variables, similar to those used by the offline τ-jet identification algorithms from section 3.3.1, were calculated. Track-based variables were also calculated, and selections were applied on these variables in order to reject fake τ-jet ROIs while optimizing true τ-jet efficiencies. As there was no vertex information available at this stage, an alternative approach was used to reject tracks coming from pile-up interactions. The Δz_0 between the highest p_T track to all other tracks within the signal cone was required to be within 2 mm.

4.2.3 Event Filter

At EF-level, more sophisticated τ-jet reconstruction and identification algorithms were possible due to the higher latency. A multivariate trigger using a BDT method [84] was employed to suppress the large backgrounds from QCD jets misidentified as τ-jets.

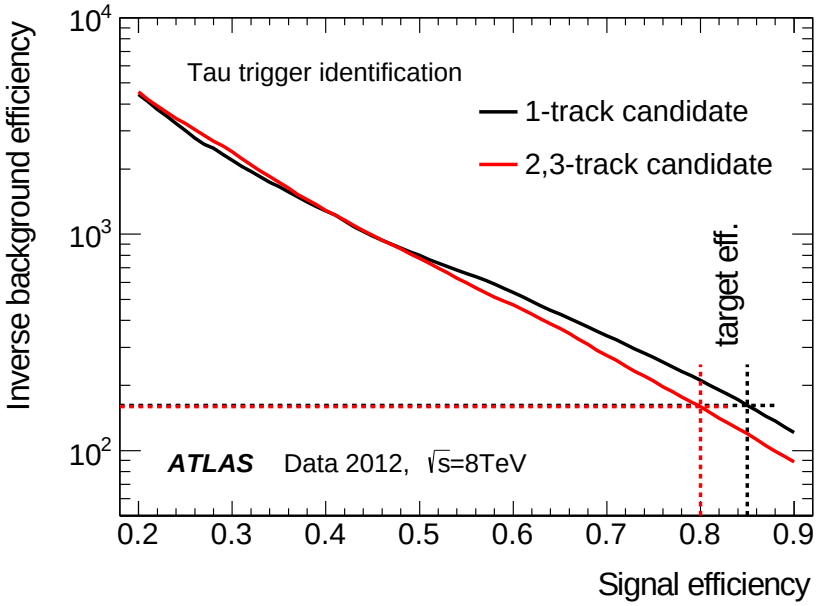

Figure 4.4 Inverse background efficiency versus signal efficiency at EF-level, for τ-jet candidates that satisfied the L1 requirements [1]. The signal efficiency was defined with respect to offline τ-jet candidates passing Medium identification. The inverse background efficiency was calculated in a sample of QCD multijet events.

This BDT method was very similar to the one used for the offline τ-jet identification described in section 3.3.1. However, since the full-event vertex reconstruction was not available at trigger level, the discriminating variables used to train the BDT were not corrected for pile-up.

The performance of the EF tau trigger is presented in figure 4.4. Three working points were defined (Loose, Medium or Tight) targeting different τ-jet identification efficiencies. The Medium working point, for example, targeted 85% and 80% efficiency with respect to offline for 1-track and multi-track candidates, respectively. This working point had an inverse background efficiency of the order of 200 for QCD jets.

4.3 Tau Trigger Performance Measurements at $\sqrt{s} = 8$ TeV

It was important to measure the performance of the tau trigger in order to confirm it was operating as expected during data taking at $\sqrt{s} = 8$ TeV. This included measuring the efficiency at which the tau trigger identified τ-jets, and checking how precise the τ-jet E_T was estimated at each level of the trigger with respect to offline.

In addition, in order to perform searches for physics processes involving τ-jets, it was essential to measure the tau trigger efficiency in data in order to correct any mismodelling of the efficiency in MC simulation. These tau trigger efficiency corrections were used in many ATLAS physics analyses based on $\sqrt{s}$ = 8 TeV data. This included the search for the SM Higgs boson in the $H\rightarrow\tau\tau$ decay channel [36], as well as many of the searches for physics beyond the SM mentioned in the introduction to this chapter.

In order to perform these measurements, a so-called tag-and-probe method was developed that targeted $Z\rightarrow\tau\tau$ decays. This section is divided into three subsections. Section 4.3.1 describes the data and MC samples that were used in this study. The tag-and-probe method is described in section 4.3.2, with the tau trigger performance measurements derived from it presented in section 4.3.3.

4.3.1 Samples

Data sample

The LHC proton-proton collision data used in this study was recorded by the ATLAS detector using a single muon trigger that required an isolated EF-level muon candidate with p_T above 24 GeV. In order to mitigate efficiency loss at high p_T due to the isolation requirement, this trigger was used in conjunction with a 36 GeV single muon trigger with no isolation requirement. A more detailed description of these single muon triggers can be found in section 3.3.2. Overall quality criteria were applied to the data as described in section 3.1.2. The $\sqrt{s}$ = 8 TeV data sample corresponds to an integrated luminosity of 20.3 fb^{-1} with an average pile-up of 21.

MC samples

Events with Z/γ^* and W boson production were generated using Alpgen [113] for the hard scattering process. Alpgen was then interfaced with Herwig [114] or Pythia6 [101], respectively, for the modeling of the parton showering, hadronization, and the underlying event. Top-quark pair production as well as single top-quark events were generated with MC@NLO interfaced with Herwig [115] with the exception of t-channel single-top events, where AcerMC+Pythia6 [116] was used instead. WZ and ZZ diboson events were simulated with Herwig, and WW events with Alpgen+Herwig. In all samples with tau leptons, such as those for $Z/\gamma^*\rightarrow\tau\tau$, Tauola [117] was used

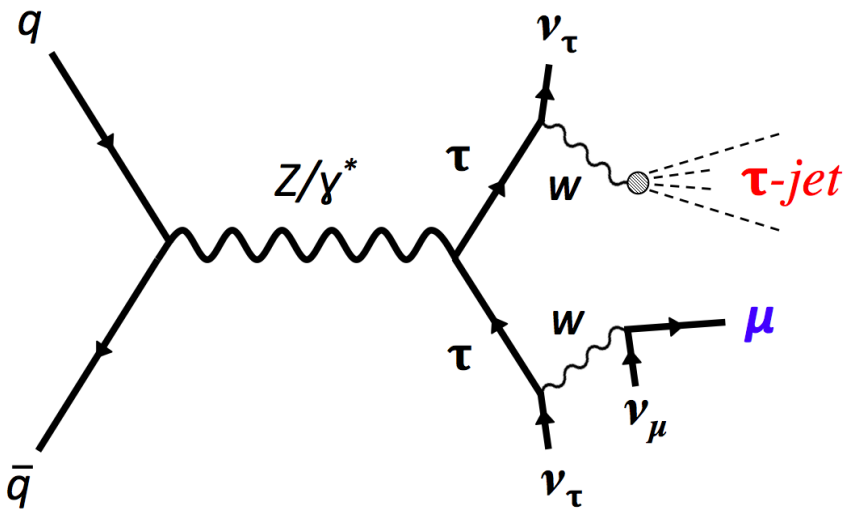

Figure 4.5 Tree-level Feynman diagram for the $Z\rightarrow \tau_\mu\tau_{\text{had}}$ process targeted by the tag-and-probe method. The tag object (the muon) is highlight in blue, while the probe object (the τ-jet) is highlight in red.

to model the tau decays. All samples were produced using the CTEQ6L1 [118] PDF set except for the MC@NLO samples, where the CT10 [119] set was used instead. Additional information on the MC samples can be found in ref. [1].

The MC samples were passed through each step of the ATLAS simulation chain described in section 3.3.3. They were then processed with the same ATLAS offline reconstruction software, derivation software and final analysis framework as the data sample. Following the recommendations of the ATLAS performance groups, additional corrections obtained from measurements in the data were applied to the MC samples. This accounted for differences between data and simulation in, for example, the reconstruction efficiencies of muons and τ-jets. Following the procedure described in section 3.3.3, the simulated events were reweighted so that the pile-up distribution matched the one observed in the data sample.

4.3.2 Tag-and-probe method using $Z\rightarrow \tau\tau$ events

The tag-and-probe method used data from a region enriched in $Z\rightarrow \tau\tau$ events, where one of the tau leptons undergoes τ_{lep} decay producing a muon, and the other decays in the τ_{had} mode producing a τ-jet. This process will be referred to as $Z\rightarrow \tau_\mu\tau_{\text{had}}$, and its tree-level Feynman diagram is shown in figure 4.5. The events entering the region enriched in this signal process will be collectively called the tag-and-probe sample.

Events entering the tag-and-probe sample were required to contain a PV, and to fire the single muon triggers described in section 4.3.1. The events were then required to contain exactly one offline muon and exactly one offline τ-jet candidate, with opposite-sign electric charges (OS). The muon acted as a clean and efficient tag for $Z\rightarrow \tau_\mu\tau_{\text{had}}$ events, while the recoiling τ-jet provided an unbiased probe of the tau trigger performance. These offline objects will be referred to, hereafter, as the tag-muon and probe-tau.

To ensure that the tag-muon in each event was on the trigger plateau, its offline p_T was required to be above 24 GeV. In addition, it was required to have $|\eta| < 2.5$ and pass the offline muon identification, impact parameter and isolation criteria listed in table 3.4 of section 3.3.1. The probe-tau was required to have offline p_T above 20 GeV, $|\eta| < 2.5$, and 1 or 3 associated tracks (1-prong or 3-prong). It was also required to pass at least the offline Loose τ-jet identification criteria and the lepton-veto selections described in section 3.3.1. That section also contains details on the offline reconstruction and selections for electrons, jets, b-tagged jets and E_T^{miss}, as well as the overlap removal procedure.

The dominant background in the tag-and-probe sample came from QCD multijet events. These events can enter the sample if one of the QCD jets is misidentified as a τ-jet and the other is misidentified as a muon[1]. The other main background source was from $W\rightarrow \mu\nu$ events, referred to as W+jets, where a QCD jet produced in such events was misidentified as a τ-jet. Additional selections were applied in order to reduce these backgrounds. These selections included[2]:

- The transverse mass of the tag-muon and E_T^{miss} system:

$$m_T = \sqrt{2p_T^{\mu} \cdot E_T^{\text{miss}}(1 - \cos\Delta\phi(\mu, E_T^{\text{miss}}))}, \tag{4.1}$$

  was required to be below 50 GeV. This quantity tends to be large for W+jets.

- The distance in the azimuthal plane between the tag-muon and E_T^{miss} and between the probe-tau and E_T^{miss}:

$$\sum \cos\Delta\phi = \cos\Delta\phi(\mu, E_T^{\text{miss}}) \; + \; \cos\Delta\phi(\tau\text{−jet}, E_T^{\text{miss}}), \tag{4.2}$$

  was required to be above -0.15. For the $Z\rightarrow \tau_\mu\tau_{\text{had}}$ process, this quantity tends to peak at zero, indicating that the neutrinos point mainly in the direction of one

[1] Note that real muons can also come from the semi-leptonic decays of B and D hadrons in QCD jets.
[2] The selections were optimized in order to maximize the purity of the tag-and-probe sample.

of the tag-muon or probe-tau. For W+jets events, the value is typically negative, indicating that the neutrino points away from the muon and misidentified τ-jet.

- The invariant mass calculated from the tag-muon and the probe-tau four-momenta:

$$m_{\mu,\tau-\text{jet}} = \sqrt{(E_\mu + E_{\tau-\text{jet}})^2 - (\mathbf{p}_\mu + \mathbf{p}_{\tau-\text{jet}})^2}, \tag{4.3}$$

was required to be between 40 GeV and 80 GeV. The invariant mass peaks within this window for the $Z\rightarrow \tau_\mu\tau_{\text{had}}$ process.

The development of the background estimation methods was not the work of this author, and the techniques that were used followed closely those from the ATLAS SM Higgs boson search in the $H\rightarrow \tau_{\text{lep}}\tau_{\text{had}}$ decay channel at $\sqrt{s}$ = 8 TeV. These methods are briefly summarized below, with a more complete description available in ref. [120].

The background estimation method relied on the assumption that, in the tag-and-probe region, the shape of the QCD multijet background was the same irrespective of whether the tag-muon and probe-tau were required to have OS or same-sign (SS) electric charge. The shape and normalization of this background was derived from a control region (CR) that followed the selections of the tag-and-probe region, but instead had an SS charge requirement. The estimation from this CR was rescaled by correction factors, derived from a QCD-multijet enriched region in data, that accounted for potential differences in the misidentification rates of muons and τ-jets introduced by the OS or SS requirements. The SS CR, while dominated by QCD multijet events, also contained contributions from other backgrounds. These backgrounds did not necessarily have an OS-SS symmetry, and so add-on terms, estimated from simulation, were applied in order to cover any excess of OS components over SS components. These OS-SS add-on terms were obtained for the W+jets background, as well as other minor backgrounds including $Z/\gamma^*\rightarrow \mu\mu$, top-quark and diboson processes.

The W+jets background was normalized to data using a CR where both the $\sum \cos\Delta\phi$ and $m_{\mu,\tau-\text{jet}}$ selections were dropped, and also requiring m_T to be above 70 GeV. The minor contribution from top-quark processes was normalized with a CR that required at least one b-tagged jet. The shape of the two previously mentioned backgrounds were taken from simulation, and both the shape and normalization were taken from simulation for the minor $Z/\gamma^*\rightarrow \mu\mu$ and diboson backgrounds.

In total, just over 60,000 events were collected in the tag-and-probe region after all selections. The purity in this tag-and-probe sample was about 81% when offline

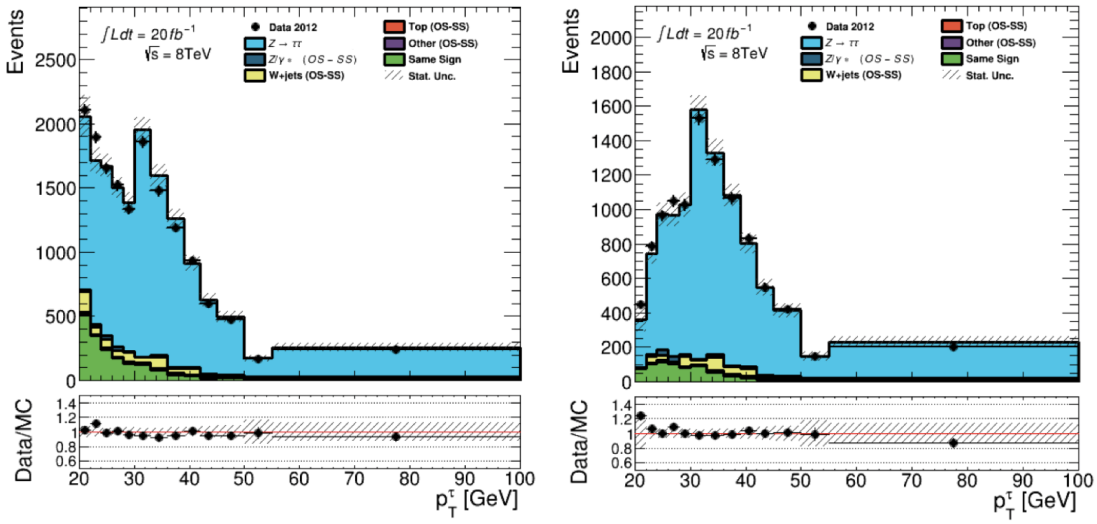

Figure 4.6 Distributions of the offline p_T of the probe-tau passing Medium offline identification in the tag-and-probe region. They are shown (a) before and (b) after a tau trigger requirement (details provided in the text). In this example, 1-prong τ-jet candidates in the barrel region of the detector are considered. The signal process ($Z \to \tau_\mu \tau_{\text{had}}$) is shown in blue, with the main QCD multijet and W+jets backgrounds shown in green and yellow. The bin widths were chosen to ensure each bin was sufficiently populated when performing the tau trigger efficiency measurement. The data (points) are compared to the total background and signal expectation (stacked filled histograms), with their ratio displayed in the lower panel. Statistical uncertainties are shown.

Medium τ-jet identification criteria was applied to the probe-tau. The probe-tau in each event was then required to fire different single tau triggers from the $\sqrt{s}$ = 8 TeV trigger menu. This was achieved by requiring the probe-tau to match, within $\Delta R < 0.2$, a corresponding τ-jet candidate at trigger level. The particular tau trigger that will be used as reference in this and the next section had a 4 GeV isolation and 11 GeV E_T threshold at L1, a 20 GeV requirement on p_T and passed Medium identification at EF. After requiring the probe-tau in each event to match an EF candidate for this trigger, the purity of the tag-and-probe sample increased to about 88%.

Distributions of the offline p_T of the probe-tau in the tag-and-probe sample, both before and after the tau trigger requirement, are shown in figures 4.6a and 4.6b. As seen in these figures, the main QCD multijet and W+jets backgrounds accumulated in the region with p_T below 40 GeV.

4.3.3 Results

The tag-and-probe method described in the previous section was used to perform many tau trigger performance measurements at $\sqrt{s} = 8$ TeV. This included measurements of the τ-jet identification efficiency in data at each trigger-level, the scale factors used to correct the simulated EF-level efficiencies in MC samples, and the resolution of the E_T estimate at each trigger-level. All of these measurements were performed using offline τ-jet reconstruction and identification as a reference. In this section, some of the main results from this body-of-work are presented.

The tau trigger efficiencies were extracted directly from the number of reconstructed τ-jet candidates before and after the tau trigger was applied (as shown in figure 4.6). The efficiency measured in data (ϵ_{data}) and simulation (ϵ_{MC}) were computed as follows:

$$\epsilon_{\text{data}} = \frac{N^{\text{data}}_{\text{ID+trig}} - N^{\text{bkg}}_{\text{ID+trig}}}{N^{\text{data}}_{\text{ID}} - N^{\text{bkg}}_{\text{ID}}}, \qquad \epsilon_{\text{MC}} = \frac{N^{\text{signal}}_{\text{ID+trig}}}{N^{\text{signal}}_{\text{ID}}} \tag{4.4}$$

In these equations N_{ID} and $N_{\text{ID+trig}}$ refer to the number of τ-jet candidates in the tag-and-probe sample passing offline identification and, in addition, the trigger requirements, respectively. The superscripts specify whether it is the number of observed ("data"), estimated total background ("bkg") or predicted $Z \rightarrow \tau_\mu \tau_{\text{had}}$ ("signal") events that are considered.

Figure 4.7a shows the measured ϵ_{data} as a function of the offline p_T with respect to τ-jet candidates passing offline Medium tau identification. The particular tau trigger considered is the same one described in the previous section. The efficiency is shown to depend minimally on p_T when on the trigger plateau (above approximately 35 GeV). The EF-level efficiency on the plateau is above 80%, meeting the performance goals of the EF trigger mentioned in section 4.2.3.

The ϵ_{data} measured as a function of the number of primary vertices in an event, which is proportional to the amount of pile-up, is shown in figure 4.7b. The trigger efficiency is shown to have minimal dependence on the pile-up conditions, demonstrating the pile-up robustness of the tau trigger system implemented during $\sqrt{s} = 8$ TeV data taking.

The measured ϵ_{data} was compared to that in simulation (ϵ_{MC}) at the EF trigger-level, for the same tau trigger, as shown in figure 4.8. The trigger efficiency is shown to be modeled reasonably well in simulation. Nevertheless, when conducting physics

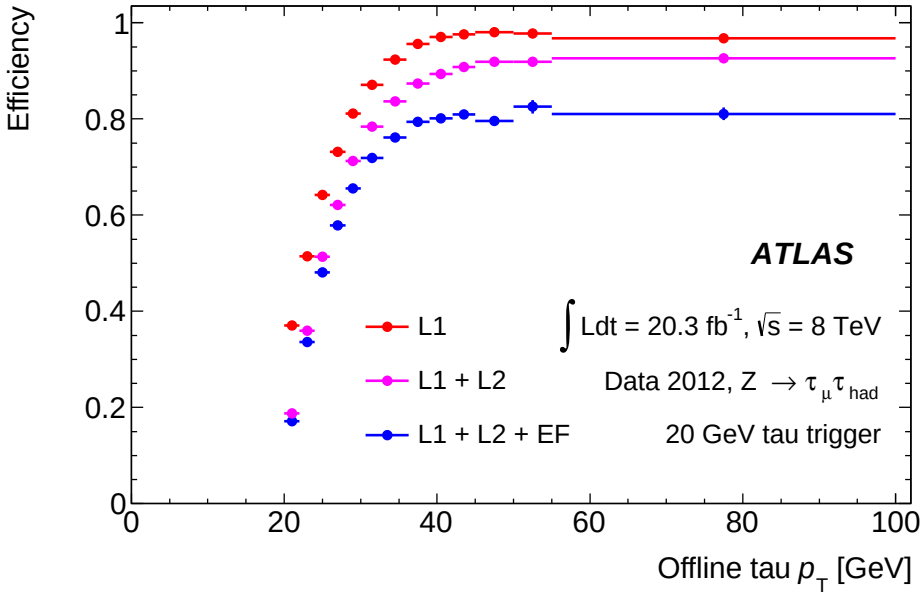

(a)

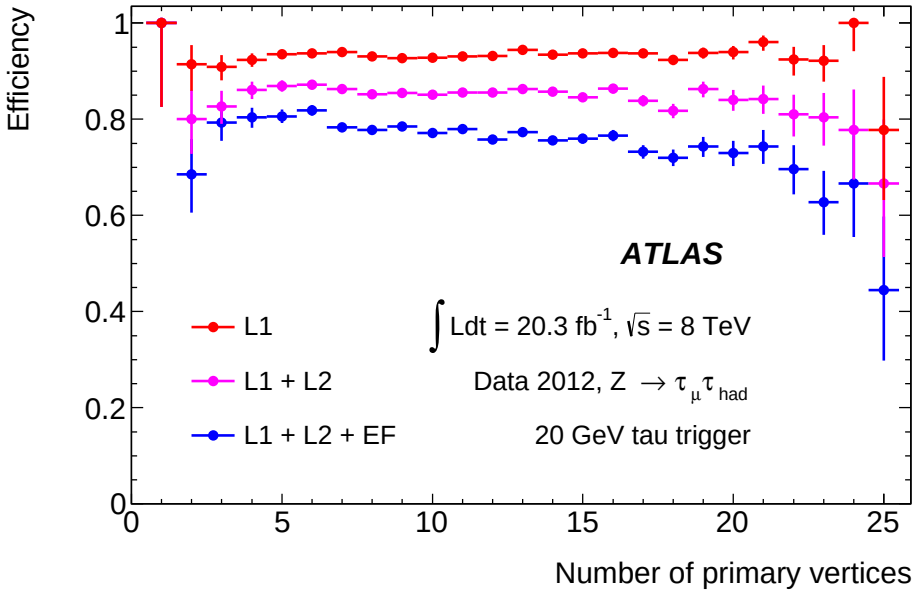

(b)

Figure 4.7 The tau trigger efficiency measured in data using the tag-and-probe method, for τ-jet candidates passing offline Medium tau identification. It is shown (a) as a function of the offline τ-jet p_T and (b) the number of primary vertices (proportional to pile-up). The 1-prong and 3-prong τ-jets and the barrel+endcal regions are combined. The efficiency measured at L1, L2 and EF trigger-level is shown in red, magenta and blue, respectively. The error bars correspond to the statistical uncertainty on the efficiency.

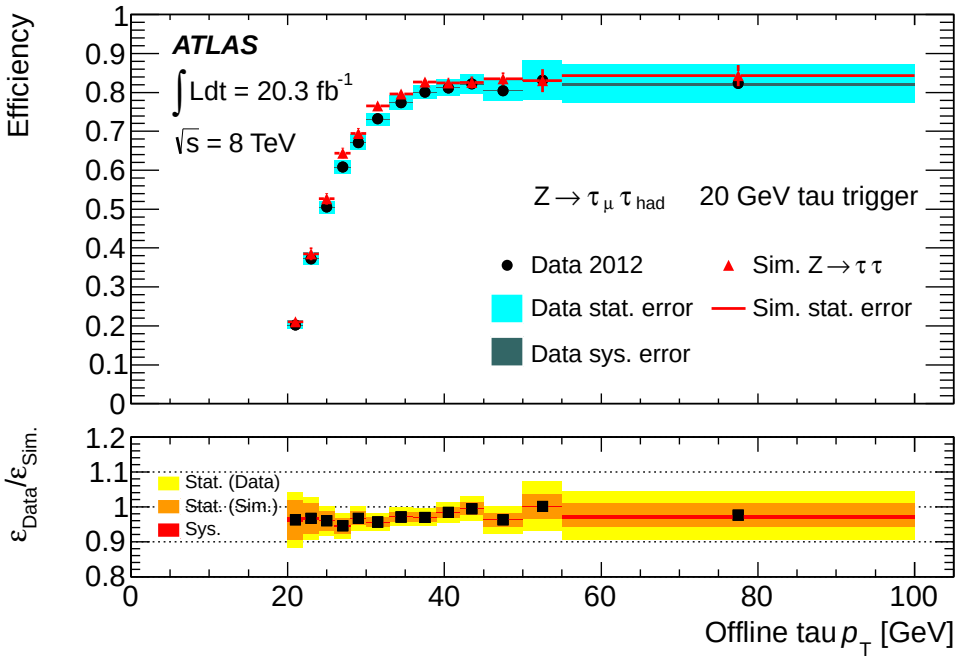

Figure 4.8 The measured tau trigger efficiency in data and simulation, for the offline τ-jet candidates passing Medium tau identification, as a function of offline τ-jet p_T. The 1-prong and 3-prong τ-jets and the barrel+endcal regions are combined. The lower panel shows the ratio of the two efficiencies (the efficiency correction factors). The uncertainty band on the ratio reflects the statistical uncertainties associated with the data (yellow) and MC samples (orange), and the systematic uncertainty associated with the background subtraction procedure when computing the efficiency in data (red).

analyses involved τ-jets with ATLAS, such as in the search for $H \to \tau\tau$, it is essential to correct in the MC samples any small differences in the trigger efficiency between data and simulation. To this end, correction factors, defined as the ratio of the tau trigger efficiency in data to simulation ($\epsilon_{data}/\epsilon_{MC}$), were derived.

The efficiency corrections factors were measured using the tag-and-probe method for a wide range of single tau triggers that were operational during $\sqrt{s} = 8$ TeV data taking, separately for 1-prong and 3-prong taus and for various offline criteria. For example, the correction factors for the previously mentioned tau trigger can be seen in the lower panel of figure 4.8. They are in general compatible with unity, with small differences of a few percent observed in the p_T region 26-38 GeV. This reinforces the importance of correcting the simulated trigger efficiencies in MC samples to match those measured directly from data.

The uncertainties on the correction factors range from 2% to 8% depending on the offline p_T of the probe-tau . The uncertainty at high p_T tend to be larger as the number of $Z \rightarrow \tau_\mu \tau_{\text{had}}$ events in the tag-and-probe sample becomes smaller. They are also sizeable in region with p_T below 30 GeV, where the background contamination in the tag-and-probe sample is the largest. The total uncertainties are dominated by the statistical component from the data and MC samples, but also include a small systematic component coming from the background subtraction procedure when computing ϵ_{data}. The main source of this systematic uncertainty originates from the background estimation method, but also includes minor contributions from variations associated to the offline reconstruction of the tag-muon and E_T^{miss}.

Recall from section 4.2 that the E_T of τ-jet candidates at L1 and L2 was estimated using dedicated algorithms that differed substantially from the offline energy reconstruction and calibration. Also recall that at the EF-level a very similar algorithm to offline was used. The tag-and probe method was utilized to measure how closely the τ-jet energy reconstruction and calibration at trigger-level matched that of offline.

The E_T resolution that was measured at each trigger-level with respect to τ-jet candidates passing offline Medium tau identification is shown in figure 4.9. The resolution is defined as:

$$E_T \text{ resolution at L1/L2/EF} = \frac{E_T^{\text{L1/L2/EF}} - p_T^{\text{offline}}}{p_T^{\text{offline}}} \tag{4.5}$$

As seen in figure 4.9a, the estimated energy at L1 was significantly underestimated with respect to offline. This was due to the fact that all cells in the trigger towers of the ROIs were combined without the use of sophisticated clustering algorithms and without a τ-jet specific energy calibration (EM scale was used). Also, the coarse energy and geometrical position granularity at L1 limited the precision of the energy estimation. These effects resulted in a significant efficiency loss at L1 for low-E_T τ-jet candidates, as was observed in figure 4.7a. The overestimation at L2 seen in figure 4.9b was due to the fact that the the clustering algorithm used at this trigger-level did not have the same noise suppression scheme as offline.

The energy estimation at EF was almost identical to offline, as seen in figure 4.9c. The slight difference between EF and offline was mainly due to the pile-up corrections, which were only applied during offline reconstruction. Some discrepancies can be seen between the resolutions measured in data and in MC simulation. This, once again, reinforces the importance of correcting the simulated trigger efficiencies used in ATLAS physics analyses to match those measured directly from data.

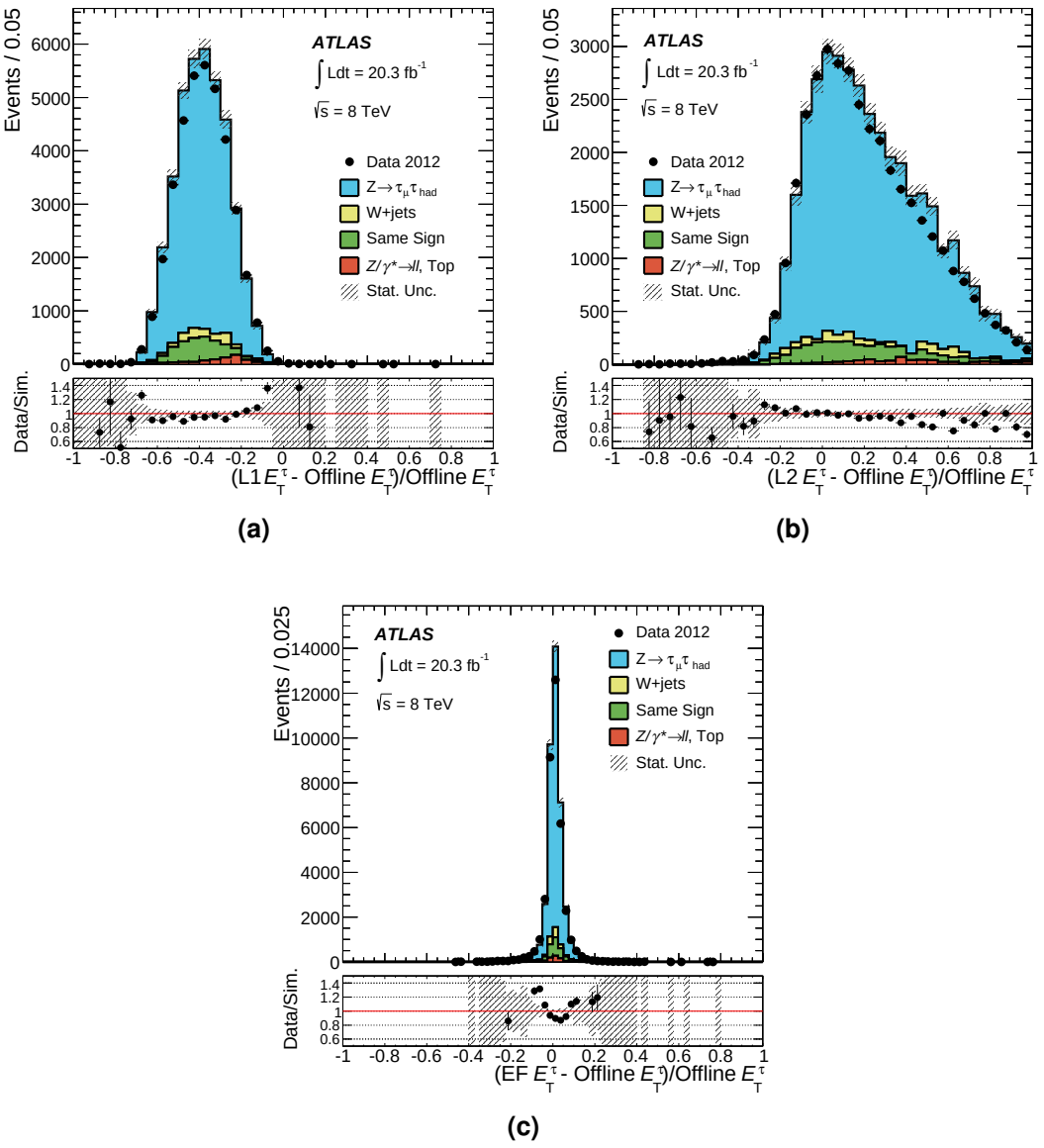

Figure 4.9 The measured tau trigger transverse energy resolution at (a) L1, (b) L2 and (c) the EF, with respect to offline τ-jet candidates passing Medium tau identification. The data (points) are compared to the total background and signal expectation (stacked filled histograms), with their ratio displayed in the lower panel. Statistical uncertainties are shown.

4.4 The ATLAS Fast Tracker Upgrade

The ATLAS trigger system was originally designed to operate at a maximum luminosity of 1×10^{34} cm^{-2}s^{-1}. During the 2012 data taking period at $\sqrt{s} = 8$ TeV the peak luminosity was 7.7×10^{33} cm^{-2}s^{-1}, and on the 29$^{\text{th}}$ of June 2016 the design luminosity was exceeded for the first time [121]. Since then, the luminosity has rapidly increased and in the coming years it is expected to reach up to two times and eventually, after the HL-LHC upgrade [41], up to five times the design luminosity [40]. As a result, the collision environment will become even more complicated resulting in substantially higher event rates and pile-up. This presents a major challenge that must be overcome in future iterations of the ATLAS trigger system. If the system is not upgraded then the trigger will not meet its performance goals and, as a result, the ATLAS Collaboration will not fulfill its ambitions physics objectives at $\sqrt{s} = 13$ and 14 TeV.

Because of its fine resolution and granularity, tracking information is critical for distinguishing which events triggered at L1 should be kept for further processing by the HLT. However, extensive software-based tracking in high pile-up environments is prohibitively expensive in terms of processing time per event. Therefore, as we saw for the ATLAS tau trigger in section 4.2, it is currently only used sparingly in the HLT within ROIs that have already been identified as potentially interesting by the L1 trigger.

The FTK upgrade [2] is a system of electronics being built for the ATLAS detector that will move track reconstruction into a hardware system with massively parallel processing. This will rapidly provide global track reconstruction, no longer limited to within the ROIs, with good resolution directly after the L1 trigger. FTK tracking, freed from the computational constraints of traditional HLT tracking, will provide an important tool box for improving the performance of the future HLT trigger. Details on how tracks are reconstructed using the FTK will provided in the following section.

4.4.1 Track reconstruction with FTK

The FTK receives the hit data from the pixel and SCT layers of the ID at the full L1 accept rate. After processing, the FTK provides access to tracking information over the full pseudorapidity range of the detector from the start of the HLT. The conversion of the hits into track helix parameters occurs in three stages: clustering, pattern recognition and track fitting. An overview of each stage will be provided, in turn, below. A more complete description can be found in ref. [2].

Clustering

The hits from the pixel and SCT layers are first grouped into those belonging to the same cluster, where a cluster is defined as a collection of contiguous hits. Clustering the hits from the SCT is relatively simple due to its one-dimensional nature. Pixel clustering is more complicated since it is two-dimensional. For each pixel hit received, neighboring hits connected either side-by-side or diagonally are considered with a maximum distance of 4 pixels along the ϕ direction and 5 pixels in the z or r direction for the barrel and endcap, respectively. After loading the neighboring hits in the grid, those contiguous with the first hit received and therefore part of the same cluster are identified. Hits within a small distance of the first hit received but not part of the same cluster will be processed again until the cluster they belong to is identified. This process is repeated until all hits are allocated to a cluster. For each cluster, the position of the centre is computed assuming equal weight for all hits. The cluster centroids themselves will be referred to, hereafter, as the "hits".

Pattern recognition

The feature that most defines the FTK is the unique way it utilizes Associative Memory (AM) to rapidly perform pattern recognition in order to find track candidates. The AM boards contain approximately one billion in total preloaded track patterns, referred to as roads, that correspond to the possible combinations of hits in 8 silicon layers. Currently 3 pixel layers (the IBL and the 2 outer pixel layers) and 5 SCT layers (the 4 axial layers and 1 stereo layer) are used for pattern recognition. The roads that enter the pattern banks of the AM boards are determined in advance from the full ATLAS simulation of single tracks.

The AM is a massively parallel system in that all roads in the pattern banks see each silicon hit nearly simultaneously. As a result, pattern recognition in FTK is complete shortly after the final hit has been transmitted into the AM board. If there are at least 7 pixel and SCT layers containing hits within a road, the road is flagged as containing track candidates and its associated hits are sent to the track fitter.

Track fitting

Track fitting is done rapidly by replacing the helical fit used in offline and HLT tracking algorithms with a simple calculation that is linear in the position of the hit in each

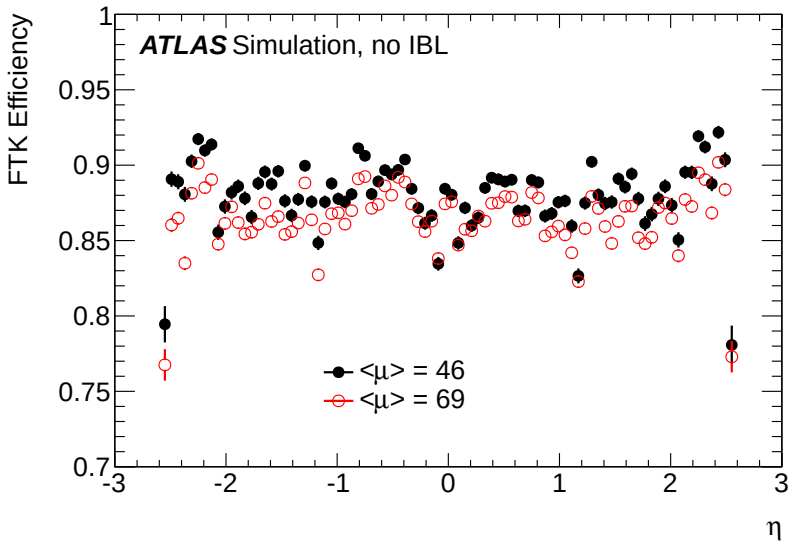

Figure 4.10 Efficiency of FTK tracking with respect to offline tracking as a function of η, measured using MC samples with an average pile-up of 46 (black) and 69 (red) [2]. The bin-by-bin fluctuations come from the number of silicon modules crossed by a track, which varies slightly with η.

layer [122]. The calculation is a set of scalar products of the hit coordinates and precalculated constants that take into account the detector geometry and alignment. This linear calculation is extremely fast since it consists of a series of integer multiply-and-accumulate steps, with of order 10^9 track candidates that can be fit per second. The helix parameter resolution obtained using the linear method is nearly as good as that obtained with a helical fit if the region covered by the set of constants is small. For the FTK that region consists of a single silicon module in each layer, typically a few centimeters wide, and so the linear calculation provides track helix parameters with good resolution.

Track fitting operates in two stages. In the first stage, the same 8 silicon layers used in the pattern recognition step are used and only tracks passing a relative loose quality selection (χ^2/ndof < 6, where "ndof" is the number of degrees of freedom) are considered. If there are two tracks in the same road passing the χ^2 requirement and they have fewer than 6 unique hits, they are considered to be duplicate tracks and the best track is retained based on the χ^2 and the numbers of layers that have a hit. Tracks from the first stage pass to a second stage where they are extrapolated into the 4 layers that were not used in the first stage. Nearby hits in those layers are found and the tracks are refit using the hits in all 12 layers. After a tighter track quality selection (χ^2/ndof < 4)

is applied, duplicate tracks are removed using the same unique hit requirement as in the first stage.

The efficiency of FTK track reconstruction with respect to offline track reconstruction, after the final track fitting step, has been checked in simulation and is shown in figure 4.10. The efficiency is high, on average approximately 88%, and generally flat in η.

4.5 Development of a Tau Trigger that uses FTK tracking

As was mentioned in section 2.4.4, one of the high priority physics goals for the ATLAS Higgs program at $\sqrt{s}$ = 13 and 14 TeV will be to claim discovery in the $H\rightarrow\tau\tau$ channel alone, and more precisely measure the Higgs coupling to tau leptons. It should also be possible to perform the first measurements of the spin and parity in this decay channel. In order to achieve these goals, a tau trigger system that remains highly efficient under challenging pile-up conditions will be essential.

An overview of the L2 tau trigger implemented during $\sqrt{s}$ = 8 TeV data taking was provided in section 4.2.2. Recall that a software-based tracking algorithm, referred to as TauB, was available to the trigger at this level. TauB tracking, although faster then HLT and offline tracking, is computationally intensive and requires a relatively large processing time per event. Therefore, in order to meet the tight latency constraints at L2, selections on calorimeter-based variables were first applied in order to reduce the number of L1 ROIs that require track reconstruction. A combination of tracking and calorimeter variables were then used for the full L2 τ-jet identification.

Calorimeter-based selections, although necessary, increased tau trigger thresholds and reduced overall trigger efficiencies at $\sqrt{s}$ = 8 TeV. Moreover, as seen in figure 4.9b, these kinds of variables tend to have poor resolution at L2 and so applying selections to them at this stage of the trigger was not ideal. As the LHC rapidly exceeds its design luminosity in future $\sqrt{s}$ =13 and 14 TeV runs, identifying τ-jets candidates at trigger-level will become significantly more challenging. If the same strategy that was used at $\sqrt{s}$ = 8 TeV is still adopted, the increased L1 ROI rates entering L2 will force even more stringent calorimeter-based selections that will further degrade the performance of the tau HLT.

Considering this, it is expected that FTK tracking, freed from the computational constraints of software-based HLT tracking, will become a key component of the future tau

trigger. The FTK will provide access to high resolution tracking with high efficiency at the very start of L2, so that rapid track-based algorithms can be implemented to massively reduces the L1 ROI rate. This would allow the L2 calorimeter-based selections to be, at the very least, relaxed and, if the reduction in rate is sufficiently high, even avoided altogether. The overall effect would be to improve the tau trigger efficiency, and so increase the sensitivity of the ATLAS experiment to $H\rightarrow\tau\tau$ signatures.

This section presents studies that were performed to explore the potential of the FTK to improve tau trigger performance at $\sqrt{s}$ = 14 TeV in high pile-up conditions. This section is divided into five subsections. Section 4.5.1 describes the MC samples that were used in this study. The tracking performance of the FTK for tracks associated to offline τ-jet candidates is presented in section 4.5.2. The FTK-based L2 τ-jet identification algorithm that was developed is described in section 4.5.3, and its performance is presented in section 4.5.4. Finally, the expected improvements to analyses targeting the $H\rightarrow\tau\tau$ decay channel is presented in section 4.5.5.

4.5.1 MC samples

The studies presented in this section were performed on MC samples generated with Pythia8 [102] at $\sqrt{s}$ = 14 TeV, and with two average pile-up configurations ($\mu_{\text{pile-up}}$ = 46 or 69). An emulation of the FTK track reconstruction, described in section 4.4.1, was included in the simulation. The IBL pixel layer was not included in the FTK emulation since, at the time of these studies, it was not yet available in the MC simulation chain.

The signal process considered was the SM Higgs boson of mass 125 GeV produced in the VBF mode with $H\rightarrow\tau\tau$ decay. One of the tau leptons was required to decay in the τ_{lep} mode, and the other in the τ_{had} mode producing a τ-jet. For background studies, the SM Higgs boson produced in the WH production mode with subsequent $WH\rightarrow\ell\nu q\bar{q}$ decay was used. This particular background process was chosen to ensure the presence of jets in the event that have a similar transverse momentum spectrum as the signal events.

4.5.2 FTK track reconstruction efficiency for τ-jets

Before developing a FTK-based tau trigger algorithm, it was important to check the FTK track reconstruction efficiency for tracks associated to offline τ-jets, and compare

this to the efficiency from traditional TauB tracking. FTK, TauB and offline tracks in the signal MC sample were considered for this check, and only if they lied within $\Delta R < 0.2$ of an offline τ-jet candidate. The offline τ-jet candidates were required to have p_T above 20 GeV, $|\eta| < 2.5$ and pass Medium offline tau identification. These selections helped suppress QCD jets misidentified as offline τ-jet candidates, particularly in the high pile-up conditions of the MC samples.

The tracks were required to have p_T above 2 GeV, and the magnitude of their d_0 and z_0 impact parameters below 2 mm and 100 mm, respectively. In addition, all tracks associated to a particular offline τ-jet candidate were required to satisfy the Δz_0 criteria described in section 4.2.2. These selections significantly reduced the number of tracks originating from pile-up, and also allowed for a more fair comparison between FTK and TauB tracks.

The measured track reconstruction efficiency for the FTK and TauB algorithms with respect to offline tracking is shown in figure 4.11. The efficiencies were measured separately for the barrel and end-cap regions of the detector, and for the 46 and 69 average pile-up configurations. FTK tracking tends to be more efficient then TauB at low track p_T, while it is less efficient at high p_T. This is due to the geometric coverage of the AM board pattern banks at the time of this study. It is expected that the efficiency loss at high track p_T will be mitigated in future iterations of the pattern banks, and with the addition of the IBL logical layer in the MC simulation.

The number of tracks around the offline τ-jet candidates was also checked. The track multiplicity distributions for FTK, TauB and offline tracks for both the signal and background samples are shown in figure 4.12. As expected for the real τ-jets in the signal sample, two peaks for 1-prong and 3-prong decays are observed in the signal cone ($\Delta R < 0.1$). In the end-caps, this feature is less prominent due to lower tracking efficiency in this region. The misidentified QCD jets in the background sample tend to have larger track multiplicities in the isolation cone ($0.1 < \Delta R < 0.3$).

4.5.3 Proposal of a L2 algorithm that uses FTK tracks

This section presents the L2 τ-jet identification algorithm using FTK tracking that was developed in this study. This section also includes a description of a typical L2 algorithm from the $\sqrt{s} = 8$ TeV trigger menu. This algorithm was used as a reference when estimating the performance improvement coming from the proposed FTK track-based algorithm.

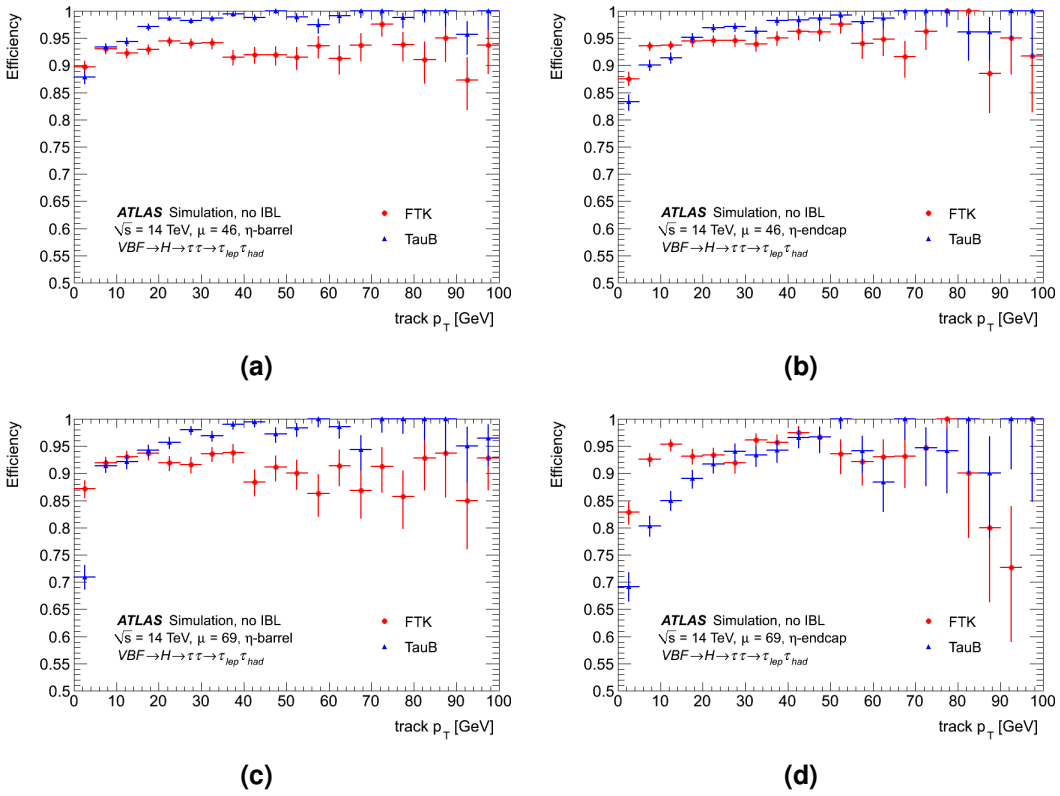

Figure 4.11 Efficiency of FTK and TauB track reconstruction as a function of track p_T, measured with respect to offline tracking. Events in the (left) barrel region, (right) end-cap region, (top) $\mu_{\text{pile-up}} = 46$ sample and (bottom) $\mu_{\text{pile-up}} = 69$ sample are shown separately.

Proposed FTK L2 algorithm

To fully exploit the potential of the FTK, the L2 algorithm that was developed had purely track-based selections. Selections on calorimeter-based variables at L2 such as E_T and f_{core}, defined in section 4.2.2, were avoided. This was done in order to recover the efficiency lost due to the coarse calorimeter requirements that are typically applied at L2, as explained in the introduction of section 4.5.

The proposed FTK-based algorithm rapidly reduces the large background rate entering L2, originating for misidentified QCD jets, by applying selections on the track multiplicity. The highest p_T FTK track within $\Delta R < 0.2$ of the L1 cluster direction was found, and from this track the algorithm builds the signal and isolation cones in the standard way described in section 4.5.2.

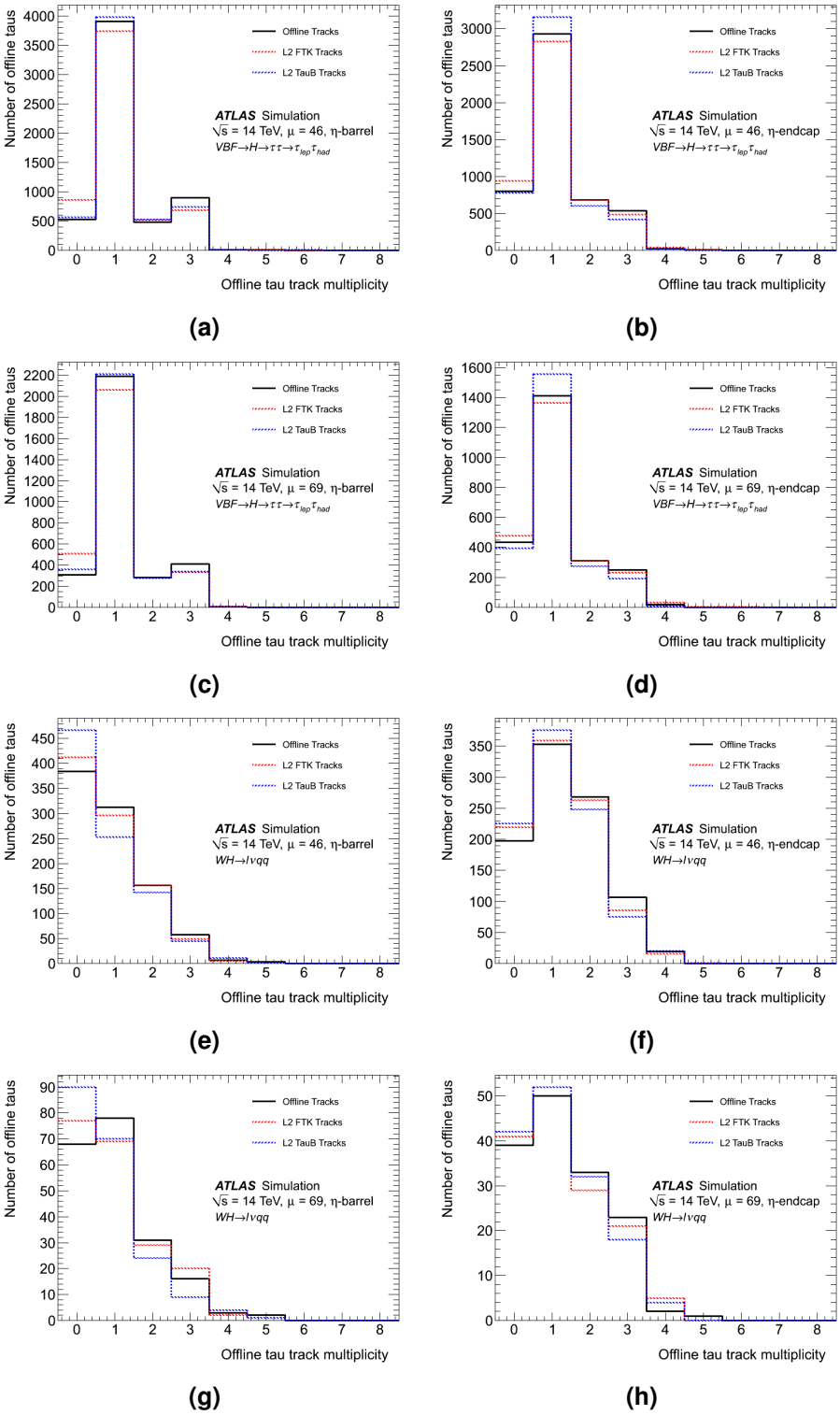

Figure 4.12 Number of FTK, TauB and offline tracks associated to the offline τ-jet candidates for (a)-(d) the signal sample in the signal cone ($\Delta R < 0.1$) and (e)-(h) the background sample in the isolation cone ($0.1 < \Delta R < 0.3$). The distributions are shown separately for the barrel region, end-cap region, $\mu_{\text{pile-up}} = 46$ sample and $\mu_{\text{pile-up}} = 69$ sample.

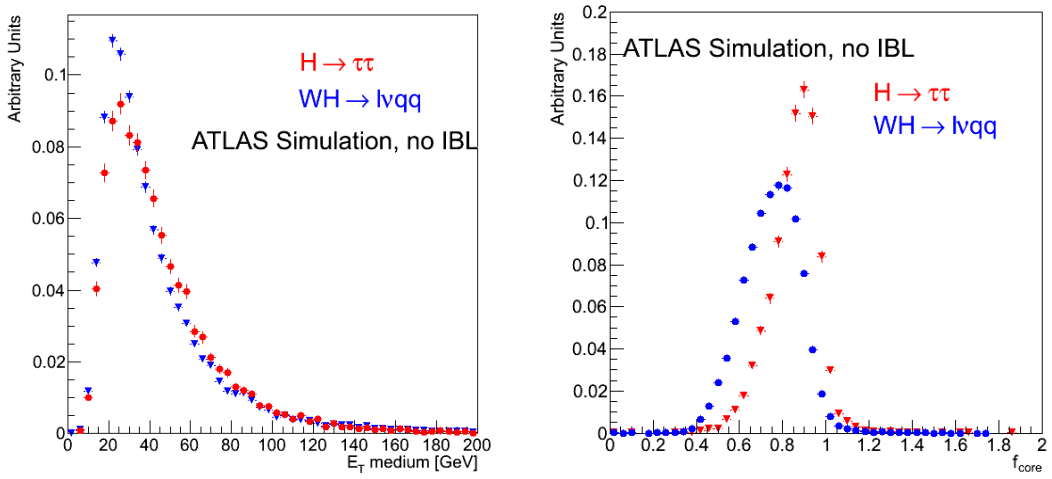

(a) **(b)**

Figure 4.13 L2 calorimeter variables (a) E_T and (b) f_{core}, for the $H\rightarrow \tau\tau$ signal (red) and $WH\rightarrow \ell\nu q\bar{q}$ background (blue) samples.

The following selections are then applied:

- the number of FTK tracks in the signal cone is less than or equal to 3
- the number of FTK tracks in the isolation cone is less than or equal to 1

The first requirement selects real τ-jet candidates as seen in figures 4.12a-4.12d, while the second requirement rejects misidentified QCD jets as seen in figures 4.12e-4.12h.

Reference L2 algorithm

Recall that traditional L2 algorithms typically apply selections on the calorimeter-based variables E_T and f_{core} prior to TauB tracking. These two variables are shown for both the signal and background samples in figure 4.13. The L2 algorithm used as a reference in this study required E_T above 15 GeV and f_{core} above 0.75, retaining 79% of the signal that passed L1 while rejecting 48% of the background. These selections ensured that the software-based TauB track reconstruction fit within the tight latency constraints of L2.

The TauB tracking algorithms were then run within the remaining ROIs. Both tracking and calorimeter information was then used to perform the final τ-jet identification at L2, as described in section 4.2.2.

4.5.4 Per-tau performance improvement from FTK

In order to compare the proposed FTK-based algorithm to the reference algorithm, the τ-jet identification efficiency at L2 was first measured for the $H\rightarrow\tau\tau$ signal sample. These trigger efficiencies were computed for each τ-jet candidate in the event sample (per-tau). The per-tau signal efficiencies were measured both with respect to truth-level and offline, and separately for 1-prong and 3-prong decays.

The per-tau L2 signal efficiency with respect to truth-level was defined as:

$$\text{L2 signal efficiency wrt truth} = \frac{N_{\text{truth}}^{\text{L1+L2}}}{N_{\text{truth}}^{\text{L1}}} \tag{4.6}$$

Where $N_{\text{truth}}^{\text{L1}}$ is the number of true τ-jets matched to L1, and $N_{\text{truth}}^{\text{L1+L2}}$ are those also passing either the FTK-based or reference L2 algorithm. The specific L1 tau trigger considered had a L1 E_T threshold of 8 GeV.

Figures 4.14 and 4.15 show the measured L2 signal efficiency with respect to truth-level for the 46 and 69 pile-up configurations, respectively. A substantial improvement in efficiency ranging from approximately 10-40% with respect to the reference L2 algorithm is observed, with the largest gains occurs in the low p_T region and for the harsher pile-up conditions. These plots also include, as an additional working point, the reference L2 algorithm where the FTK tracks are used rather then the usual TauB tracks. The reference L2 algorithm performs similarly for both kinds of tracks, with the small differences coming from the differing tracking performance for τ-jets as was shown in figure 4.11.

The per-tau L2 signal efficiency with respect to offline was defined as:

$$\text{L2 signal efficiency wrt offline} = \frac{N_{\text{offline}}^{\text{L2}}}{N_{\text{offline}}} \tag{4.7}$$

Where N_{offline} is the number of offline τ-jet candidates passing Medium offline tau identification, and $N_{\text{offline}}^{\text{L2}}$ are those also matched to a τ-jet candidate identified by either the FTK-based or reference L2 algorithm.

Figure 4.16 shows the measured L2 signal efficiency with respect to offline for the 46 pile-up configuration. Here the efficiency improvement is still significant but more modest, ranging from around 5-15%. The lower efficiency with respect to offline is due to the fact that the existing offline tau reconstruction and identification was designed to perform well for events that were selected using calorimeter variables. Therefore, in

order to more fully exploit the possible gain in efficiency provided by FTK, the offline selection will need to be re-optimized in the future.

It was also important to check that the proposed FTK-based L2 algorithm provides sufficient rejection against QCD jets misidentified as τ-jets. The misidentification probability was measured using the $WH \rightarrow \ell\nu q\bar{q}$ background sample, and defined as:

$$\text{L2 misidentification probability} = \frac{N_{\text{jets}}^{\text{L2}}}{N_{\text{jets}}^{\text{L1}}} \tag{4.8}$$

Where $N_{\text{jets}}^{\text{L1}}$ is the total number of reconstructed jets that pass L1, and $N_{\text{jets}}^{\text{L2}}$ is the number passing either the FTK-based or reference L2 algorithm.

The misidentification probability is shown in figures 4.17 and 4.18 for the 46 and 69 pile-up configurations, respectively. These plots show that the proposed FTK-based algorithm can provide a rejection factor for the QCD jet background of order 10, with respect to L1. This level of rejection is sufficient to allow the EF algorithms to run on all of the ROIs that pass the FTK track selections. In this way, the more refined variables computed at EF-level can be used to further bring down the background rate.

4.5.5 Benefits to future $H \rightarrow \tau\tau$ analyses at $\sqrt{s}$ = 14 TeV

As mentioned previously, the $H \rightarrow \tau\tau$ decay channel will play a key role in fulfilling the physics goals of the ATLAS Higgs program in future high pile-up runs at $\sqrt{s}$ = 13 and 14 TeV. In the pervious section it was shown that a significant improvement in the per-tau L2 trigger efficiency can be achieved with the proposed FTK track-based algorithm. Subsequent studies have been performed to check how this per-tau trigger efficiency gain translates into an increase to the per-event signal acceptance for $H \rightarrow \tau\tau$ analyses. These particular checks were not the work of this author, and are briefly summarized below. A more complete description can be found in ref. [123].

For these checks, there were some changes to the MC samples described in section 4.5.1. The FTK emulation included the previously missing IBL layer, and the pile-up configuration was $\mu_{\text{pile-up}} = 60$. The $H \rightarrow \tau\tau$ signal sample contained boosted Higgs boson events, defined by requiring the Higgs p_T above 60 GeV, produced in the ggF production mode with subsequent $\tau_{\text{had}}\tau_{\text{had}}$ decay. A background sample of QCD multijet events was used, to be more representative of the backgrounds that enter the $H \rightarrow \tau_{\text{had}}\tau_{\text{had}}$ analysis. The offline selections used in this check followed closely those of the boosted category of the $\sqrt{s}$ = 8 TeV analysis [36].

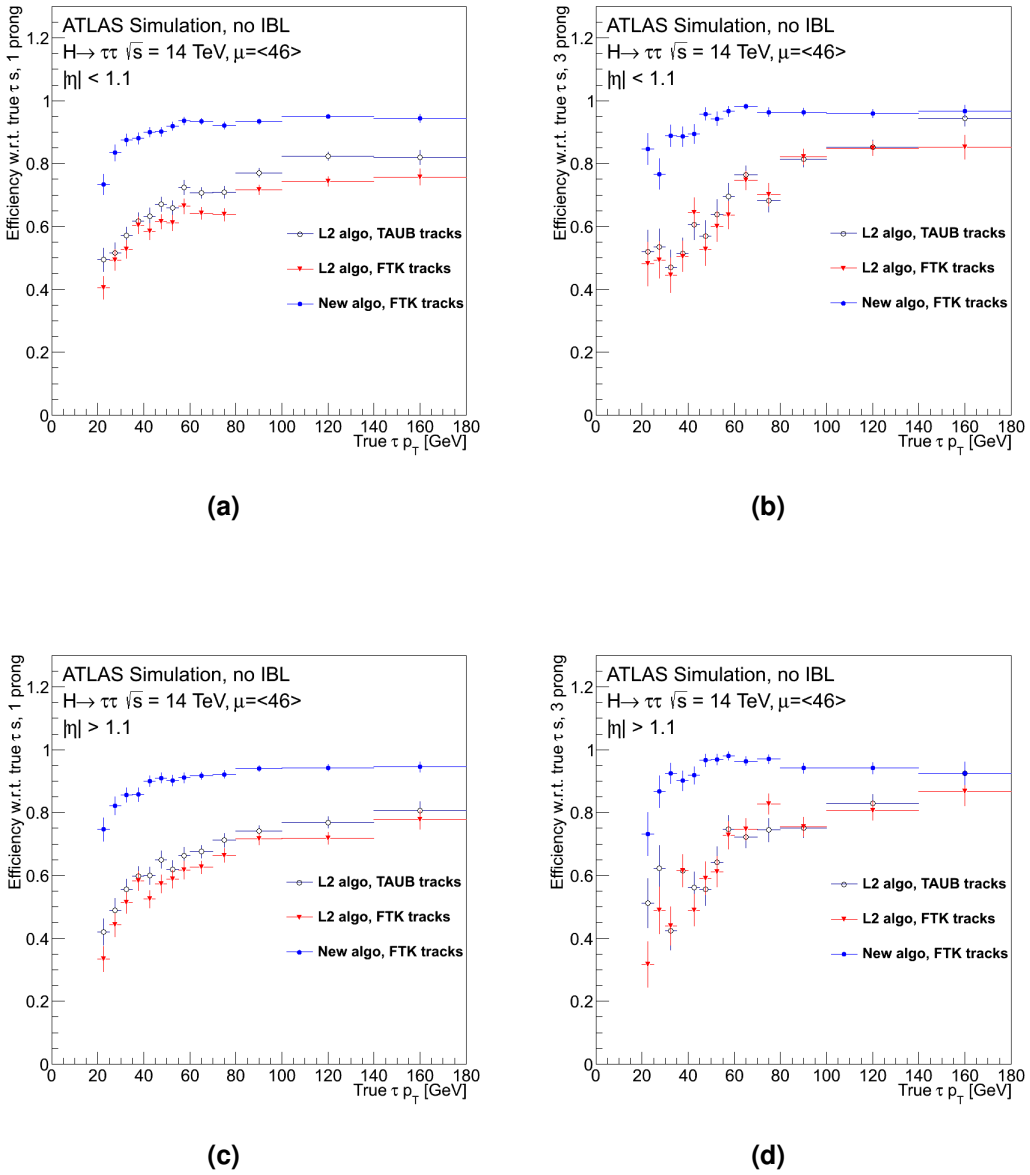

Figure 4.14 The measured per-tau L2 signal efficiency with respect to truth-level as a function of true τ-jet p_T in the $\mu_{\text{pile-up}} = 46$ sample for the 1-prong (left) and 3-prong (right) decays. The upper plots are for the barrel region and the lower ones are for the end-cap. Three working point are shown: the reference L2 algorithm using TauB tracks (black), the reference L2 algorithm using instead FTK tracks (red), and the proposed FTK track-based L2 algorithm (blue). The error bars indicate statistical uncertainties on the efficiency.

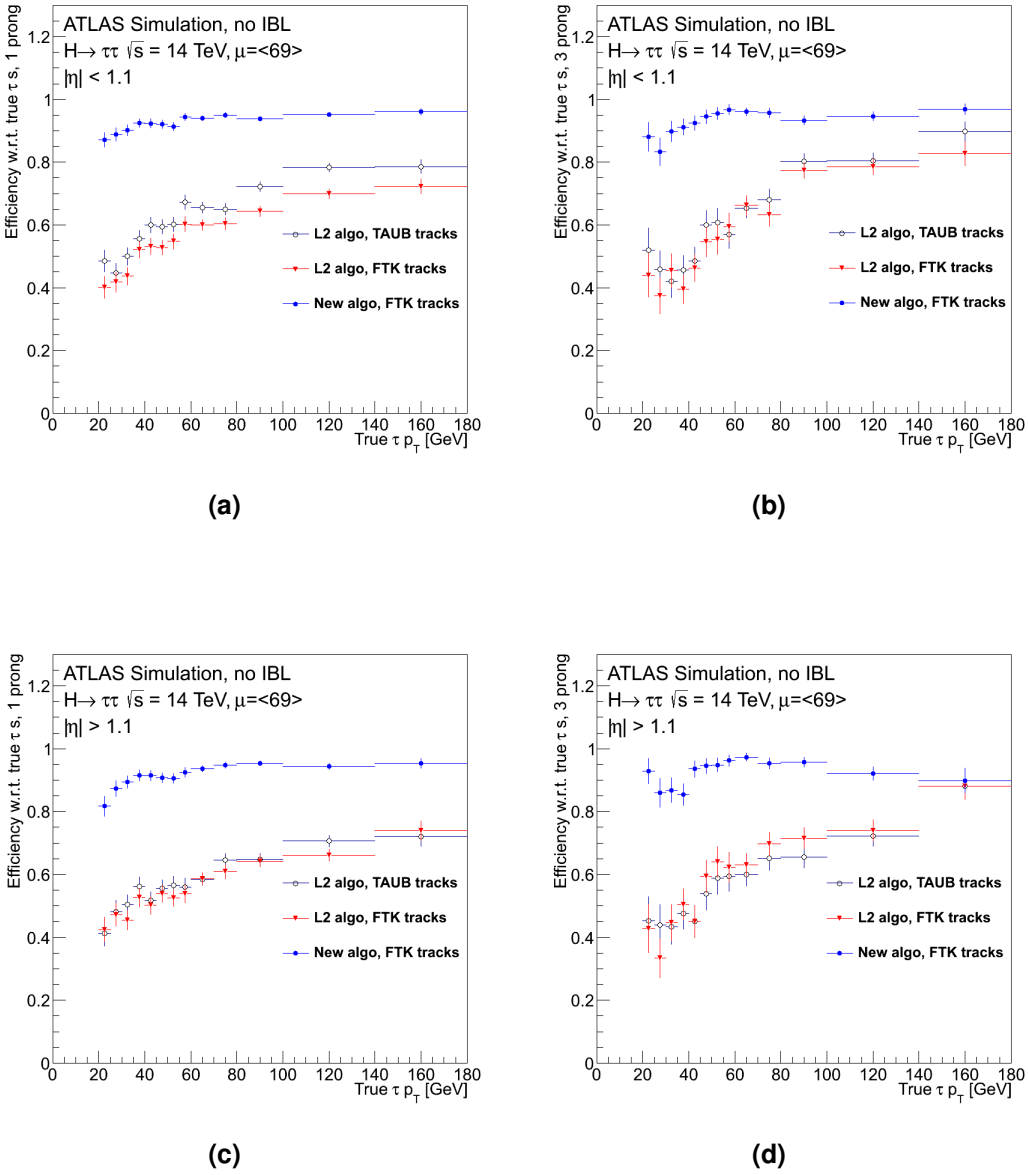

Figure 4.15 The measured per-tau L2 signal efficiency with respect to truth-level as a function of true τ-jet p_T in the $\mu_{\text{pile-up}} = 69$ sample for the 1-prong (left) and 3-prong (right) decays. The upper plots are for the barrel region and the lower ones are for the end-cap. The plotting scheme follows the one described in the caption of figure 4.14.

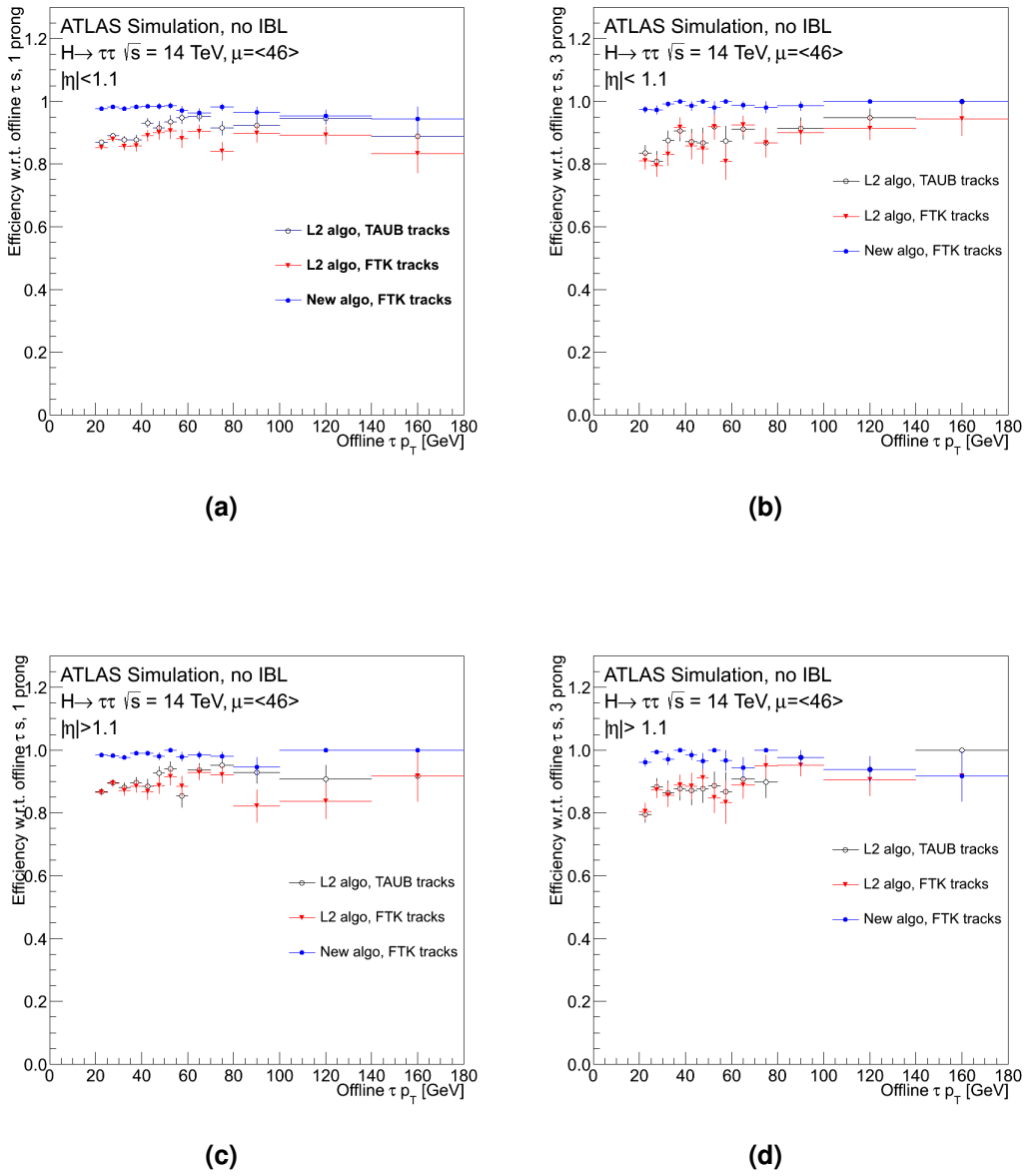

Figure 4.16 The measured per-tau L2 signal efficiency with respect to offline as a function of offline τ-jet p_T in the $\mu_{\text{pile-up}} = 46$ sample for the 1-prong (left) and 3-prong (right) decays. The upper plots are for the barrel region and the lower ones are for the end-cap. The plotting scheme follows the one described in the caption of figure 4.14.

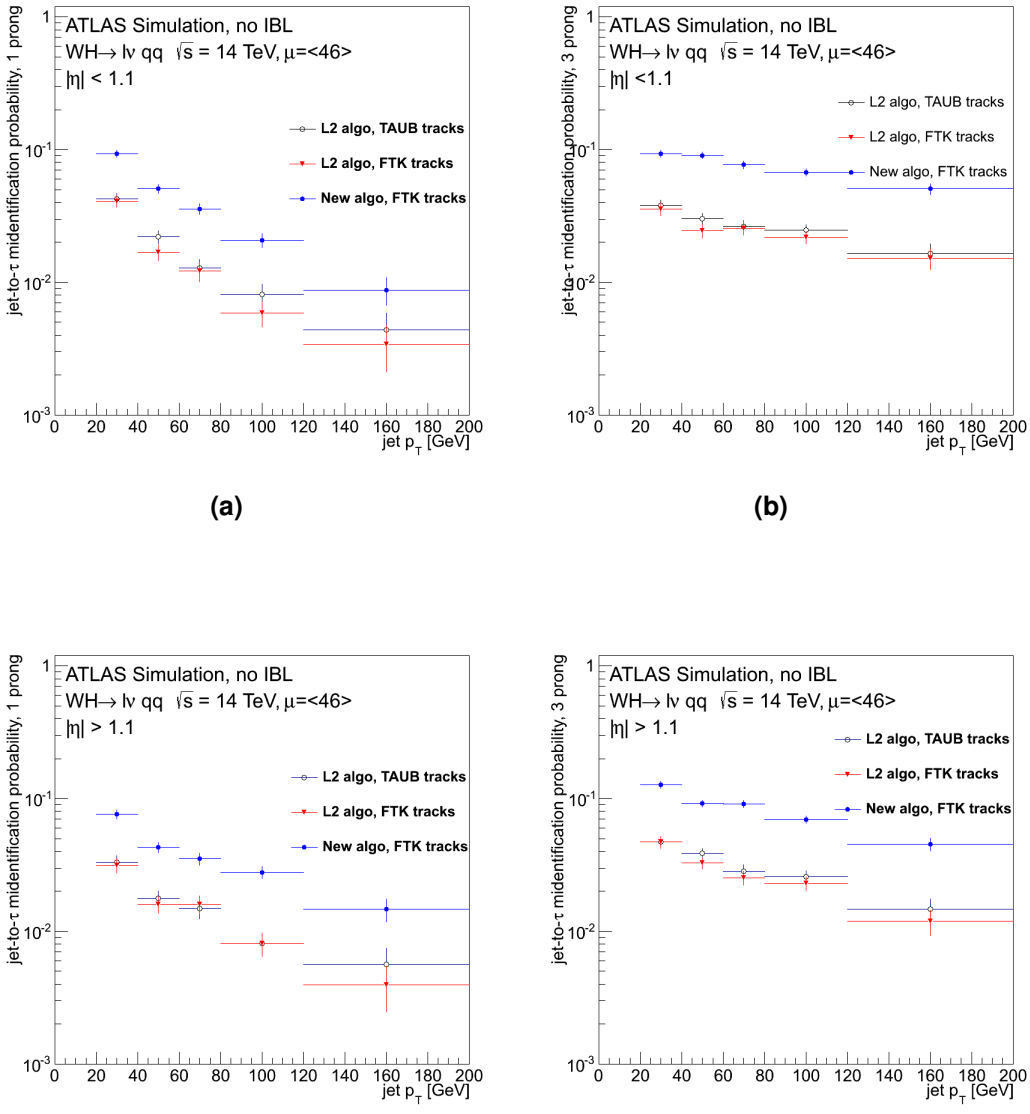

Figure 4.17 The measured misidentification probability in the background sample as a function of jet p_T in the $\mu_{\text{pile-up}} = 46$ sample for the 1-prong (left) and 3-prong (right) decays. The upper plots are for the barrel region and the lower ones are for the end-cap. The plotting scheme follows the one described in the caption of figure 4.14. The error bars indicate statistical uncertainties on the misidentification probability.

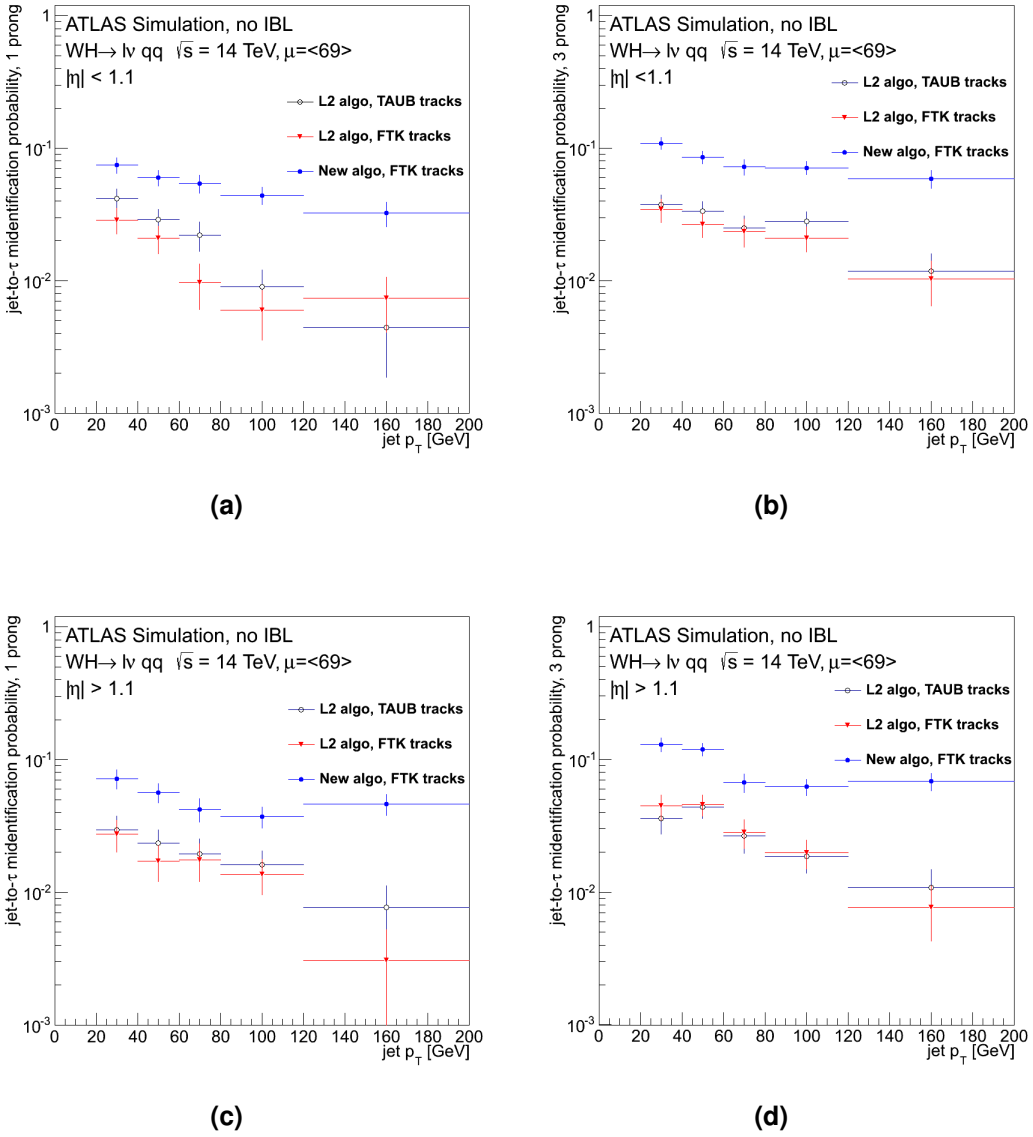

Figure 4.18 The measured misidentification probability in the background sample as a function of jet p_T in the $\mu_{\text{pile-up}} = 69$ sample for the 1-prong (left) and 3-prong (right) decays. The upper plots are for the barrel region and the lower ones are for the end-cap. The plotting scheme follows the one described in the caption of figure 4.14. The error bars indicate statistical uncertainties on the misidentification probability.

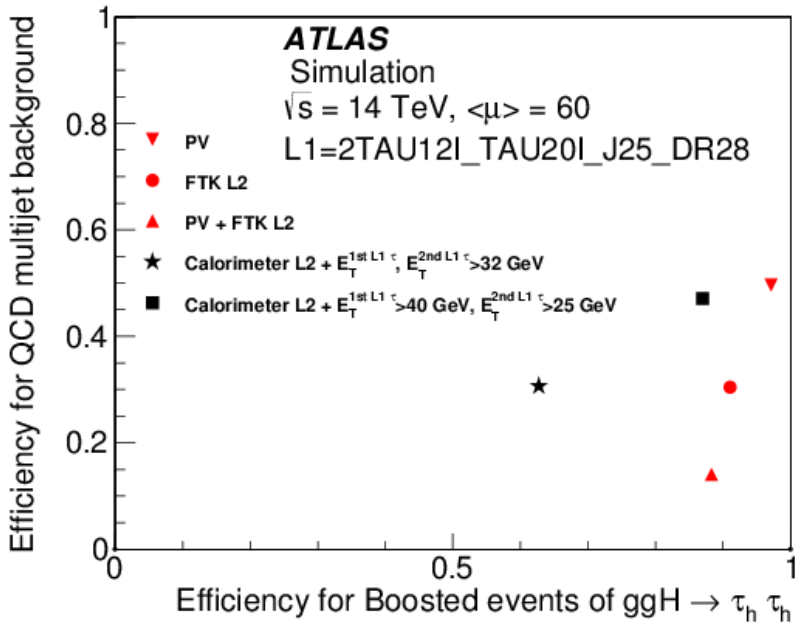

Figure 4.19 The per-event efficiency in the signal sample versus the background sample for five different L2 algorithms [123]. The particular L1 tau trigger is taken from a preliminary 2015 trigger menu. The L1 trigger requires two isolated (below 8 GeV) and separated ($\Delta R > 2.8$) L1 τ-jet candidates with E_T above 12 and 20 GeV, and an additional L1 jet candidate with E_T above 25 GeV. The red points represent FTK-based L2 algorithms. The red circle represents the FTK track-based algorithm proposed in section 4.5.3. The upward red triangle is when, in addition, the jet and at least one of the two τ-jets are required to be consistent with the PV from the FTK. The downward red triangle is for the FTK PV requirement alone. The black points represent traditional L2 algorithms that include selections on calorimeter variables, similar to the reference algorithm described in section 4.5.3. The black star has a symmetric E_T threshold on both τ-jet candidates of 32 GeV. The black square has asymmetric thresholds of 40 and 25 GeV.

Figure 4.19 shows the per-event efficiency for the previously mentioned signal sample versus the background sample for five different tau triggers. These are di-tau triggers in that the HLT requirements are applied to both ROIs identified at L1. Each trigger is distinguished by its L2 algorithm.

In this figure there are three red points representing different FTK-based L2 algorithms. The red circle represents the FTK track-based L2 algorithm proposed in section 4.5.3. The other two red points represent algorithms that also have requirements on the PV

provided by the FTK [2], and are outside the scope of the studies presented in this chapter.

The two black points refer to traditional L2 algorithms that include selections on calorimeter variables, similar to those described for the reference algorithm in section 4.5.3. The black star has symmetric thresholds on the E_T of the two τ-jet candidates, while the black square has asymmetric thresholds. Additional information on these and the previously mentioned triggers can be found in the caption of figure 4.19.

The traditional L2 algorithm with asymmetric E_T thresholds is shown to provide good signal efficiency, at the expense of poor background rejection. The opposite is true for the traditional algorithm with symmetric thresholds. However, the FTK track-based algorithm proposed in section 4.5.3 can provide both good signal efficiency and sufficient background rejection simultaneously. It is shown to provide an approximate 5% increase in signal efficiency and the same level of background rejection as the traditional algorithms with asymmetric and symmetric thresholds, respectively.

4.6 Conclusions

In this chapter two studies were presented relating to the ATLAS tau trigger. The first was the measurement of the tau trigger performance during $\sqrt{s}$ =8 TeV data taking, using a tag-and-probe method targeting $Z\rightarrow\tau\tau$ decays. The tau trigger performance with respect to efficiency and pile-up robustness was shown to meet the targets set during the design of the trigger system. The efficiency in data was shown to be well reproduced in MC simulation to a level of a few %, with the associated correction factors measured with a precision of 2-8% depending on the offline τ-jet p_T. These efficiency correction factors have been used in many ATLAS physics analyses using $\sqrt{s}$ = 8 TeV data, including the search for the SM Higgs boson in the $H\rightarrow\tau\tau$ decay channel [36]. The tag-and-probe method was also used to measure how precisely the transverse energy was reconstructed at each trigger level. The energy at L1 and L2 were shown to be significantly underestimated and overestimated, respectively, compared to offline. This is not unexpected given that these levels have dedicated energy reconstruction algorithms that significantly differ to those used offline. At the EF, the energy reconstruction and calibration followed offline closely and, as expected, the estimated energy at this level was shown to be very similar to offline.

The second study presented in this chapter investigated the potential of the FTK upgrade to improve tau trigger performance in future ATLAS runs at $\sqrt{s}$ = 14 TeV

under harsher pile-up conditions. A L2 τ-jet identification algorithm was proposed that used tracks reconstructed by the FTK. The proposed algorithm applied a purely track-based selection criteria, avoiding requirements on coarse calorimeter variables that negatively impact performance in traditional L2 algorithms. The FTK-based algorithm was shown to improve the per-tau efficiency compared to traditional algorithms by 10-40% with respect to truth and 5-15% with respect to offline. When implemented into a di-tau trigger for use in future $H\rightarrow\tau_{\text{had}}\tau_{\text{had}}$ analyses, the FTK-based algorithm outperformed traditional algorithms both in terms of the per-event signal efficiency and background rejection. Based on these observations it is clear that FTK tracking, freed from the computational constrains of software-based HLT tracking, will become a critical component of the future ATLAS tau trigger system. Moreover, FTK-based tau triggers will enable more sensitive measurements in many future ATLAS physics analyses such as those in the $H\rightarrow\tau\tau$ decay channel.

5

Search for the Higgs Boson in the WH Production Mode with $H \to WW^*$ Decay at $\sqrt{s}$ = 7, 8 and 13 TeV

Confirming the existence of the WH production mode would represent a major step towards validating the SM predictions for Higgs boson production at LHC. The $H \to WW^*$ decay channel provides a sensitive probe of WH production due its large branching fraction (21%) at the measured Higgs boson mass and its distinctive detector signature. Moreover, this combined production and decay process is interesting since the Higgs boson couples only to W bosons at both the production and decay vertices at tree-level. Therefore, this process also provides sensitivity to the H-W coupling strength and any potential deviations to it introduced by physics beyond the SM.

This chapter presents a direct search for the WH production of the SM Higgs boson with $H \to WW^*$ decay, and uses LHC proton-proton collision data collected by the ATLAS detector. The search is conducted with data taken at $\sqrt{s}$ = 7, 8 and 13 TeV corresponding to integrated luminosities of 4.5, 20.3 and 5.8 fb^{-1}, respectively. The sequential decay $WH \to WWW^* \to \ell\nu\ell\nu\ell\nu$, where ℓ is an electron or muon, is the specific signal process targeted by the search, and provides a clean signature in the ATLAS detector.

The analysis strategy was first defined using the data samples taken at $\sqrt{s}$ = 7 and 8 TeV and used to measure the signal strength, the ratio of the observed signal yield to the SM prediction, for a Higgs boson of mass 125 GeV. This analysis strategy was then extended to search for the same signal process using an early data sample at $\sqrt{s}$ = 13 TeV. The first measurement of the signal strength at 13 TeV was performed, demonstrating the validity of the analysis strategy at the higher center-of-mass energy. The results of the 7+8 TeV and 13 TeV analyses presented in this chapter were published by the ATLAS Collaboration in a paper [3] and conference note [4], respectively.

This chapter is organized as follows. Section 5.1 provides a general overview of the relevant physics processes, the analysis strategy and the statistical method. The data and MC samples are summarized in section 5.2. Sections 5.3 and 5.4 describe the event reconstruction and selection criteria, as well as the background estimation technique. The systematic uncertainties are described in section 5.5, with the final results using the $\sqrt{s}$ = 7 and 8 TeV data samples presented in section 5.6. The analysis using an early $\sqrt{s}$ = 13 TeV data sample is presented in section 5.7. Finally, a conclusion is provided in section 5.8.

5.1 Analysis Overview

5.1.1 Signal and background processes

The signal process targeted by the analyses presented in this chapter is the WH production mode, where a W boson is produced that radiates a Higgs boson, followed by $H \to WW^*$ decay. The W boson originating from the production process and the WW^* pair from the Higgs boson decay process are all required to decay leptonically ($W \to \ell\nu$, $WW^* \to \ell\nu\ell\nu$). This produces three leptons, only electrons and muons are considered, with the sum of their electric charges equal to ±1 and large missing energy from three undetected neutrinos. Figure 5.1 shows the tree-level Feynman diagram for this $WH \to WWW^* \to \ell\nu\ell\nu\ell\nu$ process.

The three leptons in the final state are labelled ℓ_0, ℓ_1 or ℓ_2 according to the following criteria. The lepton with unique charge is labelled as ℓ_0, the lepton closest to ℓ_0 in ΔR is labelled as ℓ_1, and the remaining lepton is labelled as ℓ_2. As explained in section 2.3.1, the spin-0 nature of the Higgs boson together with the properties of the weak interaction result in a preference for a small angular separation between the two

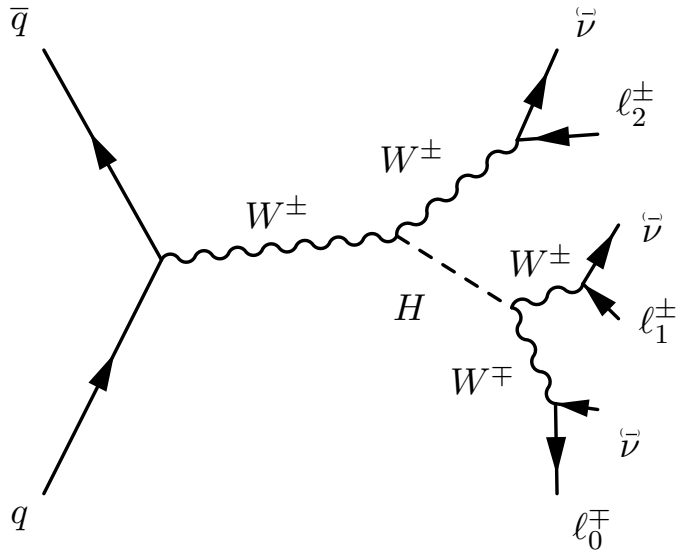

Figure 5.1 Tree-level Feynman diagram for the signal process. The arrow direction for charged lepton external lines refer to the superscripted sign.

leptons originating from the $H \to WW^*$ decay. Since leptons ℓ_0 and ℓ_1 have the smallest separation in ΔR, they are considered the $H \to WW^* \to \ell\nu\ell\nu$ candidate leptons.

When searching for the signal process, the most prominent backgrounds are those that also produce exactly three prompt leptons and large missing energy from undetected neutrinos. The most significant of these is the $WZ/W\gamma^*$ process; with WWW production also contributing although at a significantly lower rate. Details on these processes, including representative tree-level Feynman diagrams, can be found in table 5.1. The main feature that distinguishes $WZ/W\gamma^*$ from the signal process is the presence of a same-flavour and opposite-sign (SFOS) lepton pair, from $Z \to \ell\ell$ decay, that has a dilepton invariant mass ($m_{\ell\ell}$) consistent with the Z boson mass (m_Z). Although the contribution of WWW is relatively small, it is the most irreducible of all the backgrounds since it has a topology that is the most similar to the signal.

Backgrounds that do not produce exactly three prompt leptons can also contribute under certain conditions. Those with four prompt leptons can enter if one lepton goes unidentified, most likely due to its low p_T. This includes $Z\gamma$ production, where the photon undergoes a conversion into an electron-positron pair, and the continuum production of ZZ^*. The $Z\gamma$ and ZZ^* backgrounds are reducible due to their relatively small missing energy from the absence of neutrinos, and the presence of a SFOS lepton pair from $Z \to \ell\ell$ decay with $m_{\ell\ell}$ compatible with m_Z. Additional details on

these processes, including representative tree-level Feynman diagrams, are available in table 5.2.

Processes that produce only two prompt leptons can enter due to the presence of a jet misidentified as an additional lepton. This comes mainly from Z/γ^* production with additional jets, referred to hereafter as Z+jets, and top-quark processes. The top-quark contribution is dominated by $t\bar{t}$ production, but also includes smaller contributions from tW and $t\bar{t}W$ processes with $W\rightarrow \ell\nu$ decay. The Z+jets background is reducible in the same way as $Z\gamma$ and ZZ^* mentioned earlier. The top-quark processes differ from the signal process as they tend to have a larger number of jets, with at least one of them originating from a b-quark (b-jet). Additional details on these background processes are also provided in table 5.2.

Name	Process	Features
$WZ/W\gamma^*$	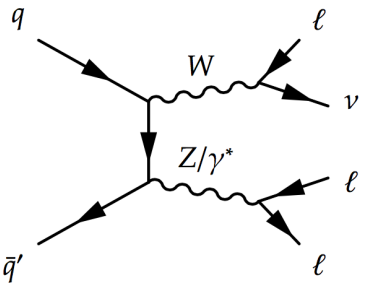	• 3 prompt leptons • Large missing energy from an undetected neutrino • For an on-shell Z boson, a SFOS lepton pair with $m_{\ell\ell}$ consistent with m_Z
WWW	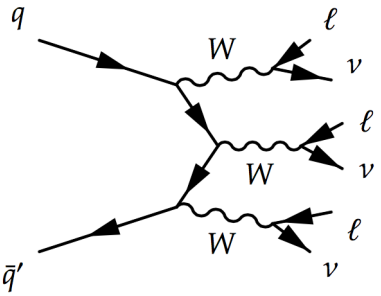	• 3 prompt leptons • Large missing energy from three undetected neutrinos

Table 5.1 Details on the $WZ/W\gamma^*$ and WWW background processes. A single representative tree-level Feynman diagrams is shown for each class of background. Virtual particles are indicated by "$*$". The key features that distinguish the detector signatures of each background are summarized in the last column.

Name	Process	Features
ZZ^*	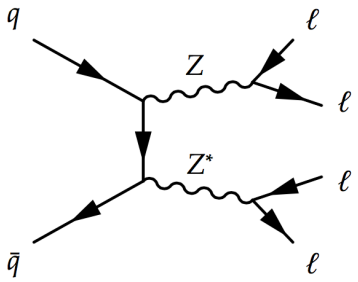	• 4 prompt leptons, one of which is unidentified • Small missing energy • SFOS lepton pair with $m_{\ell\ell}$ consistent with m_Z
$Z\gamma$	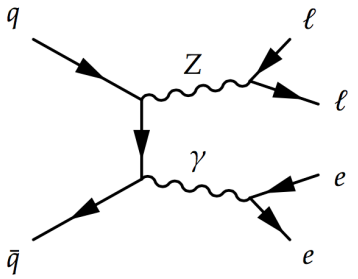	• Similar features to ZZ^* • At least one of the three identified leptons is an electron from photon conversion
Z+jets	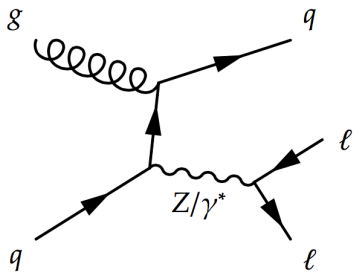	• 2 prompt leptons • Jet misidentified as a lepton • Small missing energy • SFOS lepton pair with $m_{\ell\ell}$ consistent with m_Z
$t\bar{t}$	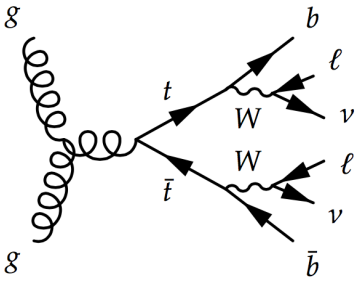	• 2 prompt leptons • b-jet misidentified as a lepton • Large missing energy from two undetected neutrinos

Table 5.2 Details on the ZZ^*, $Z\gamma$, Z+jets and $t\bar{t}$ background processes. The format of this table follows that described in the caption of table 5.1.

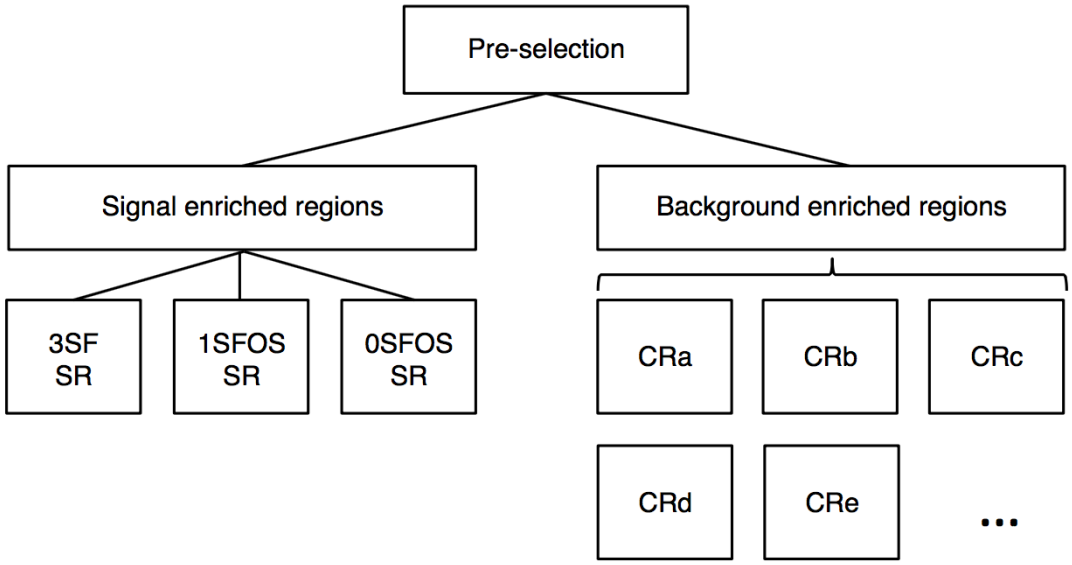

Figure 5.2 Diagram illustrating the separation of the pre-selection event sample into the SRs and CRs.

5.1.2 Analysis strategy

An analysis strategy was developed to perform a search for the signal process using the $\sqrt{s} = 7$ and 8 TeV ATLAS data samples. An overview of this strategy is presented in this section, with the full details provided throughout this chapter.

A general sample of three lepton events is first defined by applying a set of pre-selection criteria, described in section 5.3.2, to both the data and MC samples summarized in section 5.2. The events in the pre-selection sample are then separated into several statistically independent (orthogonal) regions in phase-space, as illustrated in figure 5.2, by applying in each region a unique set of event selection criteria on the lepton flavour combination and event kinematics.

Some regions are designed to be enriched in the signal, while others are enriched in the main backgrounds. These two kinds of regions are referred to as signal regions (SRs) and control regions (CRs), respectively, with each region defined separately for the $\sqrt{s} = 7$ and 8 TeV samples. The SRs have a larger signal-to-background ratio and thus drive the sensitivity of the signal strength measurement. The purpose of the CRs is to check the modeling and extract the normalizations of the main backgrounds.

The SRs are defined by a set of event selections, detailed in section 5.3.2, designed to preferentially select signal-like events while rejecting as much as possible those originating from the background processes. There are three SRs in total that are distinguished according to the number of same-flavour (SF) and opposite-sign (OS) lepton pairs within events. This includes: three same-flavour leptons (3SF), one pair of same-flavour and opposite-sign leptons (1SFOS) and zero of such lepton pairs (0SFOS). This separation is motivated by the varying sensitivities to the signal process in each SR. The 3SF and 1SFOS SRs contain about 25% and 50% of the signal, respectively, while splitting equally between them the dominant $WZ/W\gamma^*$ background. The 0SFOS SR only retains about one quarter of the signal, but nevertheless drives the sensitivity of the analysis due to the heavy suppression of the $WZ/W\gamma^*$ background.

Certain variables are used in the SRs to provide the final separation between the signal and backgrounds. In the 0SFOS SR the shape of the angular separation in R between $H\rightarrow WW^*\rightarrow \ell\nu\ell\nu$ candidate leptons ($\Delta R_{\ell_0\ell_1}$) is used. As mentioned previously, this quantity tends to be smaller for the signal process compared to the backgrounds. In the 3SF and 1SFOS SRs the shape of a multivariate discriminant from a BDT method [84] is used. This distribution is called the BDT score, and the specific BDT method that was developed is referred to as the BDT analysis. The BDT analysis is briefly described in section 5.6, with a more complete description provided in appendix A[1].

The contributions of the major background processes in the SRs are estimated by taking the kinematics from the simulated samples listed in section 5.2.2, with the normalization corrected to match what is observed in data. This correction is performed by applying normalization factors (NFs). Several CRs are defined for this purpose (referred to as CRa, CRb, CRc, etc. in figure 5.2). The NF measurement for a particular background will be largely driven by a CR designed to be enriched in that background, and is defined as the ratio of the measured yield from data to the one predicated by simulation. Information regarding the CR definitions, the measured NFs and background modeling will be provided in section 5.4.

The central result of the analysis is the observed value (μ_{obs}) of the signal strength parameter (μ), which was defined in the introduction to this chapter and in section 2.4. The expected value of this parameter is unity by definition. An observed value of zero corresponds to no signal in the data, while a value larger then unity indicates the presence of a signal larger then that predicted by the SM. The measurement of μ_{obs} involves a statistical fit procedure described in the next section.

[1] The full BDT analysis description is included in the appendix, rather then the main body of this chapter, since it was not the work of this author.

5.1.3 Statistical method

The values of μ_{obs} and the background NFs were simultaneously extracted from a statistical fit to the SRs and CRs that aimed to maximize a likelihood function. The local significance of any observed excess in the SRs could also be determined using a profile likelihood-ratio method. These statistical methods are briefly summarized in this section, with a more complete description available in ref. [35].

Likelihood function and the profile likelihood-ratio method

The likelihood function, $\mathcal{L}(\mu, \boldsymbol{\theta} \mid \boldsymbol{N})$, was built as the product of Poisson probability distribution functions of each of the SRs and CRs, where the mean values of these distributions were chosen as the sum of the expected yields of the signal and background contributions in each region. The symbol $\boldsymbol{N} = \{N_A, N_B, ...\}$ represents the set of observed events in each of the SRs and CRs. The signal and background expectations are functions of the signal strength parameter, μ, and a set of nuisance parameters, $\boldsymbol{\theta} = \{\theta_a, \theta_b, ...\}$. The nuisance parameters take into account the corrections to the background normalization to data, via the NFs, and the different sources of systematic uncertainties.

More precisely, each SR had multiple terms in the likelihood function. The 3SF and 1SFOS SRs had an entry for each bin of the final BDT score, while the 0SFOS SR had an entry for each bin of the final $\Delta R_{\ell_0\ell_1}$ distribution. The BDT score and $\Delta R_{\ell_0\ell_1}$ distributions entered the fit as six and four bins, respectively, with the intervals that defined each bin[2] shown in figures 5.8-5.10 of section 5.6. In this way, each of these bins were treated as a separate SRs in the likelihood function.

After constructing the likelihood function, a fit was performed to determine the parameters that maximize the likelihood value. The μ parameter, the main parameter of interest, and the nuisance parameters for the NFs were left as free parameters in the fit, while the constraints on the nuisance parameters for the systematic uncertainties were chosen to be log-normal distributions. The values of μ and $\boldsymbol{\theta}$ that unconditionally maximize the likelihood function are $\hat{\mu}$ and $\hat{\boldsymbol{\theta}}$, where $\hat{\mu} \equiv \mu_{\text{obs}}$ and $\hat{\boldsymbol{\theta}}$ includes the observed values of the background NFs.

[2] The bin widths were optimized for the expected signal significance, while ensuring each bin was sufficiently populated so as not to cause any instabilities in the fit.

At this point, the profile likelihood-ratio test statistic [124] can be used to test the compatibility with the background-only hypothesis. The test statistic is defined as:

$$q_\mu = -2\ln\frac{\mathcal{L}(\mu, \hat{\hat{\boldsymbol{\theta}}}_\mu)}{\mathcal{L}(\hat{\mu}, \hat{\boldsymbol{\theta}})} \tag{5.1}$$

The denominator is the unconditional maximum value of the likelihood mentioned earlier, which is a constant value. The numerator depends on the nuisance parameter values, $\hat{\hat{\boldsymbol{\theta}}}_\mu$, that maximize the likelihood function for a given value of μ. The p_0 value is computed from q_μ evaluated at $\mu = 0$, and represents the probability of obtaining a value of q_μ larger than the observed value under the background-only hypothesis [125]. The p_0 value can also be expressed in terms of the number of standard deviations, referred to as the local significance (Z_0). This is determined from p_0 by taking the Gaussian tail probability:

$$Z_0 = \sqrt{2}\mathrm{erf}^{-1}(1 - 2p_0) \tag{5.2}$$

Inclusion of systematic uncertainties

Systematic uncertainties will influence the estimated signal and background event yields through their nuisance parameters in the fit. Theoretical uncertainties include those associated to the modeling of the signal and background processes. Experimental uncertainties include those associated to the selection and reconstruction efficiencies and on the calibration of physics objects. The different sources of theoretical and experimental uncertainties will be described in section 5.5.

The experimental uncertainties were directly applied to the estimated event yields in the SRs and CRs. The same is true for the theoretical uncertainties of the signal as well as those for the backgrounds that were not normalized using NFs. For backgrounds that were normalized via NFs, the theoretical uncertainties were computed on the SR to CR extrapolation factor, and applied to the SRs. The extrapolation factor, α, is defined as:

$$\begin{aligned} N_{\text{est}}^{\text{SR, bkg}} &= \frac{N_{\text{sim}}^{\text{SR, bkg}}}{N_{\text{sim}}^{\text{CR, bkg}}} \times \left(N_{\text{obs}}^{\text{CR}} - N_{\text{sim}}^{\text{CR, other bkg}} \right), \\ &= \alpha \times \left(N_{\text{obs}}^{\text{CR}} - N_{\text{sim}}^{\text{CR, other bkg}} \right) \end{aligned} \tag{5.3}$$

where N^{SR} and N^{CR} are the number of events in an SR and a particular CR, respectively. The superscripts also indicate if the number of events is of the background source

targeted by the CR ("bkg") or the other backgrounds ("other bkg"). The subscripts indicate whether it is the observed ("obs"), estimated ("est") or simulated ("sim") number of events.

When performing measurements with the combined $\sqrt{s} = 7$ and 8 TeV event samples, the fit accounted for correlations between the two samples due to common systematic uncertainties. For the experimental uncertainties, the correlation of all respective nuisance parameters were assumed to be 100% except for those that are statistical in origin or have a different source for the two samples. For the latter two cases the nuisance parameters were treated as uncorrelated and include, for example, the statistical component of the JES calibration and the luminosity uncertainty. All theoretical uncertainties were treated as correlated between the two samples.

5.2 Samples

5.2.1 Data samples

The data samples used in this analysis were recorded by the ATLAS detector during 2011-2012 with the triggers listed in table 5.3. These single lepton triggers were fully efficient for three lepton signatures, with more details on the triggers provided in section 3.3.2. Overall quality criteria were applied to the data as described in section 3.1.2. The data samples correspond to an integrated luminosity of 4.5 fb^{-1} and 20.3 fb^{-1} at $\sqrt{s} = 7$ and 8 TeV, respectively. As described in section 3.1.3, the 8 TeV data were taken at a higher luminosity than that for the 7 TeV data producing a higher average number, 21 versus 9, of pile-up.

Trigger type	**$\sqrt{s}$ = 8 TeV data sample**	**$\sqrt{s}$ = 7 TeV data sample**
Single e	24Mi or 60M	20-22M
Single μ	24i or 36	18

Table 5.3 Summary of the HLT requirements of the single lepton triggers used to record the $\sqrt{s} = 7$ and 8 TeV data samples. The numbers indicate the minimum lepton p_T requirements (in GeV), and the letter "i" indicates an isolation requirement. The letter "M" indicates a Medium electron identification criteria. The "or" is logical. In order to mitigate efficiency loss at high-p_T, the isolated triggers were used in conjunction with a non-isolated trigger with a higher-p_T threshold.

5.2.2 MC samples

Given the large range of background processes that could contribute in the SRs, MC modeling was an important aspect of the analysis. Dedicated samples were generated for the signal process and each of the backgrounds processes. An overview of the simulation of the signal and major background processes is provided in this section. A more complete description, including details on the minor backgrounds, can be found in ref. [3].

The MC generators that were used for each process are listed in table 5.4. For the signal process all steps in the simulation chain were done with Pythia [101, 102] for $m_H = 125\,\text{GeV}$, which is compatible with the measured value. This included the generation of the hard scattering process followed by the modeling of the parton showering (PS), hadronization, and the underlying event (UE). Powheg was used for the hard scattering process in the high-mass[3] $WZ/W\gamma^*$, high-mass ZZ^*, $t\bar{t}$ and tW background processes [126–128], all of which were interfaced with Pythia for the other stages in the simulation chain and used the CT10 [119] PDF set. For the low-mass[4] $WZ/W\gamma^*$, low-mass ZZ^* and $Z\gamma$ samples Sherpa [129] was used for all steps in the simulation with the CT10 PDF set. The Z+jets samples were simulated by Alpgen interfaced with Herwig [113, 114] and used the MRSTMCal [130] PDF set. Both the $t\bar{t}W$ and WWW processes were modeled by MadGraph [131] interfaced with Pythia and used the CTEQ6L1 PDF set [118].

The cross sections for the samples were computed to different levels of accuracy: leading order (LO), next-to-leading order (NLO), next-to-next-to-leading order (NNLO) or next-to-next-to-leading-logarithm (NNLL). The calculation order for the cross sections of each process are shown in final column of table 5.4. The signal sample was normalized to NNLO in the QCD calculations [20, 132–135] with additional NLO EW corrections computed with Hawk [136]. The branching fraction for the $H \to WW^*$ decay was calculated using Hdecay [137]. The cross sections for the Z+jets samples were calculated at NNLO precision [138, 139]. The same is true for the $t\bar{t}$ samples, however they also included higher-order terms for the soft-gluon resummation up to NNLL, evaluated with Top++2.0 [140]. The $WZ/W\gamma^*$, ZZ^* , $Z\gamma$ and WWW samples were all normalized to their NLO QCD cross sections [141, 142]. The tW and $t\bar{t}W$ processes were normalized to NNLL and LO, respectively.

[3] The high-mass $WZ/W\gamma^*$ (ZZ^*) samples require the $m_{\ell\ell}$ of all SFOS lepton pairs to be above 7 (4) GeV at the event generation.

[4] The low-mass $WZ/W\gamma^*$ (ZZ^*) samples require the SFOS lepton pair with the lowest $m_{\ell\ell}$ in an event to have $m_{\ell\ell} \leq 7$ GeV ($m_{\ell\ell} \leq 4$ GeV) at the event generation.

		Generator	Calculation order of cross section
Signal	WH ($H \to WW^*$)	Pythia8, Pythia6	NNLO QCD + NLO EW
Major Backgrounds	$WZ/W\gamma^*$ (high-mass)	Powheg + Pythia8, Pythia6	NLO
	$WZ/W\gamma^*$ (low-mass)	Sherpa	NLO
	WWW	MadGraph + Pythia6	NLO
	$q\bar{q}/qg \to ZZ^*$ (high-mass)	Powheg + Pythia8, Pythia6	NLO
	$q\bar{q}/qg \to ZZ^*$ (low-mass)	Sherpa	NLO
	$Z\gamma$	Sherpa	NLO
	Z+jets (with HF)	Alpgen + Herwig	NNLO
	$t\bar{t}$	Powheg + Pythia6	NNLO+NNLL
	tW	Powheg + Pythia6	NNLL
	$t\bar{t}W$	MadGraph + Pythia6	LO
Minor Backgrounds	$gg \to ZZ^*$, WW	gg2VV + Herwig	LO
	$q\bar{q}/qg \to WW$	Powheg + Pythia6	NLO
	WWZ, ZZW, ZZZ	MadGraph + Pythia6	NLO
	$W\gamma$	Alpgen + Herwig	NLO
	W+jets	Alpgen + Pythia6, Herwig	NLO
	tZ, $t\bar{t}Z$	MadGraph + Pythia6	LO
	tb	Powheg + Pythia6	NNLL
	tqb	AcerMC + Pythia6	NNLL
Other Higgs	WH ($H \to \tau\tau$)	Pythia8, Pythia6	NNLO QCD + NLO EW
	ZH ($H \to WW^*$, $H \to \tau\tau$)	Pythia8, Pythia6	NNLO QCD + NLO EW
	ggF ($H \to WW^*$)	Powheg + Pythia8, Pythia6	NNLO+NNLL QCD + NLO EW
	VBF ($H \to WW^*$)	Powheg + Pythia8, Pythia6	NNLO QCD + NLO EW
	$t\bar{t}H$ ($H \to WW^*$)	Pythia8	NLO

Table 5.4 Summary of the MC generators and cross section accuracy used to model the signal and background processes. Wherever two comma-separated generators are specified, the first one was used at $\sqrt{s}$ = 8 TeV and the second one at 7 TeV. The version of Pythia is stated in this table (either v6 or v8), but is not specified in the text. In some cases different generators are used for the $q\bar{q}/qg$-initiated and loop-induced gg-initiated processes. The definitions of the low- and high-mass samples were provided in footnotes 3 and 4, respectively. HF refers to heavy-flavour jet production. All Higgs boson samples were generated with m_H = 125 GeV. The signal and major background samples are described in the text. A more complete description can be found in ref. [3], including details on the minor background samples and the other Higgs process samples.

The MC samples were passed through each step of the ATLAS simulation chain described in section 3.3.3. They were then processed with the same ATLAS offline reconstruction software, derivation software and final analysis framework as the data samples. Following the recommendations of the ATLAS performance groups, additional corrections obtained from measurements in the data were applied to the MC samples. This accounted for differences between data and simulation in, for example,

the reconstruction efficiencies of leptons and jets. Following the procedure described in section 3.3.3, the simulated events were reweighted so that the pile-up distribution matched the one observed in the data samples.

5.3 Event Reconstruction and Signal Region Selections

5.3.1 Event reconstruction

The signal and background processes produced collision events in the ATLAS detector containing signatures from several different kinds of physics objects such as leptons, jets and missing transverse energy from undetected neutrinos. The properties of these objects were used to separate the signal and background events, and to construct the event selections that define the SRs and CRs. Before these selections could be defined, the physics objects within the data and MC samples were reconstructed using offline algorithms.

The offline event reconstruction algorithms and object selection criteria used for the $\sqrt{s}$ = 7 and 8 TeV samples were detailed in section 3.3.1, and won't be repeated here. This included descriptions of the offline reconstruction and selections for the PV, muons, electrons, jets, b-tagged jets, E_T^{miss} and p_T^{miss}. Information was also provided regarding the procedure used to resolve overlaps between muons, electrons and jets. Recall that there were some differences between the $\sqrt{s}$ = 7 and 8 TeV offline reconstruction and selections including: the electron identification and impact parameter criteria, the JVF threshold for the jets, the lower p_T threshold used in b-jet tagging, and the inclusion of the soft term STVF scaling for the E_T^{miss}. The main reason for these differences was the more challenging pile-up conditions at 8 TeV, rather than the increased centre-of-mass energy.

5.3.2 Signal region selections

The selections that were used to define the SRs are summarized in table 5.5, and further detailed throughout this section[5]. The selections can be roughly split into four classes: pre-selections, the separation into three SRs using the lepton flavour combination, background reduction in the SRs and, finally, the targeting of the $H \to WW^* \to \ell\nu\ell\nu$ decay topology.

[5] Note that the E_T^{miss}, p_T^{miss}, dilepton invariant mass and $\Delta R_{\ell_0\ell_1}$ selections were optimized in order to maximize the expected significance for the signal process with m_H = 125 GeV.

		3SF	1SFOS	0SFOS
Pre-selections	Primary vertex	Each event contains a PV		
	Trigger	≥ 1 lepton matches a trigger		
	Num. of isolated leptons	3	3	3
	Lepton p_T [GeV]	> 15	> 15	> 15
	Total lepton charge	± 1	± 1	± 1
Lepton flavour combination	Num. of SFOS pairs	2	1	0
Background reduction	Num. of jets	≤ 1	≤ 1	≤ 1
	Num. of b-tagged jets	0	0	0
	E_T^{miss} (p_T^{miss}) [GeV]	> 30 (20)	> 30 (20)	—
	$\lvert m_{\ell^+\ell^-} - m_Z \rvert$ [GeV]	> 25	> 25	—
	Min. $m_{\ell^+\ell^-}$ [GeV]	> 12	> 12	> 6
	Max. $m_{\ell^+\ell^-}$ [GeV]	< 200	< 200	< 200
$H\rightarrow WW^*\rightarrow \ell\nu\ell\nu$ topology	$\Delta R_{\ell_0\ell_1}$	< 2.0	< 2.0	—

Table 5.5 Event selections that defined 3SF, 1SFOS and 0SFOS SRs. The selection thresholds were identical for the $\sqrt{s}$ = 7 and 8 TeV SRs. However, the SRs inherited the differences between the 7 and 8 TeV trigger and offline object selections mentioned in sections 5.2.1 and 5.3.1, respectively.

The pre-selections began with the requirement that events contained a PV and that they fired the single-lepton triggers described in section 5.2.1. An event is said to have fired a trigger if at least one offline lepton matches a lepton candidate reconstructed at trigger-level. To ensure they were on the trigger plateau, any trigger-matched leptons were required to have offline p_T greater than 24 GeV in the $\sqrt{s}$ = 8 TeV samples or 18 (22) GeV for muons (electrons) in the 7 TeV samples. Events were then required to contain exactly three isolated leptons with p_T above 15 GeV, with the sum of their electric charges equal to ± 1. After all of the above mentioned pre-selection criteria, the contributions from background processes with two misidentified leptons (such as W+jets) or three misidentified leptons (such as QCD multi-jet production) were negligible. At this point, the dominant backgrounds were the ones described in section 5.1.1: $WZ/W\gamma^*$, ZZ^*, Z+jets, $Z\gamma$, top-quark processes and to a lesser extent WWW.

Events were then separated into the 3SF, 1SFOS and 0SFOS SRs according to the number of SFOS lepton pairs as described in section 5.1.2. After this SR split, a specific set of selections were applied to each SR taking into account their different background compositions.

In order to reduce the contributions from top-quark processes, coming mainly from $t\bar{t}$ production, events in all SRs were required to contain at most one jet that was not

b-tagged. In the 3SF and 1SFOS SRs, the E_T^{miss} and p_T^{miss} were required to be above 30 GeV and 20 GeV, respectively. These missing transverse energy requirements helped suppress backgrounds without neutrinos such as ZZ^*, Z+jets and $Z\gamma$. The distribution of E_T^{miss} in the $\sqrt{s} = 8$ TeV samples for the combined 3SF and 1SFOS SRs is shown in figure 5.3a. In this figure, the backgrounds are split into five categories: diboson (VV), triboson (VVV), single boson (V), top-quark (Top), and other non-signal Higgs boson processes (Other Higgs). The processes that entered each category are summarized in table 5.6. Since the 0SFOS SR was already very clean and its main backgrounds contain neutrinos, no requirements were imposed in this region on E_T^{miss} or p_T^{miss}.

In the 3SF and 1SFOS SRs, the invariant mass of all SFOS lepton pairs was required to pass the criteria $|m_{ll} - m_Z| > 25$ GeV. This requirement, referred to as the Z-mass veto, suppressed WZ, ZZ^*, Z+jets and $Z\gamma$ events. These events contain Z bosons and so the invariant mass of the two leptons from $Z \to \ell\ell$ decay peaks around $m_Z \approx 91$ GeV as seen, for example, in the $m_{\ell_0\ell_2}$ distribution of figure 5.3b. In all the SRs, the OS lepton pair in each event that has the smallest invariant mass was identified. To reject backgrounds from heavy-flavour processes [143], the invariant mass of this lepton pair was required to be above 12 GeV in the 3SF and 1SFOS SRs, and above 6 GeV in the 0SFOS SR. While the signal can only proceed through an s-channel process, the $WZ/W\gamma^*$ background can also proceed via the t- and u-channels. This results in a larger number of combinatorial lepton pairs for $WZ/W\gamma^*$, and a broader tail at large di-lepton invariant mass values. In order to further reduce this background, the OS lepton pair with the largest invariant mass was identified and its value was required to be below 200 GeV in all SRs.

Background category	**Processes**	**Colour in plots**
VV	$WZ/W\gamma^*$, ZZ^*, $Z\gamma$ and minor diboson processes	
VVV	WWW and minor triboson processes	
V	Z+jets and minor single boson processes	
Top	$t\bar{t}$, tW and $t\bar{t}W$ and minor top-quark processes	
Other Higgs	non-signal Higgs boson processes	

Table 5.6 Categorization scheme of the background processes, including the colours used to represent them in plots. The minor backgrounds and non-signal Higgs boson processes refer to those listed in table 5.4.

.

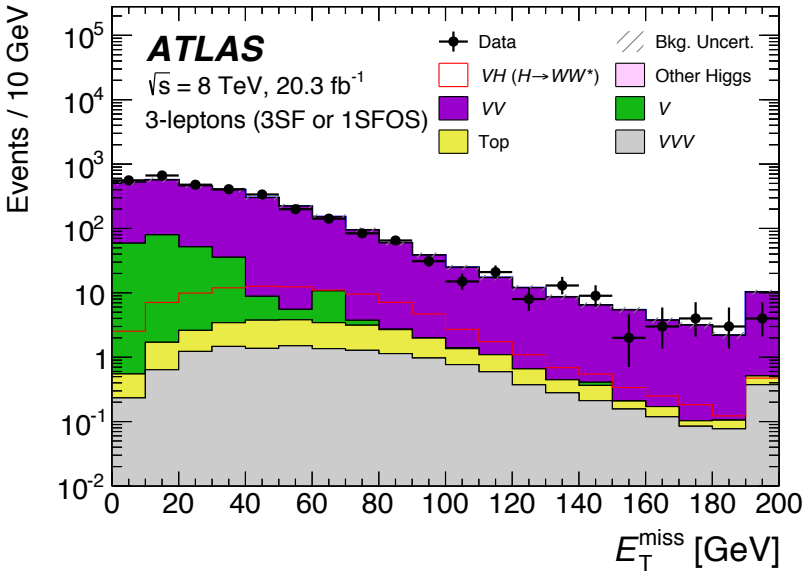

(a)

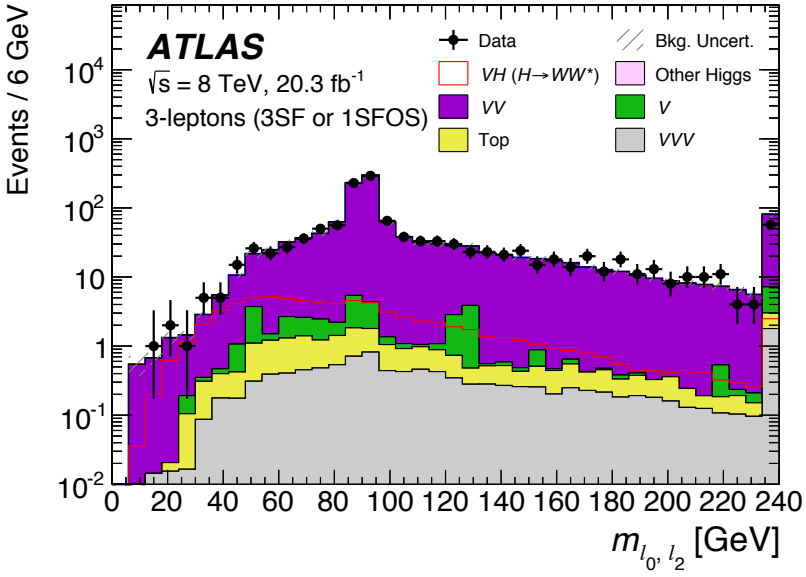

(b)

Figure 5.3 Distributions in the combined 3SF and 1SFOS SRs with the $\sqrt{s} = 8$ TeV samples of (a) E_T^{miss} after applying the selections in table 5.5 down to the number of b-tagged jets requirement, and (b) $m_{\ell_0\ell_2}$ after applying the selections down to the E_T^{miss} and p_T^{miss} requirements. The data (points) are compared to the background expectation (stacked filled histograms). The total uncertainty on the total background estimate is represented by the hatched area. This includes both the statistical and systematic components. The background NFs are applied. The final bin includes overflows. The signal (red line) is overlaid, and scaled by a factor of 20.

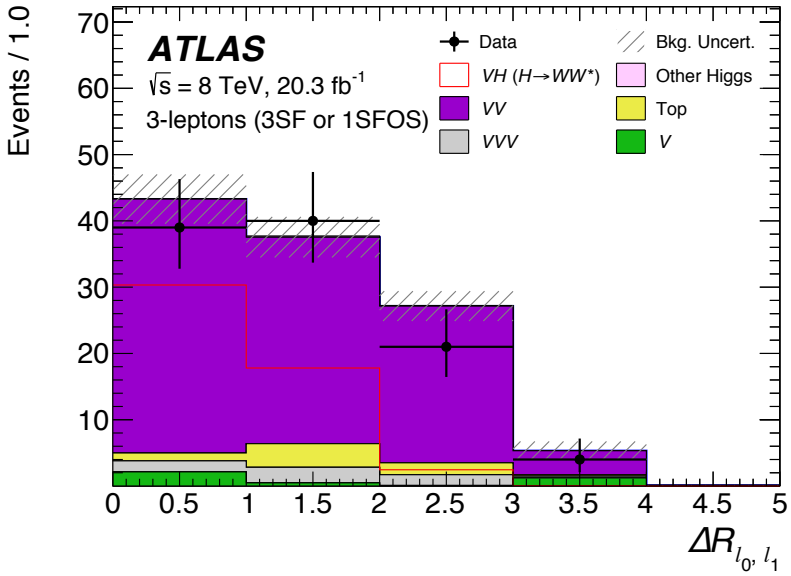

Figure 5.4 $\Delta R_{\ell_0\ell_1}$ distribution in the combined 3SF and 1SFOS SRs with the $\sqrt{s} = 8$ TeV samples, after applying the selections in table 5.5 down to the maximum $m_{\ell\ell}$ requirement. The plotting scheme following the one described in the caption of figure 5.3.

Finally, the $\Delta R_{\ell_0\ell_1}$ was required to be smaller than 2 in the 3SF and 1SFOS SRs. The distribution of $\Delta R_{\ell_0\ell_1}$ is shown in figure 5.4. As explained earlier, this quantity tends to be small for the signal topology. This selection was not applied in the 0SFOS SR since the full $\Delta R_{\ell_0\ell_1}$ distribution was used in the statistical fit.

Additional plots in the SRs can be found in section 5.6, appendix A and appendix C. These include distributions in the 0SFOS SR, as well as those in the $\sqrt{s} = 7$ TeV SRs.

5.4 Background Modeling

The backgrounds in this analysis that were normalized using CRs, via NFs, were the $WZ/W\gamma^*$, ZZ^*, $Z\gamma$, Z+jets and top-quark processes. Each of these backgrounds had a corresponding CR defined separately for the $\sqrt{s} = 7$ and 8 TeV samples. The CRs were enriched in their respective background and made orthogonal to the SRs by inverting some selections with respect to the SR definitions. These selections are summarized in table 5.7, and detailed throughout this section.

CR name	Main backgrounds	Changes w.r.t. reference SRs
WZ CR	$WZ/W\gamma^*$	inverted Z-mass veto
ZZ CR	ZZ^*	no Z-mass veto $\lvert m_{\ell\ell\ell} - m_Z\rvert < 15$ GeV inverted E_T^{miss} and p_T^{miss} selections only $ee\mu, \mu\mu\mu$
$Z\gamma$ CR	$Z\gamma$ ZZ^*	no Z-mass veto $\lvert m_{\ell\ell\ell} - m_Z\rvert < 15$ GeV inverted E_T^{miss} and p_T^{miss} selections only $eee, \mu\mu e$
Z+jets CR	Z+jets $WZ/W\gamma^*$ ZZ^*	inverted Z-mass veto inverted E_T^{miss} and p_T^{miss} selections $\lvert m_{\ell\ell\ell} - m_Z\rvert > 15$ GeV NFs were derived separately for e-fake and μ-fake samples (μ-fake dropped for $\sqrt{s} = 7$ TeV)
Top CR	Top-quark processes (mainly $t\bar{t}$)	at least one jet at least one b-tagged jet no max. $m_{\ell^+\ell^-}$ and $\Delta R_{\ell_0\ell_1}$ selections

Table 5.7 Event selection criteria used to define the CRs, given with respect to the selections of the reference 3SF and 1SFOS SRs. The CRs were defined within the 3SF and 1SFOS topologies, and the derived NFs were applied to all SRs. This choice was dictated by the larger number of events available when requiring at least one SFOS lepton pair. The second column in this table lists the backgrounds that have significant contributions in each CR.

Three of the CRs were designed to be enriched in the $WZ/W\gamma^*$, ZZ^* and $Z\gamma$ backgrounds. The respective names of these CRs are the WZ CR, ZZ CR and $Z\gamma$ CR. The WZ CR was defined by inverting the Z-mass veto selection of the SRs in order to select, rather then reject, events containing $Z\rightarrow\ell\ell$ decays. For the ZZ CR and $Z\gamma$ CR, the Z-mass veto selection was dropped entirely while requiring the invariant mass of the three leptons ($m_{\ell\ell\ell}$) to be consistent with m_Z. The ZZ^* and $Z\gamma$ backgrounds do not contain neutrinos, and so the ZZ CR and $Z\gamma$ CR inverted the E_T^{miss} and p_T^{miss} selections of the SRs. The events with three electrons (eee) or two muons and one electron ($\mu\mu e$)

were dropped from the ZZ CR since they had a large contamination from $Z\gamma$ events. The events with those lepton flavour combinations instead entered the $Z\gamma$ CR.

In order to target Z+jets events, a Z+jets CR was defined by inverting the Z-mass veto, E_T^{miss} and p_T^{miss} selections of the SRs. For this CR, the previously mentioned $m_{\ell\ell\ell}$ selection was inverted in order to ensure orthogonality with the ZZ CR and $Z\gamma$ CR. Since misidentified muons and misidentified electrons have different properties, the Z+jets CR was split into two components: the e-fake sample and the μ-fake sample. The e-fake sample was enriched in misidentified electrons by considering only the events containing three electrons or two muons and one electron. The remaining events were enriched in misidentified muons, and entered the μ-fake sample. Both the e-fake and μ-fake components of the Z+jets CR entered the statistical fit separately, and the corresponding background contributions were assigned their own distinct NF.

The $\sqrt{s} = 7$ TeV μ-fake sample was dropped from the statistical fit, and so the normalization of the corresponding background contribution in the 7 TeV SRs was taken directly from MC simulation. This was done because the number of events in the 7 TeV μ-fake sample was too small to reliably extract the corresponding NF. Moreover, the contribution of this background in the 7 TeV SRs is negligible.

A Top CR was defined in order to derive the normalization of the top-quark processes that are dominated by $t\bar{t}$. This region was defined by requiring at least one jet, with at least one of them b-tagged. The population of events in this region was enhanced by dropping the maximum $m_{\ell^+\ell^-}$ and $\Delta R_{\ell_0\ell_1}$ selections of the SRs. A single NF was derived for and applied to the total top-quark contribution in each of the SRs. This treatment was justified since the ratio between the contributions from $t\bar{t}$ and tW or $t\bar{t}W$ were found to be compatible amongst all of the CRs and SRs.

Note that due to the low cross section of the WWW process, it was difficult to define a CR targeting this background that would be statistically meaningful. Therefore, the normalization for the WWW background was taken directly from MC simulation.

5.4.1 Normalization factors

The background NFs were simultaneously extracted through the statistical fit described in section 5.1.3. This was done separately for the $\sqrt{s} = 7$ and 8 TeV samples. The measured NFs are presented in table 5.8.

Process	NF for $\sqrt{s}$ = 8 TeV	NF for $\sqrt{s}$ = 7 TeV
$WZ/W\gamma^*$	$1.08\ ^{+0.08}_{-0.06}$	$1.02\ ^{+0.12}_{-0.11}$
ZZ^*	$1.28\ ^{+0.22}_{-0.20}$	$1.78\ ^{+0.51}_{-0.42}$
$Z\gamma$	$0.62\ ^{+0.15}_{-0.14}$	$0.45\ ^{+0.09}_{-0.09}$
Z+jets, μ-fake	$0.80\ ^{+0.68}_{-0.53}$	—
Z+jets, e-fake	$0.33\ ^{+0.12}_{-0.11}$	$0.68\ ^{+0.16}_{-0.15}$
Top-quark	$1.36\ ^{+0.34}_{-0.30}$	$1.25\ ^{+0.66}_{-0.52}$

Table 5.8 The measured background NFs in the $\sqrt{s}$ = 7 and 8 TeV samples. The uncertainties on the NFs include both the statistical and systematic components.

Not all of the CRs had a high purity. In particular, the Z+jets CR contained contributions from $WZ/W\gamma^*$ and ZZ^* that were of a similar size to the targeted Z+jets process. Since the NFs were extracted simultaneously in the statistical fit, such cross-contamination between CRs introduced correlations between the NFs which were properly taken into account in the fit. So, for example, the NFs for the Z+jets e-fake and μ-fake processes were not only constrained by the Z+jets CR but also, in part, by both the ZZ CR and WZ CR.

The measured NFs shown in table 5.8 are generally consistent between the $\sqrt{s}$ = 7 and 8 TeV samples within the uncertainties. Some minor tension is present for the Z+jets e-fake NF, possibly indicating that there was a difference in the electron misidentified rate between the 7 and 8 TeV samples. This would not be unexpected since the 7 and 8 TeV samples had different pileup conditions, as well as differences in the offline reconstruction and selections for electrons as mentioned in section 5.3.1.

5.4.2 Composition of control regions

The number of observed events, the total number of estimated events, and the background and signal composition in the CRs are shown in table 5.9a for the $\sqrt{s}$ = 8 TeV samples and in table 5.9b for the 7 TeV samples. The $m_{\ell_0\ell_2}$ distributions in each of the 8 TeV CRs are shown in figures 5.5-5.7. Additional CR plots in both the 8 and 7 TeV samples can be found in appendix C. In these tables and figures, the measured NFs from table 5.8 are applied to the appropriate backgrounds. The background categorization scheme differs from the one presented earlier in table 5.6. The backgrounds that

are normalized via NFs are shown separately, with the other backgrounds grouped together in a single category (Others).

Good agreement between the observed data and the total background estimation is achieved in all CRs, and there is no significant signal leakage within them. Combined with the good agreement in the SR distributions shown in figures 5.3 and 5.4, as well as the plots in appendices A and C, this establishes confidence in the background estimation methods.

(a) $\sqrt{s} = 8$ TeV samples

	***WZ* CR**	***ZZ* CR**	***Z*+jets CR**	**Top CR**	***Zγ* CR**
Observed	578	60	251	55	156
Estimated	576 ± 63	60 ± 10	249 ± 46	55 ± 12	155 ± 31
Composition [%]					
$WZ/W\gamma^*$	89 ± 2	5.5 ± 1.0	26 ± 4	20 ± 4	1.7 ± 0.31
ZZ^*	6.7 ± 1.2	90 ± 2	38 ± 5	3.6 ± 1.2	47 ± 6
$Z\gamma$	0.54 ± 0.17	0.62 ± 0.50	5.5 ± 1.5	2.4 ± 0.94	43 ± 7
Z+jets	1.1 ± 0.51	2.1 ± 1.5	29 ± 7	5.5 ± 3.3	8.3 ± 3.4
Top-quark	0.66 ± 0.18	0.27 ± 0.13	0.081 ± 0.034	64 ± 6	0.13 ± 0.063
Others	0.80 ± 0.16	1.2 ± 0.20	0.87 ± 0.13	3.6 ± 0.64	0.33 ± 0.061
Signal	0.93 ± 0.16	0.26 ± 0.11	0.37 ± 0.092	0.52 ± 0.13	0.052 ± 0.011

(b) $\sqrt{s} = 7$ TeV samples

	***WZ* CR**	***ZZ* CR**	***Z*+jets CR**	**Top CR**	***Zγ* CR**
Observed	101	18	68	9	123
Estimated	101 ± 16	18 ± 5	67 ± 15	8.3 ± 4.1	123 ± 26
Composition [%]					
$WZ/W\gamma^*$	88 ± 3	3.1 ± 1.1	6.9 ± 1.4	14 ± 5	0.61 ± 0.15
ZZ^*	7.4 ± 2.1	93 ± 2	26 ± 6	4.2 ± 2.5	32 ± 7
$Z\gamma$	1.8 ± 0.82	0.51 ± 0.42	48 ± 7	6.2 ± 4.2	59 ± 7
Z+jets	1.5 ± 0.82	3.0 ± 1.4	19 ± 5	0.40 ± 2.2	8.2 ± 2.1
Top-quark	0.71 ± 0.44	0.013 ± 0.20	0.073 ± 0.13	71 ± 10	0.032 ± 0.042
Others	0.56 ± 0.11	0.44 ± 0.11	0.12 ± 0.021	4.2 ± 1.4	0.053 ± 0.17
Signal	0.53 ± 0.080	0.11 ± 0.030	0.044 ± 0.0081	0.41 ± 0.17	0.015 ± 0.0027

Table 5.9 The number of observed events, the total number of estimated events, and the background and signal composition (in %) in the CRs for the (a) $\sqrt{s} = 8$ TeV and (b) 7 TeV samples. The background NFs are applied. The uncertainties include both the statistical and systematic components.

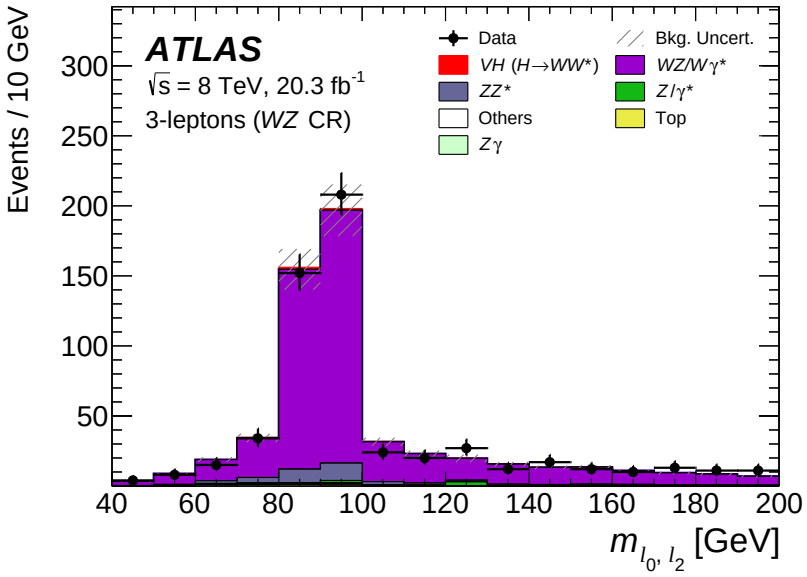

(a)

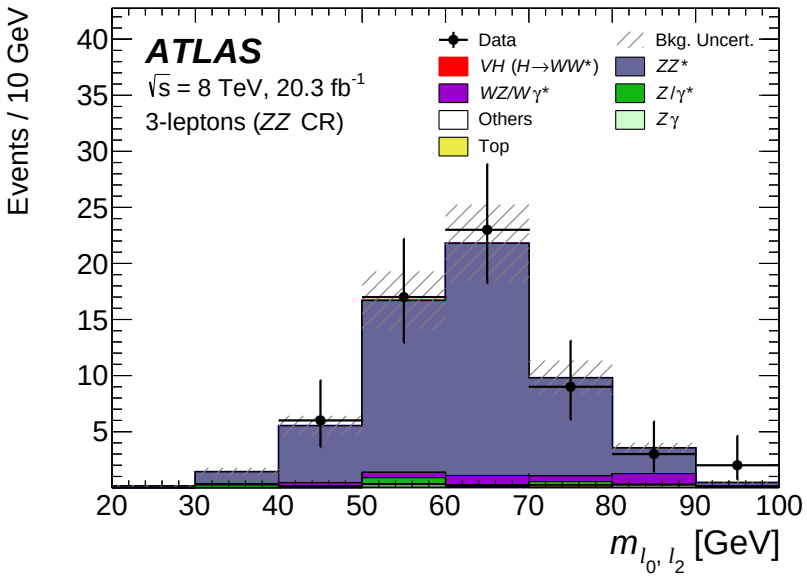

(b)

Figure 5.5 Distributions of $m_{\ell_0\ell_2}$ for the $\sqrt{s} = 8$ TeV samples in the (a) WZ CR and (b) ZZ CR. The background NFs are applied. The total uncertainty on the total background estimate is represented by the hatched area, and includes both the statistical and systematic components. The signal (red) is stacked on top of the total background estimation.

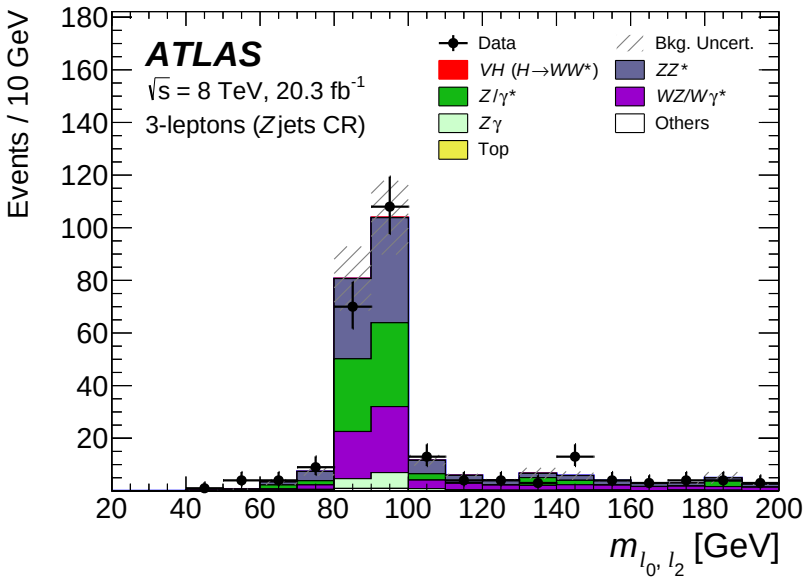

(a)

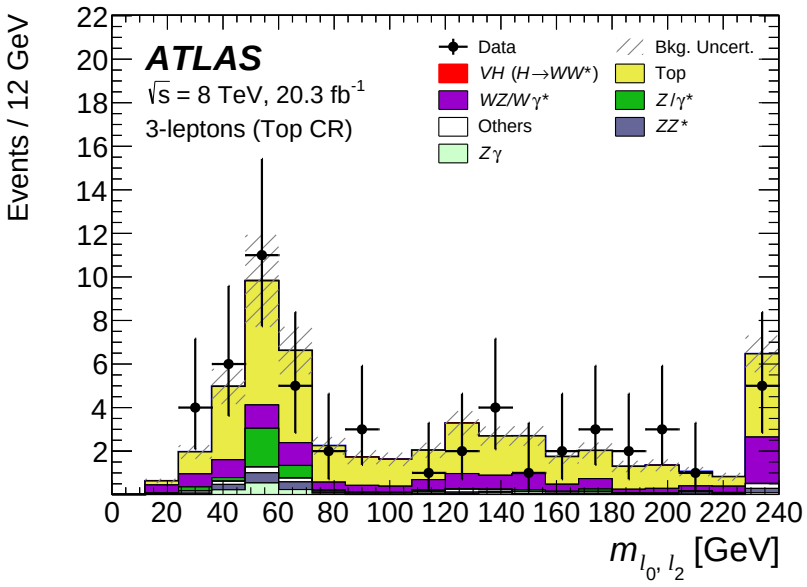

(b)

Figure 5.6 Distributions of $m_{\ell_0\ell_2}$ for the $\sqrt{s}$ = 8 TeV sample in the (a) Z+jets CR and (b) Top CR. The plotting scheme follows the one described in the caption of figure 5.5.

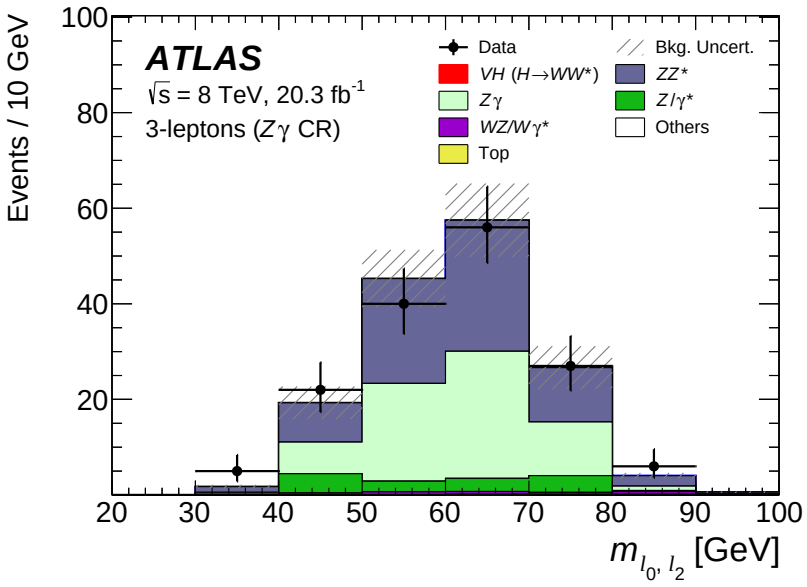

Figure 5.7 Distribution of $m_{\ell_0\ell_2}$ for the $\sqrt{s}$ = 8 TeV samples in the $Z\gamma$ CR. The plotting scheme follows the one described in the caption of figure 5.5.

5.5 Systematic Uncertainties

This analysis took into account the effects of both theoretical and experimental sources of systematic uncertainty on the estimated signal and background event yields. Recall that a general definition of both kinds of uncertainty was provided in section 5.1.3, as well as a description of how the uncertainties were included into the statistical fit used to extract the observed signal strength and background NFs.

A summary of the impact of the systematic uncertainties on the estimated event yields in the SRs is provided in table 5.10. Each field in this table represents a certain category of systematic uncertainty, and the details of how they were estimated will be provided in this section. The sources of theoretical uncertainty will be described first in section 5.5.1, followed by the experimental uncertainties in section 5.5.2.

5.5.1 Theoretical uncertainties

The theoretical uncertainties on the *WH* production cross section and the Higgs decay branching ratio were evaluated by following the recommendations of the LHC Higgs cross section working group [20, 132, 133]. The cross section uncertainties included those concerning the QCD scales, the PDF model used and the value of α_S.

In addition to the uncertainties associated to the signal sample normalization that were just mentioned, uncertainties for the acceptance of the signal process in the analysis regions were also considered. These are included in the "Acceptance" field in table 5.10a, and were the main source of theoretical uncertainty on the signal process. The leading components of this uncertainty were the missing higher-order QCD contributions in Pythia and the PS uncertainty. The first component amounted to a 7% uncertainty, and was evaluated by comparing the nominal Pythia prediction to a sample that was generated using the MiNLO approach [144] interfaced with Pythia. The second component was evaluated by comparing the previously mentioned MiNLO+Pythia sample to another MiNLO sample interfaced with Herwig, and accounted for a further 7% uncertainty. The "NLO EW corrections" field refers to the uncertainties associated to the LO to NLO EW corrections that were computed using Hawk [136].

The QCD scale uncertainties for the background processes were evaluated by independently varying the scales up and down by a factor of two using MCFM [141]. For the dominant $WZ/W\gamma^*$ background in the 3SF and 1SFOS SRs, these uncertainties ranged from 3-6% and were evaluated in each bin of the BDT score distribution that entered the statistical fit. In order to estimate the PDF uncertainties for the background processes, the PDF4LHC recipe [145] was followed and involved taking the envelope of the variations when using the MSTW [146], CT10 or NNPDF [147] PDF sets. The "*WWW* NLO corrections" field in table 5.10b refers to the 33% uncertainty on the LO to NLO corrections for the *WWW* background estimated using VBFNLO [142]. Since this background makes its most significant contribution in the 0SFOS SR, this uncertainty was evaluated for each bin of the $\Delta R_{\ell_0,\ell_1}$ distribution that entered the statistical fit and ranged from 1-6%.

The uncertainties for the dominant $WZ/W\gamma^*$ background associated to the modeling of the UE, PS and the matching of the hard scatter process to the PS are included in the "$WZ/W\gamma^*$ modeling" field in table 5.10b. These uncertainties were evaluated by comparing the predictions of the nominal Powheg+Pythia samples to those of alternative samples using MC@NLO interfaced with Herwig [115].

5.5.2 Experimental uncertainties

Some of the dominant sources of experimental uncertainties in this analysis are those associated to the offline JES calibration and jet energy resolution (JER). They are included in the "Jet" fields in tables 5.10a and 5.10b, and were estimated from a combination of simulation, test-beam data, and in-situ measurements [67, 148]. These uncertainties contained contributions for the jet flavour composition, η-intercalibration,

single particle response, calorimeter response to different jet flavours, and pile-up. The per-jet uncertainties associated to the JES and JER ranged from 1-7% and 2-40%, respectively, depending on the value of the jet p_T and η.

The "b-tagging" fields in tables 5.10a and 5.10b include uncertainties on the b-jet identification efficiency of the MV1 algorithm, as well as those associated to the misidentification rates for light-quark or gluon initiated jets [80, 149]. The per-jet identification efficiency uncertainties ranged from 1-8% depending on the p_T and η of the b-tagged jet, while the misidentification rate uncertainties ranged from 6-19%.

The uncertainties associated to the offline reconstruction efficiency, identification efficiency, energy scales and isolation efficiency for muons and electrons are included in the "Muon" and "Electron" fields, respectively. The trigger-level efficiency uncertainties are included in the "Trigger" fields. These offline and trigger-level uncertainties were estimated using $J/\psi\rightarrow\ell\ell$, $Z\rightarrow\ell\ell$ and $W\rightarrow\ell\nu$ decays [63, 71]. Each individual component that contributes to the Muon, Electron and Trigger fields in the tables had a per-lepton uncertainty of order of 1% or smaller.

The systematic variations associated to the energy scales and resolution of jets and leptons were propagated to the offline E_T^{miss} reconstruction algorithms, and the resulting variations are included in the previously mentioned Jet, Muon and Electron fields. Recall from section 3.3.1 that the evaluation of E_T^{miss} not only included the offline reconstructed objects that entered the analysis, but also any remaining jets and clusters of calorimeter cells in the events. The uncertainties associated to including these remaining soft objects into E_T^{miss} [86, 89, 90] enter the "E_T^{miss} soft term" fields.

Although relatively rare, it is possible for the ATLAS offline reconstruction algorithms to mis-assign the electric charge of a lepton. Such an occurrence is called a charge-flip, and the dominant charge-flip contribution in this analysis accounts for about 30% of the $WZ/W\gamma^*$ background in the 0SFOS SR[6]. This background can enter this SR when the electron from $Z/\gamma^*\rightarrow e^+e^-$ decay emits a hard bremsstrahlung photon that undergoes asymmetric conversion into an electron-position pair. If most of the energy is imparted to the positron, then the wrong charge can be assigned to the initial electron during offline reconstruction. To account for any potential mismodeling of the charge-flip effect in MC simulation, a "charge mis-assignment" uncertainty was evaluated by comparing the number of opposite-sign and same-sign electron pairs under the Z-boson mass peak between data and simulation. The resulting 16% uncertainty was assigned to the $WZ/W\gamma^*$ background in the 0SFOS SR.

[6]Note that the remaining $WZ/W\gamma^*$ events in the 0SFOS SR originate from $Z/\gamma^*\rightarrow\tau\tau\rightarrow e\nu_\tau\mu\nu_\tau$ decays.

The uncertainty associated to the pile-up reweighting procedure described in section 3.3.3 is included in the"Pile-up" fields in tables 5.10a and 5.10b. The "Luminosity" fields include the 2.8% (1.8%) uncertainties on the size of the $\sqrt{s}$ = 8 (7) TeV [150] data samples. This uncertainty is not applied to the backgrounds normalized via NFs.

(a) Impact of systematic uncertainties on the signal [%]

		3SF SR	1SFOS SR	0SFOS SR
Theoretical uncertainties	QCD scale	1.2	1.0	1.0
	PDF and α_S	2.1	2.2	2.2
	Higgs decay BR	4.2	4.2	4.2
	Acceptance	9.9	9.9	9.9
	NLO EW corrections	1.9	1.9	1.9
Experimental uncertainties	Jet	2.5	2.5	2.9
	E_T^{miss} soft term	—	—	—
	Electron	1.6	2.2	2.2
	Muon	2.2	1.8	1.7
	Trigger	0.4	0.3	0.3
	b-tagging	0.9	0.8	0.8
	Pile-up	2.0	1.4	0.8
	Luminosity	2.8	2.8	2.8

(b) Impact of systematic uncertainties on the total background [%]

		3SF SR	1SFOS SR	0SFOS SR
Theoretical uncertainties	QCD scale	1.0	0.9	—
	PDF and α_S	0.3	0.3	1.6
	WWW NLO corrections	1.1	1.9	0.5
	$WZ/W\gamma^*$ modeling	7.0	6.6	—
Experimental uncertainties	Jet	3.2	1.8	4.1
	E_T^{miss} soft term	1.8	1.9	0.5
	Electron	1.0	0.4	1.1
	Muon	0.4	0.7	0.2
	Trigger	0.2	—	—
	b-tagging	0.6	0.8	2.6
	Charge mis-assignment	—	—	1.4
	Pile-up	1.4	0.3	1.2
	Luminosity	0.1	0.2	0.7

Table 5.10 The impact of the systematic uncertainties (in %) on the estimated SR event yields for (a) the signal and (b) the total background. Any uncertainties that either do not apply or are negligible are indicated by a dash. The values in this table are obtained via the statistical fit.

5.6 Results

The number of observed, estimated background and predicted signal events in the SRs, after applying all of the selections listed in table 5.5, are shown in tables 5.11a and 5.11b for the $\sqrt{s}$ = 8 and 7 TeV samples, respectively. The leading backgrounds in the final 3SF and 1SFOS SRs are $WZ/W\gamma^*$ and ZZ^*. They account for about 80% of the total background yield in these SRs, 65% from $WZ/W\gamma^*$ and 15% from ZZ^*, with the remaining background fraction shared between the $Z\gamma$, Z+jets, WWW and top-quark processes. The 0SFOS SR contains a total background yield that is about eight times lower then the previously mentioned SRs, with the background split almost equally between top-quark production, $WZ/W\gamma^*$ and WWW. In addition to having significantly lower background rates, the 0SFOS SR contains about 40% of the total signal yield the enters the final SRs. This demonstrates how the 0SFOS SR drives the sensitivity of the analysis.

A small excess in the number of observed events with respect to the estimated total background event yield is present in the 1SFOS and 0SFOS SRs for the $\sqrt{s}$ = 8 TeV samples. However, this excess is consistent with both the background-only and background-plus-signal event yields within the uncertainties.

As mentioned in section 5.1.2, the shapes of certain variables were used to provide the final separation between signal and backgrounds in the SRs. In the 0SFOS SR the shape of $\Delta R_{\ell_0\ell_1}$ was used, while in the 3SF and 1SFOS SRs it was the BDT score from the BDT analysis. Recall that the value of $\Delta R_{\ell_0\ell_1}$ tends to be smaller for the signal process due to the $H\rightarrow WW^*\rightarrow \ell\nu\ell\nu$ topology, whereas a high BDT score indicates a more signal-like event. The BDT analysis is briefly described below, with a more complete description available in appendix A.

The main purpose of the BDT analysis was to use a multivariate classifier, the BDT score, to distinguish between the signal and the dominant $WZ/W\gamma^*$ and ZZ^* backgrounds in the 3SF and 1SFOS SRs. The BDT was trained using the signal, $WZ/W\gamma^*$ and ZZ^* MC samples described in section 5.2.2, and its parameters were chosen to ensure robustness against statistical fluctuations in the training samples. Nine discriminating variables were used to train the BDT including: $p_{\mathrm{T}}^{\ell_0}$, $p_{\mathrm{T}}^{\ell_1}$, $p_{\mathrm{T}}^{\ell_2}$, the magnitude of their vectorial sum ($|\Sigma \mathbf{p}_{\mathrm{T}}{}^{\mathrm{lep}}|$), $m_{\ell_0\ell_1}$, $m_{\ell_0\ell_2}$, E_T^{miss}, p_T^{miss} and $\Delta R_{\ell_0\ell_1}$.

The distributions of $\Delta R_{\ell_0\ell_1}$ in the final 0SFOS SR and the BDT score in the final 3SF and 1SFOS SRs are shown in figures 5.8-5.10. The binning shown in these plots is the same as those used in the statistical fit. In each distribution, the observed data is in

agreement with both the background-only and background-plus-signal expectations within the uncertainties.

(a) $\sqrt{s} = 8$ TeV samples

	3SF SR	**1SFOS SR**	**0SFOS SR**
Signal	0.73 ± 0.10	1.6 ± 0.24	1.4 ± 0.21
V	0.22 ± 0.16	1.9 ± 0.63	0.37 ± 0.15
VV	19 ± 3	28 ± 4	4.7 ± 0.60
VVV	0.81 ± 0.33	2.2 ± 0.72	2.9 ± 0.34
Top-quark	0.91 ± 0.26	2.4 ± 0.62	3.7 ± 0.94
Other Higgs	0.13 ± 0.019	0.24 ± 0.029	0.25 ± 0.035
Total background	22 ± 4	34 ± 6	12 ± 2
Observed	22	38	14

(b) $\sqrt{s} = 7$ TeV samples

	3SF SR	**1SFOS SR**	**0SFOS SR**
Signal	0.13 ± 0.013	0.33 ± 0.034	0.29 ± 0.031
V	0.36 ± 0.30	0.59 ± 0.34	0.36 ± 0.22
VV	4.1 ± 0.63	5.7 ± 1.0	1.3 ± 0.22
VVV	0.082 ± 0.028	0.21 ± 0.071	0.34 ± 0.031
Top-quark	0.12 ± 0.14	0.43 ± 0.32	0.44 ± 0.29
Other Higgs	0.021 ± 0.0038	0.052 ± 0.0074	0.076 ± 0.011
Total background	4.6 ± 1.1	7.0 ± 1.9	2.5 ± 0.73
Observed	5	6	2

Table 5.11 The number of observed, estimated background and predicted signal events in the final SRs for (a) the $\sqrt{s} = 8$ TeV samples and (b) the 7 TeV samples. The background NFs are applied. The uncertainties include both the statistical and systematic components.

5.6.1 Signal strength measurement

The $\sqrt{s} = 7$ and 8 TeV samples were analyzed separately and then combined in the statistical fit in order to extract the observed signal strength for the signal process with $m_H = 125$ GeV. The small contributions for other non-signal Higgs boson processes, listed in the Other Higgs category in table 5.4, were treated as background with their relative strengths fixed to the SM values.

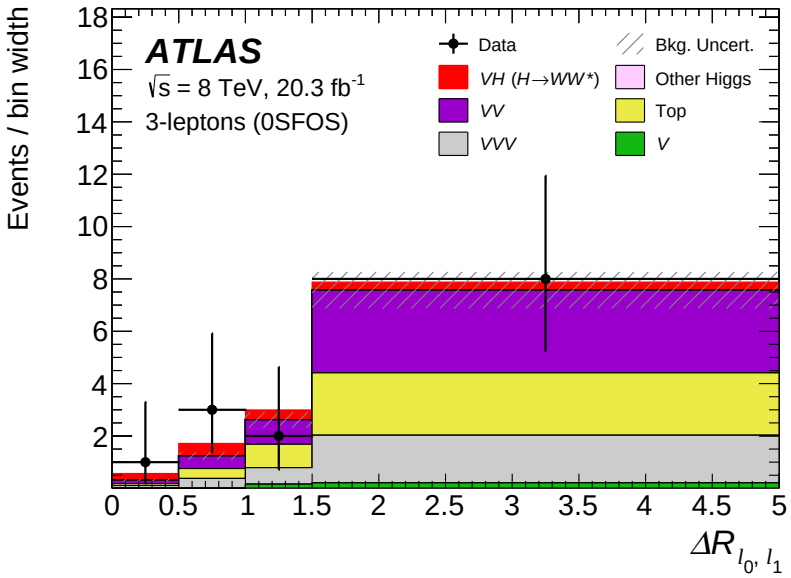

(a)

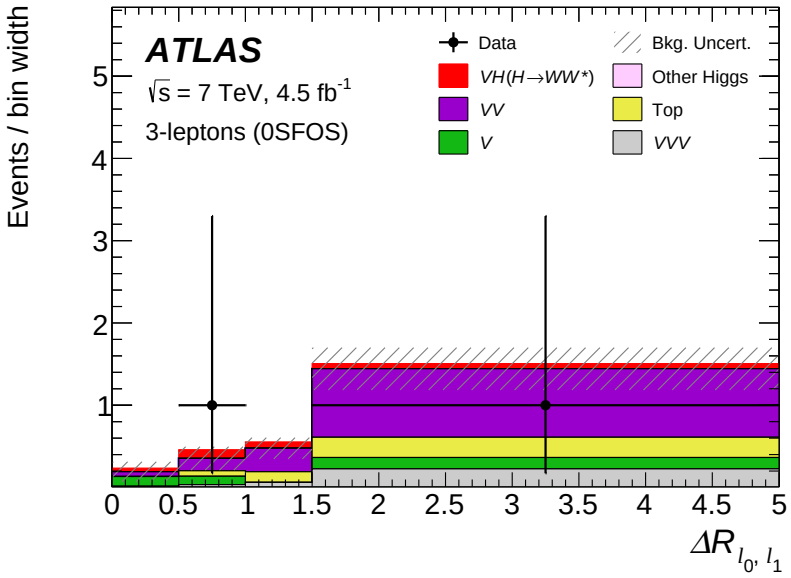

(b)

Figure 5.8 Distributions of $\Delta R_{\ell_0\ell_1}$ in the 0SFOS SR for the (a) $\sqrt{s}$ = 8 TeV samples and (b) $\sqrt{s}$ = 7 TeV samples. All of the selections listed in table 5.5 are applied. The data (points) are compared to the background-plus-signal expectations (stacked filled histograms, with the signal in red). The background NFs are applied. The hatched area on the histogram represents the total uncertainty, including both the statistical and systematic components.

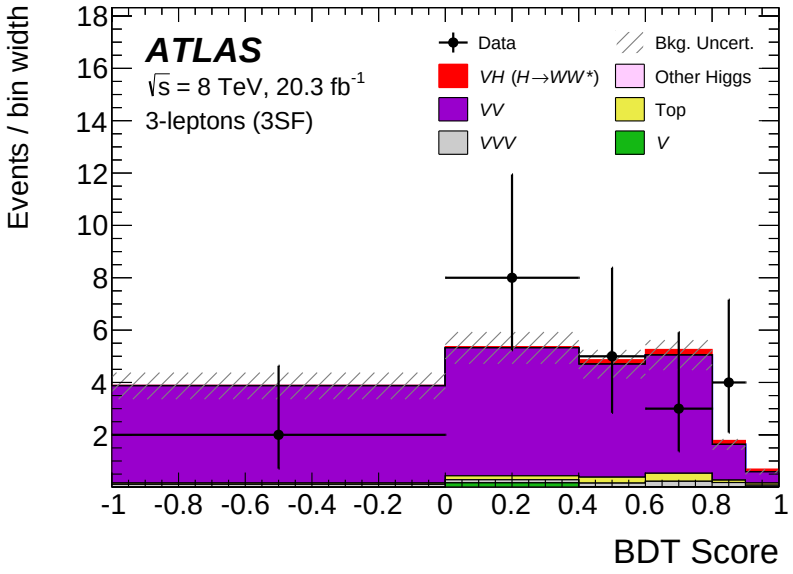

(a)

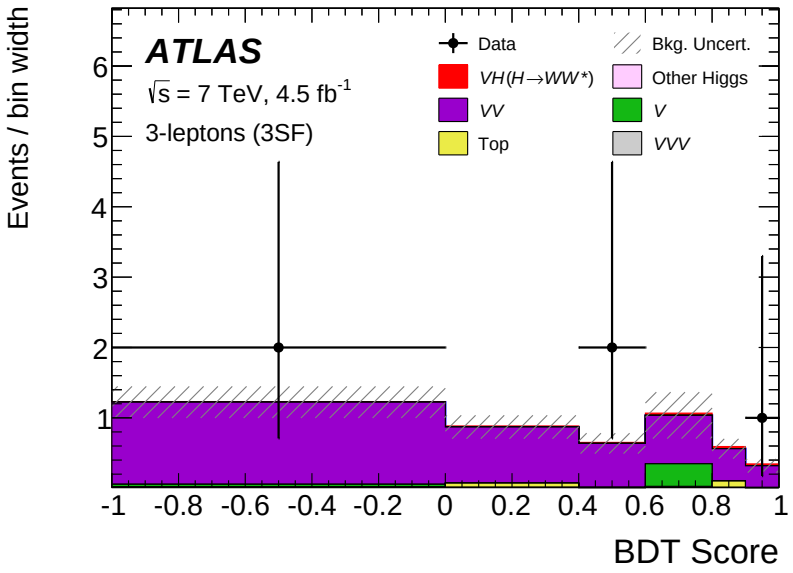

(b)

Figure 5.9 Distributions of the BDT score in the 3SF SR for the (a) $\sqrt{s}$ = 8 TeV samples and (b) $\sqrt{s}$ = 7 TeV samples. All of the selections listed in table 5.5 are applied. The plotting scheme follows the one described in the caption of figure 5.8.

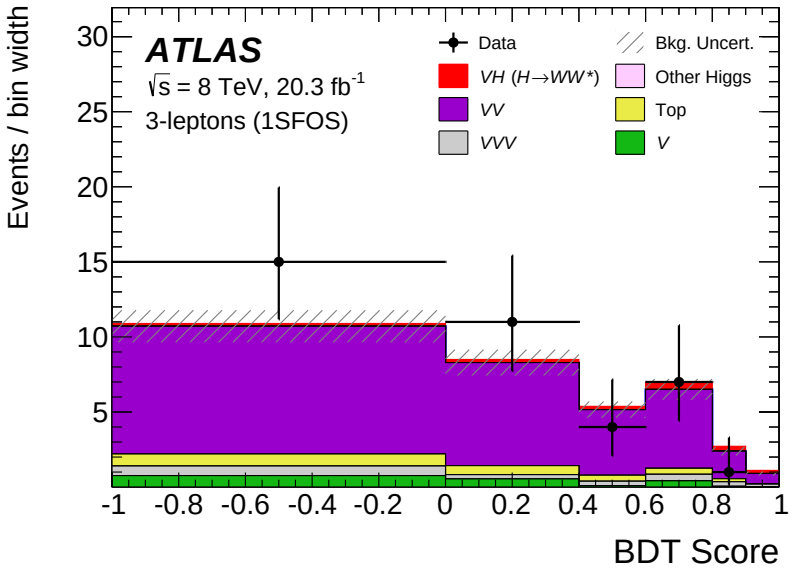

(a)

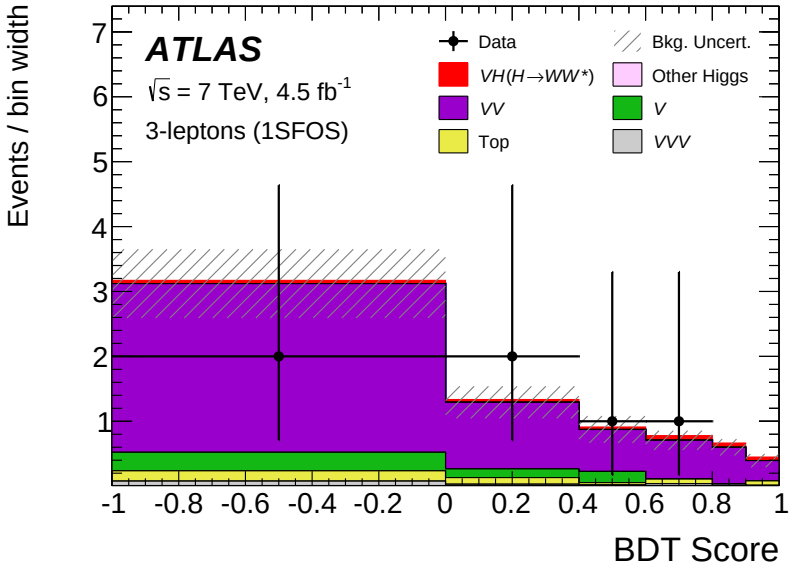

(b)

Figure 5.10 Distributions of the BDT score in the 1SFOS SR for the (a) $\sqrt{s} = 8$ TeV samples and (b) $\sqrt{s} = 7$ TeV samples. All of the selections listed in table 5.5 are applied. The plotting scheme follows the one described in the caption of figure 5.8.

Source	$\Delta\mu_{obs}/\mu_{obs}$ [%]
$WZ/W\gamma^*$ modeling	+24 / -17
JER	+14 / -9
b-tagging	+11 / -8
JES in-situ method	+9 / -7
WWW NLO corrections	+8 / -7
JES η intercalibration	+8 / -6
JES flavour composition	+7 / -5
Signal acceptance	+7 / -4
Background PDF and α_s	+7 / -4
Pile-up	+5 / -3

Table 5.12 List of the ten leading sources of systematic uncertainty on the μ_{obs} measurement. The impact of the uncertainties are given as a percentage of the observed value.

Following the statistical procedure described in section 5.1.3, the observed signal strength for the signal process was measured to be:

$$\mu_{obs}^{7+8\text{ TeV}} = \frac{\sigma_{obs}^{7+8\text{ TeV}}}{\sigma_{SM}} = 0.72\,^{+1.2}_{-1.1}\,(\text{stat.})\,^{+0.4}_{-0.3}\,(\text{sys.}) \tag{5.4}$$

This is consistent with the SM prediction of unity within the uncertainties. The leading sources of systematic uncertainty on the μ_{obs} measurement are shown in table 5.12, with their descriptions provided in section 5.5. The local significance of the overall excess observed in the SRs with respect to the background-only hypothesis is 0.66 standard deviations (σ), where 0.79σ was expected in the presence of the signal.

An event display for a candidate signal event entering the 0SFOS SR in the $\sqrt{s}$ = 8 TeV data sample is shown in figure 5.11. This event is typical of one originating from the signal process since it has three high-p_T leptons with a total electric charge of +1, large E_T^{miss}, and a small angular separation between two of the leptons (the $H\rightarrow WW^*\rightarrow \ell\nu\ell\nu$ candidate leptons).

Several other searches for the Higgs boson in the $H\rightarrow WW^*$ decay channel were performed by the ATLAS Collaboration using the $\sqrt{s}$ = 7 and 8 TeV data samples. These included analyses targeting the ggF, VBF and ZH production modes. They were all combined with the analysis presented in this chapter to perform additional signal strength measurements, as well as measurements of the Higgs boson coupling strengths. The main results from this combination are provided in appendix B.

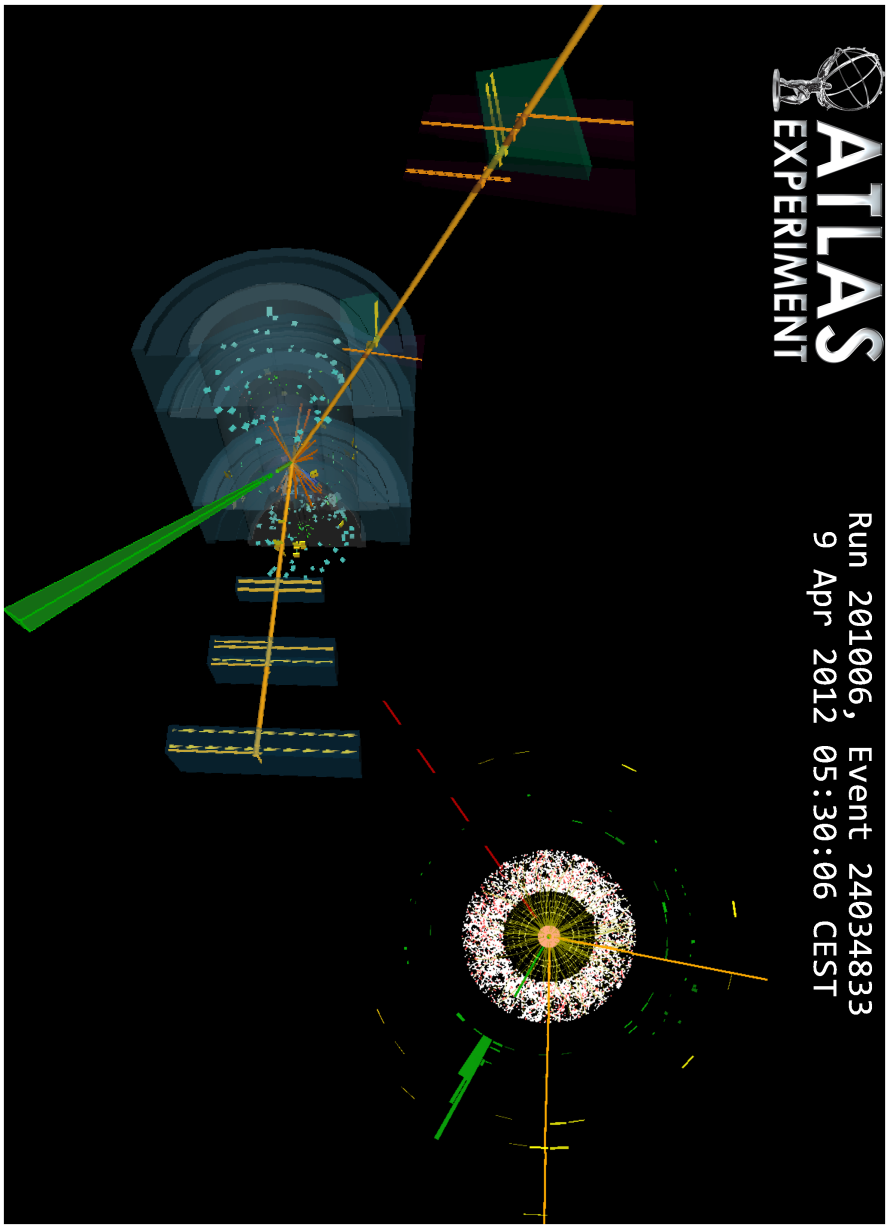

Figure 5.11 Event display for an observed collision event at $\sqrt{s}$ = 8 TeV that entered the final 0SFOS SR . The view from the side of the ATLAS detector is shown on the bottom left, with the transverse plane shown in the top right. This event contained one electron (green) and two muons (orange), and a large E_T^{miss} represented by the dashed red line in the transverse plane. The offline reconstructed p_T values for the three leptons were 23.5 GeV (μ^+), 25.2 GeV (μ^+) and 88.5 GeV (e^-).

5.7 Analysis using an Early $\sqrt{s}$ = 13 TeV Dataset

In late 2015 the LHC began colliding protons at an increased energy of $\sqrt{s}$ = 13 TeV. In this section, a search for the WH production of the Higgs boson with sequential $WH \rightarrow WWW^* \rightarrow \ell\nu\ell\nu\ell\nu$ decay is presented using an early 5.8 fb^{-1} ATLAS data sample at $\sqrt{s}$ = 13 TeV. The analysis strategy followed closely the one that was previously developed for the $\sqrt{s}$ = 7 and 8 TeV analysis. Considering this, the contents of this section will focus more on what changed with respect to what has already been presented in this chapter.

The increase from $\sqrt{s}$ = 8 to 13 TeV provided a substantial boost to the cross section of the WH production mode. As shown in table 5.13 the production cross section increased by a factor of approximately two. This opens up new possibilities for directly observing the WH production mode with $H \rightarrow WW^*$ decay, approaching the sensitivity of the $\sqrt{s}$ = 7 and 8 TeV analysis with only around 10-15 fb^{-1} of 13 TeV data.

$\sqrt{s}$ [TeV]	σ^{WH} [pb]	QCD scale [%]	PDF + α_s [%]
8	0.703	$^{+0.6}_{-0.9}$	±2.0
13	1.373	$^{+0.5}_{-0.7}$	±1.9

Table 5.13 The WH production cross sections for a Higgs boson of mass 125 GeV, together with the corresponding theoretical uncertainties [39].

The most prominent backgrounds were the same as for $\sqrt{s}$ = 7 and 8 TeV analysis described in section 5.1.1. However, the relative contributions of these backgrounds changed at 13 TeV. To help illustrate this, a summary of the cross section measurements from ATLAS for some of the main SM processes are summarized in figure 5.12. Like the signal process, the cross sections for the $WZ/W\gamma^*$, WWW, ZZ^*, $Z\gamma$ and Z+jets backgrounds increased by a factor of approximately two. A more substantial boost occurred for the top-quark background, coming mainly from $t\bar{t}$, which increased by a factor of almost four. This is due to the fact that the parton luminosity for gluon-gluon initiated processes, such as $t\bar{t}$, is higher at larger $\sqrt{s}$ as shown in figure 5.13. In this way, top-quark production became a more significant component of the total background in the $\sqrt{s}$ = 13 TeV analysis.

This section is divided into six subsections. The data and MC samples used in the $\sqrt{s}$ = 13 TeV analysis are summarized in section 5.7.1, with details on the event reconstruction provided in section 5.7.2. Section 5.7.3 describes the SR selection criteria, followed by

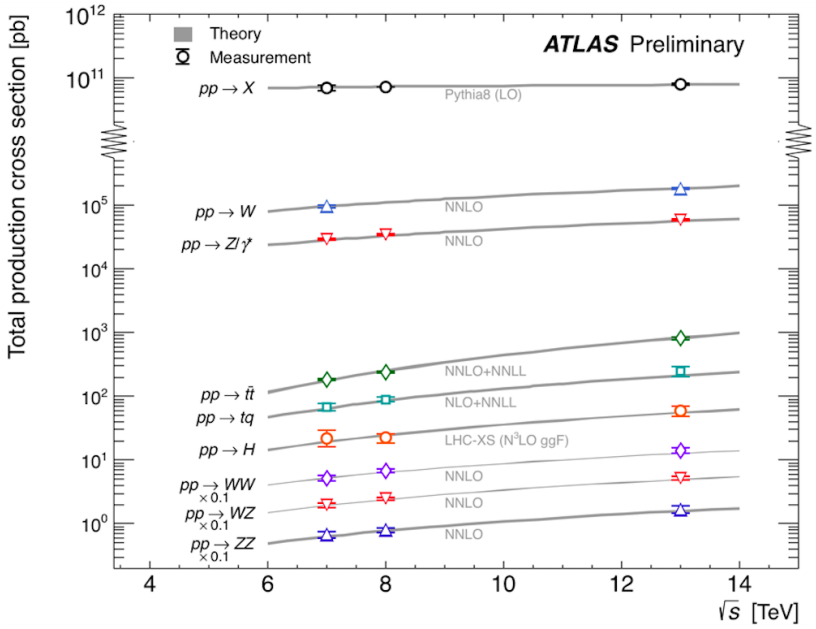

Figure 5.12 Total production cross section measurements performed by ATLAS for a few selected processes from $\sqrt{s}$ = 7 to 13 TeV [151].

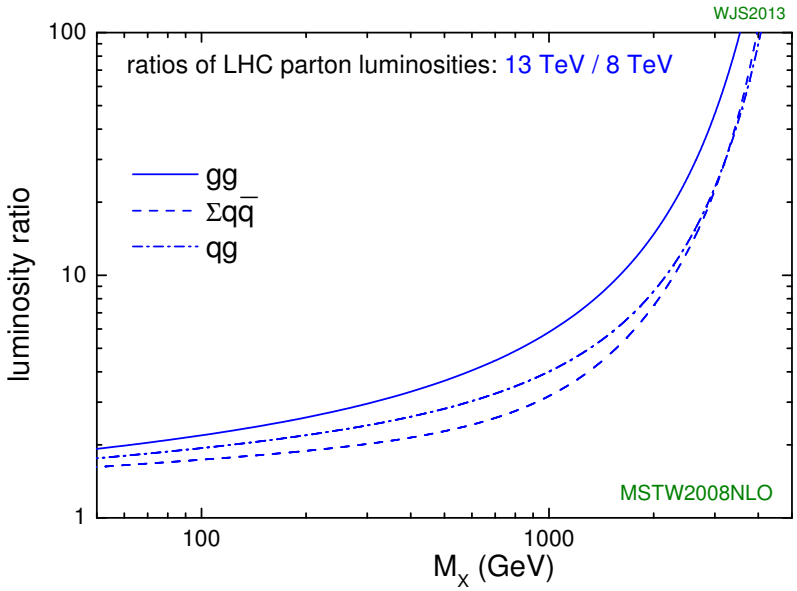

Figure 5.13 Ratio of parton luminosities at $\sqrt{s}$ = 8 TeV compared to 13 TeV [152] at the LHC, calculated using the MSTW PDFs [146]. The ratios are shown separately for gluon-gluon, quark-gluon and the sum of all quark-antiquark initiated production of a generic particle of mass M_X.

a description of the background estimation method in section 5.7.4. The systematic uncertainties are described in section 5.7.5 and, finally, the results of the $\sqrt{s}$ = 13 TeV analysis are presented in section 5.7.6.

5.7.1 Data and MC samples

The $\sqrt{s}$ = 13 TeV ATLAS collision data used in this analysis was recorded during 2015-2016 using the single lepton triggers summarized in table 5.14. Additional information for these triggers was provided in section 3.3.2. Overall quality criteria was applied to the data, and the total data sample corresponds to an integrated luminosity of 5.8 fb^{-1}. As described in section 3.1.3, the average pile-up in this data sample was 21 and 14 for the 2016 and 2015 components, respectively.

Trigger type	2016 data sample	2015 data sample
Single e	24Ti or 60M or 120L	24M or 60M or 120L
Single μ	24i or 50	20i or 50

Table 5.14 Summary of the HLT requirements of the single lepton triggers used to record the $\sqrt{s}$ = 13 TeV data sample. The numbers indicate the minimum lepton p_T requirements (in GeV), and the letter "i" indicates an isolation requirement. The letters "L", "M" and "T" indicates a Loose, Medium or Tight electron identification criteria, respectively. The "or" is logical.

The generators and the precision of the cross section calculations used for the MC samples are summarized in table 5.15. Details regarding the simulation of the signal and main background processes are provided below. A more complete description of the MC samples can be found in ref. [4].

The signal process was generated with Powheg [153–155] interfaced with Pythia [102] using the MiNLO approach [144] and CTEQ6L1 PDF set [118]. The Higgs boson mass was set to 125 GeV in the generation. Powheg + Pythia [101] and the CTEQ6L1 PDF set was also used for the $t\bar{t}$ and tW samples. The $WZ/W\gamma^*$, ZZ^*, $Z\gamma$ and WWW processes were simulated using Sherpa [129] at all stages of the simulation chain, and used the CT10 PDF set [119]. The production of Z+jets and $t\bar{t}W$ was modeled using MadGraph [156] interfaced with Pythia and the CTEQ6L1 PDF set.

		Generator	Calculation order of cross section
Signal	WH ($H\rightarrow WW^*$)	Powheg + Pythia8	NNLO QCD + NLO EW
Major Backgrounds	$WZ/W\gamma^*$	Sherpa	NLO
	WWW	Sherpa	NLO
	$q\bar{q}/qg \rightarrow ZZ^*$	Sherpa	NLO
	$Z\gamma$	Sherpa	LO
	Z+jets (with HF)	MadGraph + Pythia8	LO
	$t\bar{t}$	Powheg + Pythia6	NNLO+NNLL
	tW	Powheg + Pythia6	NLO
	$t\bar{t}W$	MadGraph + Pythia8	LO
Minor Backgrounds	$gg \rightarrow ZZ^*$, WW	Sherpa	NLO
	$q\bar{q}/qg \rightarrow WW$	Sherpa	NLO
	WWZ, ZZW, ZZZ	Sherpa	NLO
	$W\gamma$	Sherpa	LO
	W+jets	Powheg + Pythia8	NLO
	tZ, $t\bar{t}Z$	MadGraph	LO
	tb, tqb	Powheg + Pythia6	NLO
Other Higgs	WH ($H \rightarrow \tau\tau$)	Powheg + Pythia8	NNLO QCD + NLO EW
	ZH ($H\rightarrow WW^*$, $H \rightarrow \tau\tau$)	Powheg + Pythia8	NNLO QCD + NLO EW
	ggF ($H\rightarrow WW^*$)	Powheg + Pythia8	NNLO QCD + NLO EW
	VBF ($H\rightarrow WW^*$)	Powheg + Pythia8	NNLO QCD + NLO EW

Table 5.15 Summary of the MC generators and cross section accuracy used to model the signal and background processes in the $\sqrt{s}$ = 13 TeV analysis. The version of Pythia used is stated in the table (either v6 or v8), but will not be specified in the text. All Higgs boson samples were generated with m_H = 125 GeV. The signal and major background samples are described in the text. A more complete description can be found in ref. [4], including details on the minor background samples and the other Higgs process samples.

The cross section for the signal sample was calculated at NNLO in QCD accuracy [135, 157] and NLO EW accuracy [134], with the branching fraction for the $H \rightarrow WW^*$ decay calculated using Hdecay [137]. The $t\bar{t}$ cross section was calculated using the Top++2.0 program to NNLO in QCD, including soft-gluon resummation to NNLL [140,158–164]. The $WZ/W\gamma^*$, ZZ^*, tW and WWW processes were normalized at NLO [165]. LO calculations were used for the $Z\gamma$, Z+jets, and $t\bar{t}W$ samples [166].

As in the $\sqrt{s}$ = 7 and 8 TeV analysis, the $\sqrt{s}$ = 13 TeV MC samples were passed through the full ATLAS processing chain described in section 3.3.3. Corrections were applied to the MC samples following the recommendations of the ATLAS performance groups, and they were reweighted to ensure that the simulated pile-up distribution matched the one observed in the data samples..

5.7.2 Event reconstruction

The offline event reconstruction algorithms and object selection criteria used for the $\sqrt{s} = 13$ TeV samples were detailed in section 3.3.1, and won't be repeated here. This included descriptions of the offline reconstruction and selections for the PV, muons, electrons, jets, b-tagged jets and E_T^{miss}. Information regarding the overlap removal procedure was also provided, as well as the changes at $\sqrt{s} = 13$ TeV with respect to 7 and 8 TeV.

5.7.3 Signal region selections

The SR selections generally followed those of the $\sqrt{s} = 7$ and 8 TeV analysis described in section 5.3.2, with the thresholds of some existing selections modified and some new selections added[7]. The SR definitions are summarized in table 5.16. This section will focus on what changed in the $\sqrt{s} = 13$ TeV SR selections, as highlighted by the blue entries in the previously mentioned table.

The 3SF and 1SFOS SRs of the $\sqrt{s} = 7$ and 8 TeV analysis were combined into a single SR. This combination improved the stability of the statistical fit given the smaller $\sqrt{s} = 13$ TeV data sample, while not significantly impacting the sensitivity of the measurements. This SR contained all the events with at least one SFOS lepton pair, and so it retained the bulk of the backgrounds involving $Z \to \ell\ell$ decays. With this in mind, this region will be referred to, hereafter, as the Z-dominated SR. Also, following this new naming scheme, what was previously called the 0SFOS SR is re-named the Z-depleted SR.

The selections that were motivated by background reduction had some minor modifications and new additions. The threshold for the E_T^{miss} selection in the Z-dominated SR was increased to 50 GeV, and provided better rejection against the larger Z+jets, ZZ^* and $Z\gamma$ backgrounds at the higher centre-of-mass energy. No selection was applied to the track-based p_T^{miss} since, given the harder E_T^{miss} selection, its impact on the expected significance was found to be negligible. A charge-flip veto selection was added to the Z-depleted SR, where any event in this region containing a same-sign electron pair was rejected if at least one of the electrons had $|\eta| > 0.8$ and their dilepton invariant mass was within 10 GeV of m_Z. This selection helped reduce the minor charge-flip contribution from $WZ/W\gamma^*$ in the Z-depleted SR, as described in section 5.5.2.

[7] Note that the E_T^{miss}, dilepton invariant mass and $\Delta R_{\ell_0\ell_1}$ selections were optimized in order to maximize the expected significance for the signal process with $m_H = 125$ GeV.

		Z-dominated	*Z*-depleted
Pre-selections	Primary vertex	Each event contains a PV	
	Trigger	≥ 1 lepton matches a trigger	
	Num. of isolated leptons	3	3
	Lepton p_T [GeV]	> 15	> 15
	Total lepton charge	±1	±1
Lepton flavour combination	Num. of SFOS pairs	1 or 2	0
Background reduction	Num. of jets	≤ 1	≤ 1
	Num. of b-tagged jets	0	0
	E_T^{miss} [GeV]	> 50	—
	$\lvert m_{\ell^+\ell^-} - m_Z\rvert$ [GeV]	> 25	—
	Charge-flip veto (New)	—	applied
	Min. $m_{\ell^+\ell^-}$ [GeV]	> 12	> 6
	Max. $m_{\ell^+\ell^-}$ [GeV]	< 200	< 200
$H\to WW^*\to \ell\nu\ell\nu$ topology	$\Delta R_{\ell_0\ell_1}$	< 2.0	< 2.0

Table 5.16 Event selections that defined the Z-dominated and Z-depleted SRs of the $\sqrt{s}$ = 13 TeV analysis. Selections that changed with respect to the $\sqrt{s}$ = 7 and 8 TeV analysis are highlighted in blue.

Figures 5.14a and 5.14b show the $m_{\ell_0\ell_2}$ distribution in the Z-dominated and the Z-depleted SRs, respectively. As the name suggests, the Z-dominated SR was dominated by the diboson processes involving $Z/\gamma^*\to\ell\ell$ decays ($WZ/W\gamma^*$, ZZ^* and $Z\gamma$) as well as Z+jets events where a jet was misidentified as a lepton. The Z-depleted SR was instead dominated by top-quark processes, coming mainly from $t\bar{t}$, with marginal contamination from $WZ/W\gamma^*$ and Z+jets events. Additional plots in the $\sqrt{s}$ = 13 TeV SRs can be found in appendix D.

Finally, $\Delta R_{\ell_0\ell_1}$ was required to be below 2 also in the Z-depleted SR. Recall that in the $\sqrt{s}$ = 7 and 8 TeV analysis this selection was applied only in the Z-dominated SR (then the 3SF and 1SFOS SRs). This selection was included in the Z-depleted SR since the shape of the $\Delta R_{\ell_0\ell_1}$ distribution was no longer used in the statistical fit. Rather, each SR contributed to the likelihood function as a single bin. Additional information regarding the changes to the statistical fit will be provided in section 5.7.6.

5.7.4 Background modeling

The background estimation method used in the $\sqrt{s}$ = 13 TeV analysis followed the same principal as the $\sqrt{s}$ = 7 and 8 TeV method from section 5.4, where CRs were defined to drive the measurements of the NFs for the main backgrounds. In the 13 TeV

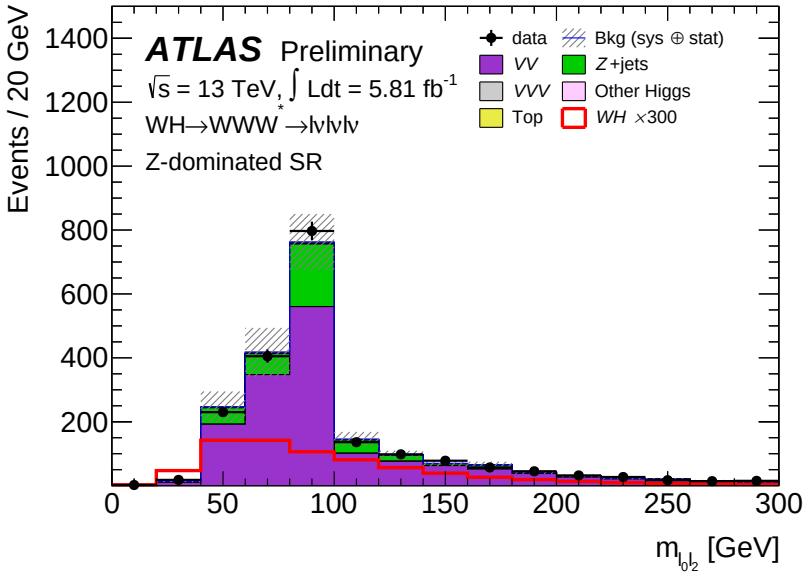

(a)

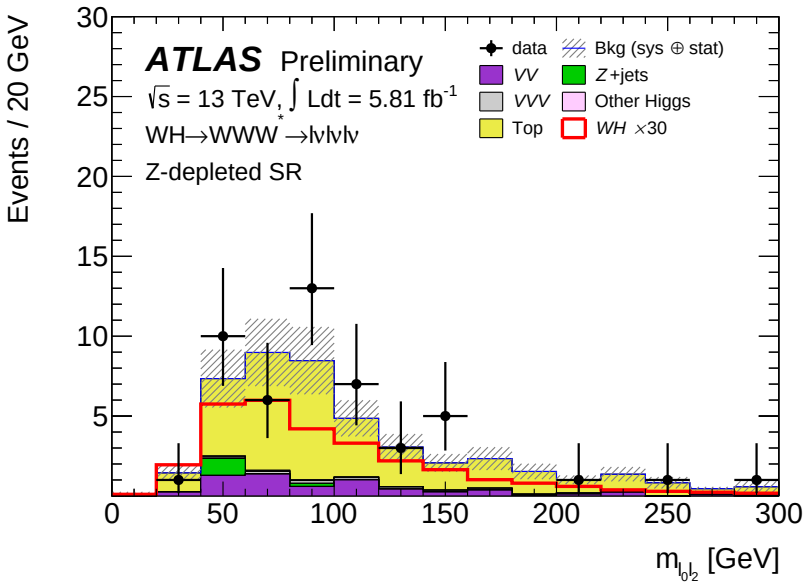

(b)

Figure 5.14 Distributions of $m_{\ell_0\ell_2}$ for the $\sqrt{s} = 13$ TeV samples in the (a) Z-dominated SR and (b) Z-depleted SR, after applying the selections in table 5.16 down to the number of b-tagged jets requirement in (a) and the lepton flavour combination in (b). The data (points) are compared to the background expectation (stacked filled histograms). The total uncertainty on the total background estimate is represented by the hatched area, and includes both the statistical and systematic components. The background NFs are applied. The signal (red line) is overlaid, and scaled by a factor 300 in (a) and 30 in (b).

analysis, CRs were defined to target the $WZ/W\gamma^*$, $Z\gamma$, Z+jets and top-quark production backgrounds. The event selections that defined these CRs are summarized in table 5.17, with the changes compared to the corresponding $\sqrt{s} = 7$ and 8 TeV CRs highlight in blue and detailed in this section.

CR name	Main backgrounds	Changes w.r.t. reference SR
WZ CR	$WZ/W\gamma^*$	inverted Z-mass veto
$Z\gamma$ CR	$Z\gamma$	no Z-mass veto $\lvert m_{\ell\ell\ell} - m_Z\rvert < 15$ GeV inverted E_T^{miss} selection only $eee, \mu\mu e$
Z+jets CR	Z+jets $WZ/W\gamma^*$	inverted Z-mass veto inverted E_T^{miss} selection $\lvert m_{\ell\ell\ell} - m_Z\rvert > 15$ GeV ≥ 2 isolated leptons NFs were derived separately for e-fake and μ-fake samples
Top CR Z-dominated	Top-quark processes (mainly $t\bar{t}$)	at least one jet one b-tagged jet no max. $m_{\ell^+\ell^-}$ and $\Delta R_{\ell_0\ell_1}$ selections ≥ 2 isolated leptons
Top CR Z-depleted (New)	Top-quark processes (mainly $t\bar{t}$)	at least one jet one b-tagged jet no max. $m_{\ell^+\ell^-}$ and $\Delta R_{\ell_0\ell_1}$ selections ≥ 2 isolated leptons

Table 5.17 Event selection criteria used to define the CRs of the $\sqrt{s}$ = 13 TeV analysis, given with respect to the selections of the corresponding reference SR. The reference SR was the Z-dominated SR for all CRs except the Z-depleted Top CR, where it was instead the Z-depleted SR. The derived NFs were applied in both SRs, with the exception of the Z-enriched and Z-depleted Top NFs which were applied only in the Z-dominated SR and Z-depleted SR, respectively. The second column in this table lists the backgrounds that have significant contributions in each CR. Selections that differ compared to the CRs of the $\sqrt{s}$ = 7 and 8 TeV analysis are highlighted in blue.

The selection strategy used to define the WZ and $Z\gamma$ CRs were unchained with respect to the corresponding CRs from the $\sqrt{s} = 7$ and 8 TeV analysis. The events that entered the CRs targeting backgrounds with a jet misidentified (faking) a lepton, namely Z+jets and top-quark production, were required to pass a less stringent isolation criteria compared to the SRs. This criteria required at least two, rather then exactly three, leptons in each event to pass the offline isolation selections described in section 3.3.1. This was done in order to increase the statistics in these CRs given the smaller $\sqrt{s} =$ 13 TeV data sample. In addition, it improved the purity in these CRs for the targeted backgrounds while not significantly changing the fake lepton composition compared to the SRs.

Considering that the top-quark production background made up a more significant fraction of the total background at $\sqrt{s} = 13$ TeV, its estimation method underwent some modifications in order to make it more robust. In addition to the Top CR defined within the Z-dominated topology, a new Top CR was added that followed the selections of the Z-depleted SR. This was done in order to account for any differences in the top-quark contributions entering each SR, which might be introduced due to the different lepton flavour combination or E_T^{miss} thresholds. In addition, both Top CRs were required to contain exactly one b-tagged jet, which was found to select a sample of top-quark events with a fake composition more similar to the SRs.

Note that the contribution from ZZ^* in the analysis was taken directly from MC simulation, since the smaller $\sqrt{s} = 13$ TeV data sample made it difficult to define a CR for this background with sufficient statistics so as not to cause instabilities in the statistical fit. A ZZ validation region (VR) was instead defined in order to check whether the normalization of this background was reasonably reproduced by MC simulation, although no NF was calculated. The event selections used for the ZZ VR followed those of the ZZ CR from the $\sqrt{s} = 7$ and 8 TeV analysis, and are shown in table 5.18.

VR name	Main backgrounds	Changes w.r.t. reference SR
ZZ VR	ZZ^*	no Z-mass veto
		$\lvert m_{\ell\ell\ell} - m_Z \rvert < 15$ GeV
		inverted E_T^{miss} selection
		only $ee\mu, \mu\mu\mu$

Table 5.18 Event selection criteria used to define the ZZ VR, given with respect to the selections of its reference SR. In this case, the reference SR was the Z-enriched SR.

Table 5.19 shows the measured background NFs for the $\sqrt{s}$ = 13 TeV analysis. These NFs were simultaneously extracted from the statistical fit, and properly took into account correlations between the NFs due to cross-contamination of the targeted backgrounds between the CRs.

Process	NF
$WZ/W\gamma^*$	1.24 ± 0.11
$Z\gamma$	0.83 ± 0.22
Z+jets, μ-fake	0.70 ± 0.15
Z+jets, e-fake	0.69 ± 0.16
Top-quark, Z-dominated	0.97 ± 0.07
Top-quark, Z-depleted	0.89 ± 0.07

Table 5.19 The measured background NFs from the $\sqrt{s}$ = 13 TeV samples. The uncertainties on the NFs include both the statistical and systematic components.

The number of observed, estimated background and predicted signal events in the CRs and ZZ VR for the $\sqrt{s}$ = 13 TeV samples are shown in table 5.20. In this table, the measured NFs shown above are applied to the appropriate backgrounds. Good agreement between the observed data and the total background estimation was achieved in all CRs, and there was no significant signal leakage within them. Moreover, the agreement between data and simulation in the ZZ VR was also good, indicating that the normalization of the ZZ^* background was well reproduced by MC simulation. Combined with the good agreement observed in the SR distributions from figure 5.14, as well as the plots in appendix D, this establishes confidence in the background estimation methods used in the $\sqrt{s}$ = 13 TeV analysis.

5.7.5 Systematic uncertainties

The theoretical and experimental systematic uncertainties for the $\sqrt{s}$ = 13 TeV analysis entered the statistical fit in the same way as described in section 5.1.3. A summary of the impact of both kinds of uncertainty on the estimated event yields in the SRs is provided in table 5.21. Details on the different sources of theoretical and experimental uncertainty will provided, in turn, in this section.

	WZ CR	**$Z\gamma$ CR**	**Z+jets CR e-fake**	**Z+jets CR μ-fake**	**Top CR Z-dominated**	**Top CR Z-depleted**	**ZZ VR**
Signal	0.3 ± 0.1	0.1 ± 0.0	0.1 ± 0.0	0.1 ± 0.0	0.1 ± 0.0	0.0 ± 0.0	0.1 ± 0.0
VV	207 ± 15	163 ± 53	156 ± 13	163 ± 14	4.4 ± 0.8	1.0 ± 0.5	30 ± 7
VVV	0.9 ± 0.2	0.0 ± 0.0	0.2 ± 0.0	0.2 ± 0.0	0.2 ± 0.1	0.2 ± 0.0	0.0 ± 0.0
Z+jets	2.5 ± 1.2	0.0 ± 0.0	230 ± 83	212 ± 73	2 ± 0.7	0.1 ± 0.1	9.2 ± 4.1
Top-quark	3.7 ± 0.6	0.4 ± 0.2	7.3 ± 0.9	9.1 ± 1.2	234 ± 19	194 ± 19	0.5 ± 0.3
Other Higgs	0.8 ± 0.0	0.0 ± 0.0	0.4 ± 0.0	0.4 ± 0.0	0.1 ± 0.0	0.0 ± 0.0	0.03 ± 0.0
Total background	215 ± 15	163 ± 52	394 ± 82	385 ± 71	240 ± 20	195 ± 19	40 ± 8
Observed	217	163	393	387	241	195	40

Table 5.20 The number of observed, estimated background and predicted signal events in the CRs and ZZ VR for the $\sqrt{s}$ = 13 TeV samples. The background NFs are applied. The uncertainties include both the statistical and systematic components.

Theoretical uncertainties

As was the case for the $\sqrt{s}$ = 7 and 8 TeV analysis, the theoretical uncertainties on the WH production cross section and the Higgs decay branching ratio were evaluated by following the recommendations of the LHC Higgs cross section working group [39]. Signal acceptance uncertainties associated to both QCD scale and PDF set variations were also considered. The QCD scale acceptance uncertainties were evaluated by independently varying the scales up and down by a factor of 2 or 0.5 in the Powheg calculations. The acceptance uncertainties related to the choice of PDF set were evaluated by taking the envelope of the acceptance variations from different configurations in the CT10 set and when using the alternative MSTW [146] and NNPDF [147] sets.

QCD scale and PDF uncertainties were also evaluated for the main background processes by following a similar procedure to the one described in section 5.5.1. Uncertainties on the WWW cross section and MC modeling were estimated by comparing the predictions between Sherpa and VBFNLO [167–169]. MC modeling uncertainties were also calculated for the dominant $WZ/W\gamma^*$ and top-quark production backgrounds. The $WZ/W\gamma^*$ modeling uncertainty was estimated by comparing the predictions from Sherpa to Powheg+Pythia. The resulting 4% and 8% uncertainties were assigned to the $WZ/W\gamma^*$ contribution in the Z-dominated and Z-depleted SRs, respectively. The main components of the top-quark modeling uncertainty were linked to the choice of generator for the hard scatter process and the PS/UE model for the $t\bar{t}$ background. These uncertainties were estimated by comparing Powheg+Herwig with MG5_aMC+Herwig [156] and Powheg+Pythia with Powehg+Herwig, respectively. The generator uncertainty on the $t\bar{t}$ background was the dominant contribution and ranged from 18-21% depending on the analysis region.

Experimental uncertainties

The methods used to evaluate the experimental uncertainties associated to jets, leptons, the trigger, b-tagging and the E_T^{miss} soft term followed those described in section 5.5.2. Although similar methods were used, the uncertainty estimations were updated using $\sqrt{s}$ = 13 TeV ATLAS data and MC samples [64, 69, 72, 79].

A "CR isolation" uncertainty was evaluated for the Z+jets background where a jet was misidentified as an electron (e-fake). This uncertainty accounted for differences in the jet flavour composition of the fake electron between the SRs and the Z+jets e-fake CR, originating from the less stringent lepton isolation criteria used in the CR.

An 18% uncertainty was estimated by taking the envelope of the fluctuations of the corresponding NF when the lepton isolation criteria was varied. The uncertainty associated to the pile-up reweighting procedure was included, and the preliminary uncertainty on the combined 2015+2016 integrated luminosity was 2.0%. This was evaluated following a similar methodology to the one described in ref. [150].

(a) Impact of systematic uncertainties on the signal [%]

		Z-dominated SR	*Z*-depleted SR
Theoretical uncertainties	QCD scale	0.7	0.7
	PDF and α_S	1.9	1.9
	Higgs decay BR	1.5	1.5
	Acceptance	6.4	6.4
Experimental uncertainties	Jet	4.2	4.5
	E_T^{miss} soft term	0.3	—
	Electron	1.8	2.0
	Muon	0.8	0.7
	Trigger	0.4	0.3
	b-tagging	0.7	0.6
	Pile-up	0.8	0.9
	Luminosity	2.0	2.0

(b) Impact of systematic uncertainties on the total background [%]

		Z-dominated SR	*Z*-depleted SR
Theoretical uncertainties	QCD scale	3.6	2.0
	PDF and α_S	1.3	0.4
	WWW norm. and modeling	0.7	1.5
	$WZ/W\gamma^*$ modeling	2.9	1.4
	Top modeling	5.7	13
Experimental uncertainties	Jet	18	14
	E_T^{miss} soft term	3.8	—
	Electron	2.2	3.0
	Muon	0.8	0.6
	Trigger	0.5	0.3
	b-tagging	2.4	3.2
	CR isolation	0.2	1.7
	Pile-up	0.9	7.8
	Luminosity	0.2	0.3

Table 5.21 The impact of the systematic uncertainties (in %) on the estimated SR event yields for (a) the signal and (b) the total background. Any uncertainties that either do not apply or are negligible are indicated by a dash. The values in this table are obtained via the statistical fit.

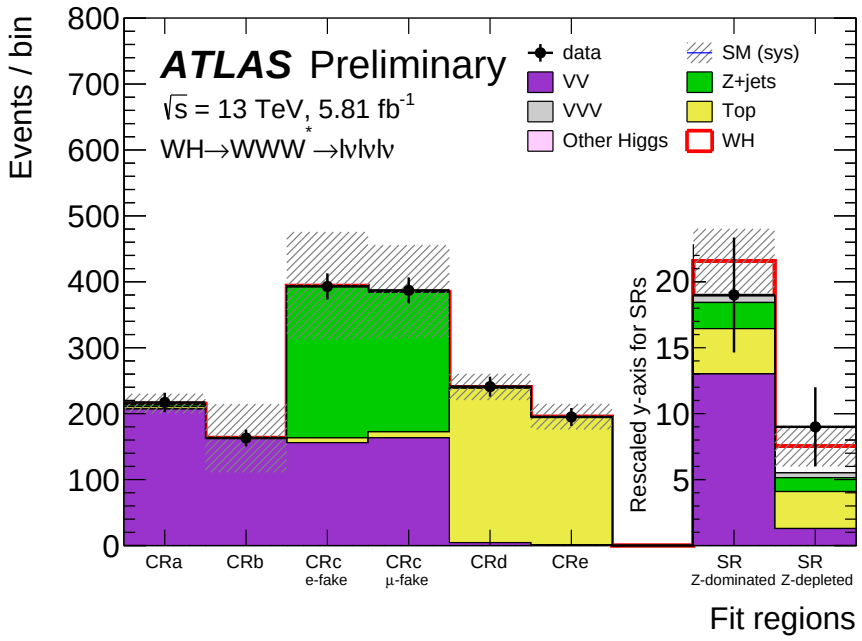

Figure 5.15 The event yields in each of the regions that entered the statistical fit for the $\sqrt{s}$ = 13 TeV analysis. The signal and main backgrounds are normalized to the results of the fit via μ_{obs} and the NFs, respectively. The SRs are displayed with a different y-axis to make the signal contribution, stacked on top of the total background, more visible. The uncertainties on the total background yield include both the statistical and systematic components. The bins labelled CRa, CRb, CRc, CRd and CRe correspond to the WZ CR, $Z\gamma$ CR, Z+jets CR, Z-dominated Top CR, and Z-depleted Top CR, respectively.

5.7.6 Results

The statistical fit procedure that was used for the $\sqrt{s}$ = 13 TeV analysis followed closely the one described in section 5.1.3, with some changes to how the likelihood function was constructed. Recall that the 0SFOS SR of the $\sqrt{s}$ = 7 and 8 TeV analysis had an entry in the likelihood function for each bin of the final $\Delta R_{\ell_0\ell_1}$ distribution in that region, and that each individual bin of the BDT score in the 3SF and 1SFOS SRs also entered the fit. This strategy was not found to be viable given the significantly smaller $\sqrt{s}$ = 13 TeV data sample. Instead, a simplified approach was adopted where only the total event yields in the Z-dominated and Z-depleted SRs entered the fit as single bins.

The post-fit event yields in each of the regions that entered the fit are shown in figure 5.15. The CR event yields are shown in the first six bins of this figure, and good agreement between the observed data and the total background estimation is achieved in each of them.

The number of observed, estimated background and predicted signal events in the Z-dominated and Z-depleted SRs, after applying all of the selections listed in table 5.16, are shown in the final two bins of figure 5.15 and in table 5.22[8]. In the Z-dominated SR, $WZ/W\gamma^*$ and ZZ^* represent the leading background contributions accounting for about 70% of the total background yield; with top-quark production, Z+jets, $Z\gamma$ and WWW together making up the remaining background fraction. Most of the sensitivity came from the Z-depleted SR with a total background yield that was over four times smaller then the previously mentioned SR, while retaining about 40% of the total signal yield. Top-quark production makes up about half of the total background in this SR, with the remainder split between $WZ/W\gamma^*$, Z+jets and WWW.

	Z-dominated SR	**Z-depleted SR**
Signal	0.83 ± 0.31	0.63 ± 0.25
VV	13.0 ± 1.6	1.3 ± 0.4
VVV	0.5 ± 0.1	0.4 ± 0.1
Z+jets	2.0 ± 1.6	1.1 ± 1.1
Top-quark	3.4 ± 0.9	2.8 ± 0.8
Other Higgs	0.1 ± 0.0	0.1 ± 0.0
Total background	19.1 ± 2.4	5.6 ± 1.5
Observed	19	9

Table 5.22 The number of observed, estimated background and predicted signal events in the SRs of the $\sqrt{s} = 13$ TeV analysis. The background NFs are applied. The uncertainties include both the statistical and systematic components.

A small excess in the number of observed events with respect to the estimated total background event yield is present in the Z-depleted SR. However, this excess is consistent with both the background-only and background-plus-signal expectations within the uncertainties.

The observed signal strength at $\sqrt{s} = 13$ TeV for the WH production of the Higgs boson of mass 125 GeV with $H \to WW^*$ decay is:

$$\mu_{\text{obs}}^{13\text{ TeV}} = 3.2\ ^{+3.7}_{-3.2}\ (\text{stat})\ ^{+2.3}_{-2.7}\ (\text{sys}), \tag{5.5}$$

This is consistent with the SM expectation of unity within the uncertainties, as well as the corresponding measurement at $\sqrt{s} = 7$ and 8 TeV from section 5.6.1. The leading

[8] Note that the signal yields in figure 5.15 are scaled by μ_{obs}, while in table 5.22 they are scaled by $\mu = 1$.

Source	$\Delta\mu_{\text{obs}}/\mu_{\text{obs}}$ [%]
Pile-up	+22 / -26
JER	+22 / -23
Top-quark generator	+17 / -20
b-tagging	+10 / -11
Top-quark PS/UE	+7 / -8
JES flavour composition	+8 / -5
JES η intercalibration	+7 / -6
$WZ/W\gamma^*$ modeling	+7 / -6
Top-quark QCD scales	+6 / -7
$WZ/W\gamma^*$ QCD scales	±5

Table 5.23 List of the ten leading sources of systematic uncertainty on the μ_{obs} measurement at $\sqrt{s} = 13$ TeV. The impact of the uncertainties are given as a percentage of the observed value.

sources of systematic uncertainty on the μ_{obs} measurement are shown in table 5.23, with their descriptions provided in section 5.7.5. The local significance of the overall excess observed in the SRs with respect to the background-only hypothesis is 0.77σ, where 0.24σ was expected.

5.8 Conclusions

In this chapter, a search for the sequential decay process $WH \to WWW^* \to \ell\nu\ell\nu\ell\nu$ was presented using LHC proton-proton collision data collected by the ATLAS detector. The search was conducted using data samples at $\sqrt{s}$ = 7, 8 and 13 TeV corresponding to integrated luminosities of 4.5, 20.3 and 5.8 fb^{-1}, respectively.

In order to search for this signal process, an analysis strategy was first developed using the $\sqrt{s} = 7$ and 8 TeV data samples and it was used to measure the relative signal strength with respect to the SM expectation. For a Higgs boson of mass 125 GeV, which is compatible with the measured value, the observed signal strength was determined to be:

$$\mu_{\text{obs}}^{7+8\ \text{TeV}} = 0.72\ ^{+1.2}_{-1.1}\ (\text{stat.})\ ^{+0.4}_{-0.3}\ (\text{sys.})$$

An overall small excess was observed with respect to the background-only hypothesis corresponding to a local significance of 0.66σ, where 0.79σ was expected in the presence

of the signal. The analysis method was then extended to perform the first measurement of the signal strength at $\sqrt{s} = 13$ TeV:

$$\mu_{\text{obs}}^{13\text{ TeV}} = 3.2\ ^{+3.7}_{-3.2}\ (\text{stat})\ ^{+2.3}_{-2.7}\ (\text{sys})$$

Again, a small overall excess was observed corresponding to a local significance of 0.77σ, where 0.24σ was expected. All of the measurements at $\sqrt{s} = 7$, 8 and 13 TeV are consistent with the SM expectations within the uncertainties.

These measurements potentially show some early hints of the WH production of the SM Higgs boson with $H \rightarrow WW^*$ decay. However, the current measurements are statistically limited and more data is clearly required before making more definitive conclusions regarding the existence of this process.

6

Conclusion

The SM of particle physics, although incomplete, has predicted a wide variety of phenomena and through many experiments has become one of the most well-tested theories in physics. Particles can attain mass in the SM by breaking its electroweak symmetry via the Higgs Mechanism, and the associated Higgs boson is the final particle predicted by the SM to exist. Considering this, the discovery of the SM Higgs boson is considered one of the most important goals in modern particle physics.

This goal was partially achieved in July 2012, when the ATLAS and CMS experiments at the LHC announced the discovery of a Higgs-like particle with a mass of around 125 GeV. The next step for both experiments is to scrutinize the properties of this new particle in order to confirm whether it is the SM Higgs boson. Using LHC proton-proton collision data at $\sqrt{s}$ = 7 and 8 TeV, the ATLAS Collaboration measured the signal strengths, coupling strengths, spin and parity of the new particle and showed them all to be consistent with the SM expectations within the uncertainties. The ggF production mode and decays into ZZ^*, $\gamma\gamma$ and WW^* were all confirmed at over 5σ significance. Strong evidence at over 4σ was observed for the VBF production mode and $\tau\tau$ decay channel. Although substantial progress has been made, there is still much work to be done before a definitive statement can be made regarding whether this new particle is the SM Higgs boson or something more exotic.

One important future objective of the ATLAS experiment is to claim discovery in the $H\to\tau\tau$ channel alone, more tightly constrain the tau lepton Yukawa coupling and perform the first measurements in this channel of the spin and parity. In order to collect the collision data for these measurements, it is essential for the ATLAS tau trigger system to by capable of efficiently identifying interesting events containing tau leptons under high luminosity and pile-up conditions.

This thesis presented two studies relating to the ATLAS tau trigger system. The first was the measurement of its performance during $\sqrt{s}$ = 8 TeV data taking using a tag-and-probe method targeting $Z\to\tau\tau$ decays. This method was used to measure the efficiencies, pile-up dependence and energy resolutions at each level of the tau trigger. All of these measurements were shown to be compatible with the performance goals set during the design of the trigger. The second study explored the potential of using the FTK upgrade to improve tau trigger performance at $\sqrt{s}$ = 14 TeV under harsher pile-up conditions. A purely FTK track-based algorithm was proposed, and shown to improve per-tau efficiency compared to traditional algorithms by 10-40% with respect to truth and 5-15% with respect to offline. When implemented into a di-tau trigger, the FTK-based algorithm outperforms traditional algorithms both in terms of the signal efficiency for $H\to\tau\tau$ events and the rejection of QCD multijet background events. Considering this, it is clear that FTK tracking will become a critical component of the future ATLAS tau trigger system.

Another high priority goal of the ATLAS experiment is to confirm the SM predictions for Higgs boson production at the LHC. As mentioned earlier, the dominant ggF production mode has already been confirmed by ATLAS and significant evidence has been observed for the VBF mode. In order to complete the picture of SM Higgs boson production, it is also necessary to first find evidence for and eventually claim discoveries of the rare WH, ZH and $t\bar{t}H$ production modes.

The main result presented in this thesis contributed to this objective and involved a direct search for the WH production of the SM Higgs boson in collision events containing three leptons (electrons or muons). This search was performed in the $H\to WW^*$ decay channel, and the specific signal that it targeted was the sequential decay process $WH\to WWW^*\to \ell\nu\ell\nu\ell\nu$. $H\to WW^*$ decays provide a sensitive probe of WH production due to their large branching ratio, and the three leptons and large missing energy of the signal process provides a clean signature in the ATLAS detector. In addition, this process is interesting since the Higgs boson couples only to W bosons at both the production and decay vertices at tree-level. Therefore, this process also

provides sensitivity to the coupling strength between the Higgs and W bosons, and any potential deviations to it introduced by physics beyond the SM.

The search was conducted using ATLAS data at $\sqrt{s}$ = 7, 8 and 13 TeV corresponding to integrated luminosities of 4.5, 20.3 and 5.8 fb^{-1}, respectively. The analysis strategy was first developed using the $\sqrt{s}$ = 7 and 8 TeV data samples, and used to measure the relative signal strength with respect to the SM expectation for the WH production mode with $H \to WW^*$ decay. For a Higgs boson of mass 125 GeV, which is compatible with the measured value, the observed signal strength was determined to be $0.72\ ^{+1.2}_{-1.1}$ (stat.) $^{+0.4}_{-0.3}$ (sys.). The analysis method was then extended to perform the first measurement of the signal strength at $\sqrt{s}$ = 13 TeV. This quantity was measured to be $3.2\ ^{+3.7}_{-3.2}$ (stat) $^{+2.3}_{-2.7}$ (sys). Both measurements are consistent with the SM expectation of unity within the current degree of precision.

In both the $\sqrt{s}$ = 7+8 TeV analysis and the 13 TeV analysis, a small overall excess was observed in the signal regions with respect to the background-only hypothesis. The observed significance of the excess in the $\sqrt{s}$ = 7 and 8 TeV data corresponds to a local significance of 0.66σ, while for the 13 TeV data it is 0.77σ. These results potentially show some early hints of the WH production mode, although more data is clearly required before claiming there is any statistically significant evidence for the existence of this process.

The analysis strategy presented in this thesis sets the stage for more precise measurements using future ATLAS proton-proton collision events at $\sqrt{s}$ = 13 and 14 TeV. By the end of the second run of data taking in late 2018, the LHC is expected to deliver about 100 fb^{-1} of data. With a data sample of this size, prospect studies for the previously mentioned three lepton analysis [170] showed that over 3σ evidence for the WH production mode should be within reach. Looking further ahead, the LHC is expected to deliver about 300 fb^{-1} of data during its third run starting around 2021, and up to 2 a^{-1} during the HL-LHC run that should start in 2025. With these substantially larger data samples it should be possible, in the three lepton analysis alone, to confirm the WH production mode at over 5σ significance and to perform precise measurements of the H-W coupling strength.

Bibliography

[1] **ATLAS** Collaboration, "Identification and energy calibration of hadronically decaying tau leptons with the ATLAS experiment in *pp* collisions at $\sqrt{s}$=8 TeV," *Eur. Phys. J.* **C75** no. 7, (2015) 303, arXiv:1412.7086 [hep-ex]. vii, 54, 55, 63, 66, 68, 70

[2] **ATLAS** Collaboration, "Fast TracKer Technical Design Report," *ATLAS-TDR-021* (2013) . vii, 44, 64, 79, 81, 96

[3] **ATLAS** Collaboration, "Study of $(W/Z)H$ production and Higgs boson couplings using $H \to WW^*$ decays with the ATLAS detector," *JHEP* **08** (2015) 137, arXiv:1506.06641 [hep-ex]. viii, 18, 100, 109, 110, 180, 182

[4] **ATLAS** Collaboration, "Measurements of the Higgs boson production cross section via Vector Boson Fusion and associated WH production in the $WW^* \to \ell\nu\ell\nu$ decay mode with the ATLAS detector at $\sqrt{s}$ = 13 TeV," *ATLAS-CONF-2016-112* (2016) . viii, 100, 135, 136

[5] **ATLAS** Collaboration, "Observation of a new particle in the search for the Standard Model Higgs boson with the ATLAS detector at the LHC," *Phys.Lett.* **B716** (2012) 1–29, arXiv:1207.7214 [hep-ex]. 2, 16

[6] **CMS** Collaboration, "Observation of a new boson at a mass of 125 GeV with the CMS experiment at the LHC," *Phys. Lett.* **B716** (2012) 30–61, arXiv:1207.7235 [hep-ex]. 2, 16

[7] **ATLAS** Collaboration, "Measurements of the Higgs boson production and decay rates and coupling strengths using pp collision data at $\sqrt{s}$ = 7 and 8 TeV in the ATLAS experiment," *Eur. Phys. J.* **C76** no. 1, (2016) 6, arXiv:1507.04548 [hep-ex]. 2, 20, 21, 22, 23

[8] S. L. Glashow, "Partial Symmetries of Weak Interactions," *Nucl. Phys.* **22** (1961) 579–588. 4

[9] S. Weinberg, "A Model of Leptons," *Phys. Rev. Lett.* **19** (1967) 1264–1266. 4

[10] A. Salam, *Elementary Particle Theory*. Almqvist and Wiksell, 1968. 4

[11] S. L. Glashow, J. Iliopoulos, and L. Maiani, "Weak Interactions with Lepton-Hadron Symmetry," *Phys. Rev.* **D2** (1970) 1285–1292. 4

[12] C. Campagnari and M. Franklin, "The Discovery of the top quark," *Rev. Mod. Phys.* **69** (1997) 137–212, `arXiv:hep-ex/9608003 [hep-ex]`. 4

[13] **ATLAS, CMS** Collaboration, "Measurements of the Higgs boson production and decay rates and constraints on its couplings from a combined ATLAS and CMS analysis of the LHC pp collision data at $\sqrt{s} = 7$ and 8 TeV," *JHEP* **08** (2016) 045, `arXiv:1606.02266 [hep-ex]`. 4, 16

[14] E. Noether, "Invariant Variation Problems," *Gott. Nachr.* **1918** (1918) 235–257, `arXiv:physics/0503066 [physics]`. 6

[15] F. Englert and R. Brout, "Broken Symmetry and the Mass of Gauge Vector Mesons," *Phys. Rev. Lett.* **13** (1964) 321–323. 6

[16] P. W. Higgs, "Broken symmetries, massless particles and gauge fields," *Phys. Lett.* **12** (1964) 132–133. 6

[17] P. W. Higgs, "Spontaneous Symmetry Breakdown without Massless Bosons," *Phys. Rev.* **145** (1966) 1156–1163. 6

[18] G. S. Guralnik, C. R. Hagen, and T. W. B. Kibble, "Global Conservation Laws and Massless Particles," *Phys. Rev. Lett.* **13** (1964) 585–587. 6

[19] F. Mandl and G. Shaw, *Quantum Field Theory*. A Wiley-Interscience publication. John Wiley & Sons, 2010. 8

[20] S. Heinemeyer *et al.*, "Handbook of LHC Higgs Cross Sections: 3. Higgs Properties," *CERN-2013-004* (2013) , `arXiv:1307.1347 [hep-ph]`. 9, 10, 11, 13, 109, 122

[21] Particle Data Group, "Review of Particle Physics (RPP)," *Phys. Rev.* **D86** (2012) 010001. 11, 64

[22] J. M. Cornwall, D. N. Levin, and G. Tiktopoulos, "Uniqueness of spontaneously broken gauge theories," *Phys. Rev. Lett.* **30** (1973) 1268–1270. 15

[23] J. M. Cornwall, D. N. Levin, and G. Tiktopoulos, "Derivation of Gauge Invariance from High-Energy Unitarity Bounds on the s Matrix," *Phys. Rev.* **D10** (1974) 1145. 15

[24] C. H. Llewellyn Smith, "High-Energy Behavior and Gauge Symmetry," *Phys. Lett.* **46B** (1973) 233–236. 15

[25] B. W. Lee, C. Quigg, and H. B. Thacker, "Weak Interactions at Very High-Energies: The Role of the Higgs Boson Mass," *Phys. Rev.* **D16** (1977) 1519. 15

[26] J. F. Gunion, H. E. Haber, G. L. Kane, and S. Dawson, "The Higgs Hunter's Guide," *Front. Phys.* **80** (2000) 1–404. 15

[27] G. Degrassi, S. Di Vita, J. Elias-Miro, J. R. Espinosa, G. F. Giudice, G. Isidori, and A. Strumia, "Higgs mass and vacuum stability in the Standard Model at NNLO," *JHEP* **08** (2012) 098, `arXiv:1205.6497 [hep-ph]`. 15

[28] Tevatron Electroweak Working Group, CDF, DELPHI, SLD Electroweak and Heavy Flavour Groups, ALEPH, LEP Electroweak Working Group, SLD, OPAL, D0 and L3, "Precision Electroweak Measurements and Constraints on the Standard Model," `arXiv:1012.2367 [hep-ex]`. 15

[29] OPAL, DELPHI, LEP Working Group for Higgs boson searches, ALEPH and L3, "Search for the standard model Higgs boson at LEP," *Phys. Lett.* **B565** (2003) 61–75, `arXiv:hep-ex/0306033 [hep-ex]`. 15

[30] **CDF** Collaboration, "Combined search for the standard model Higgs boson decaying to a bb pair using the full CDF data set," *Phys. Rev. Lett.* **109** (2012) 111802, `arXiv:1207.1707 [hep-ex]`. 15

[31] **D0** Collaboration, "Combined Search for the Standard Model Higgs Boson Decaying to $b\bar{b}$ Using the D0 Run II Data Set," *Phys. Rev. Lett.* **109** (2012) 121802, `arXiv:1207.6631 [hep-ex]`. 15

[32] **CDF, D0** Collaboration, "Evidence for a particle produced in association with weak bosons and decaying to a bottom-antibottom quark pair in Higgs boson searches at the Tevatron," *Phys. Rev. Lett.* **109** (2012) 071804, arXiv:1207.6436 [hep-ex]. 15

[33] **CMS** Collaboration, "Precise determination of the mass of the Higgs boson and tests of compatibility of its couplings with the standard model predictions using proton collisions at 7 and 8 TeV," *Eur. Phys. J.* **C75** no. 5, (2015) 212, arXiv:1412.8662 [hep-ex]. 16

[34] **ATLAS** Collaboration, "Measurement of the Higgs boson mass from the $H \to \gamma\gamma$ and $H \to ZZ^* \to 4\ell$ channels with the ATLAS detector using 25 fb^{-1} of pp collision data," *Phys. Rev.* **D90** no. 5, (2014) 052004, arXiv:1406.3827 [hep-ex]. 16, 17

[35] **ATLAS** Collaboration, "Observation and measurement of Higgs boson decays to WW* with the ATLAS detector," *Phys. Rev.* **D92** no. 1, (2015) 012006, arXiv:1412.2641 [hep-ex]. 18, 106, 180

[36] **ATLAS** Collaboration, "Evidence for the Higgs-boson Yukawa coupling to tau leptons with the ATLAS detector," *JHEP* **04** (2015) 117, arXiv:1501.04943 [hep-ex]. 19, 63, 69, 89, 96

[37] **ATLAS** Collaboration, "Search for the $b\bar{b}$ decay of the Standard Model Higgs boson in associated $(W/Z)H$ production with the ATLAS detector," *JHEP* **01** (2015) 069, arXiv:1409.6212 [hep-ex]. 19

[38] **ATLAS** Collaboration, "Study of the spin and parity of the Higgs boson in diboson decays with the ATLAS detector," *Eur. Phys. J.* **C75** no. 10, (2015) 476, arXiv:1506.05669 [hep-ex]. 22

[39] LHC Higgs Cross Section Working Group, "Handbook of LHC Higgs Cross Sections: 4. Deciphering the Nature of the Higgs Sector," *CERN-2016-002-M* (2016) , arXiv:1610.07922 [hep-ph]. 24, 133, 144

[40] LHC schedule. http://lhc-commissioning.web.cern.ch/lhc-commissioning/schedule/LHC-schedule-update.pdf. 25, 79

[41] I. Bejar Alonso and L. Rossi, "HiLumi LHC Technical Design Report," *CERN-ACC-2015-0140* (2015) . 25, 79

[42] O. S. Bruning, P. Collier, P. Lebrun, S. Myers, R. Ostojic, J. Poole, and P. Proudlock, "LHC Design Report Vol.1: The LHC Main Ring," *CERN-2004-003* (2004) . 27, 30, 32

[43] **ATLAS** Collaboration, "The ATLAS Experiment at the CERN Large Hadron Collider," *JINST* **3** (2008) S08003. 27, 30, 32, 33, 34, 35, 37, 39, 40, 42

[44] J.-L. Caron, "Overall view of LHC experiments," *LHC-PHO-1998-349* (1998) . 28

[45] C. Lefèvre, "The CERN accelerator complex," *CERN-DI-0812015* (2008) . 29

[46] **ATLAS** Collaboration, "Luminosity determination in pp collisions at $\sqrt{s} = 8$ TeV using the ATLAS detector at the LHC," *Eur. Phys. J.* **C76** no. 12, (2016) 653, `arXiv:1608.03953 [hep-ex]`. 30, 31, 32, 33

[47] **ATLAS** Collaboration, "Luminosity Determination in *pp* Collisions at $\sqrt{s} = 7$ TeV Using the ATLAS Detector at the LHC," *Eur. Phys. J.* **C71** (2011) 1630, `arXiv:1101.2185 [hep-ex]`. 30, 31, 32, 33

[48] ATLAS Luminosity Public Results for Run 1. `https://twiki.cern.ch/twiki/bin/view/AtlasPublic/LuminosityPublicResults`. 30, 31, 32, 33

[49] ATLAS Luminosity Public Results for Run 2. `https://twiki.cern.ch/twiki/bin/view/AtlasPublic/LuminosityPublicResultsRun2`. 30, 31, 32, 33

[50] **ATLAS** Collaboration, "Pile-up corrections for jets from proton-proton collisions at $\sqrt{s} = 7$ TeVin ATLAS in 2011," *ATLAS-CONF-2012-064* (2012) . 32

[51] **ATLAS** Collaboration, "Insertable B-Layer Technical Design Report," *ATLAS-TDR-19* (2010) . 38

[52] C. W. Fabjan and F. Gianotti, "Calorimetry for particle physics," *Rev. Mod. Phys.* **75** (2003) 1243–1286. 40

[53] **ATLAS TDAQ** Collaboration, "The ATLAS Data Acquisition and High Level Trigger system," *JINST* **11** no. 06, (2016) P06008. 43

[54] **ATLAS** Collaboration, "Performance of the ATLAS Trigger System in 2015," *Eur. Phys. J.* **C77** no. 5, (2017) 317, `arXiv:1611.09661 [hep-ex]`. 43, 44, 58, 59,

67

[55] **ATLAS** Collaboration, "Performance of the ATLAS Trigger System in 2010," *Eur. Phys. J.* **C72** (2012) 1849, arXiv:1110.1530 [hep-ex]. 43, 44

[56] **ATLAS** Collaboration, "Performance of the ATLAS Inner Detector Track and Vertex Reconstruction in the High Pile-Up LHC Environment," *ATLAS-CONF-2012-042* (2012) . 45

[57] T. Cornelissen, M. Elsing, S. Fleischmann, W. Liebig, and E. Moyse, "Concepts, Design and Implementation of the ATLAS New Tracking (NEWT)," *ATL-SOFT-PUB-2007-007* (2007) . 45

[58] **ATLAS** Collaboration, "Expected Performance of the ATLAS Experiment - Detector, Trigger and Physics," *CERN-OPEN-2008-020* (2008) , arXiv:0901.0512 [hep-ex]. 45

[59] **ATLAS** Collaboration, "Performance of the ATLAS Track Reconstruction Algorithms in Dense Environments in LHC Run 2," *Eur. Phys. J.* **C77** no. 10, (2017) 673, arXiv:1704.07983 [hep-ex]. 45

[60] I. Gavrilenko, "Description of Global Pattern Recognition Program (XKalman)," *ATL-INDET-97-165, ATL-I-PN-165* (1997) . 46

[61] **ATLAS** Collaboration, "Performance of primary vertex reconstruction in proton-proton collisions at $\sqrt{s}$ =7 TeV in the ATLAS experiment," *ATLAS-CONF-2010-069* (2010) . 46

[62] W. Lampl, S. Laplace, D. Lelas, P. Loch, H. Ma, S. Menke, S. Rajagopalan, D. Rousseau, S. Snyder, and G. Unal, "Calorimeter clustering algorithms: Description and performance," *ATL-LARG-PUB-2008-002, ATL-COM-LARG-2008-003* (2008) . 47

[63] **ATLAS** Collaboration, M. Aaboud *et al.*, "Electron efficiency measurements with the ATLAS detector using 2012 LHC proton–proton collision data," *Eur. Phys. J.* **C77** no. 3, (2017) 195, arXiv:1612.01456 [hep-ex]. 47, 50, 124

[64] **ATLAS** Collaboration, "Electron efficiency measurements with the ATLAS detector using the 2015 LHC proton-proton collision data," *ATLAS-CONF-2016-024* (2016) . 47, 50, 51, 144

[65] **ATLAS** Collaboration, "Properties of Jets and Inputs to Jet Reconstruction and Calibration with the ATLAS Detector Using Proton-Proton Collisions at $\sqrt{s}$ = 7 TeV," *ATLAS-CONF-2010-053* (2010) . 47

[66] **ATLAS** Collaboration, "Topological cell clustering in the ATLAS calorimeters and its performance in LHC Run 1," *Eur. Phys. J.* **C77** (2017) 490, arXiv:1603.02934 [hep-ex]. 47

[67] **ATLAS** Collaboration, "Jet energy measurement and its systematic uncertainty in proton-proton collisions at $\sqrt{s}$ = 7 TeV with the ATLAS detector," *Eur. Phys. J. C* **75** (2015) 17, arXiv:1406.0076 [hep-ex]. 47, 52, 123

[68] **ATLAS** Collaboration, "Properties of Jets and Inputs to Jet Reconstruction and Calibration with the ATLAS Detector Using Proton-Proton Collisions at $\sqrt{s}$ = 13 TeV," *ATL-PHYS-PUB-2015-036* (2015) . 47

[69] **ATLAS** Collaboration, "Jet Calibration and Systematic Uncertainties for Jets Reconstructed in the ATLAS Detector at $\sqrt{s}$ = 13 TeV," *ATL-PHYS-PUB-2015-015* (2015) . 47, 52, 144

[70] **ATLAS** Collaboration, "Single hadron response measurement and calorimeter jet energy scale uncertainty with the ATLAS detector at the LHC," *Eur. Phys. J.* **C73** no. 3, (2013) 2305, arXiv:1203.1302 [hep-ex]. 47

[71] **ATLAS** Collaboration, "Measurement of the muon reconstruction performance of the ATLAS detector using 2011 and 2012 LHC proton–proton collision data," *Eur. Phys. J.* **C74** no. 11, (2014) 3130, arXiv:1407.3935 [hep-ex]. 48, 124

[72] **ATLAS** Collaboration, "Muon reconstruction performance of the ATLAS detector in proton-proton collision data at $\sqrt{s}$ =13 TeV," *Eur. Phys. J.* **C76** no. 5, (2016) 292, arXiv:1603.05598 [hep-ex]. 48, 49, 144

[73] S. Hassani, L. Chevalier, E. Lancon, J. F. Laporte, R. Nicolaidou, and A. Ouraou, "A muon identification and combined reconstruction procedure for the ATLAS detector at the LHC using the (MUONBOY, STACO, MuTag) reconstruction packages," *Nucl. Instrum. Meth.* **A572** (2007) 77–79. 48

[74] **ATLAS** Collaboration, "Electron reconstruction and identification efficiency measurements with the ATLAS detector using the 2011 LHC proton-proton collision data," *Eur. Phys. J.* **C74** no. 7, (2014) 2941, arXiv:1404.2240 [hep-ex].

50

[75] M. Cacciari, G. P. Salam, and G. Soyez, "The anti-k_t jet clustering algorithm," *JHEP* **04** (2008) 063, arXiv:0802.1189 [hep-ph]. 52

[76] M. Cacciari and G. P. Salam, "Dispelling the N^3 myth for the k_t jet-finder," *Phys. Lett.* **B641** (2006) 57–61, arXiv:hep-ph/0512210 [hep-ph]. 52

[77] **ATLAS** Collaboration, "Pile-up subtraction and suppression for jets in ATLAS," *ATLAS-CONF-2013-083* (2013) . 52

[78] **ATLAS** Collaboration, "Tagging and suppression of pileup jets," *ATLAS-CONF-2014-018* (2014) . 53

[79] **ATLAS** Collaboration, "Performance of b-Jet Identification in the ATLAS Experiment," *JINST* **11** (2016) P04008, arXiv:1512.01094 [hep-ex]. 53, 144

[80] **ATLAS** Collaboration, "Calibration of the performance of b-tagging for c and light-flavour jets in the 2012 ATLAS data," *ATLAS-CONF-2014-046* (2014) . 53, 54, 124

[81] **ATLAS** Collaboration, "Expected performance of the ATLAS b-tagging algorithms in Run-2," *ATL-PHYS-PUB-2015-022* (2015) . 53, 54

[82] **ATLAS** Collaboration, "Identification of the Hadronic Decays of Tau Leptons in 2012 Data with the ATLAS Detector," *ATLAS-CONF-2013-064* (2013) . 54, 55

[83] **ATLAS** Collaboration, "Performance of the Reconstruction and Identification of Hadronic Tau Decays with ATLAS," *ATLAS-CONF-2011-152* (2011) . 54

[84] A. Hoecker *et al.*, "TMVA - Toolkit for Multivariate Data Analysis," arXiv:physics/0703039 [physics]. 55, 67, 105, 171, 172, 173

[85] D. Adams *et al.*, "Recommendations of the Physics Objects and Analysis Harmonisation Study Groups 2014," *ATL-PHYS-INT-2014-018* (2014) . 56

[86] **ATLAS** Collaboration, "Performance of Missing Transverse Momentum Reconstruction in Proton-Proton Collisions at 7 TeV with ATLAS," *Eur.Phys.J.* **C72** (2012) 1844, arXiv:1108.5602 [hep-ex]. 57, 124

[87] **ATLAS** Collaboration, "Expected performance of missing transverse momentum reconstruction for the ATLAS detector at $\sqrt{s}$ = 13 TeV," *ATL-PHYS-PUB-2015-023* (2015) . 57

[88] **ATLAS** Collaboration, "Performance of missing transverse momentum reconstruction for the ATLAS detector in the first proton-proton collisions at at $\sqrt{s}$= 13 TeV," *ATL-PHYS-PUB-2015-027* (2015) . 57

[89] **ATLAS** Collaboration, "Pile-up Suppression in Missing Transverse Momentum Reconstruction in the ATLAS Experiment in Proton-Proton Collisions at $\sqrt{s}$ = 8 TeV," *ATLAS-CONF-2014-019* (2014) . 57, 124

[90] **ATLAS** Collaboration, "Measurement of the missing transverse momentum based on tracks in proton-proton collisions at $\sqrt{s}$ = 900 GeV centre-of-mass energy with the ATLAS detector," *ATLAS-CONF-2010-020* (2010) . 57, 124

[91] **ATLAS** Collaboration, "Performance of the ATLAS muon trigger in 2011," *ATLAS-CONF-2012-099* (2012) . 58

[92] R. Achenbach *et al.*, "The ATLAS level-1 calorimeter trigger," *JINST* **3** (2008) P03001. 59

[93] V. Andrei *et al.*, "The upgrade of the PreProcessor system of the ATLAS level-1 calorimeter trigger," *Journal of Instrumentation* **7** no. 12, (2012) C12026. 59

[94] **ATLAS** Collaboration, "The ATLAS Simulation Infrastructure," *Eur. Phys. J.* **C70** (2010) 823–874, `arXiv:1005.4568 [physics.ins-det]`. 61, 62

[95] **ATLAS** Collaboration, "ATLAS computing: Technical design report," *CERN-LHCC-2005-022, ATLAS-TRD-017* (2005) . 61

[96] **ATLAS** Collaboration, "ATLAS analysis model," *J. Phys. Conf. Ser.* **119** (2008) 042012. 61

[97] A. Buckley *et al.*, "Implementation of the ATLAS Run 2 event data model," *J. Phys. Conf. Ser.* **664** no. 7, (2015) 072045. 61, 62

[98] **ATLAS** Collaboration, "AGIS: The ATLAS Grid Information System," *J. Phys. Conf. Ser.* **513** (2014) 032001. 61

[99] R. Brun and F. Rademakers, "ROOT: An object oriented data analysis framework," *Nucl. Instrum. Meth.* **A389** (1997) 81–86. 61

[100] **GEANT4** Collaboration, "GEANT4: A Simulation toolkit," *Nucl. Instrum. Meth.* **A506** (2003) 250–303. 62

[101] T. Sjöstrand, S. Mrenna, and P. Z. Skands, "PYTHIA 6.4 Physics and Manual," *JHEP* **05** (2006) 026, arXiv:hep-ph/0603175 [hep-ph]. 62, 69, 109, 135

[102] T. Sjöstrand, S. Mrenna, and P. Z. Skands, "A Brief Introduction to PYTHIA 8.1," *Comput. Phys. Commun.* **178** (2008) 852–867, arXiv:0710.3820 [hep-ph]. 62, 83, 109, 135

[103] **ATLAS** Collaboration, "Simulation of Pile-up in the ATLAS Experiment," *J. Phys. Conf. Ser.* **513** (2014) 022024. 62

[104] **ATLAS** Collaboration, "Search for charged Higgs bosons through the violation of lepton universality in $t\bar{t}$ events using pp collision data at $\sqrt{s} = 7$ TeV with the ATLAS experiment," *JHEP* **03** (2013) 076, arXiv:1212.3572 [hep-ex]. 63

[105] **ATLAS** Collaboration, "Search for charged Higgs bosons decaying via $H^+ \to \tau\nu$ in top quark pair events using pp collision data at $\sqrt{s} = 7$ TeV with the ATLAS detector," *JHEP* **06** (2012) 039, arXiv:1204.2760 [hep-ex]. 63

[106] **ATLAS** Collaboration, "Search for the neutral Higgs bosons of the Minimal Supersymmetric Standard Model in pp collisions at $\sqrt{s} = 7$ TeV with the ATLAS detector," *JHEP* **02** (2013) 095, arXiv:1211.6956 [hep-ex]. 63

[107] **ATLAS** Collaboration, "Search for a heavy narrow resonance decaying to $e\mu$, $e\tau$, or $\mu\tau$ with the ATLAS detector in $\sqrt{s} = 7$ TeV pp collisions at the LHC," *Phys. Lett.* **B723** (2013) 15–32, arXiv:1212.1272 [hep-ex]. 63

[108] **ATLAS** Collaboration, "Search for supersymmetry in events with large missing transverse momentum, jets, and at least one tau lepton in 20 fb^{-1} of $\sqrt{s} = 8$ TeV proton-proton collision data with the ATLAS detector," *JHEP* **09** (2014) 103, arXiv:1407.0603 [hep-ex]. 63

[109] **ATLAS** Collaboration, "Search for the direct production of charginos, neutralinos and staus in final states with at least two hadronically decaying taus and missing transverse momentum in pp collisions at $\sqrt{s} = 8$ TeV with the

ATLAS detector," *JHEP* **10** (2014) 096, arXiv:1407.0350 [hep-ex]. 63

[110] **ATLAS** Collaboration, "A search for high-mass resonances decaying to $\tau^+\tau^-$ in *pp* collisions at $\sqrt{s} = 7$ TeV with the ATLAS detector," *Phys. Lett.* **B719** (2013) 242–260, arXiv:1210.6604 [hep-ex]. 63

[111] **ATLAS** Collaboration, "Search for third generation scalar leptoquarks in pp collisions at $\sqrt{s} = 7$ TeV with the ATLAS detector," *JHEP* **06** (2013) 033, arXiv:1303.0526 [hep-ex]. 63

[112] **ATLAS** Collaboration, "Performance of the ATLAS tau trigger in 2011," *ATLAS-CONF-2013-006* (2013) . 66

[113] M. L. Mangano, M. Moretti, F. Piccinini, R. Pittau, and A. D. Polosa, "ALPGEN, a generator for hard multiparton processes in hadronic collisions," *JHEP* **07** (2003) 001, arXiv:hep-ph/0206293 [hep-ph]. 69, 109

[114] G. Corcella *et al.*, "HERWIG 6: An Event generator for hadron emission reactions with interfering gluons (including supersymmetric processes)," *JHEP* **01** (2001) 010, arXiv:hep-ph/0011363 [hep-ph]. 69, 109

[115] S. Frixione and B. R. Webber, "Matching NLO QCD computations and parton shower simulations," *JHEP* **06** (2002) 029, arXiv:hep-ph/0204244 [hep-ph]. 69, 123

[116] B. P. Kersevan and E. Richter-Was, "The Monte Carlo event generator AcerMC versions 2.0 to 3.8 with interfaces to PYTHIA 6.4, HERWIG 6.5 and ARIADNE 4.1," *Comput. Phys. Commun.* **184** (2013) 919–985, arXiv:hep-ph/0405247 [hep-ph]. 69

[117] Z. Was and P. Golonka, "TAUOLA as tau Monte Carlo for future applications," *Nucl. Phys. Proc. Suppl.* **144** (2005) 88–94, arXiv:hep-ph/0411377 [hep-ph]. 69

[118] P. M. Nadolsky et al., "Implications of CTEQ global analysis for collider observables," *Phys. Rev. D* **78** (2008) 013004, arXiv:0802.0007 [hep-ph]. 70, 109, 135

[119] H.-L. Lai *et al.*, "New parton distributions for collider physics," *Phys. Rev. D* **82** (2010) 074024, arXiv:1007.2241 [hep-ph]. 70, 109, 135

[120] **ATLAS** Collaboration, "Search for the Standard Model Higgs boson in $H \to \tau\tau$ decays in proton-proton collisions with the ATLAS detector," *ATLAS-CONF-2012-160* (2012) . 72

[121] LHC Performance Reaches New Highs. `https://home.cern/about/updates/2016/07/lhc-performance-reaches-new-highs`. 79

[122] H. Wind, "Principal component analysis, Pattern recognition for track finding, Interpolation and functional representation," *CERN-EP-INT-81-12-REV* (1982) . 81

[123] ATLAS FTK Public Results. `https://twiki.cern.ch/twiki/bin/view/AtlasPublic/FTKPublicResults`. 89, 95

[124] G. Cowan, K. Cranmer, E. Gross, and O. Vitells, "Asymptotic formulae for likelihood-based tests of new physics," *Eur. Phys. J. C* **71** (2011) 1554 [*Erratum ibid.* **C 73** (2013) 2501], `arXiv:1007.1727 [physics.data-an]`. 107

[125] A.L. Read, "Presentation of search results: the CL_s technique," *J. Phys. G* **28** (2002) 2693. 107

[126] T. Melia, P. Nason, R. Rontsch, and G. Zanderighi, "W^+W^-, WZ and ZZ production in the POWHEG BOX," *JHEP* **11** (2011) 078, `arXiv:1107.5051 [hep-ph]`. 109

[127] S. Frixione, P. Nason, and G. Ridolfi, "A Positive-weight next-to-leading-order Monte Carlo for heavy flavour hadroproduction," *JHEP* **09** (2007) 126, `arXiv:0707.3088 [hep-ph]`. 109

[128] E. Re, "Single-top Wt-channel production matched with parton showers using the POWHEG method," *Eur. Phys. J. C* **71** (2011) 1547, `arXiv:1009.2450 [hep-ph]`. 109

[129] T. Gleisberg *et al.*, "Event generation with SHERPA 1.1," *JHEP* **02** (2009) 007, `arXiv:0811.4622 [hep-ph]`. 109, 135

[130] A. Sherstnev and R. S. Thorne, "Parton distributions for the LHC," *Eur. Phys. J. C* **55** (2009) 553, `arXiv:0711.2473 [hep-ph]`. 109

[131] J. Alwall, M. Herquet, F. Maltoni, O. Mattelaer, and T. Stelzer, "MadGraph 5 : Going Beyond," *JHEP* **06** (2011) 128, arXiv:1106.0522 [hep-ph]. 109

[132] S. Dittmaier *et al.*, "Handbook of LHC Higgs Cross Sections: 1. Inclusive Observables," *CERN-2011-002* (2011) , arXiv:1101.0593 [hep-ph]. 109, 122

[133] S. Dittmaier *et al.*, "Handbook of LHC Higgs Cross Sections: 2. Differential Distributions," *CERN-2012-002* (2012) , arXiv:1201.3084 [hep-ph]. 109, 122

[134] M. Ciccolini, S. Dittmaier, and M. Krämer, "Electroweak radiative corrections to associated WH and ZH production at hadron colliders," *Phys. Rev. D* **68** (2003) 073003, arXiv:hep-ph/0306234 [hep-ph]. 109, 136

[135] O. Brein, A. Djouadi, and R. Harlander, "NNLO QCD corrections to the Higgs-strahlung processes at hadron colliders," *Phys. Lett. B* **579** (2004) 149–156, arXiv:hep-ph/0307206 [hep-ph]. 109, 136

[136] A. Denner, S. Dittmaier, S. Kallweit, and A. Muck, "EW corrections to Higgs strahlung at the Tevatron and the LHC with HAWK," *PoS* **EPS-HEP2011** (2011) 235, arXiv:1112.5258 [hep-ph]. 109, 123

[137] A. Djouadi, J. Kalinowski, and M. Spira, "HDECAY: A Program for Higgs boson decays in the standard model and its supersymmetric extension," *Comput. Phys. Commun.* **108** (1998) 56–74, arXiv:hep-ph/9704448 [hep-ph]. 109, 136

[138] S. Catani, L. Cieri, G. Ferrera, D. de Florian, and M. Grazzini, "Vector boson production at hadron colliders: a fully exclusive QCD calculation at NNLO," *Phys. Rev. Lett.* **103** (2009) 082001, arXiv:0903.2120 [hep-ph]. 109

[139] S. Catani and M. Grazzini, "An NNLO subtraction formalism in hadron collisions and its application to Higgs boson production at the LHC," *Phys. Rev. Lett.* **98** (2007) 222002, arXiv:hep-ph/0703012 [hep-ph]. 109

[140] M. Czakon and A. Mitov, "Top++: A Program for the Calculation of the Top-Pair Cross-Section at Hadron Colliders," *Comput. Phys. Commun.* **185** (2014) 2930, arXiv:1112.5675 [hep-ph]. 109, 136

[141] J. M. Campbell and R. Ellis, "MCFM for the Tevatron and the LHC," *Nucl. Phys. Proc. Suppl.* **205-206** (2010) 10–15, arXiv:1007.3492 [hep-ph]. 109, 123

[142] T. Binoth, G. Ossola, C. Papadopoulos, and R. Pittau, "NLO QCD corrections to tri-boson production," *JHEP* **06** (2008) 082, arXiv:0804.0350 [hep-ph]. 109, 123

[143] P. Perret, "Status and Prospects for Heavy Flavour Physics at LHC," *PoS* **HQL2010** (2010) 081, arXiv:1012.0511 [hep-ex]. 113

[144] G. Luisoni, P. Nason, C. Oleari, and F. Tramontano, "$HW^{\pm}$/HZ + 0 and 1 jet at NLO with the POWHEG BOX interfaced to GoSam and their merging within MiNLO," *JHEP* **10** (2013) 083, arXiv:1306.2542 [hep-ph]. 123, 135

[145] M. Botje *et al.*, "The PDF4LHC Working Group Interim Recommendations," arXiv:1101.0538 [hep-ph]. 123

[146] A. D. Martin, W. J. Stirling, R. S. Thorne, and G. Watt, "Parton distributions for the LHC," *Eur. Phys. J.* **C63** (2009) 189–285, arXiv:0901.0002 [hep-ph]. 123, 134, 144

[147] R. D. Ball *et al.*, "Parton distributions with LHC data," *Nucl. Phys.* **B867** (2013) 244–289, arXiv:1207.1303 [hep-ph]. 123, 144

[148] **ATLAS** Collaboration, "Jet energy resolution in proton–proton collisions at $\sqrt{s} = 7$ TeV recorded in 2010 with the ATLAS detector," *Eur. Phys. J. C* **73** (2013) 2306, arXiv:1210.6210 [hep-ex]. 123

[149] **ATLAS** Collaboration, "Calibration of b-tagging using dileptonic top pair events in a combinatorial likelihood approach with the ATLAS experiment," *ATLAS-CONF-2014-004* (2014) . 124

[150] **ATLAS** Collaboration, "Improved luminosity determination in pp collisions at $\sqrt{s} = 7$ TeV using the ATLAS detector at the LHC," *Eur. Phys. J. C* **73** (2013) 2518, arXiv:1302.4393 [hep-ex]. 125, 145

[151] Summary plots from the ATLAS Standard Model physics group. https://atlas.web.cern.ch/Atlas/GROUPS/PHYSICS/CombinedSummaryPlots/SM/. 134

[152] 13/8 TeV LHC luminosity ratios. http://www.hep.ph.ic.ac.uk/~wstirlin/plots/plots.html. 134

[153] P. Nason, "A new method for combining NLO QCD with shower Monte Carlo algorithms," *JHEP* **11** (2004) 040, arXiv:hep-ph/0409146 [hep-ph]. 135

[154] S. Frixione, P. Nason, and C. Oleari, "Matching NLO QCD computations with Parton Shower simulations: the POWHEG method," *JHEP* **11** (2007) 070, arXiv:0709.2092 [hep-ph]. 135

[155] S. Alioli, P. Nason, C. Oleari, and E. Re, "A general framework for implementing NLO calculations in shower Monte Carlo programs: the POWHEG BOX," *JHEP* **06** (2010) 043, arXiv:1002.2581 [hep-ph]. 135

[156] J. Alwall *et al.*, "The automated computation of tree-level and next-to-leading order differential cross sections, and their matching to parton shower simulations," *JHEP* **07** (2014) 079, arXiv:1405.0301 [hep-ph]. 135, 144

[157] T. Han and S. Willenbrock, "QCD correction to the $pp \to WH$ and ZH total cross-sections," *Phys. Lett.* **B273** (1991) 167–172. 136

[158] M. Aliev *et al.*, "HATHOR: HAdronic Top and Heavy quarks crOss section calculatoR," *Comput.Phys.Commun.* **182** (2011) 1034–1046, arXiv:1007.1327 [hep-ph]. 136

[159] M. Beneke, P. Falgari, S. Klein, and C. Schwinn, "Hadronic top-quark pair production with NNLL threshold resummation," *Nucl.Phys.* **B855** (2012) 695–741, arXiv:1109.1536 [hep-ph]. 136

[160] M. Czakon, P. Fiedler, and A. Mitov, "The total top quark pair production cross-section at hadron colliders through $O(\alpha_S^4)$," arXiv:1303.6254 [hep-ph]. 136

[161] M. Czakon and A. Mitov, "NNLO corrections to top pair production at hadron colliders: the quark-gluon reaction," *JHEP* **1301** (2013) 080, arXiv:1210.6832 [hep-ph]. 136

[162] M. Czakon and A. Mitov, "NNLO corrections to top-pair production at hadron colliders: the all-fermionic scattering channels," *JHEP* **1212** (2012) 054, arXiv:1207.0236 [hep-ph]. 136

[163] P. Baernreuther, M. Czakon, and A. Mitov, "Percent Level Precision Physics at the Tevatron: First Genuine NNLO QCD Corrections to $q\bar{q} \to t\bar{t} + X$,"

Phys.Rev.Lett. **109** (2012) 132001, arXiv:1204.5201 [hep-ph]. 136

[164] M. Cacciari, M. Czakon, M. Mangano, A. Mitov, and P. Nason, "Top-pair production at hadron colliders with next-to-next-to-leading logarithmic soft-gluon resummation," *Phys.Lett.* **B710** (2012) 612–622, arXiv:1111.5869 [hep-ph]. 136

[165] S. Hoeche, F. Krauss, M. Schonherr, and F. Siegert, "QCD matrix elements + parton showers: The NLO case," *JHEP* **04** (2013) 027, arXiv:1207.5030 [hep-ph]. 136

[166] S. Hoeche, F. Krauss, S. Schumann, and F. Siegert, "QCD matrix elements and truncated showers," *JHEP* **05** (2009) 053, arXiv:0903.1219 [hep-ph]. 136

[167] K. Arnold *et al.*, "VBFNLO: A Parton level Monte Carlo for processes with electroweak bosons," *Comput. Phys. Commun.* **180** (2009) 1661–1670, arXiv:0811.4559 [hep-ph]. 144

[168] K. Arnold *et al.*, "VBFNLO: A Parton Level Monte Carlo for Processes with Electroweak Bosons – Manual for Version 2.5.0," arXiv:1107.4038 [hep-ph]. 144

[169] J. Baglio *et al.*, "Release Note - VBFNLO 2.7.0," arXiv:1404.3940 [hep-ph]. 144

[170] $VH \to WW$ Prospects and Challenges for Run2. https://indico.cern.ch/event/307593/contributions/1676392/attachments/586786/807629/HSG3_VH_Rome_v0.pdf. 153

[171] I. Chakravarti, R. Laha, and J. Roy, *Handbook of methods of applied statistics*. No. v. 1 in Wiley series in probability and mathematical statistics. Wiley, 1967. 176, 184, 202

Appendix A: BDT Analysis

In chapter 5, a search for the WH production of the Higgs boson was presented using proton-proton collision data at $\sqrt{s} = 7$ and 8 TeV. In that analysis, the shapes of certain variables were used to provide the final separation between the signal and background processes in the signal regions (SRs). The variable that serves this purpose in the 3SF and 1SFOS SRs is the multivariate classifier from a Boosted Decision Trees (BDT) method [84]. This variable is called the "BDT score", and the specific BDT method that was developed is referred to as the BDT analysis. An overview of the BDT analysis is provided in this appendix.

BDT method

The BDT method begins with the training of a single decision tree. The training procedure involving a sample of signal events, a sample of background events and a set of discriminating variables. The events in the training samples are successively split using the variables, where each split defines a node. At each node the variable that gives the best separation between signal and background events is found, as well as the optimal value of the cut on this variable. The training of the decision tree is complete after a certain number of splits, and the tree is defined by the collection of cuts from each of its nodes. Continuing with the tree analogy, the final node in a sequence of cuts is called a *leaf*.

Once trained, the decision tree can be used to classify input events as either signal or background. A given input event will pass a particular sequence of cuts in the tree and end up at a particular leaf. A certain number of signal and background events from the training samples will also accumulate at that leaf. Depending on whether there is a majority of signal or background training events, the input event will be classified as signal or background, respectively.

A second decision tree is then trained, where an increased weight or *boost* is given to any signal and background events in the training samples that were misidentified by the first tree. In this way, the second tree will focus on the events misidentified by the first tree. A third tree is then trained that focuses on the events misidentified by the second tree and so on, until there is a collection of $O(1000)$ trees that make up the so-called *forest*. A weighted average is taken of the classification from all trees in the forest to form a discriminant called the *BDT score*.

This *boosting* procedure stabilizes the response of the decision trees to fluctuations in the training samples, and is able to considerably enhance the performance with respect to a single tree. The performance of the BDT method depends on the type of boosting used. The BDT analysis presented in this appendix uses a gradient scheme (BDTGs), as described in section 7.2 of ref. [84]. This boosting scheme is a common one that is used in many ATLAS BDT analyses.

BDT setup

Although the BDT analysis uses many of the default BDT parameters described in ref. [84], several parameters were optimized in order to maximize performance. These parameters include:

- The number of trees in the forest (NTrees).
- The minimum number of training events in a leaf (nEventsMin).
- Whether each tree is trained using only a random subsample of the total number of training events (UseBaggedGrad) and, if so, the fraction of the total that is used (GradBaggingFraction).
- The learning rate of the BDT (Shrinkage).
- The maximum number of layers in one tree (MaxDepth).

The above mentioned BDT parameters were tuned in order to ensure that the BDT analysis is robust against statistical fluctuations in the training samples. That is to say, there was no significant overtraining of the BDT. The tuned values of these parameters are shown in table A.1

BDT parameter	Value used
NTrees	1000
nEventsMin	1430
UseBaggedGrad	True
GradBaggingFraction	0.5
Shrinkage	0.1
MaxDepth	3

Table A.1 Parameters used in the BDT analysis.

BDT training

The BDT was trained using the signal, $WZ/W\gamma^*$ and ZZ^* MC samples described in section 5.2.2. The $WZ/W\gamma^*$ and ZZ^* processes were chosen since they are the dominant backgrounds in the 3SF and 1SFOS SRs. This corresponds to a signal training sample of 45000 events and a total background training sample of 180000 events. The training events are split into two sub-samples: one containing those with an even event-number (even sample), and the other containing those with an odd event-number (odd sample). The BDT is trained separately using the even and odd samples.

Prior to training, the events in in both the event and odd samples are required to pass selection criteria that follow those of the combined 3SF and 1SFOS SRs. These include the selections listed in table 5.5 down to the number of b-tagged jets requirement, followed by a looser E_T^{miss} threshold of 15 GeV. This looser threshold improves the statistics of the training samples, while still selecting a subset of events that are representative of those entering the final SRs.

An optimization study was performed to identify the set of discriminating variables, used in the training, that give the best separation between signal and background. The optimal set of variables were found to be: $p_{\text{T}}^{\ell_0}$, $p_{\text{T}}^{\ell_1}$, $p_{\text{T}}^{\ell_2}$, the magnitude of their vectorial sum ($|\Sigma \mathbf{p}_{\text{T}}{}^{\text{lep}}|$), $m_{\ell_0\ell_1}$, $m_{\ell_0\ell_2}$, E_T^{miss}, p_T^{miss} and $\Delta R_{\ell_0\ell_1}$. Figures A.1 and A.2 show the distributions of these nine variables after the training selections. The linear correlation amongst these variables are shown in figure A.3, while table A.2 lists each variables separation and importance[1].

[1] The separation $< S^2 >$ of a variable y is defined by the integral: $< S^2 >= \frac{1}{2}\int \frac{(\hat{y}_S(y)-\hat{y}_B(y))^2}{(\hat{y}_S(y)+\hat{y}_B(y))} dy$, where $\hat{y}_S$ and $\hat{y}_B$ are the signal and background PDFs of y, respectively [84]. The importance of a variable is derived by counting how many times it is used at a decision tree node, weighting each occurrence by the separation gain-squared it has achieved and by the number of events in the node [84].

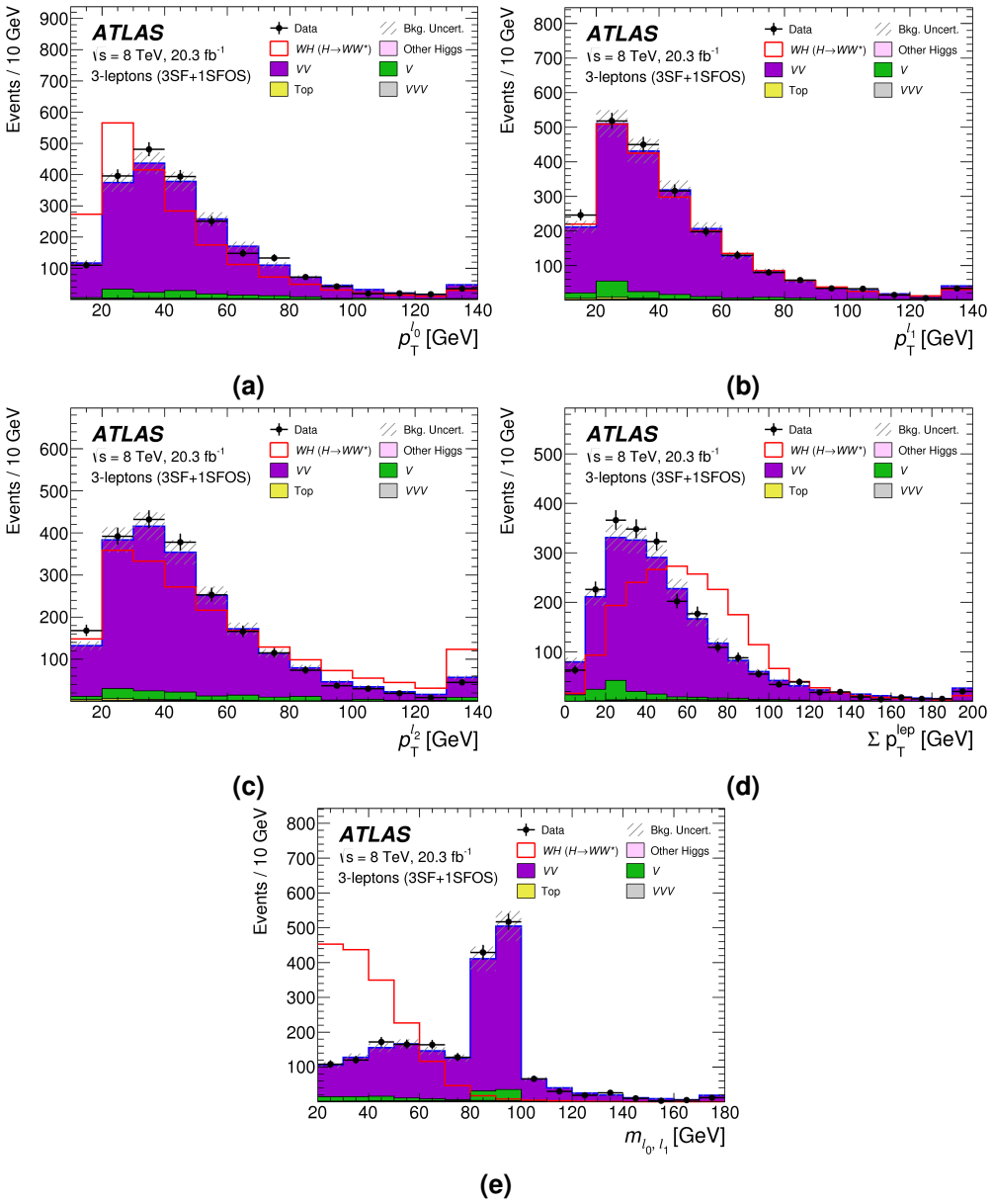

Figure A.1 Training variable distributions after the training selections: (a) $p_{\mathrm{T}}^{\ell_0}$, (b) $p_{\mathrm{T}}^{\ell_1}$, (c) $p_{\mathrm{T}}^{\ell_2}$, (d) $|\Sigma \mathbf{p}_{\mathrm{T}}{}^{\mathrm{lep}}|$ and (d) $m_{\ell_0\ell_1}$. The data (points) are compared to the background expectation (stacked filled histograms). The total uncertainty on the total background estimate is represented by the hatched area, and includes both the statistical and systematic components. The background NFs are applied. The signal (red line) is overlaid, and scaled by a factor of 500.

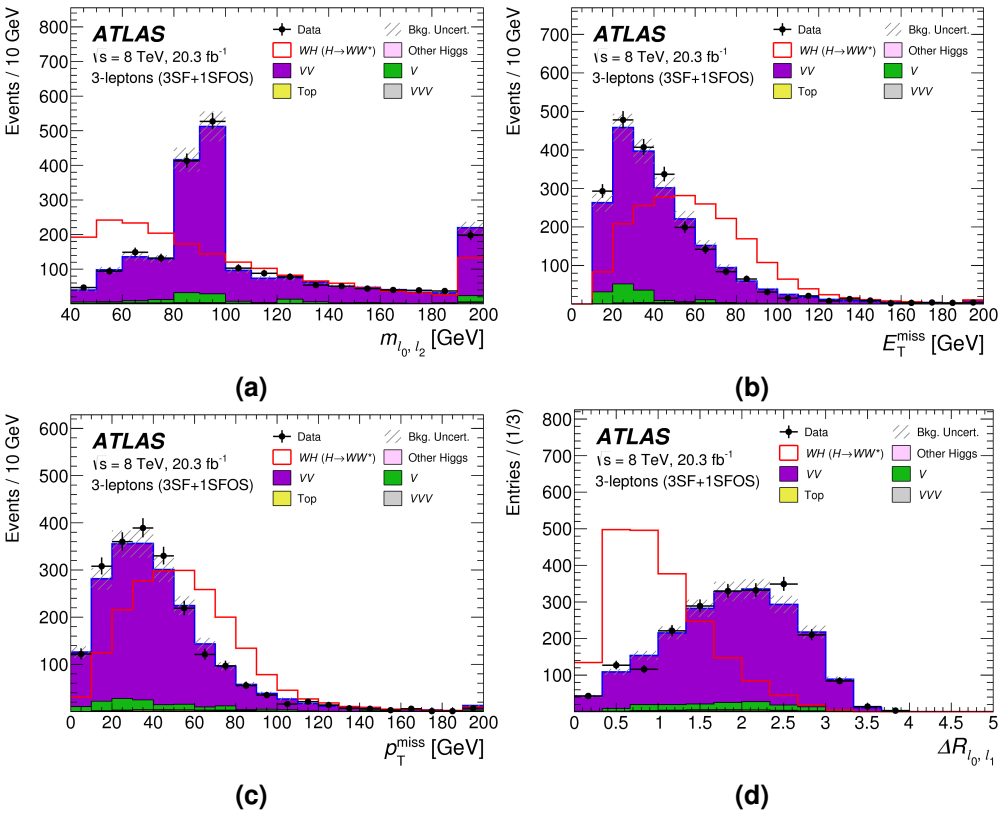

Figure A.2 Training variable distributions after the training selections: (a) $m_{\ell_0\ell_2}$, (b) E_T^{miss}, (c) p_T^{miss} and (d) $\Delta R_{\ell_0\ell_1}$. The plotting scheme follows the one described in the caption of figure A.1.

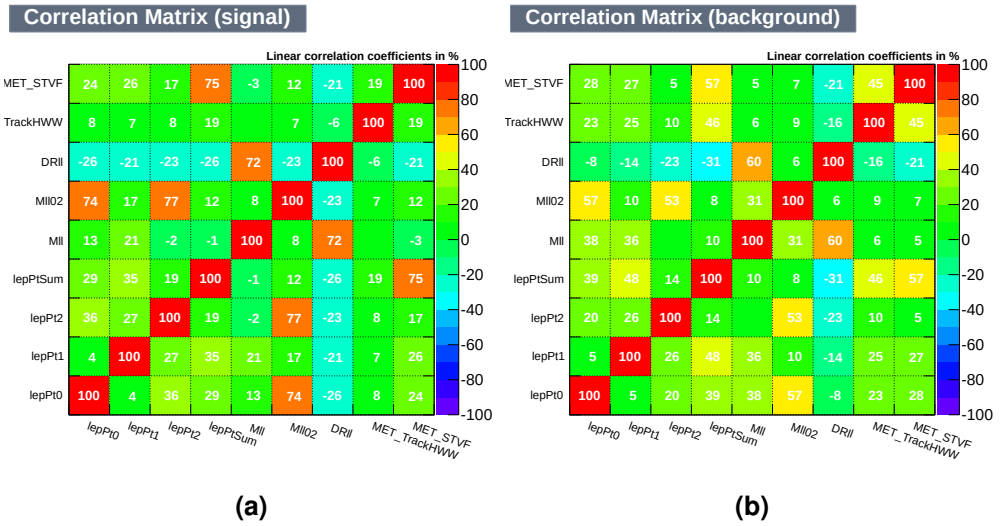

Figure A.3 The linear correlation amongst the training variables for (a) the signal and (b) the backgrounds.

Variable	Separation [%]	Importance [%]
$m_{\ell_0\ell_1}$	42.9	19.1
$\Delta R_{\ell_0\ell_1}$	29.9	14.1
$m_{\ell_0\ell_2}$	16.4	17.5
E_T^{miss}	6.81	9.3
$p_{\text{T}}^{\ell_0}$	4.7	7.6
p_T^{miss}	4.3	6.0
$\lvert\Sigma \mathbf{p}_{\text{T}}{}^{\text{lep}}\rvert$	3.5	10.0
$p_{\text{T}}^{\ell_2}$	1.9	8.1
$p_{\text{T}}^{\ell_1}$	0.4	8.4

Table A.2 Separation and importance for the training variables.

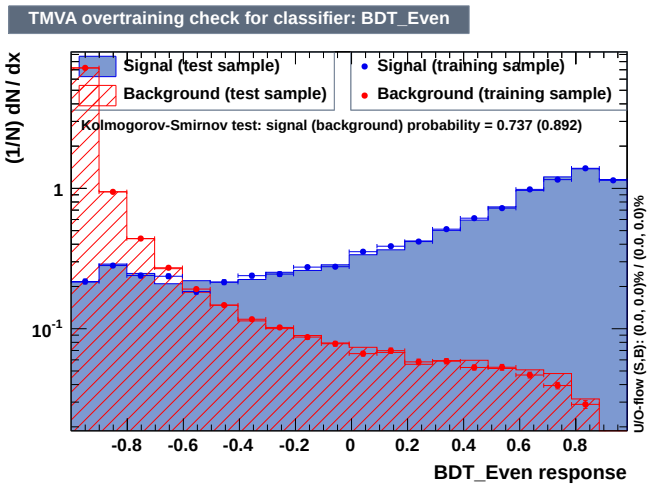

Figure A.4 Result of the Kolmogorov-Smirnov test to check the compatibility of the training and testing samples for the signal and the background.

In order to check that there is no significant overtraining of the BDT, a Kolmogorov-Smirnov (KS) test [171] is performed. Events in the even sample are classified using the BDT score from the odd sample training, and vice-versa. After this, the training and test samples are compared and the KS probability is evaluated. The KS test results are shown in figure A.4. The high values of the KS probability (0.74 for signal, 0.89 for background) are an indication of the robustness of the BDT against statistical fluctuations in the training samples.

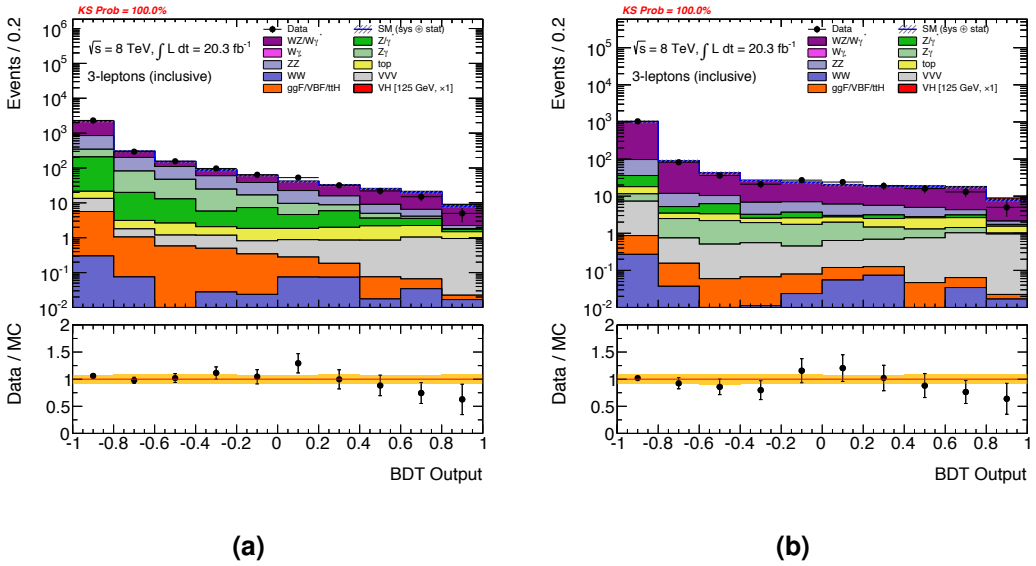

Figure A.5 Distributions of the BDT score in the combined 3SF and 1SFOS SRs, after applying the selections listed in table 5.5 up until (a) the number of b-tagged jets requirement and (b) the E_T^{miss} and p_T^{miss} requirements. The plotting scheme follows the one described in the caption of figure A.1, but with a more fine separation of the background categories, and with the signal (red) stacked on top of the total background. The KS test probability is indicated on the top left of each plot. The lower panel shows the ratio between the observed data and the total background expectation.

BDT classification

Each event in the data samples and all of MC samples described in section 5.2.2 can be classified using the BDT and assigned a BDT score. The classification scheme follows a similar principal to that of the KS test mentioned earlier. Input data and MC events with an even event-number are classified using the BDT score from the odd training sample, and vice-versa.

Distributions of the BDT score in the 3SF and 1SFOS SRs are shown in figure A.5. The distributions in the final SRs, with the binning used in the statistical fit, were shown in figures 5.9 and 5.10.

The BDT score distribution in each of the control regions is shown in figure A.6. Good agreement between the observed data and the background estimation is observed in all CRs.

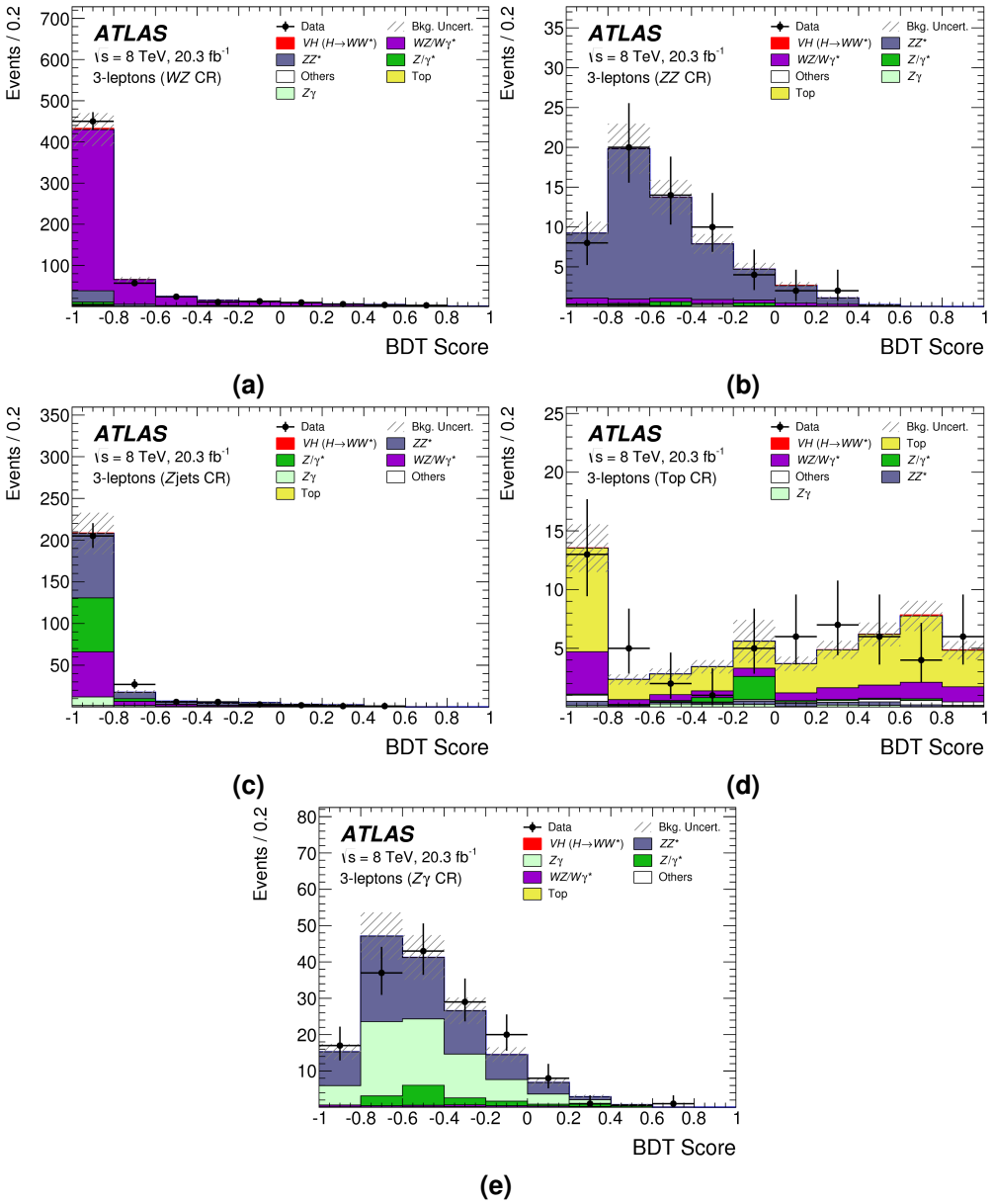

Figure A.6 Distributions of the BDT score in the (a) WZ CR, (b) ZZ CR, (c) Z+jets CR, (d) Top CR and (e) $Z\gamma$ CR. The total uncertainty on the total background estimate is represented by the hatched area, and includes both the statistical and systematic components. The background NFs are applied. The signal (red) is stacked on top of the total background estimation.

Appendix B: Results from the $H \rightarrow WW^*$ Combination

In chapter 5, a search for the Higgs boson decaying to WW^* was presented that used proton-proton collision data at $\sqrt{s} = 7$ and 8 TeV. This analysis specifically targeted the WH production mode with subsequent $WH \rightarrow WWW^* \rightarrow \ell\nu\ell\nu\ell\nu$ decay, where ℓ is an electron or muon. Several other $H \rightarrow WW^*$ analyses were also performed by the ATLAS Collaboration using the $\sqrt{s} = 7$ and 8 TeV data samples, with each analysis targeting a different production mode and subsequent decay process. All of these analyses were combined in order to maximize the precision of the signal strength and coupling measurements. The main results from this $H \rightarrow WW^*$ combination will be presented in this appendix.

$H \rightarrow WW^*$ analyses

In total, six analyses entered the ATLAS $H \rightarrow WW^*$ combination at $\sqrt{s} = 7$ and 8 TeV. These include:

1. A search for the ggF production mode with $H \rightarrow WW^* \rightarrow \ell\nu\ell\nu$ decay. This analysis targets events containing two opposite-sign leptons and at most one jet.

2. A search for the VBF production mode with $H \rightarrow WW^* \rightarrow e\nu\mu\nu$ decay. This analysis targets events containing two different-flavour and opposite-sign leptons, and at least two jets.

3. A search for the WH production mode with $WH \rightarrow WWW^* \rightarrow \ell\nu\ell\nu\ell\nu$ decay. This analysis targets events containing three leptons.

4. A search for the WH production mode with $WH \to WWW^* \to q\bar{q}e\nu\mu\nu$ decay. Here, the W boson from the production process decays hadronically ($W \to q\bar{q}$). This analysis targets events containing two different-flavour and opposite-sign leptons, and at least two jets.

5. A search for the WH production mode with $WH \to WWW^* \to \ell\nu q\bar{q}\ell\nu$ decay. Here, there is a hadronic decacy of one of the W bosons originating from the Higgs boson decay. This analysis targets events containing two same-sign leptons and at least two jets. Only the $\sqrt{s} = 8$ TeV data sample is used in this analysis.

6. A search for the ZH production mode with $ZH \to ZWW^* \to \ell\ell\ell\nu\ell\nu$ decay. This analysis targets events containing four leptons.

The ggF and VBF analyses were briefly described in section 2.4, with full details available in ref. [35]. The analysis targeting the WH production mode in events with three leptons was presented in chapter 5. The other analyses targeting the WH production mode and also the one targeting the ZH mode are described in ref. [3].

Combined signal strength measurements

The six previously mentioned $H\to WW^*$ analyses were combined in a statistical fit that follows a similar method as the one described in section 5.1.3. The likelihood function of the combined fit includes Poisson probability terms for every signal and control region in each analysis. For the experimental and theoretical uncertainties, the nuisance parameters are correlated amongst analyses if they originate from the same source. The nuisance parameters associated to background normalization factors are uncorrelated between analyses, since they cover different regions of phase-space. More information on the combined statistical fit procedure is available in refs. [3, 35].

A signal strength parameter is introduced into the fit for each of the Higgs boson production modes (μ^{ggF}, μ^{VBF}, μ^{WH} and μ^{ZH}), and they are correlated amongst analyses. Therefore, when extracting the observed signal strength for a particular production mode, the contributions from the other modes are treated as background with their yields determined by the global fit. All measurements are performed for a Higgs boson mass of 125 GeV, which is compatible with the measured value.

Using the combined statistical fit, the observed signal strengths for the WH and ZH production modes are measured to be:

$$\mu_{\text{obs}}^{WH} = 2.1\,^{+1.5}_{-1.3}\,(\text{stat.})\,^{+1.2}_{-0.8}\,(\text{sys.}), \qquad \mu_{\text{obs}}^{ZH} = 5.1\,^{+3.8}_{-3.0}\,(\text{stat.})\,^{+1.9}_{-0.9}\,(\text{sys.}) \tag{B.1}$$

The observed (expected) deviation from the background-only hypothesis corresponds to a local significance of 1.4 (0.77) σ for the WH mode and 2.0 (0.3) σ for the ZH mode.

The observed signal strength for the combined VH production modes ($VH = WH+ZH$) can also be measured:

$$\mu_{\text{obs}}^{VH} = 3.0\,^{+1.3}_{-1.1}\,(\text{stat.})\,^{+1.0}_{-0.7}\,(\text{sys.}) \tag{B.2}$$

This corresponds to an observed local significance of 2.5 σ, where 0.93 σ is expected in the presence of the signal.

For the ggF and VBF production modes, the observed signal strengths are measured to be:

$$\mu_{\text{obs}}^{\text{ggF}} = 0.98\,^{+0.19}_{-0.19}\,(\text{stat.})\,^{+0.22}_{-0.18}\,(\text{sys.}), \qquad \mu_{\text{obs}}^{\text{VBF}} = 1.28\,^{+0.45}_{-0.40}\,(\text{stat.})\,^{+0.32}_{-0.25}\,(\text{sys.}), \tag{B.3}$$

The combination provides evidence at 3.2 σ for the VBF production mode (2.6 σ expected), and strong evidence at 4.4 σ for the ggF mode (4.2 σ expected).

Finally, the observed signal strength for the combined ggF, VBF and VH production modes is measured to be:

$$\mu_{\text{obs}}^{\text{ggF+VBF+VH}} = 1.16\,^{+0.16}_{-0.15}\,(\text{stat.})\,^{+0.18}_{-0.15}\,(\text{sys.}) \tag{B.4}$$

The existence of the $H\to WW^*$ decay channel is confirmed at 6.5 σ, where 5.9 σ is expected. All of the measurements presented in this section are compatible with the SM expectations for a Higgs boson of mass 125 GeV.

Measurement of the couplings to vector bosons and fermions

The $H\to WW^*$ combination at $\sqrt{s} = 7$ and 8 TeV was also used to measure the coupling strength of the Higgs boson to vector bosons and fermions. These measurements were performed within the leading-order coupling framework described in section 2.4, and using the same benchmark model. This model assumes a universal coupling strength

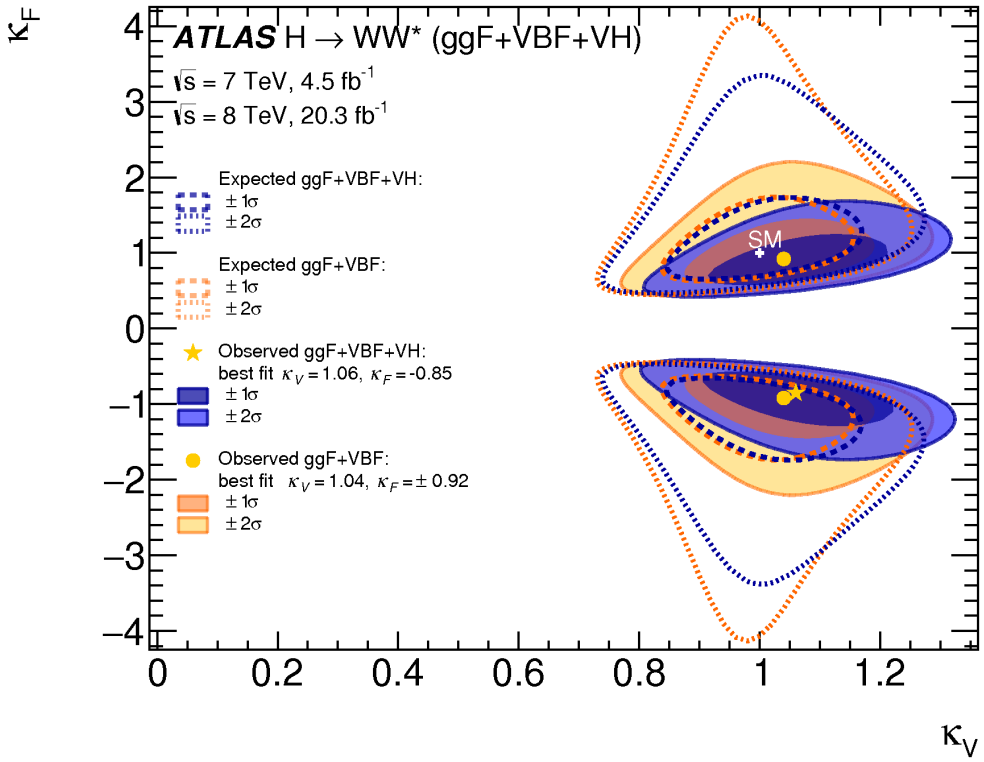

Figure B.1 The likelihood contours for the universal scale factors κ_V and κ_F, both with (purple) and without (orange) the contributions from the VH production mode analyses [3]. Both the expected (dashed) and observed (solid) contours are shown, corresponding to the 68% and 95% confidence levels. The yellow star and circles indicate the best fit values to the data, and the white cross represents the SM expectation.

scale factor to vector bosons (κ_V) and fermions (κ_F), and that no undetected or invisible Higgs boson decays exist.

The results of the combined fit for the benchmark model is shown in figure B.1. With the full $H\rightarrow WW^*$ combination including also the VH analyses, the best fit values for the magnitude of κ_V and κ_F are:

$$|\kappa_F| \;=\; 0.85\,^{+0.26}_{-0.20}\,, \qquad |\kappa_V| \;=\; 1.06\,^{+0.10}_{-0.10}\,, \tag{B.5}$$

which are compatible with the SM expectations of unity within the uncertainties.

The fit to the data has two local minima, with a slight preference for the negative κ_F solution at 0.5 σ. Sensitivity to the sign of κ_F comes from the analysis targeting the ZH production mode, and originates from the negative interference between the box and triangle diagrams in the $gg \rightarrow ZH$ process [3].

Appendix C: Additional Plots from the $\sqrt{s} = 7$ and 8 TeV Analysis

This appendix contains additional plots from the $\sqrt{s} = 7$ and 8 TeV analysis presented in chapter 5 that searched for the WH production of the Higgs boson with $H \rightarrow WW^*$ decay. This will include:

- Distributions in the control regions for the $\sqrt{s} = 8$ TeV samples (figures C.1-C.5).
- Distributions in the signal regions for the $\sqrt{s} = 8$ TeV samples (figures C.6-C.8).
- Distributions in the control regions for the $\sqrt{s} = 7$ TeV samples (figures C.9-C.13).
- Distributions in the signal regions for the $\sqrt{s} = 7$ TeV samples (figures C.14-C.16).
- A summary of the performance of the statistical fit for the combined $\sqrt{s} = 7$ and 8 TeV samples (figure C.17).

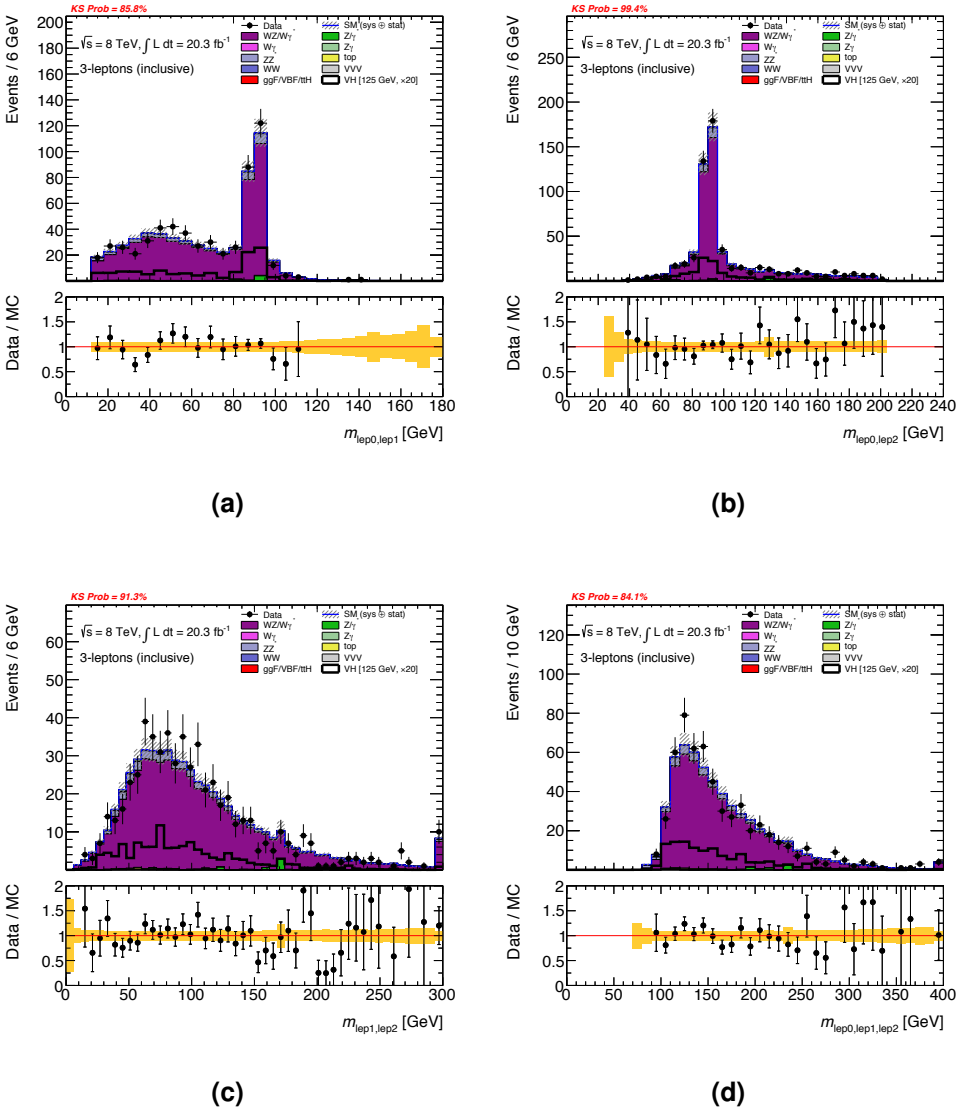

Figure C.1 Distributions in the WZ CR of the $\sqrt{s} = 8$ TeV analysis for (a) $m_{\ell_0\ell_1}$, (b) $m_{\ell_0\ell_2}$, (c) $m_{\ell_1\ell_2}$ and (d) $m_{\ell\ell\ell}$. The data (points) are compared to the background expectation (stacked filled histograms). The total uncertainty on the total background estimate is represented by the hatched area, and includes both the statistical and systematic components. The background NFs are applied. The signal (black line) is overlaid, and scaled by a factor of 20. The KS test probability [171] is indicated on the top left of each plot. The lower panel shows the ratio between the observed data and the total background expectation.

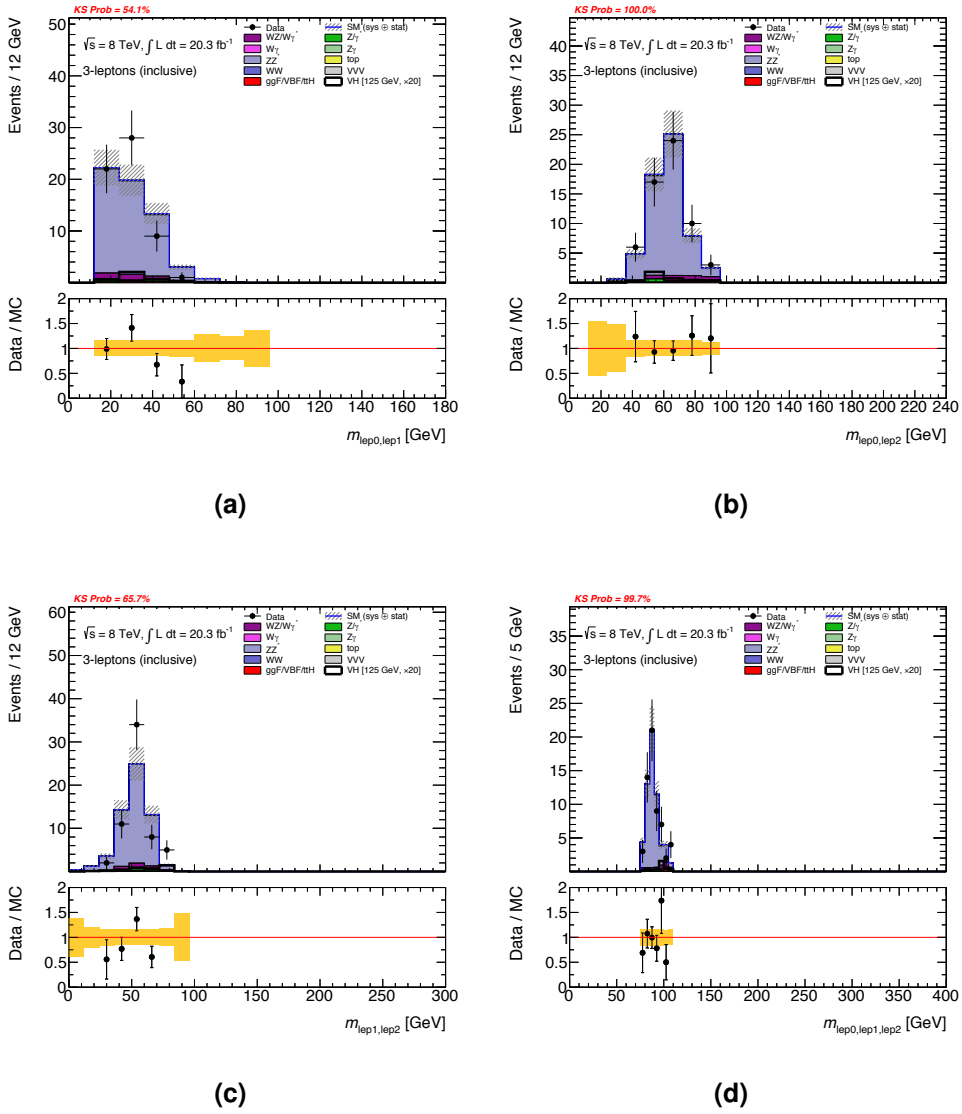

Figure C.2 Distributions in the ZZ CR of the $\sqrt{s} = 8$ TeV analysis for (a) $m_{\ell_0\ell_1}$, (b) $m_{\ell_0\ell_2}$, (c) $m_{\ell_1\ell_2}$ and (d) $m_{\ell\ell\ell}$. The plotting scheme follows the one described in the caption of figure C.1.

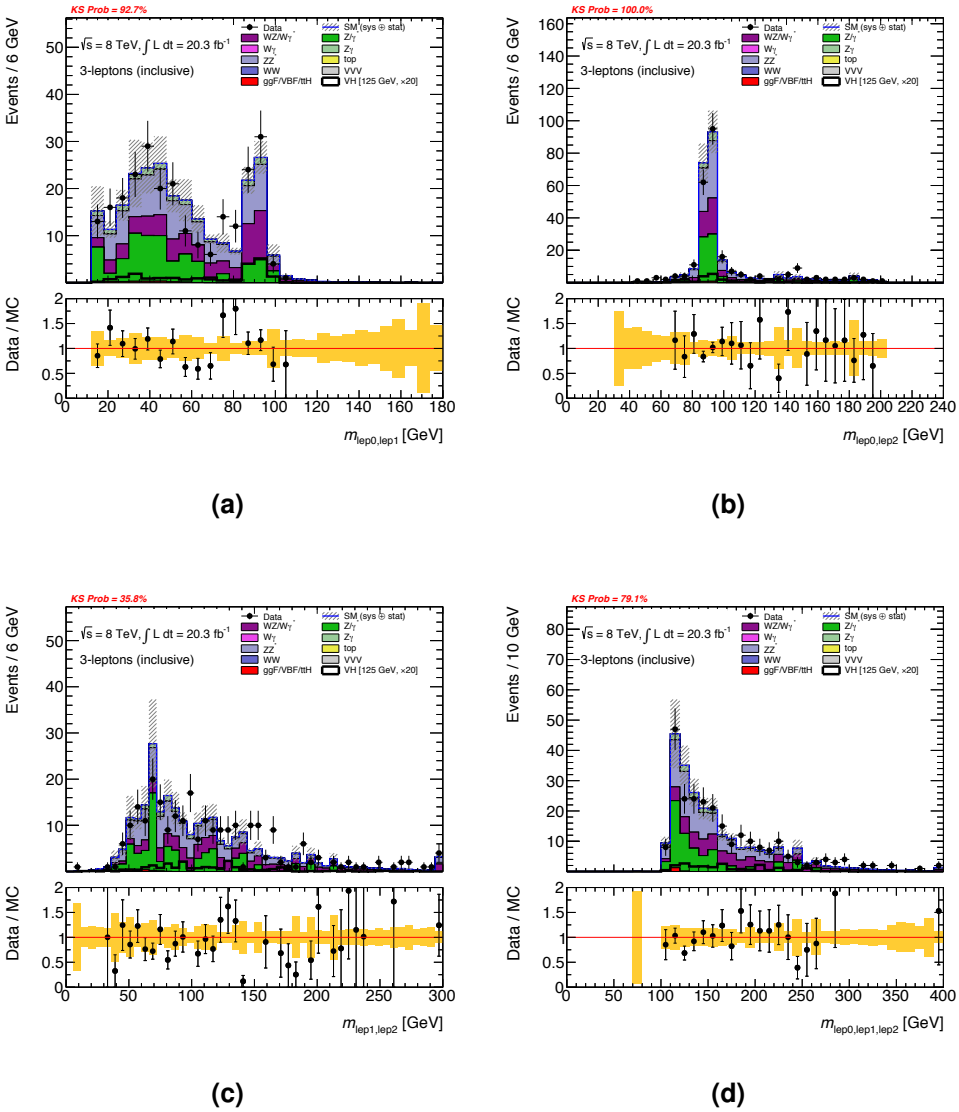

Figure C.3 Distributions in the Z+jets CR of the $\sqrt{s} = 8$ TeV analysis for (a) $m_{\ell_0\ell_1}$, (b) $m_{\ell_0\ell_2}$, (c) $m_{\ell_1\ell_2}$ and (d) $m_{\ell\ell\ell}$. The plotting scheme follows the one described in the caption of figure C.1.

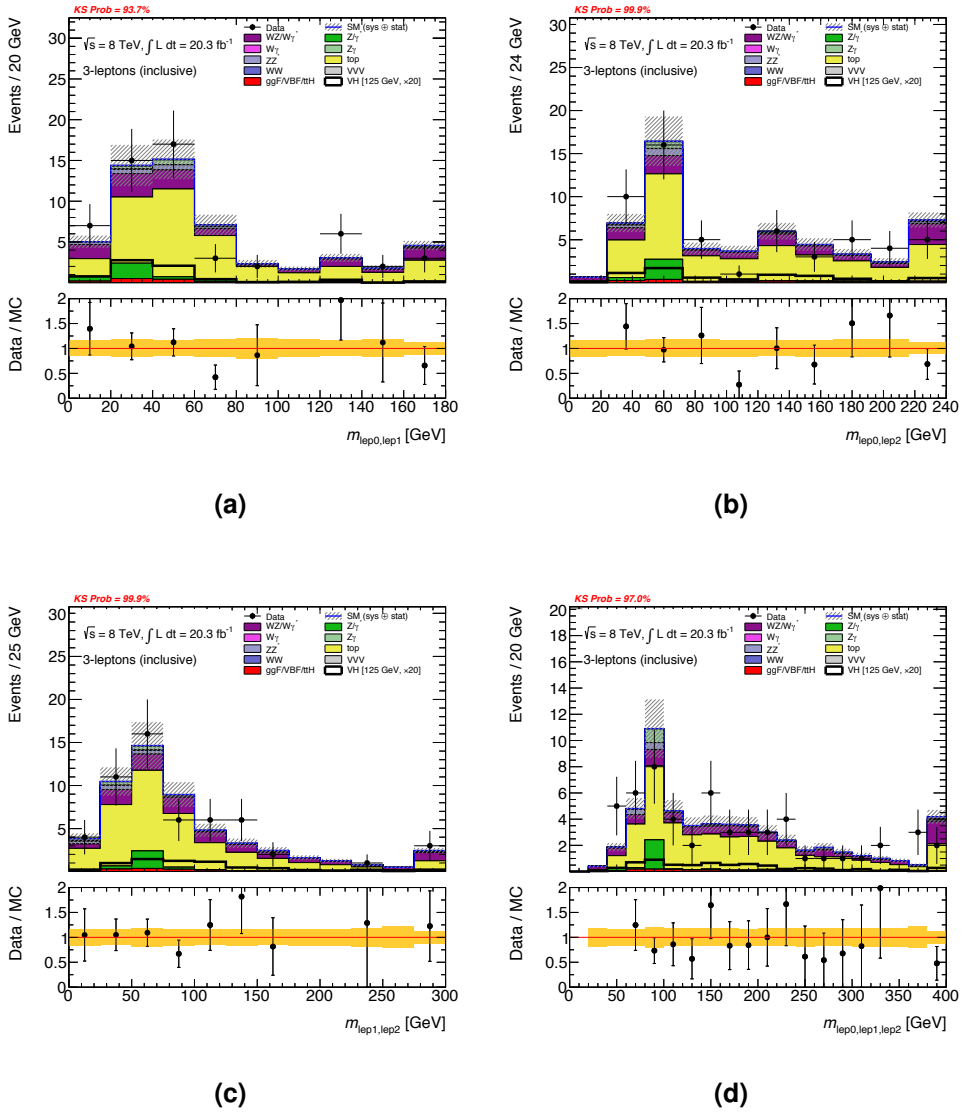

Figure C.4 Distributions in the Top CR of the $\sqrt{s} = 8$ TeV analysis for (a) $m_{\ell_0\ell_1}$, (b) $m_{\ell_0\ell_2}$, (c) $m_{\ell_1\ell_2}$ and (d) $m_{\ell\ell\ell}$. The plotting scheme follows the one described in the caption of figure C.1.

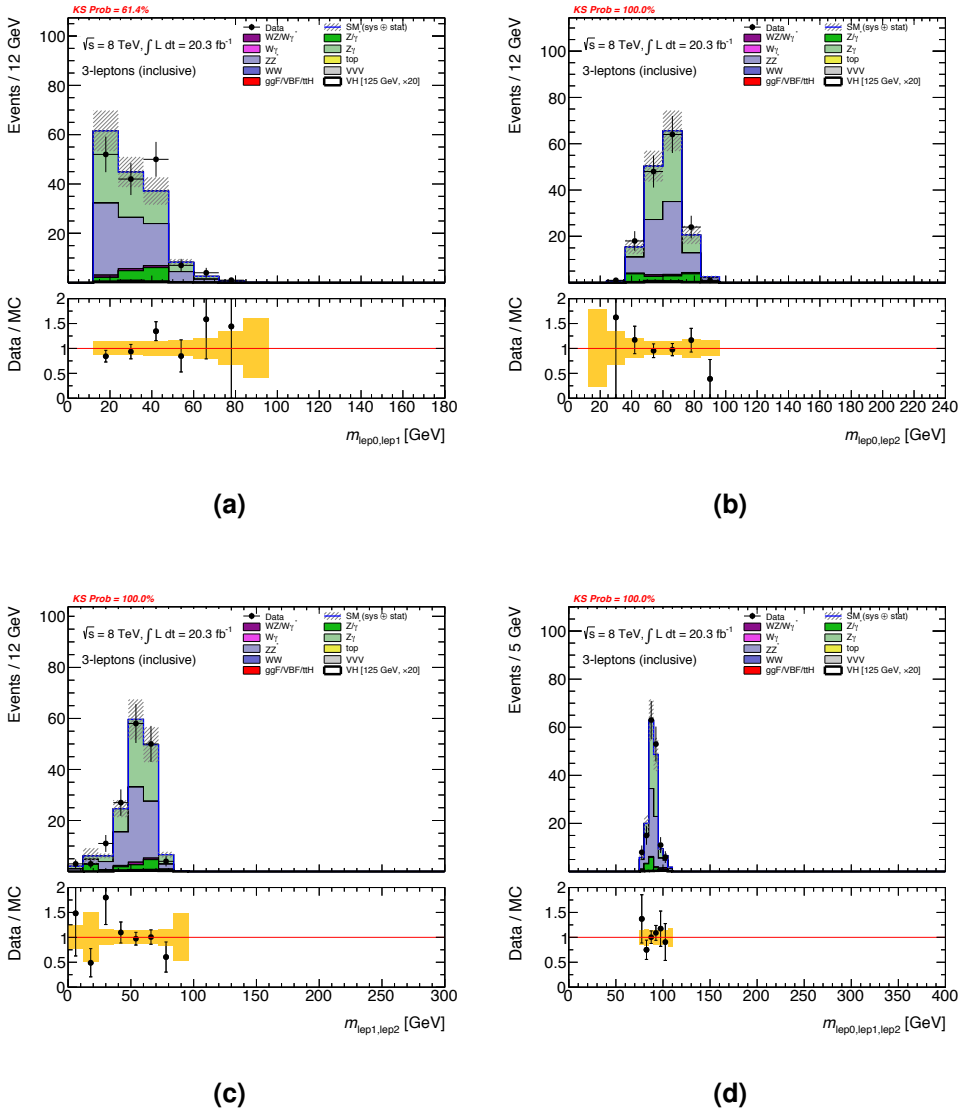

Figure C.5 Distributions in the $Z\gamma$ CR of the $\sqrt{s} = 8$ TeV analysis for (a) $m_{\ell_0\ell_1}$, (b) $m_{\ell_0\ell_2}$, (c) $m_{\ell_1\ell_2}$ and (d) $m_{\ell\ell\ell}$. The plotting scheme follows the one described in the caption of figure C.1.

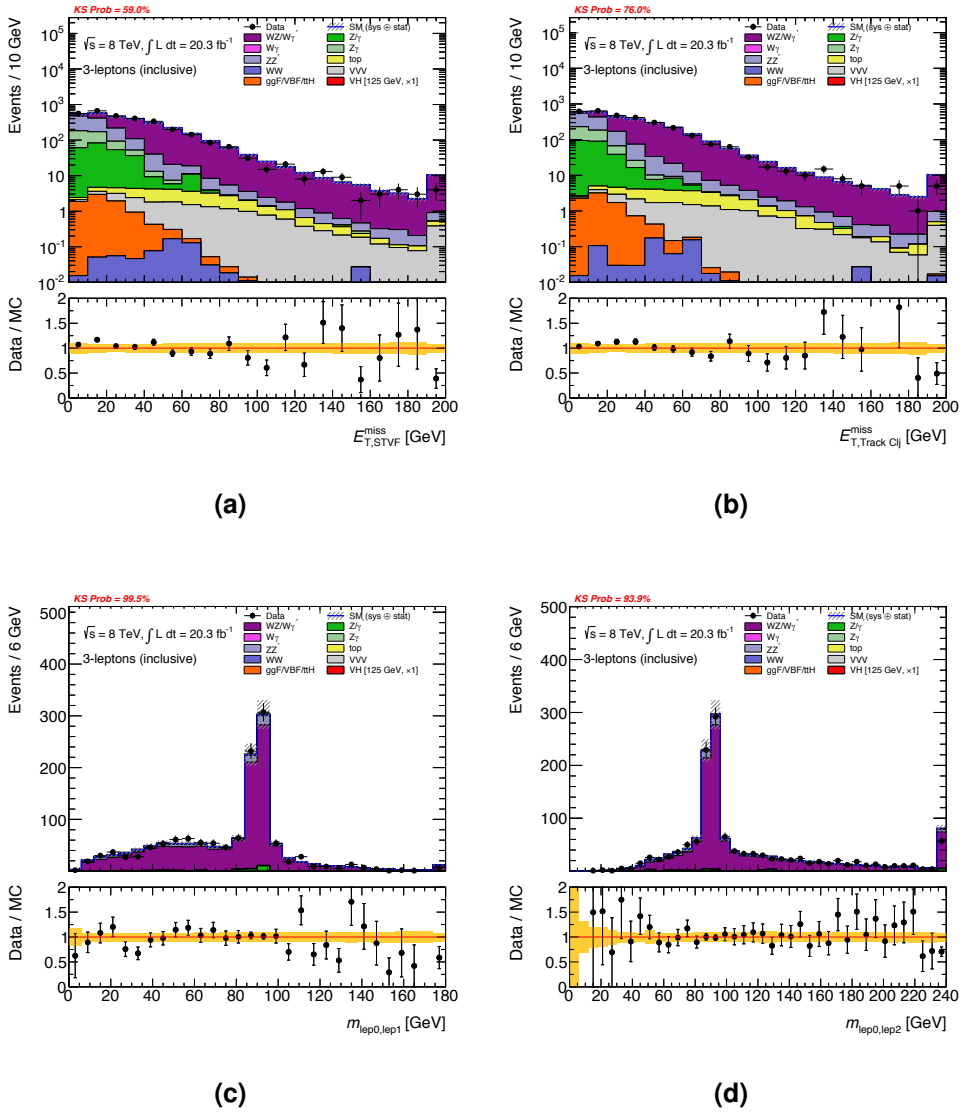

Figure C.6 Distributions in the combined 3SF and 1SFOS SRs of the $\sqrt{s} = 8$ TeV analysis for (a) E_T^{miss}, (b) p_T^{miss}, (c) $m_{\ell_0\ell_1}$ and (d) $m_{\ell_0\ell_2}$. Distributions (a) and (b) are after applying the selections in table 5.5 down to the number of b-tagged jets requirement, while (c) and (d) are after the E_T^{miss} and p_T^{miss} selections. The plotting scheme follows the one described in the caption of figure C.1, but with the signal (red) stacked on top of the total background.

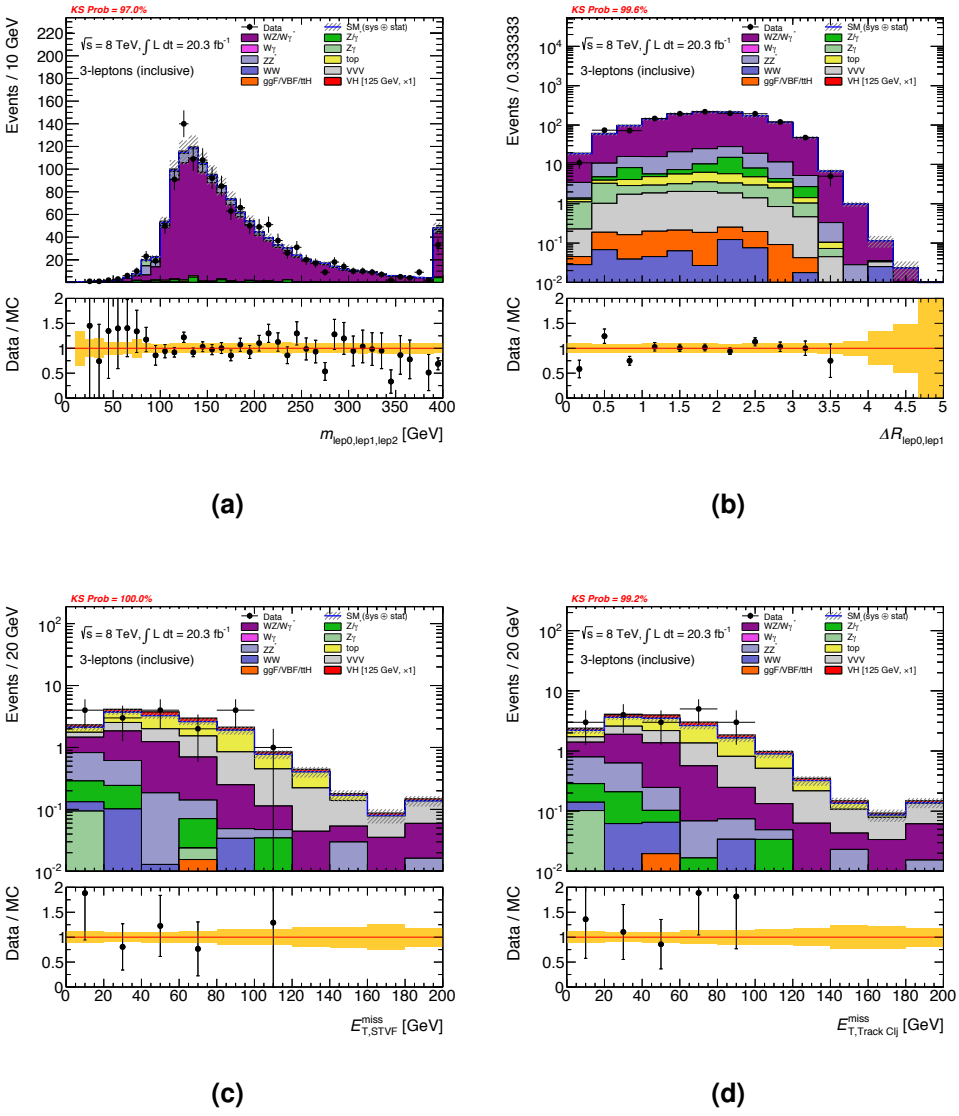

Figure C.7 Distributions of (a) $m_{\ell\ell\ell}$ and (b) $\Delta R_{\ell_0\ell_1}$ in the combined 3SF and 1SFOS SRs of the $\sqrt{s}$ = 8 TeV analysis, as well as (c) E_T^{miss} and (d) p_T^{miss} in the 0SFOS SR. Distributions (a) and (b) are after applying the selections in table 5.5 down to the E_T^{miss} and p_T^{miss} requirements, while (c) and (d) are after the number of b-tagged jets requirement. The plotting scheme follows the one described in the caption of figure C.6.

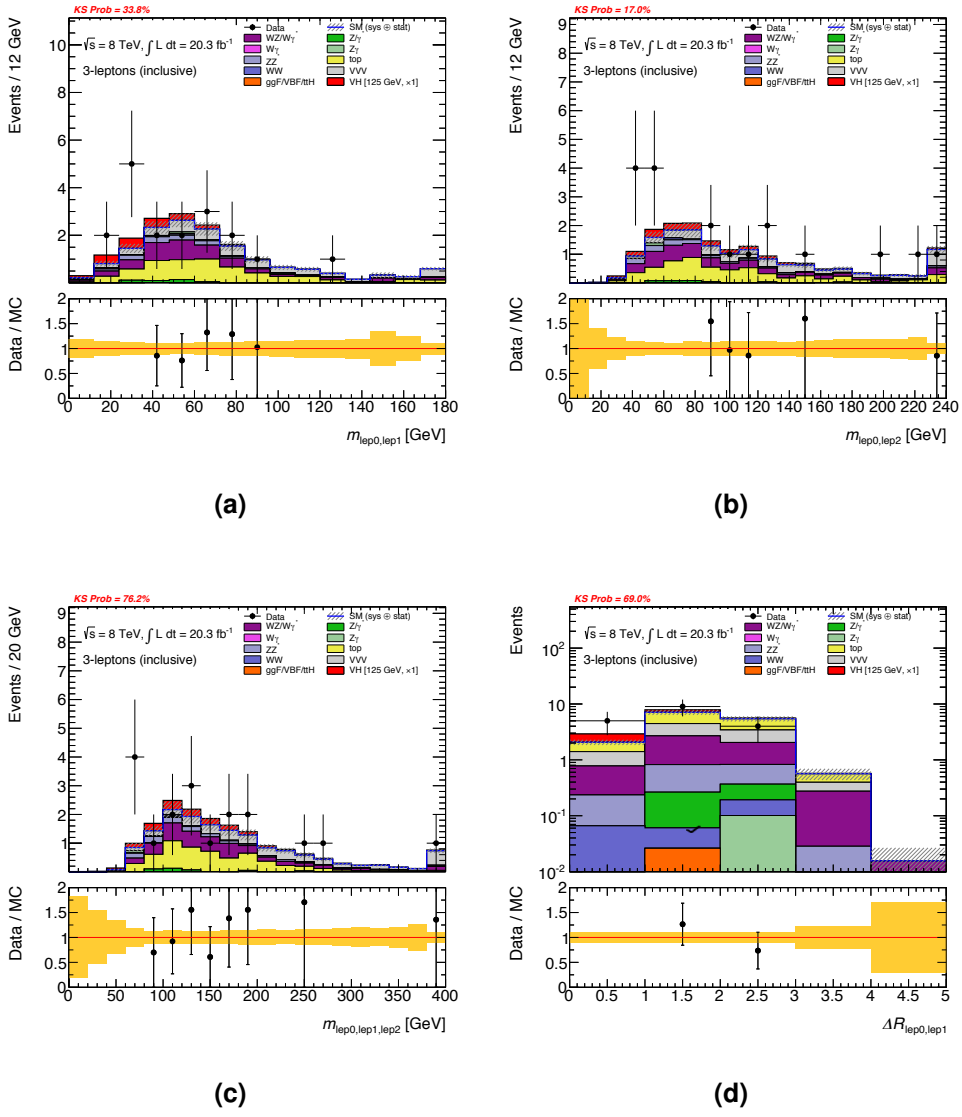

Figure C.8 Distributions in the 0SFOS SR of the $\sqrt{s} = 8$ TeV analysis for (a) $m_{\ell_0\ell_1}$, (b) $m_{\ell_0\ell_2}$, (c) $m_{\ell\ell\ell}$ and (d) $\Delta R_{\ell_0\ell_1}$. All distributions are after applying the selections in table 5.5 down to the number of b-tagged jets requirement. The plotting scheme follows the one described in the caption of figure C.6.

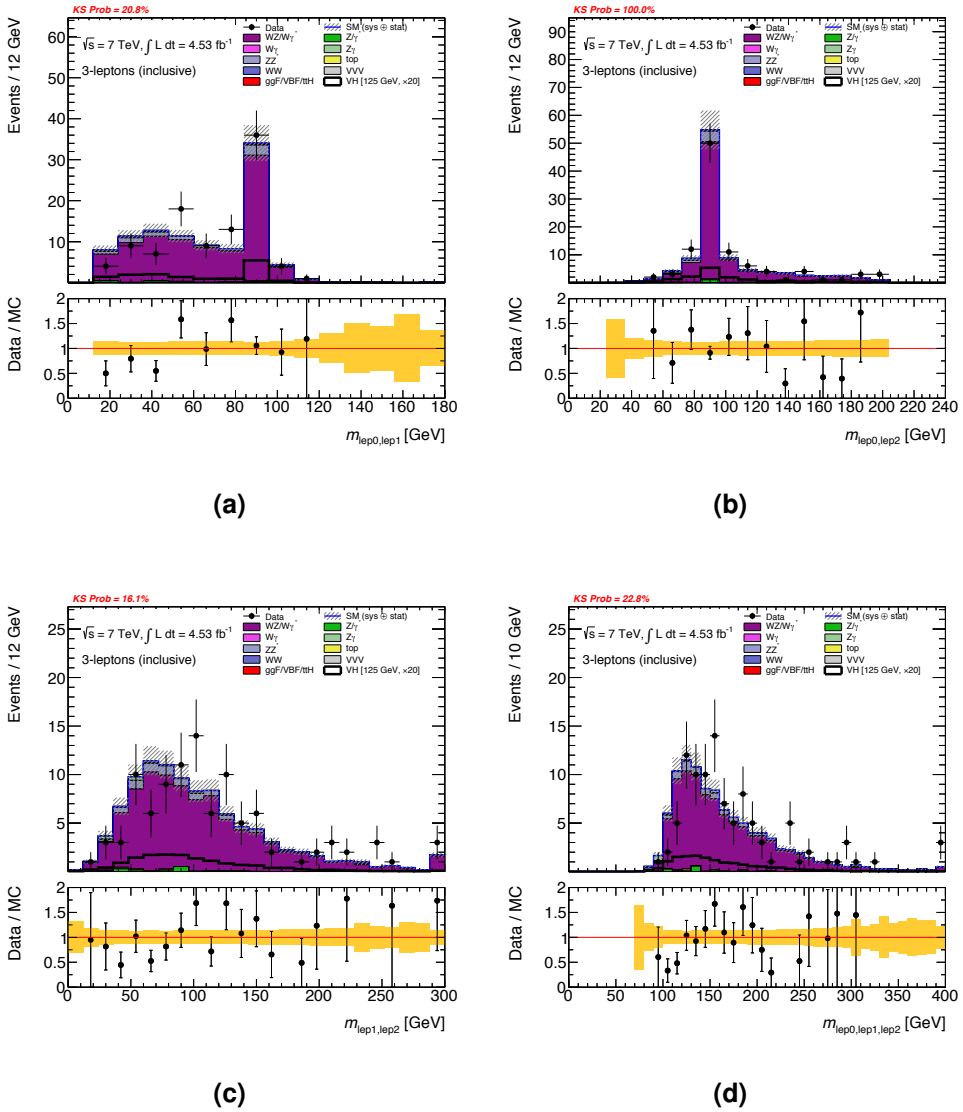

Figure C.9 Distributions in the WZ CR of the $\sqrt{s} = 7$ TeV analysis for (a) $m_{\ell_0\ell_1}$, (b) $m_{\ell_0\ell_2}$, (c) $m_{\ell_1\ell_2}$ and (d) $m_{\ell\ell\ell}$. The plotting scheme follows the one described in the caption of figure C.1.

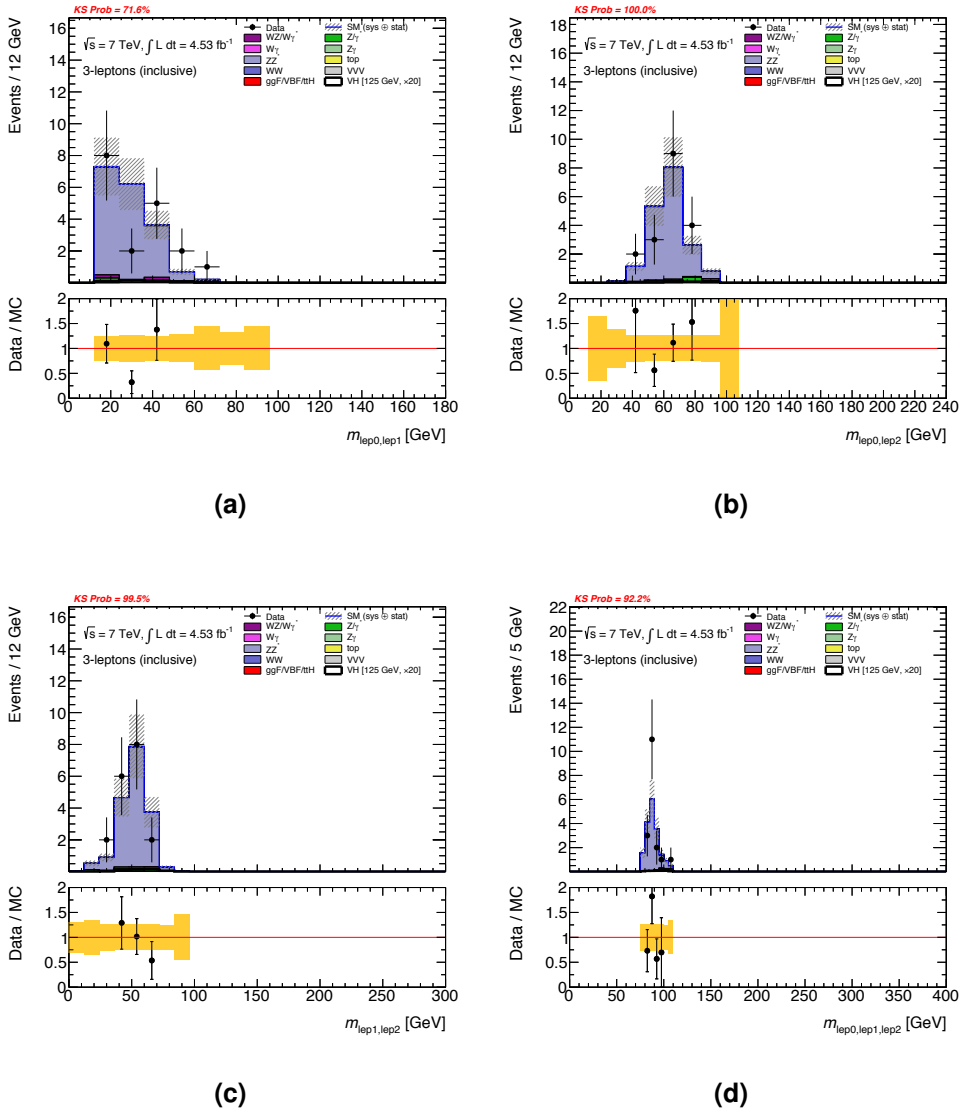

Figure C.10 Distributions in the ZZ CR of the $\sqrt{s} = 7$ TeV analysis for (a) $m_{\ell_0\ell_1}$, (b) $m_{\ell_0\ell_2}$, (c) $m_{\ell_1\ell_2}$ and (d) $m_{\ell\ell\ell}$. The plotting scheme follows the one described in the caption of figure C.1.

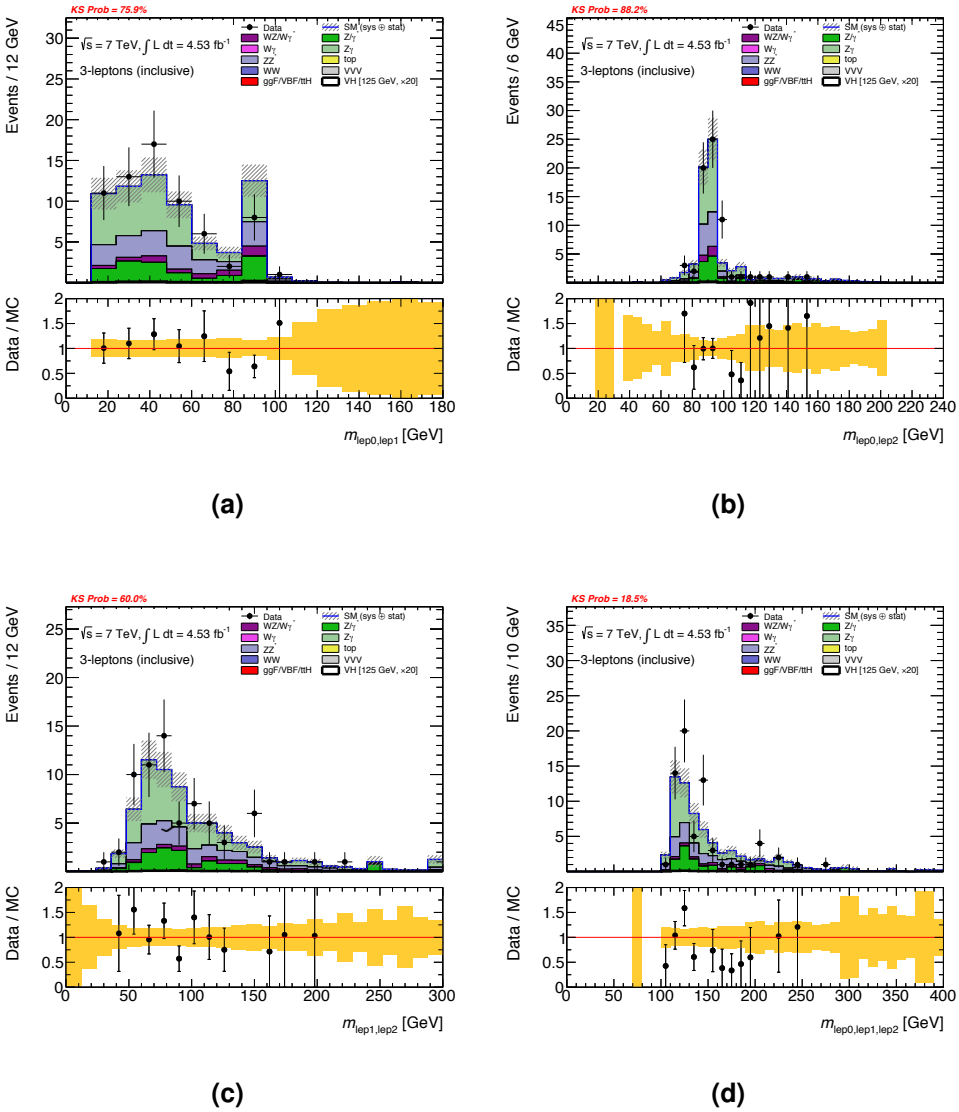

Figure C.11 Distributions in the Z+jets CR of the $\sqrt{s} = 7$ TeV analysis for (a) $m_{\ell_0\ell_1}$, (b) $m_{\ell_0\ell_2}$, (c) $m_{\ell_1\ell_2}$ and (d) $m_{\ell\ell\ell}$. The plotting scheme follows the one described in the caption of figure C.1.

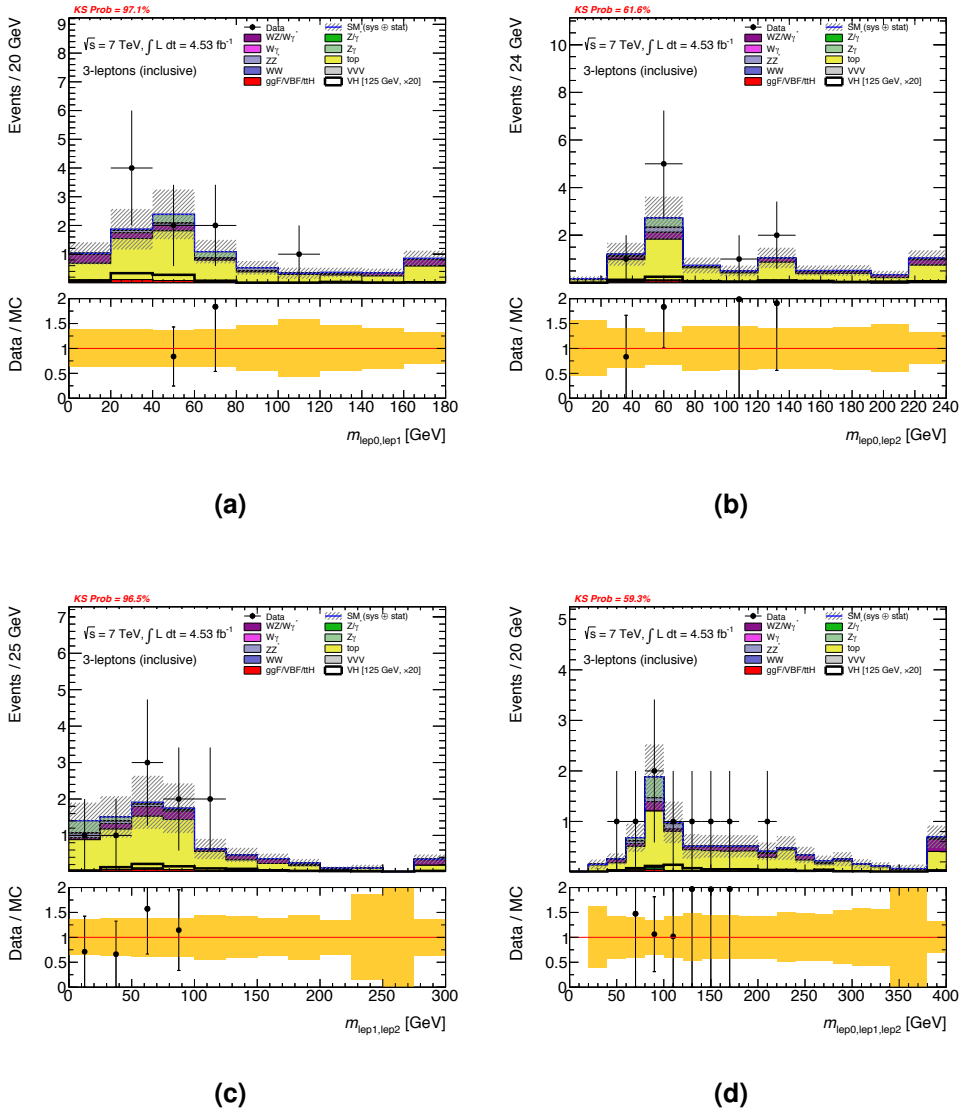

Figure C.12 Distributions in the Top CR of the $\sqrt{s} = 7$ TeV analysis for (a) $m_{\ell_0\ell_1}$, (b) $m_{\ell_0\ell_2}$, (c) $m_{\ell_1\ell_2}$ and (d) $m_{\ell\ell\ell}$. The plotting scheme follows the one described in the caption of figure C.1.

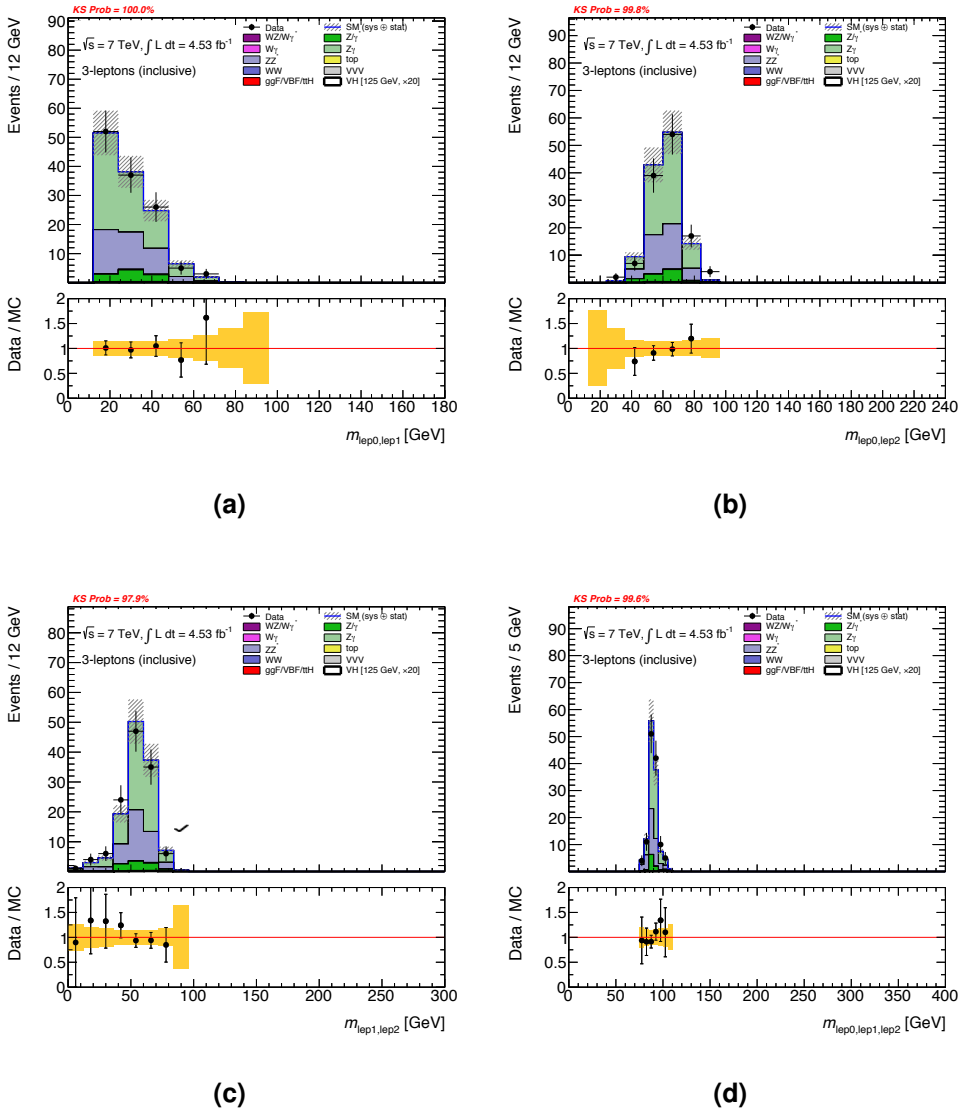

Figure C.13 Distributions in the $Z\gamma$ CR of the $\sqrt{s} = 7$ TeV analysis for (a) $m_{\ell_0\ell_1}$, (b) $m_{\ell_0\ell_2}$, (c) $m_{\ell_1\ell_2}$ and (d) $m_{\ell\ell\ell}$. The plotting scheme follows the one described in the caption of figure C.1.

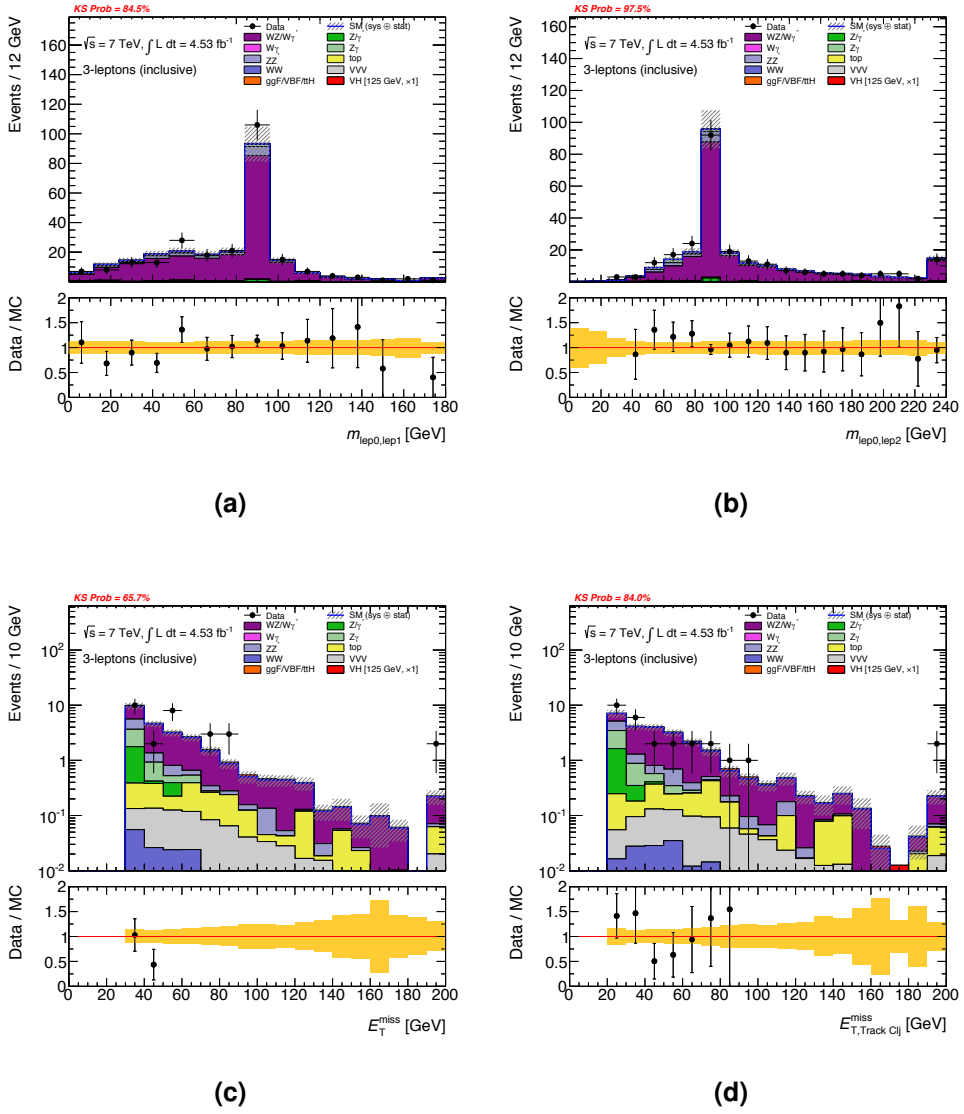

Figure C.14 Distributions in the combined 3SF and 1SFOS SRs of the $\sqrt{s} = 7$ TeV analysis for (a) $m_{\ell_0\ell_1}$, (b) $m_{\ell_0\ell_2}$, (c) E_T^{miss} and (d) p_T^{miss}. Distributions (a) and (b) are after applying the selections in table 5.5 down to the E_T^{miss} and p_T^{miss} requirements, while (c) and (d) are after the Z-mass veto requirement. The plotting scheme follows the one described in the caption of figure C.6.

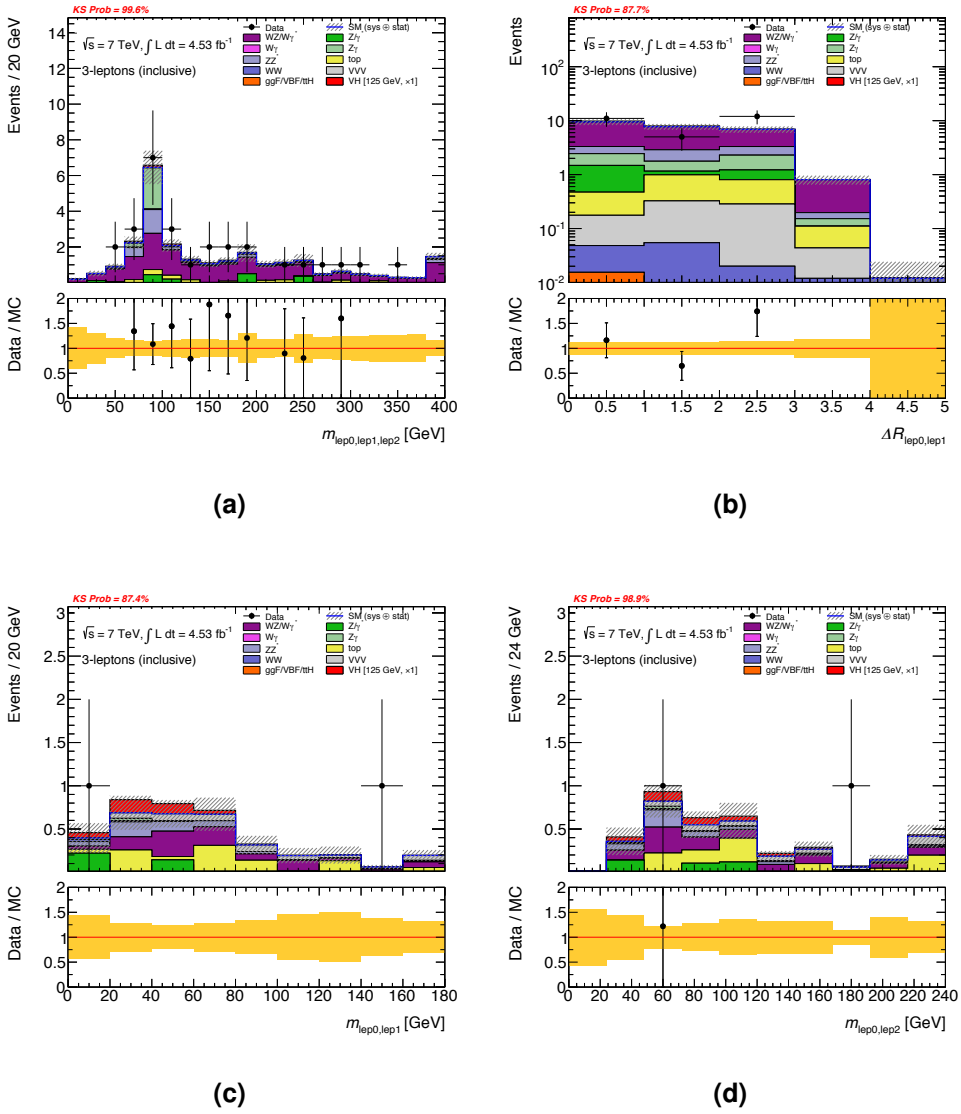

Figure C.15 Distributions of (a) $m_{\ell\ell\ell}$ and (b) $\Delta R_{\ell_0\ell_1}$ in the combined 3SF and 1SFOS SRs of the $\sqrt{s} = 7$ TeV analysis, as well as (c) $m_{\ell_0\ell_1}$ and (d) $m_{\ell_0\ell_2}$ in the 0SFOS SR. Distributions (a) and (b) are after applying the selections in table 5.5 down to Z-mass veto requirement, while (c) and (d) are after the number of b-tagged jets requirement. The plotting scheme follows the one described in the caption of figure C.6.

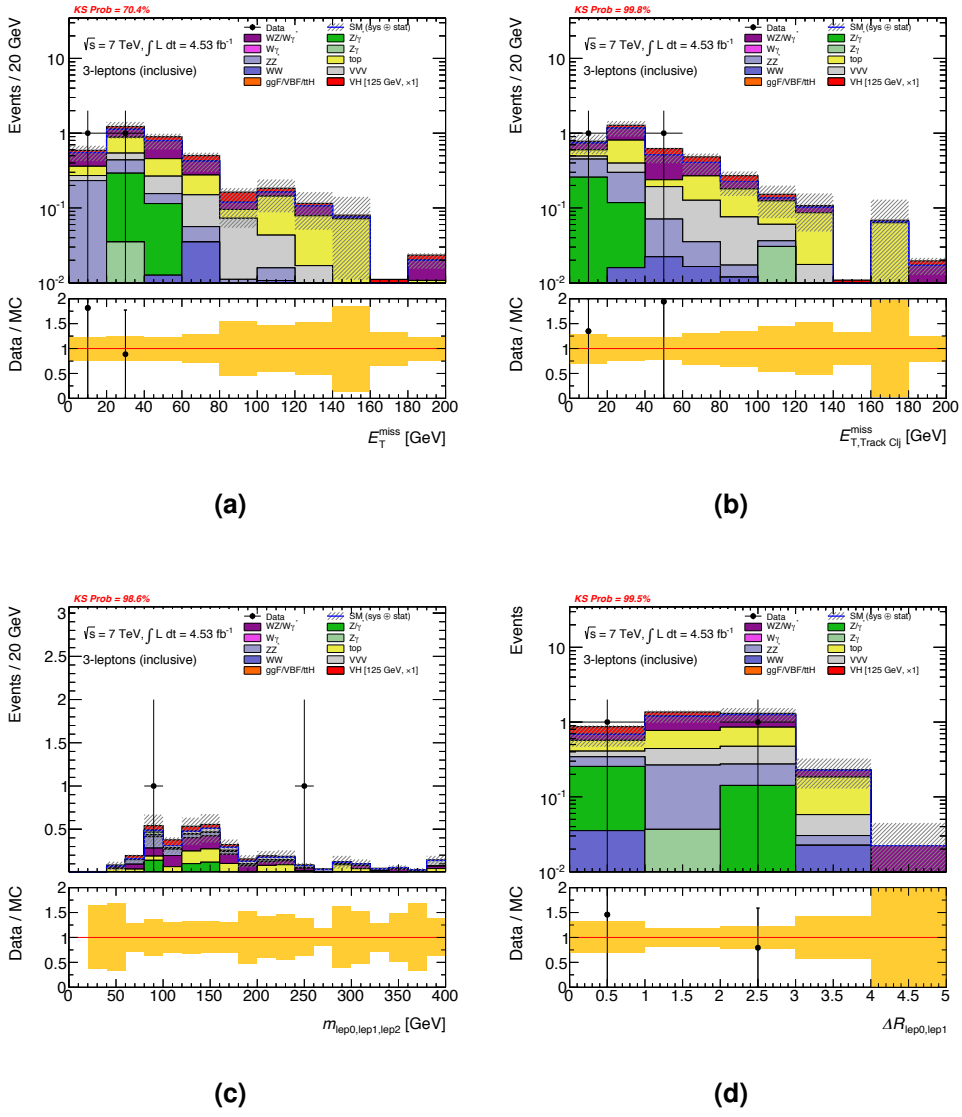

Figure C.16 Distributions in the 0SFOS SR of the $\sqrt{s} = 7$ TeV analysis for (a) E_T^{miss}, (b) p_T^{miss}, (c) $m_{\ell\ell\ell}$ and (d) $\Delta R_{\ell_0\ell_1}$. All distributions are after applying the selections in table 5.5 down to the number of b-tagged jets requirement. The plotting scheme follows the one described in the caption of figure C.6.

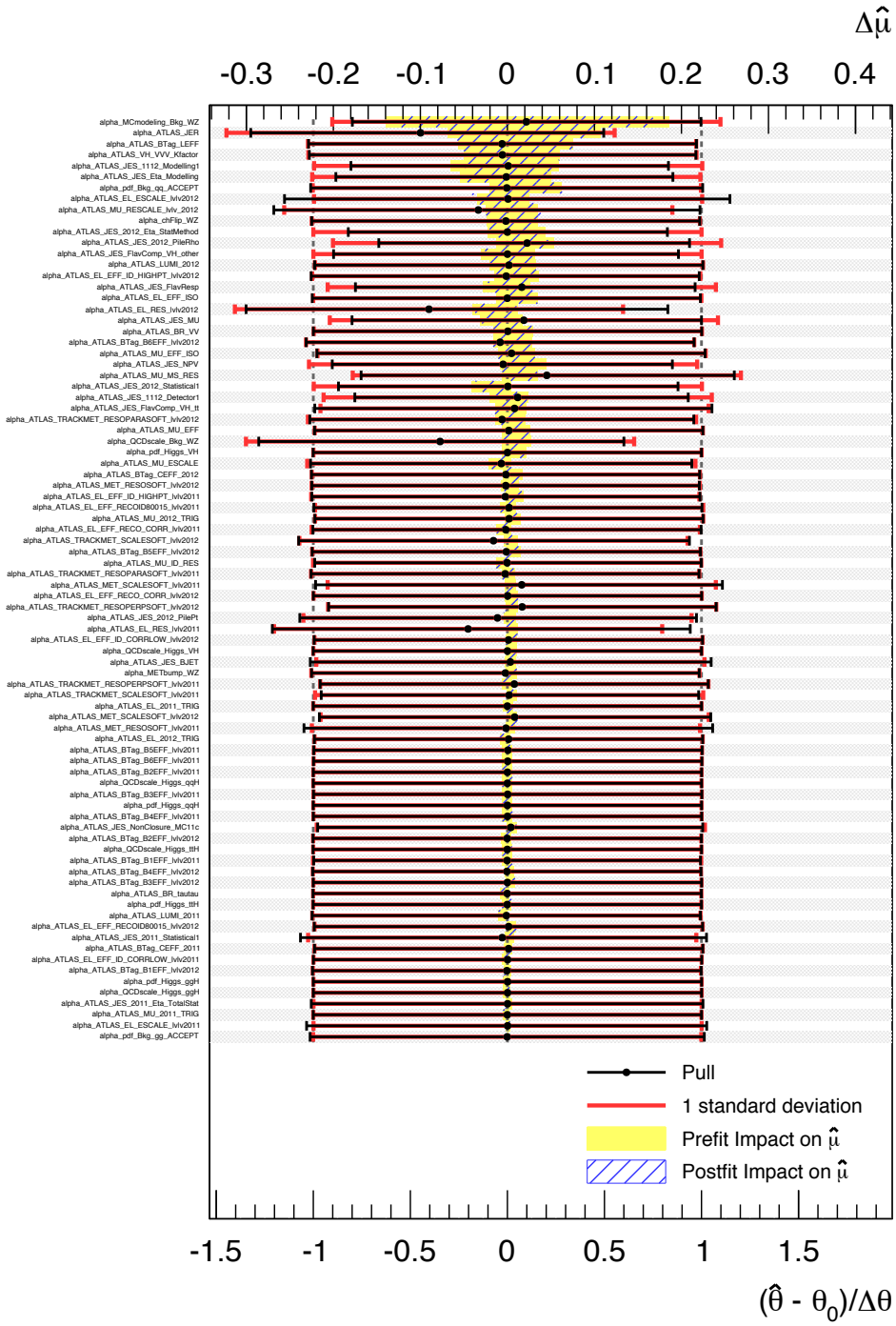

Figure C.17 Summary of the performance of the statistical fit for the combined $\sqrt{s}$ = 7 and 8 TeV analysis. The black points indicate the fitted values of the nuisance parameters associated to the systematic uncertainties ($\hat{\boldsymbol{\theta}}$) compared to the nominal values ($\boldsymbol{\theta}_0$), relative to the 1σ uncertainty on those values ($\Delta\boldsymbol{\theta}$). The nominal uncertainties on the nuisance parameters are shown by the red lines. The blue and yellow bands show the post-fit and pre-fit impact, respectively, on the fitted value of the signal strength ($\hat{\mu}$). The systematic uncertainties are listed in decreasing order of their impact on $\hat{\mu}$.

Appendix D: Additional Plots from the $\sqrt{s} = 13$ TeV Analysis

This appendix contains additional plots from the $\sqrt{s} = 13$ TeV analysis presented in chapter 5 that searched for the WH production of the Higgs boson with $H \rightarrow WW^*$ decay. This will include:

- Distributions in the control regions (figures D.1-D.6).
- Distributions in the ZZ validation region (figure D.7).
- Distributions in the signal regions (figures D.8-D.10).
- A summary of the performance of the statistical fit (figure D.11).

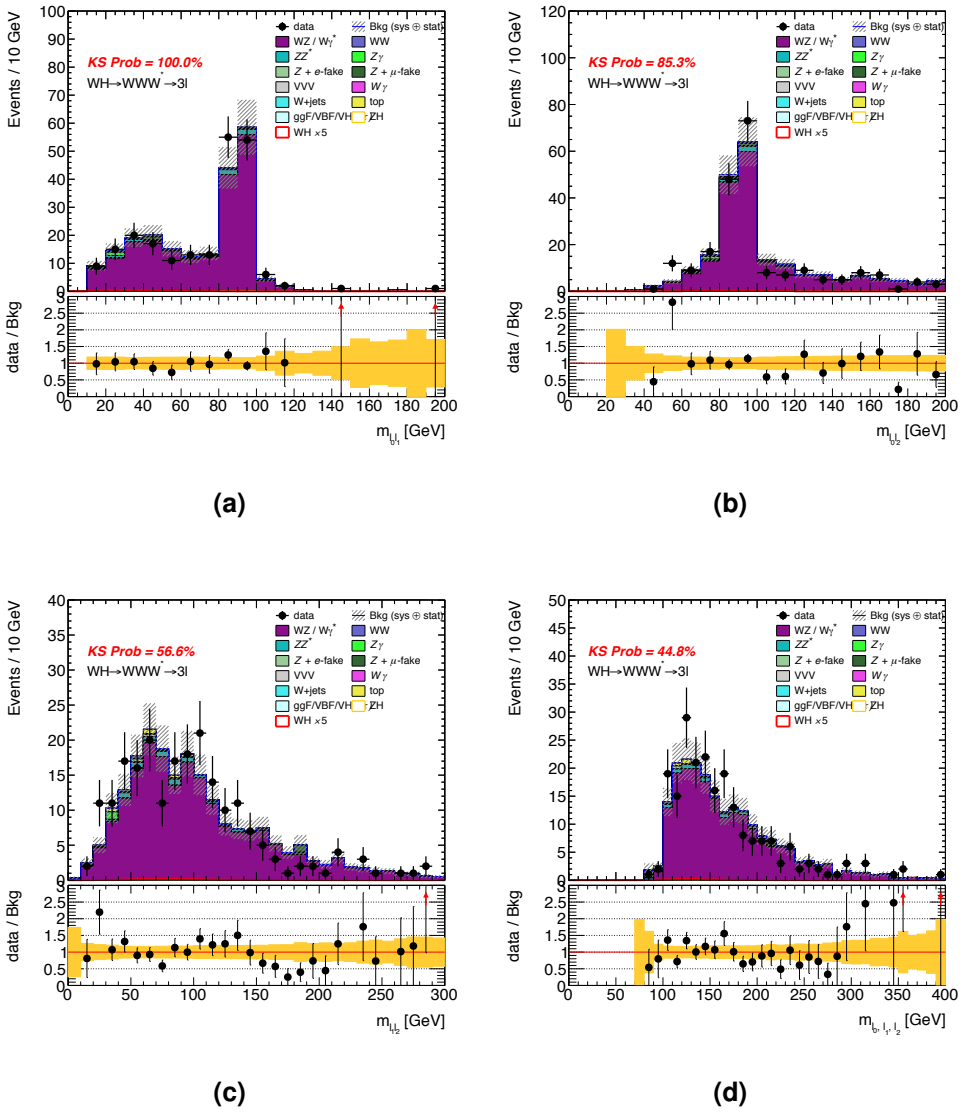

Figure D.1 Distributions in the WZ CR of the $\sqrt{s} = 13$ TeV analysis for (a) $m_{\ell_0\ell_1}$, (b) $m_{\ell_0\ell_2}$, (c) $m_{\ell_1\ell_2}$ and (d) $m_{\ell\ell\ell}$. The data (points) are compared to the background expectation (stacked filled histograms). The total uncertainty on the total background estimate is represented by the hatched area, and includes both the statistical and systematic components. The background NFs are applied. The signal (red line) is overlaid, and scaled by a factor of 5. The KS test probability [171] is indicated on the top left of each plot. The lower panel shows the ratio between the observed data and the total background expectation.

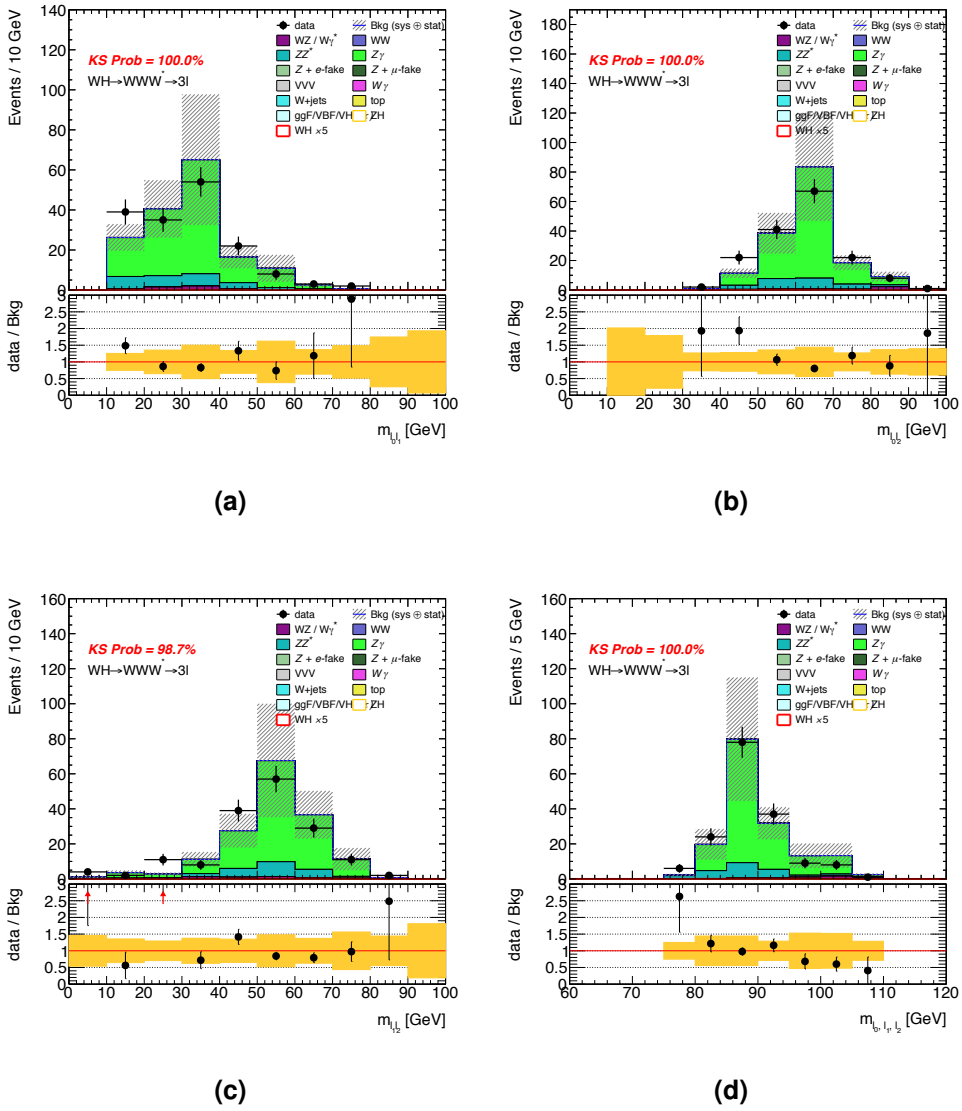

Figure D.2 Distributions in the $Z\gamma$ CR of the $\sqrt{s} = 13$ TeV analysis for (a) $m_{\ell_0\ell_1}$, (b) $m_{\ell_0\ell_2}$, (c) $m_{\ell_1\ell_2}$ and (d) $m_{\ell\ell\ell}$. The plotting scheme follows the one described in the caption of figure D.1.

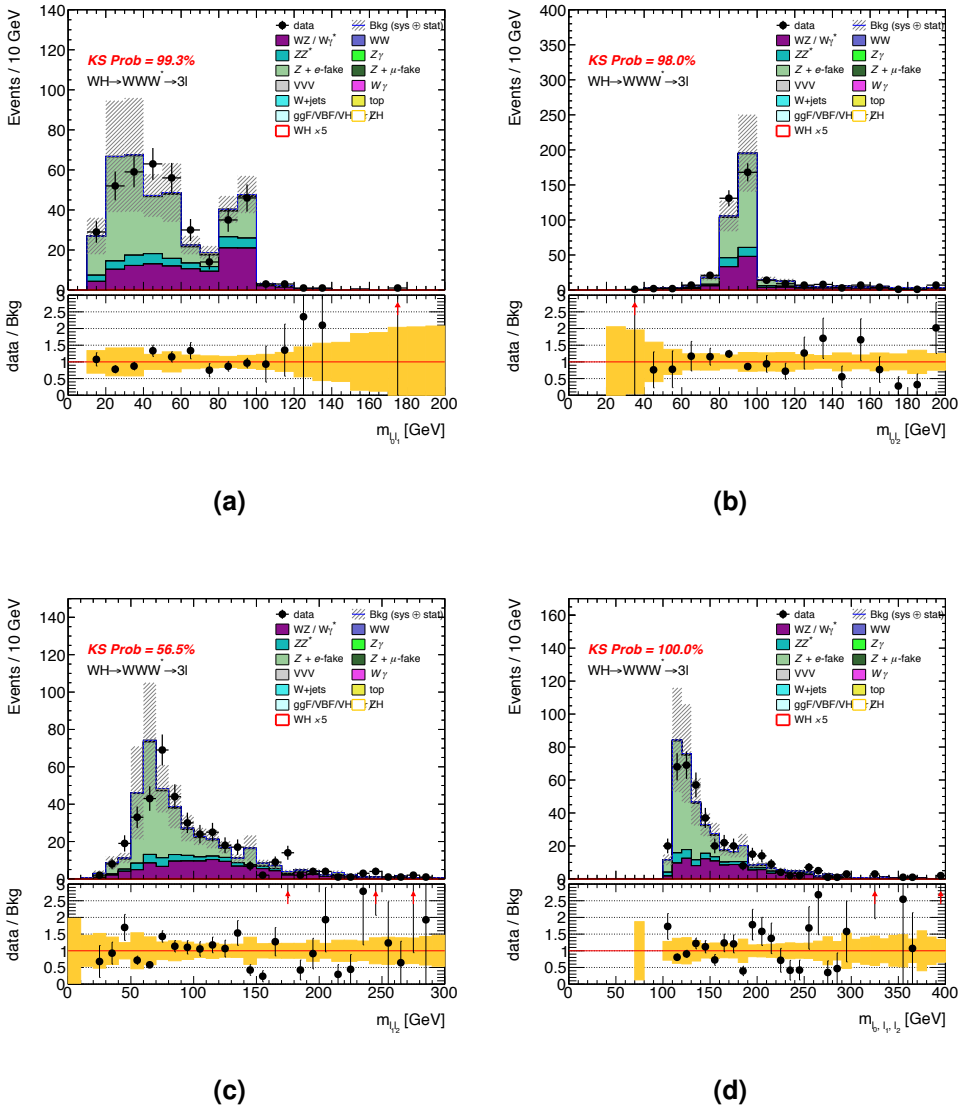

Figure D.3 Distributions in the Z+jets CR (e-fake) of the $\sqrt{s} = 13$ TeV analysis for (a) $m_{\ell_0\ell_1}$, (b) $m_{\ell_0\ell_2}$, (c) $m_{\ell_1\ell_2}$ and (d) $m_{\ell\ell\ell}$. The plotting scheme follows the one described in the caption of figure D.1.

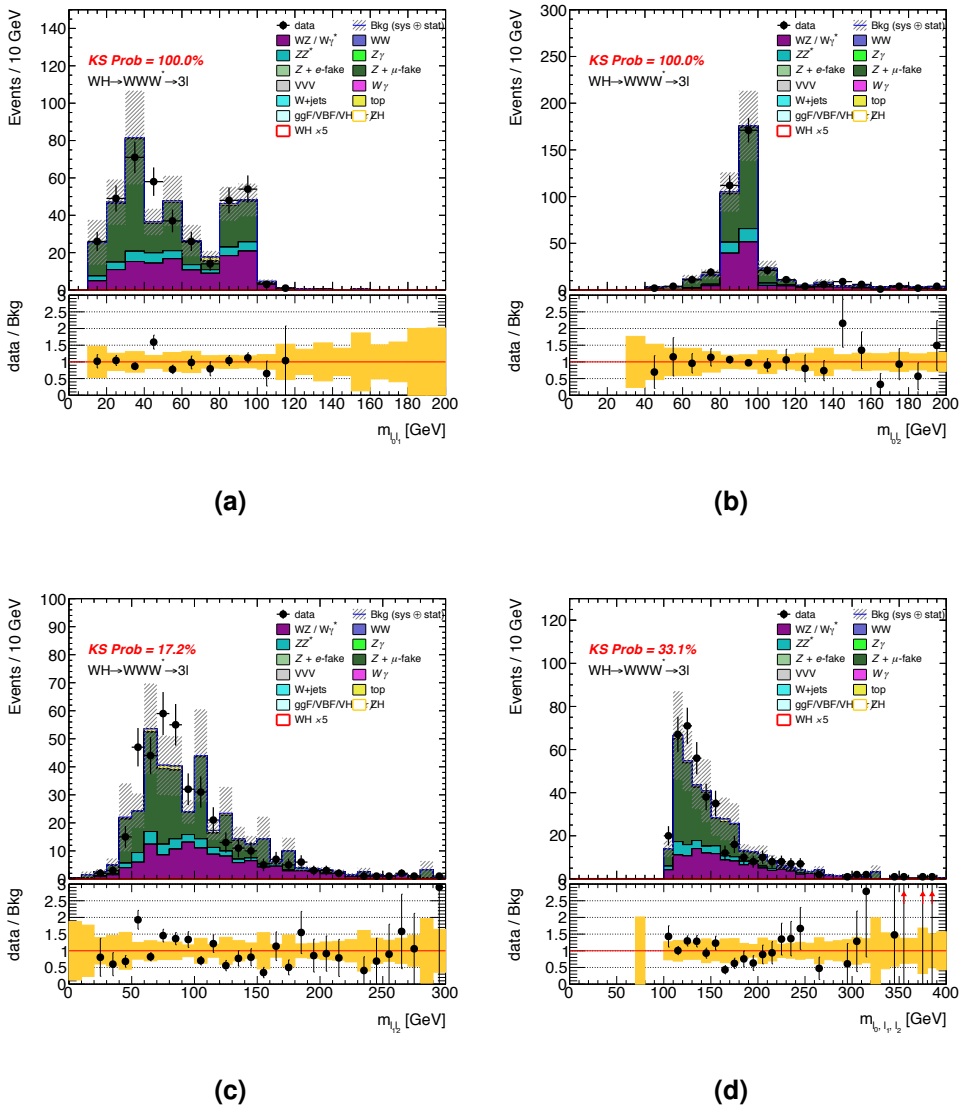

Figure D.4 Distributions in the Z+jets CR (μ-fake) of the $\sqrt{s} = 13$ TeV analysis for (a) $m_{\ell_0\ell_1}$, (b) $m_{\ell_0\ell_2}$, (c) $m_{\ell_1\ell_2}$ and (d) $m_{\ell\ell\ell}$. The plotting scheme follows the one described in the caption of figure D.1.

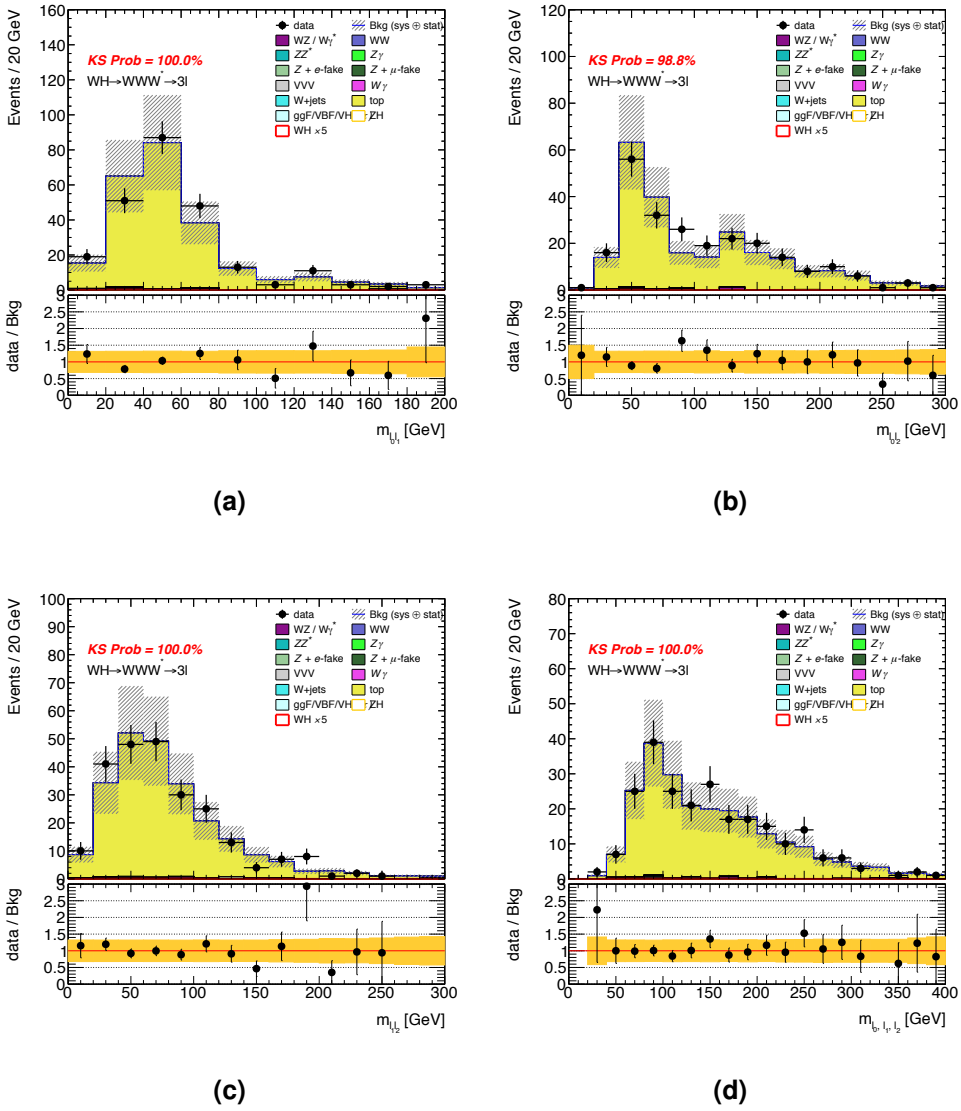

Figure D.5 Distributions in the Top CR (Z-dominated) of the $\sqrt{s} = 13$ TeV analysis for (a) $m_{\ell_0\ell_1}$, (b) $m_{\ell_0\ell_2}$, (c) $m_{\ell_1\ell_2}$ and (d) $m_{\ell\ell\ell}$. The plotting scheme follows the one described in the caption of figure D.1.

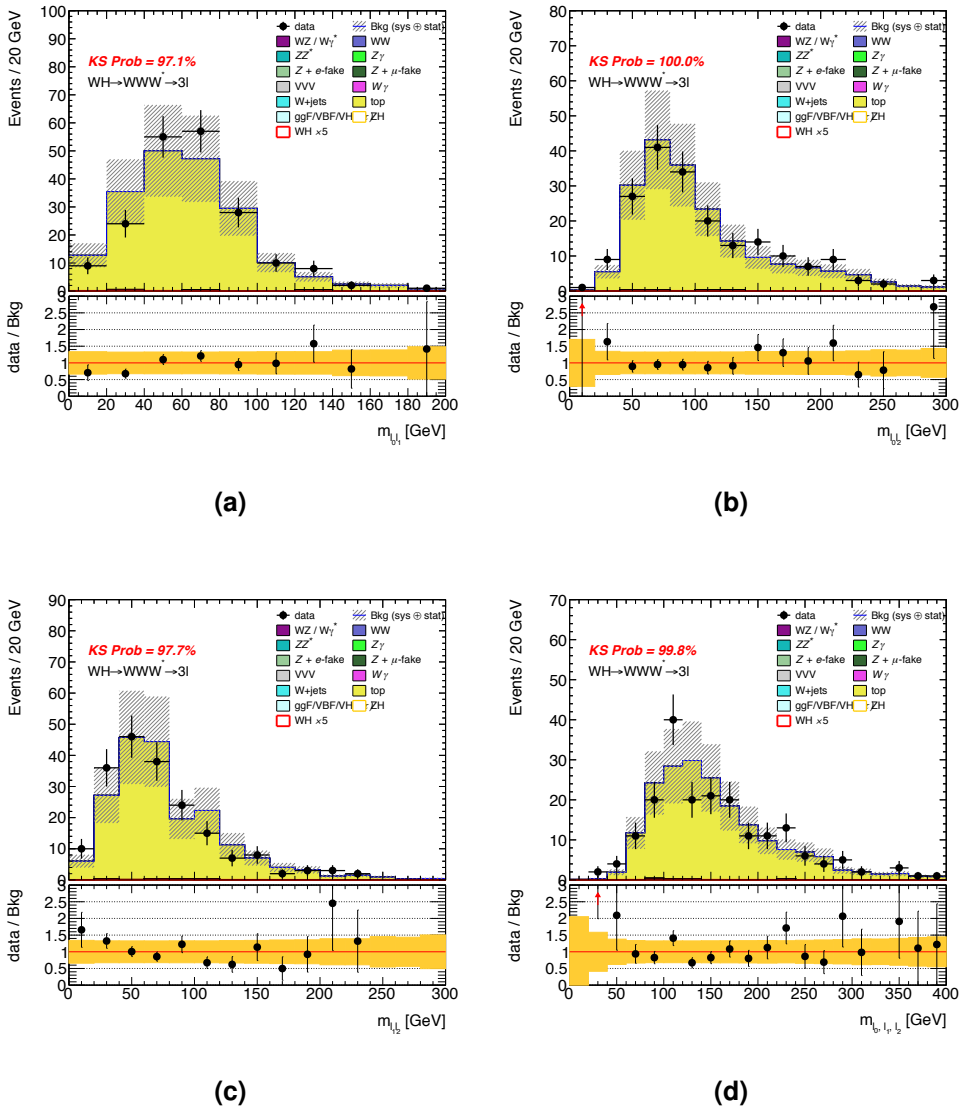

Figure D.6 Distributions in the Top CR (Z-depleted) of the $\sqrt{s}$ = 13 TeV analysis for (a) $m_{\ell_0\ell_1}$, (b) $m_{\ell_0\ell_2}$, (c) $m_{\ell_1\ell_2}$ and (d) $m_{\ell\ell\ell}$. The plotting scheme follows the one described in the caption of figure D.1.

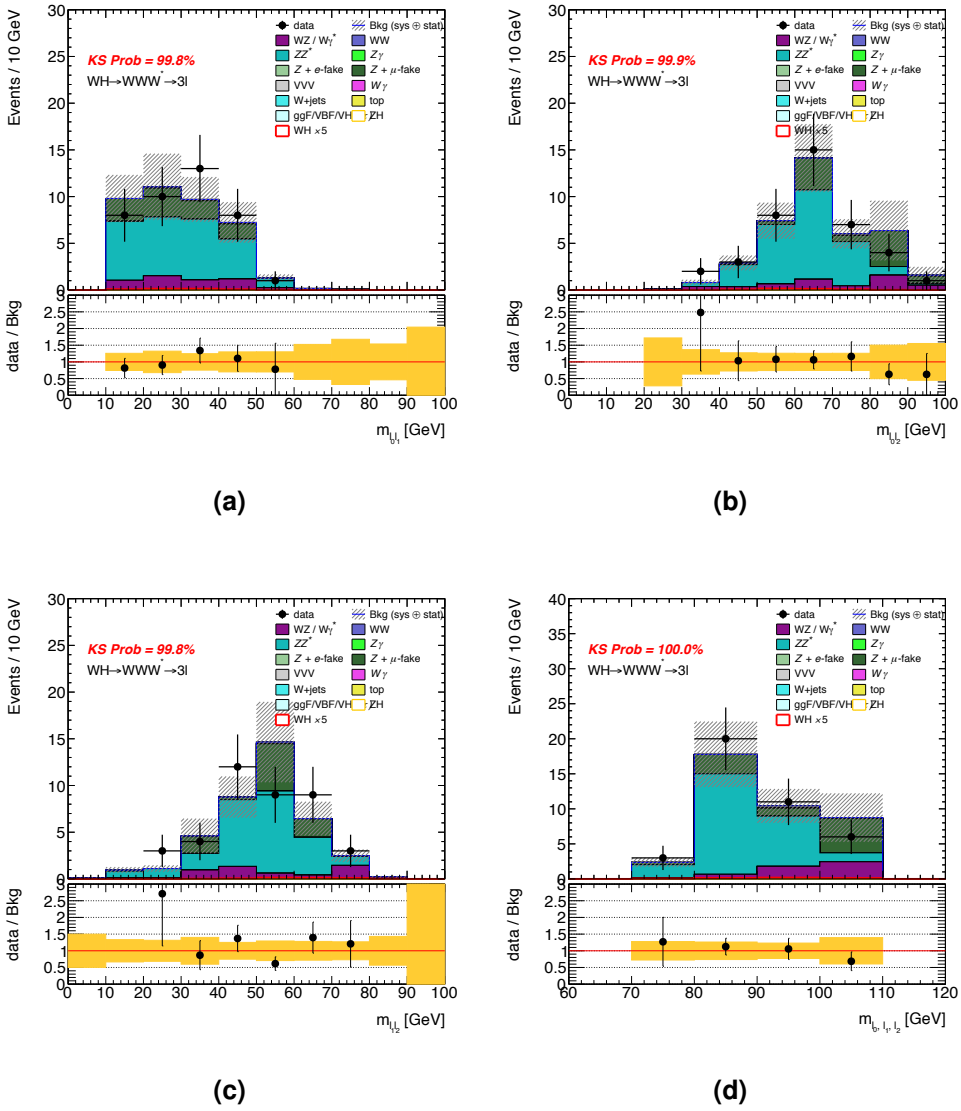

Figure D.7 Distributions in the ZZ VR of the $\sqrt{s} = 13$ TeV analysis for (a) $m_{\ell_0\ell_1}$, (b) $m_{\ell_0\ell_2}$, (c) $m_{\ell_1\ell_2}$ and (d) $m_{\ell\ell\ell}$. The plotting scheme follows the one described in the caption of figure D.1.

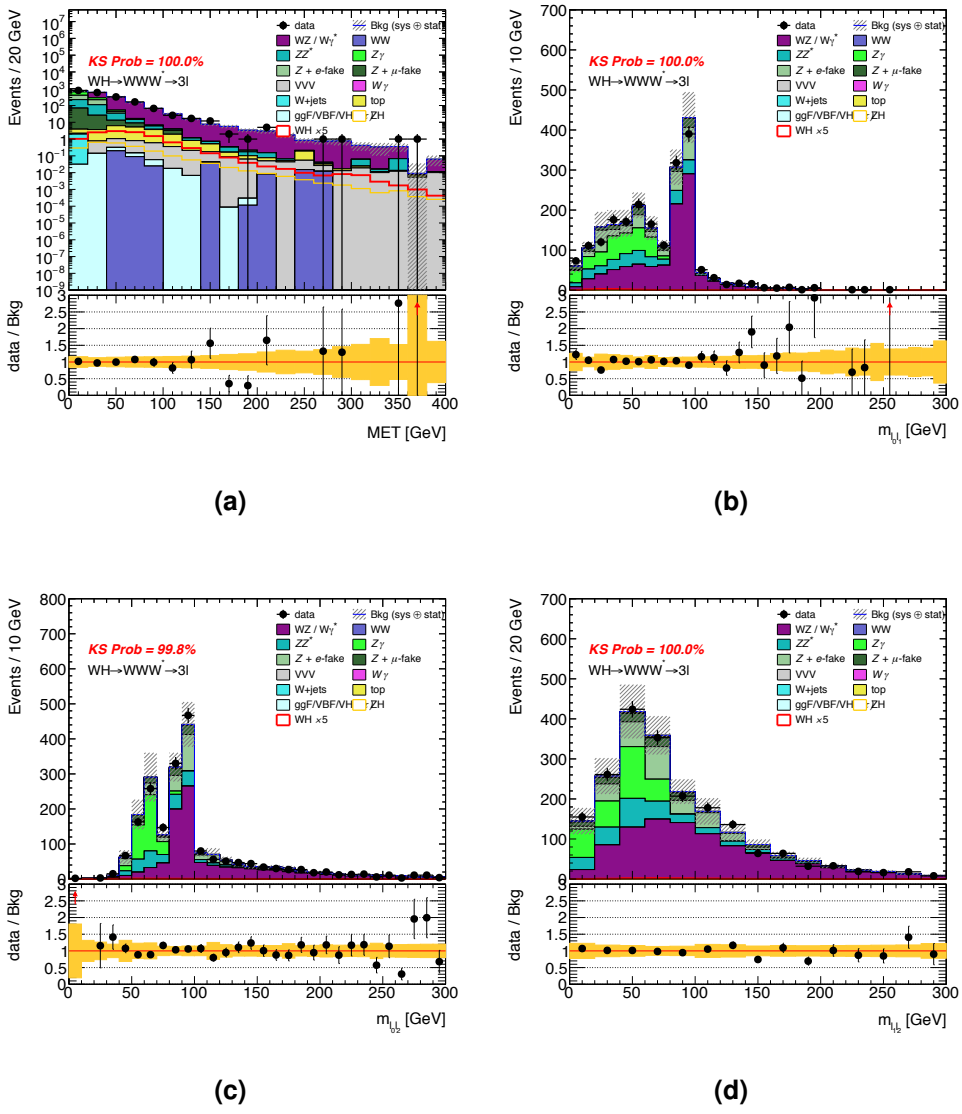

Figure D.8 Distributions in the Z-dominated SR of the $\sqrt{s}$ = 13 TeV analysis for (a) E_T^{miss}, (b) $m_{\ell_0\ell_1}$, (c) $m_{\ell_0\ell_2}$ and (d) $m_{\ell_1\ell_2}$. All distributions are after applying the selections in table 5.16 down to the number of b-tagged jets requirement. The plotting scheme follows the one described in the caption of figure D.1.

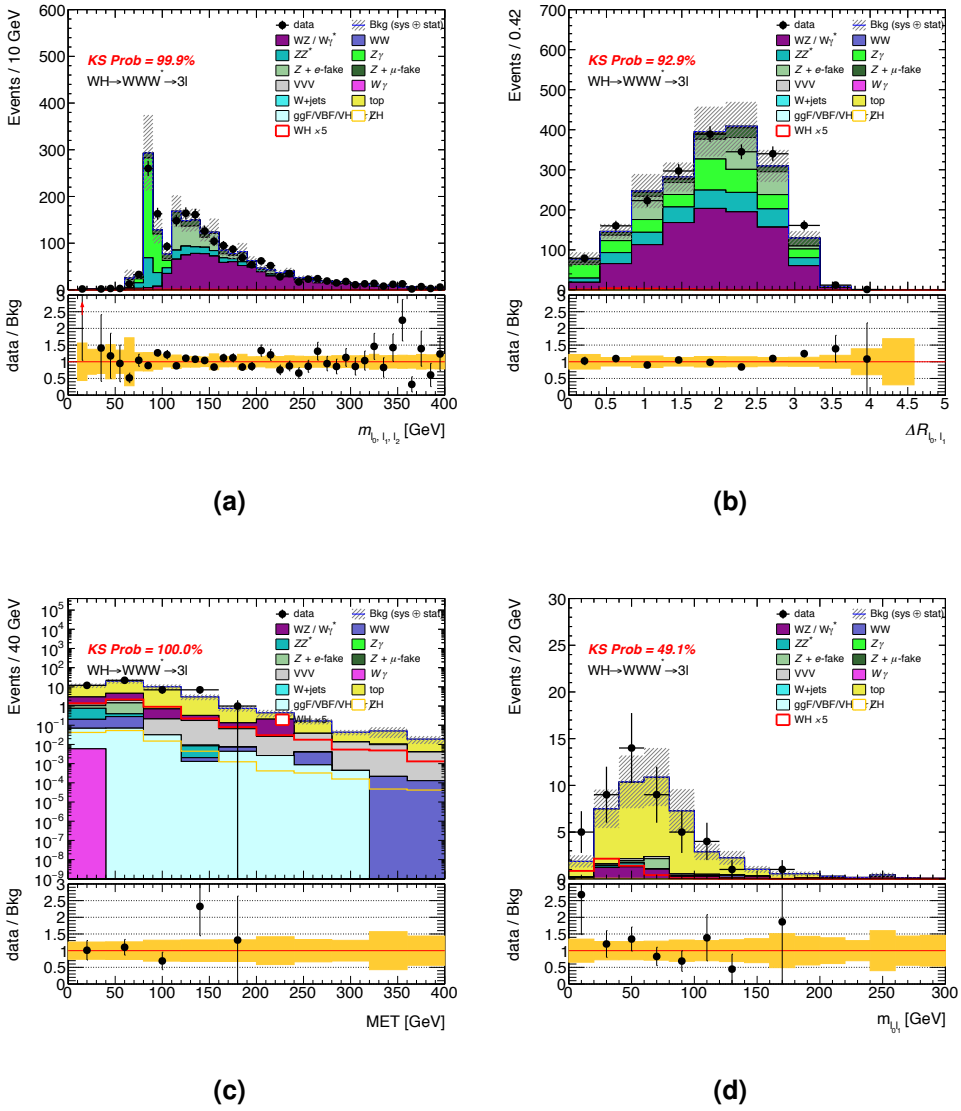

Figure D.9 Distributions of (a) $m_{\ell\ell\ell}$ and (b) $\Delta R_{\ell_0\ell_1}$ in the Z-dominated SR of the $\sqrt{s} = 13$ TeV analysis, as well as (c) E_T^{miss} and (d) $m_{\ell_0\ell_1}$ in the Z-depleted SR. Distributions (a) and (b) are after applying the selections in table 5.16 down to the number of b-tagged jets requirement, while (c) and (d) are after the requirement on the lepton flavour combination. The plotting scheme follows the one described in the caption of figure D.1.

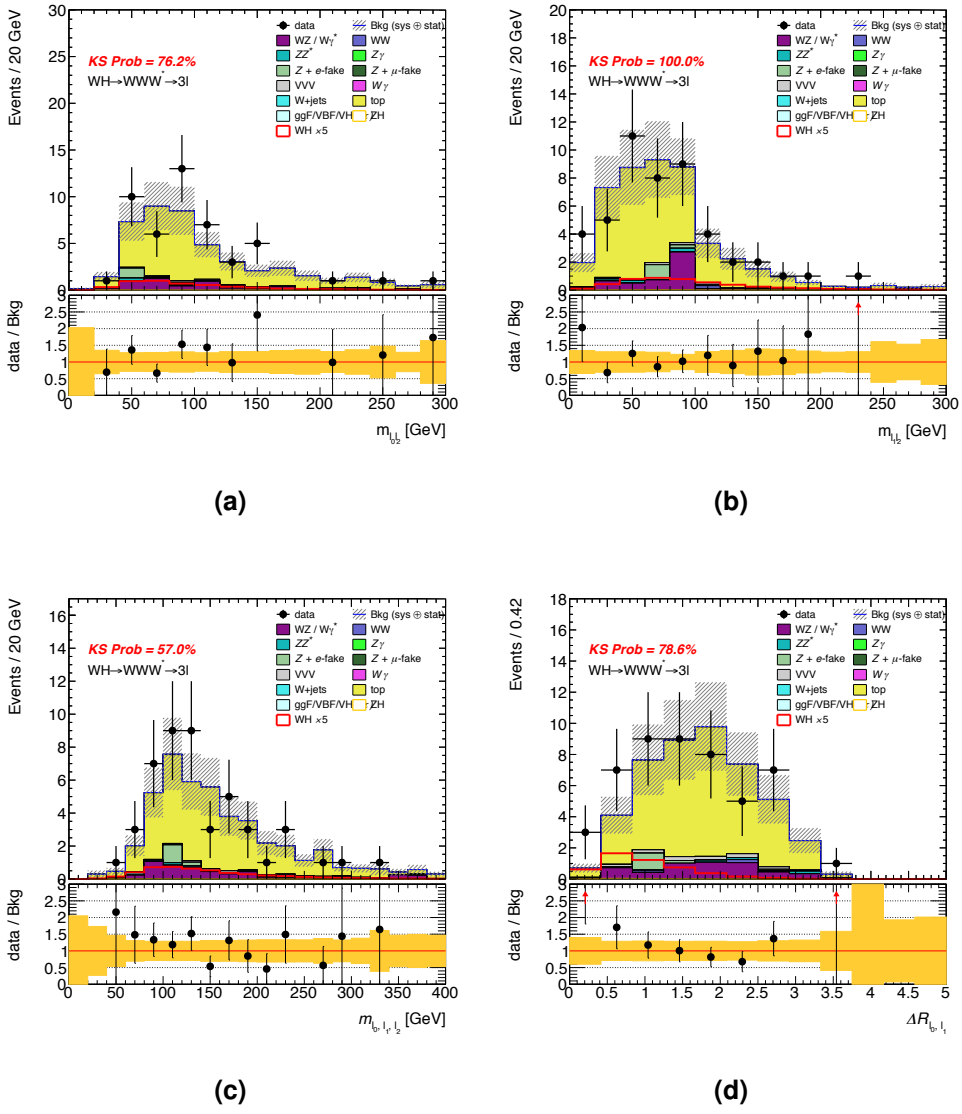

Figure D.10 Distributions in the Z-depleted SR of the $\sqrt{s}$ = 13 TeV analysis for (a) $m_{\ell_0\ell_2}$, (b) $m_{\ell_1\ell_2}$, (c) $m_{\ell\ell\ell}$ and (d) $\Delta R_{\ell_0\ell_1}$. All distributions are after applying the selections in table 5.16 down to the requirement on the lepton flavour combination. The plotting scheme follows the one described in the caption of figure D.1.

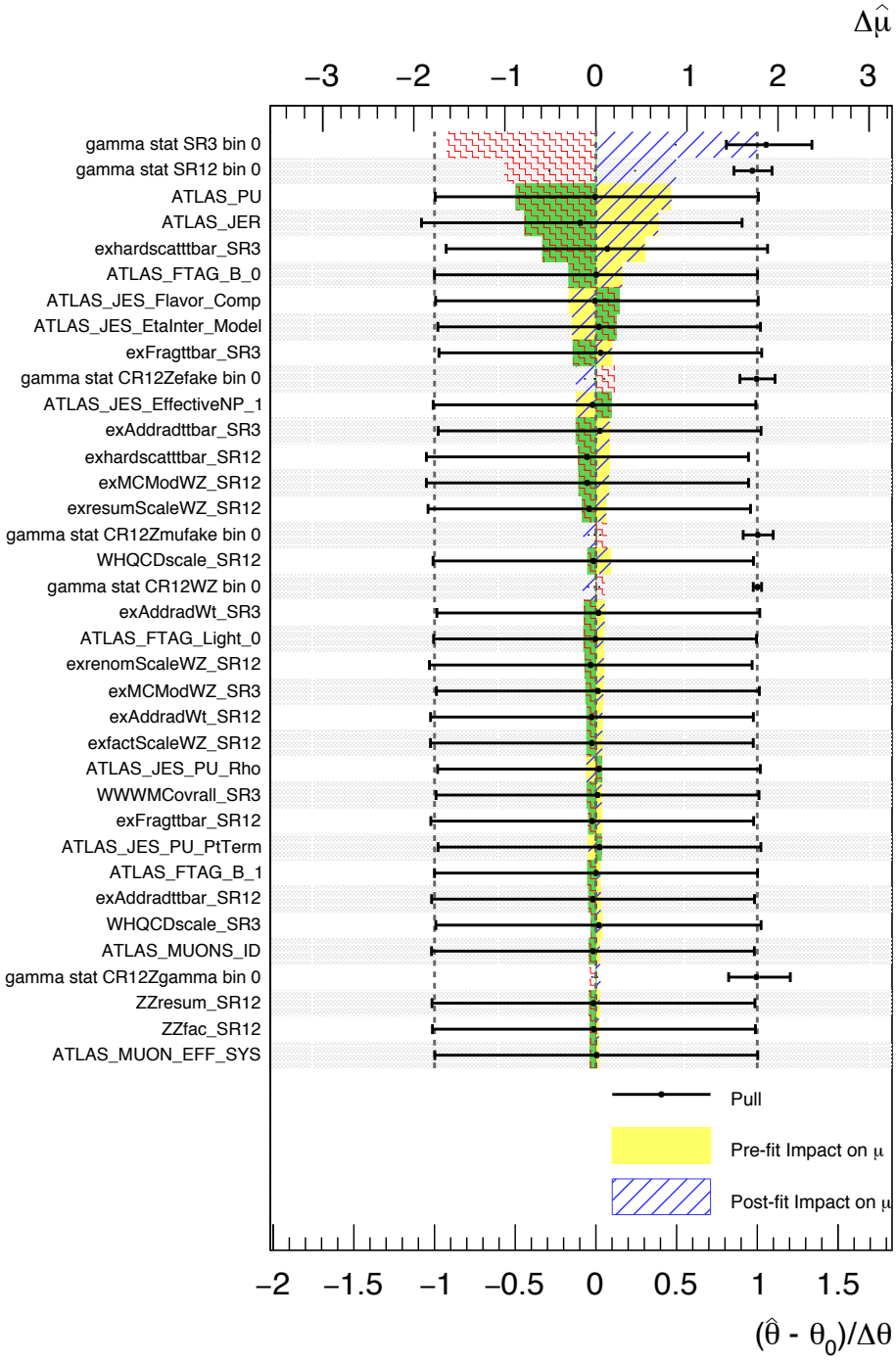

Figure D.11 Summary of the performance of the statistical fit for the $\sqrt{s} = 13$ TeV analysis. The black points indicate the fitted values of the nuisance parameters ($\hat{\boldsymbol{\theta}}$) compared to the nominal values ($\boldsymbol{\theta}_0$), relative to the 1σ uncertainty on those values ($\Delta\boldsymbol{\theta}$). The blue and yellow bands show the post-fit and pre-fit impact, respectively, on the fitted value of the signal strength ($\hat{\mu}$). The nuisance parameters are listed in decreasing order of their impact on $\hat{\mu}$.

List of Tables

List of Figures